Large eddy simulations of Arctic stratus clouds

Thomas Daniel Pleavin

University of Leeds

School of Earth and Environment

Submitted in accordance with the requirements for the degree of

Doctor of Philosophy

March 2013

Declaration of authorship

The candidate confirms that the work submitted is his own and that appropriate credit has been given where reference has been made to the work of others. This copy has been supplied on the understanding that it is copyright material and that no quotation from the thesis may be published without proper acknowledgement.

Acknowledgements

First and foremost i would like to thank my supervisors Ian Brooks and Steven Dobbie for all the help, support and encouragement they have given me throughout my PhD. I would also like to thank my external supervisor Adrian Lock of the UK Met office, for his good advice, encouragement and guidance during this time.

This research project was made possible through funding from the U.K. Natural Environmental Research Council with a CASE award from the UK Met Office. A further thanks goes out to the UK Met Office for providing the use of the UK Large Eddy Model and to Adrian Hill, Ben Shipway and Steven Pickering for their invaluable support in running the model.

This work is part of ASCOS (the Arctic Summer Cloud Ocean Study), an IPY project under the AICIA - IPY umbrella and an endorsed SOLAS project. ASCOS was made possible by funding from the Knut and Alice Wallenberg Foundation and the DAMOCLES European Union 6th Framework Program Integrated Research Project. The Swedish Polar Research Secretariat (SPRS) provided access to the icebreaker Oden and logistical support. I am grateful to the Chief Scientists Caroline Leck and Michael Tjernström for planning and coordinating ASCOS, to the SPRS logistical staff and to Oden's Captain Mattias Peterson and his crew. A special thanks is also given to the ASCOS meteorology team: Michael Tjernström, Ian Brooks, Thorsten Mauritsen, Ola Persson, Matthew Shupe, Cathryn Birch and Joe Sedlar; and to Barbara Brooks of the Arctic Mechanisms of Interaction between the Surface and Atmosphere (AMISA) campaign.

On a personal note, the project couldn't have been completed with the support and friendship from a number of people. Thanks to Adham, Peter, Camille, Rachel, Doyle, Alex, James, Dan, Robbie, Elly, and to my loving family: Susan, John, Rachel, Joseph and Daisy.

Abstract

Mixed-phase Arctic stratocumulus clouds are ubiquitous to the region during the summer months. However, despite their prevalence, very little is known about the processes which maintain the cloud. Recent observations have shown that Arctic stratocumulus commonly extend into the temperature inversion which caps the Arctic boundary layer. This is atypical to sub-tropical stratocumulus where the cloud top is found in the vicinity of the inversion base, and unexpected as strong longwave radiative cooling would be expected to keep the cloud top and inversion base heights in equilibrium. Uniquely to the Arctic, inversions in specific humidity are also commonly observed coincident with temperature inversions, and this is thought to contribute to the clouds' subsistence in the strongly stable inversion layer.

In this thesis, observations from the Arctic Summer Cloud Ocean Study (ASCOS) are used to characterize the lower Arctic atmosphere and provide the basis for simulations of stratocumulus cloud encroachment into the Arctic temperature inversion. Observations show that cloud extending into the inversion by more than 100 m was a common occurrence during ASCOS, which is consistent with measurements made during previous summer field campaigns. Simulations made with the Met Office Large Eddy Model (LEM) were used to model the encroachment, and results suggest that the depth of encroachment has a high correlation with the humidity inversion strength.

A number of different cloud-inversion regimes were identified from the model simulations. When specific humidity fell off inside the temperature inversion, the high relative humidity of the region just above the inversion base was found to allow encroachment of cloud up to 40 m into the inversion layer. While in the presence of a specific humidity inversion the encroachment was larger reaching a maximum of 200 m. The presence of specific humidity inversions and their relationship to the encroaching cloud was determined to be self-sustaining, and the cloud found to remain at a quasi-stable depth for as long as a moisture source is available to replenish the loss of water from ice precipitation. However, encroachment of cloud into the inversion was shown to cause a significant reduction in the buoyant production of TKE at cloud top, which led to turbulence shutting off completely in the clouds with the largest encroachment depth. This caused a thermal adjustment of the inversion layer to the cloud which led a reduction in the encroachment

depth. The overall impact of encroachment on boundary layer turbulence was found to be significant, with TKE reduced by up to 90 % in the simulations with the largest encroachment depth.

Contents

List of figures

List of tables

Abbreviations

AOE-97	Arctic Ocean Experiment - 1997
AOE-2001	Arctic Ocean Experiment - 2001
ASE	Arctic Stratus Experiment
ASCOS	Arctic Summer Cloud Ocean Study
AMISA	Arctic Mechanisms of Interaction between the Surface and Atmosphere
BASE	Beaufort and Arctic Storms Experiment
BL	Boundary Layer
CCN	Cloud Condensation Nuclei
CRM	Cloud Resolving Model
CTEI	Cloud Top Entrainment Instability
ECMWF	European Centre for Medium-Range Weather Forecasts
EZ	Entrainment Zone
FIRE	First International Satellite Cloud Climatology Project Regional Experiment
GCM	General Circulation Model
GCSS	Global Water and Energy Experiment Cloud System Study
IAOE-91	International Arctic Ocean Experiment - 1991
ISDAC	Indirect and Semi-Direct Aerosol Campaign
IWC	Ice Water Content
IWP	Ice Water Path
IN	Ice Nuclei
LEM	Large Eddy Model
LES	Large Eddy Simulation
LW	Longwave
LWC	Liquid Water Content
LWP	Liquid Water Path
M-PACE	Mixed Phase Arctic Cloud Experiment
ML	Mixed Layer
MMCR	Millimeter Cloud Radar
MWR	Microwave Radiometer
NASA	National Aeronautics and Space Administration

RCM	Regional Climate Model
RH	Relative Humidity
SHEBA	Surface Heat Budget of the Arctic Ocean Experiment
SGS	Sub-grid Scale
STBL	Stratocumulus Topped Boundary Layer
SW	Shortwave
TKE	Turbulent Kinetic Energy
UKMO	UK Met Office

Parameters

z	Height above ground level
z_{cb}	Cloud base height
z_{ct}	Cloud top height
z_{cbi}	Ice cloud base height
z_{cbi}	Ice cloud top height
z_i	Boundary layer top
z_{ib}	Temperature inversion base height
z_{it}	Temperature inversion top height
z_{max}	Maximum normalised height within cloud where instability is incited
z_{i+}	Depth cloud top extends inside the temperature inversion
t	Time
g	Acceleration due to gravity
Ω	Earth's angular velocity
p	Pressure
p_0	Pressure at the surface
C_p	Specific heat capacity at constant pressure
ρ	Density of air
T	Temperature
T_v	Virtual temperature
T_{ib}	Inversion base temperature
T_{it}	Inversion top temperature
θ	Potential temperature
θ_v	Virtual potential temperature
θ_v	Equivalent potential temperature
θ_l	Liquid water potential temperature
x	Position vector
u	Horizontal velocity
w	Vertical velocity
w_e	Entrainment velocity
w_s	Subsidence velocity
w_{max}	Domain maximum vertical velocity

w_{min}	Domain minimum vertical velocity
$(\partial\theta/\partial t)_{LS}$	Large scale source term for heat
$(\partial q_n/\partial t)_{LS}$	Large scale source term for scalars
w_{LS}	Large scale vertical velocity
ρ_w	Density of water
L_v	Latent heat of vaporisation
q	Water constituent mass mixing ratio
q_v	Water vapour mass mixing ratio
q_{spec}	Specific humidity
q_l	Liquid water mass mixing ratio
q_s	Snow water mass mixing ratio
q_i	Ice water mass mixing ratio
q_t	Total water mass mixing ratio
N	Water constituent number concentration
N_l	Liquid water number concentration
N_s	Snow water number concentration
N_i	Ice water number concentration
N_{in}	The number of ice nuclei available for primary ice nucleation
q_t^{bl}	Initial total water mixing ratio at the BL top
q_t^{inv}	Initial total water mixing ratio at the top of the temperature inversion
q_v^{ib}	Water vapour mixing ratio at the humidity inversion base
q_v^{it}	Water vapour mixing ratio at the humidity inversion top
q_l^{i+}	Percentage of total liquid water mass inside the inversion
LWP^{i+}	Integrated mass of liquid water inside the inversion
r	Particle radius
D	Particle diameter
N_o	Intercept parameter of the water constituent number size distributions
λ	Slope parameter of the water constituent number size distributions
μ	Shape parameter of the water constituent number size distributions
$\bar{r}$	Geometric mean dry radius
σ	Geometric standard deviation
N_a	Total aerosol number concentration
S_{max}	Maximum supersaturation
r_{ci}	Critical aerosol activation size
S_{ci}	Critical supersaturation of a particle of size $\bar{r}_i$

N_{act}	Potential number of activated aerosol particles
$\overline{w'\theta'}$	Vertical flux of potential temperature
$\overline{w'\theta'_v}$	Vertical flux of virtual potential temperature
$\frac{g}{T_v}\overline{w'\theta'_v}$	Buoyancy flux
$\overline{w'q}$	Vertical flux of water constituent
F_{LW}	Flux of LW radiation
σ_{SB}	Stefan-Boltzmann constant
ε	Emissivity
k_{abs}	Mass absorption coefficient
k_{ext}	Mass extinction coefficient
k_{sca}	Mass scattering coefficient
τ	Optical depth
r_e	Cloud droplet effective radius
D_e	Ice crystal effective diameter
H	Radiative heating rate
L	Latent heating rate
R_{sn}	Radiative-heating stability number
L_{sn}	Latent-heating stability number
C_{sn}	Combined stability number
dF^+	Upward net radiative flux density divergence
dF^-	Downward net radiative flux density divergence
α_1	Radiative weighting function 1
α_2	Radiative weighting function 2
Q^+	Positive radiative source function
Q^-	Positive radiative source function
τ^s	Sub-grid stress
h^θ	Sub-grid scalar flux of θ
h^{q_n}	Sub-grid scalar flux of q_n
B'	Buoyancy term in the momentum equation
δ_{i3}	Kroneker delta function
ϵ_{ijk}	Alternating pseudo-tensor
$V_{q_l x}$	Terminal particle fall speed
ν	Sub-grid eddy viscosity
ν_h	Sub-grid diffusivity for scalars
S_{ij}	Rate of strain tensor
λ_e	Basic mixing length for eddy diffusivity and viscosity calculations
Ri_p	Pointwise Richardson number
Ri_c	Critical Richardson number
Q_1	θ budget tendency due to diabatic heating/cooling

Q_2^n	Water constituent tendency due to diabatic moistening due to phase changes
W_f	Wavelet covariance transform
a	Dilation
z_b	Lower limit of profile
z_t	Upper limit of profile
h	Haar function
b	Location at which the Haar function is centred

Chapter 1

Introduction

Global mean sea surface temperatures have risen by around 0.8 ^{o}C since the beginning of the 20th century; an increase which is primarily a consequence of anthropogenic climate change caused by the emission of greenhouse gases to the Earth's atmosphere, and a rise which is projected to continue at a faster rate in the future. Although atmospheric temperatures have risen across the planet, the Arctic - a region which acts as an important regulator of the global climate system - has experienced the most dramatic change over the past few decades; with surface temperatures rising at a higher rate than anywhere else on the Earth and summer sea ice extent and thickness decreasing significantly. A change recently highlighted by the record sea-ice minimum of 2012, in which sea-ice extent was down 49 % on the 1979 - 2000 average.

Changes to the Arctic climate are likely to have a substantial impact on the local environment; impacting the people, wildlife and vegetation which are reliant and in some cases specially adapted to the unique Arctic ecosystem. Arctic climate change is also predicted to impact on the lower latitudes through the modification of weather patterns and ocean circulation, and if the region becomes completely ice-free, may potentially lead to the Earth's climate reaching a tipping point; bringing about irreversible changes to the natural environment.

These impacts highlight the need for accurate predictions of Arctic climate change in informing decisions on environmental policy. Climate models currently struggle to predict Arctic temperature change with the consequence that Arctic sea-ice loss is underestimated. The reasons for this divergence between models and observation are severalfold, however the lack of understanding of several unique physical, chemical and biological processes which occur in the region are thought to be a major contributor to the uncertainty. This is especially true in the central Arctic, where the harsh environmental conditions have prevented the collection of an extensive in-situ measurement set needed

to develop Arctic specific paramaterizations in climate models.

Low-level Arctic stratiform cloud and in particular its interaction and feedback with the underlying sea-ice surface has been highlighted as one area of the Arctic climate system in need of further investigation. Arctic stratus clouds are ubiquitous during the summer months, with a semi-persistent layer covering much of the central Arctic Ocean. However despite their prevalence, regional and global climate models fail to simulate both their macrophysical properties: occurrence and extent, and microphysical properties: cloud phase, ice crystal and cloud droplet number; with the consequence that the Arctic surface energy budget is poorly represented.

While superficially similar to their sub-tropical and mid-latitudinal marine counterparts a number of differences exist, for instance Arctic stratocumulus are commonly composed of both ice crystals and supercooled liquid water. Another major difference and one which has so far received very little attention is the observation of Arctic stratocumulus cloud top extending into the temperature inversion which caps the central Arctic boundary layer. Because of the strong stability of the temperature inversion, the encroachment of cloud into the inversion layer is unexpected and sub-tropical marine stratocumulus are always assumed to have a cloud top coincident with the base of the temperature inversion. While previous research has identified that the encroachment of Arctic stratocumulus into the inversion is related to the presence of specific humidity inversions - which are also commonly found situated coincident with the Arctic temperature inversion - their remains an open question as to the exact mechanisms which control this relationship, and the sensitivity of the encroachment to the specific humidity inversion strength and other atmospheric properties is yet to be examined. Furthermore, the effect that the encroachment has on the development of the cloud and boundary layer is so far undetermined, therefore it is uncertain whether there is a need for cloud-inversion encroachment to be represented in climate and weather prediction models.

This project aims to investigate the encroachment of Arctic stratocumulus cloud into the temperature inversion, quantify the prevalence of the regime in the central Arctic and better determine its relationship to the coincident humidity inversion under a variety of atmospheric conditions. The will be carried out with the intention that the research generate a more detailed and complete mechanistic description of the cloud encroachment into the inversion layer, and if its effect on BL development is shown to be important provide a basis for the development of Arctic boundary layer cloud parameterizations for use in global and regional climate models.

To achieve this aim, the methodology of this project firstly consists of analysis of measurements collected during the Arctic Summer Cloud Ocean study (ASCOS). This recent Swedish-led field campaign to the central Arctic had a primary purpose of understanding the life cycle of summertime Arctic stratocumulus clouds, including their observed

encroachment into the temperature inversion. Analysis of ASCOS data will focus on the identification of the inversion from the measurement set and on determining statistical relationships between measures of the cloud-inversion encroachment and other atmospheric properties. Numerical simulations using the Met Office Large Eddy Model (LEM) will then be made using the ASCOS observations as a basis to constrain the model runs. A number of simulations in which the strength of the humidity inversion is varied will be made to understand its effect on the encroachment. The simulations aim to quantify and gain a process based understanding of the radiative-microphysical-dynamical mechanisms which control the encroachment and determine any feedbacks the encroachment has on the development of the Arctic boundary layer.

The help achieve the aims of this project a number of research questions will be investigated:

- How similar were ASCOS conditions to those found in previous Arctic field campaigns, and do ASCOS observations support the evidence suggesting that cloud encroachment into the temperature inversion is prevalent in Arctic clouds?
- Is the assumption that the top of sub-tropical marine stratocumulus cloud is always coincident with the inversion base realistic?
- What are the fundamental radiative-microphysical-dynamical mechanisms which support the encroachment?
- What physical effect does the encroachment of cloud into the inversion have on boundary layer development, and how is this effect determined by the depth or amount of cloud mass with encroaches inside the inversion layer?
- What relationships between encroachment statistics can be derived - either directly from the ASCOS dataset or from numerical simulations - which may lead the way for a parameterization of the cloud encroachment into the temperature inversion?

Chapter 2 provides an overview of the background science and literature which is essential to this study. This includes details on relevant aspects of boundary layer meteorology, including a discussion of the macro and microphysical properties of both sub-tropical marine and mixed-phase Arctic stratocumulus, Arctic climate change, an overview of previous Arctic field campaigns, and lastly the entrainment mechanism and a discussion on available definitions of the entrainment zone. Chapter 3 gives a description of the large eddy model including the models governing equations and all major physical parametrizations: sub-grid motions, cloud microphysics, radiation, boundary conditions and large scale forcing. A description of the algorithm added to the model to diagnostically determine the inversion layer boundaries is also given, and a discussion of any merits

and deficiencies of the modelling framework is provided. In Chapter 4 this is followed by a validation of the numerical model. Validation is achieved through simulating a widely studied Arctic stratocumulus case study and comparing to a wide range of model results from a cloud model inter-comparison. Chapter 5 introduces the ASCOS field campaign, describes the campaign logistics, objectives and general meteorological conditions, along with a description of the observations used in this research. Analysis of the observations is also made with the aim of understanding cloud-inversion properties: how these relate to observations from different studies; and to other measured atmospheric variables. Chapter 6 uses a case study developed from the ASCOS dataset to model a mixed-phase Arctic stratocumulus cloud and its encroachment into the elevated Arctic temperature inversion. The simulation is forced by a large scale water vapour source in the inversion layer; and compared against simulations where no forcing is present. Chapter 7 extends the analysis of the simulated cloud to look at the effect that the forcing specification has on the encroachment, and the sensitivity of the BL to the subsequent change in encroachment. Finally in Chapter 8, a summary of the results is presented and recommendations for future work are provided.

Chapter 2

Background

Chapter 1 introduced the subject of this research, which is the study of mixed-phase Arctic stratocumulus and the encroachment of cloud top into the elevated temperature inversion which is commonly observed above the Arctic boundary layer. In this chapter, background to this topic will be given through an in-depth review of relevant literature. The focus here will not just be on the physics of mixed-phase Arctic stratocumulus; dynamical, cloud microphysical and radiative properties, but will also address their relationship to the more extensively studied sub-tropical marine stratocumulus and the wider Arctic climate. To aid the reader the definition a number of atmospheric variables and general meteorological concepts used throughout the study will also be provided.

2.1 The atmospheric boundary layer

2.1.1 Structure of the lower atmosphere

When discussing the Earth's atmosphere it is useful to separate it into layers dependent on their vertical thermal structure. The troposphere which extends from the Earth's surface up to around 12 km is where most atmospheric mass is situated and is generally defined as the region of the atmosphere where temperature falls with height at the adiabatic lapse rate. Above the troposphere, temperature increase with height in a layer of the atmosphere known as the stratosphere, this is followed by the upper atmospheric layers; the mesosphere, thermosphere and exosphere. The influence of the Earth's surface is essentially limited to the troposphere. It is also the region where weather systems occur, making it the principal region for meteorological analysis.

The troposphere can be separated into two further layers called the free troposphere and the planetary or atmospheric boundary layer, hereafter referred to as the boundary layer

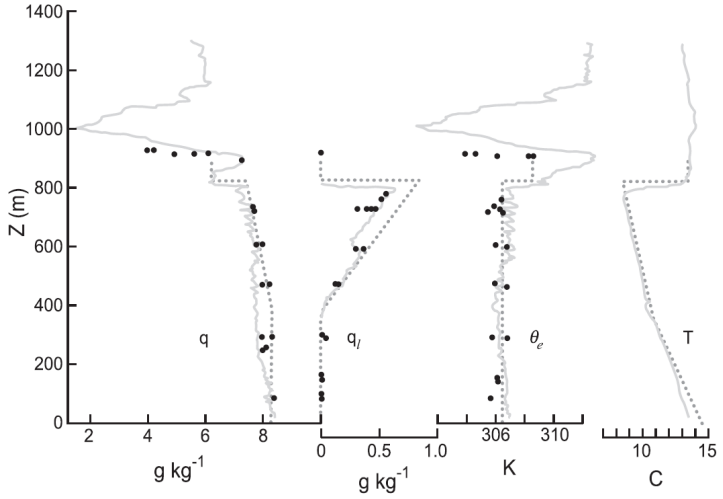

Figure 2.1: Vertical profiles of water vapour, q_v and liquid water, q_l mass mixing ratios, equivalent potential temperature, θ_e and temperature, T measured on flights through a summertime mid-latitude marine stratocumulus topped boundary layer. Dots represent the means of horizontal legs and dotted lines the values expected for a well-mixed layer. Reproduced from Wood (2012) who adapted the original image from Nicholls (1984).

(BL). As its name suggests the boundary layer is the region of the troposphere closest to the Earth's surface. Stull (1988) defines it as the *'part of the troposphere that is directly influenced by the earth's surface, and responds to surface forcings with a timescale of about an hour or less'*. The BL often has a depth in the order of 1 km or less, and is characteristically defined by strong turbulent motions, a strong diurnal cycle and the presence of fog, stratocumulus and fair weather cumulus clouds.

The free troposphere is situated above the BL and occupies the remainder of the troposphere. The free troposphere is generally more quiescent, containing much weaker turbulence, slower mixing and a weaker diurnal variation - except in the presence of deep convection or active frontal systems. The two layers are often separated by a region of rapidly increasing temperature known as an inversion. The significant increase in temperature across the inversion makes it extremely stable, essentially capping the BL below and preventing steady mixing of BL and free tropospheric air. Occasionally buoyant parcels of air manage to overshoot the base of the inversion and mix free-tropospheric air into the BL in a processes known as entrainment.

2.1.2 The stratocumulus topped boundary layer

Stratocumulus clouds are found over almost all regions of the Earth. From the vast sheets which cover thousands of kilometres of the Eastern sub-tropical oceans, through

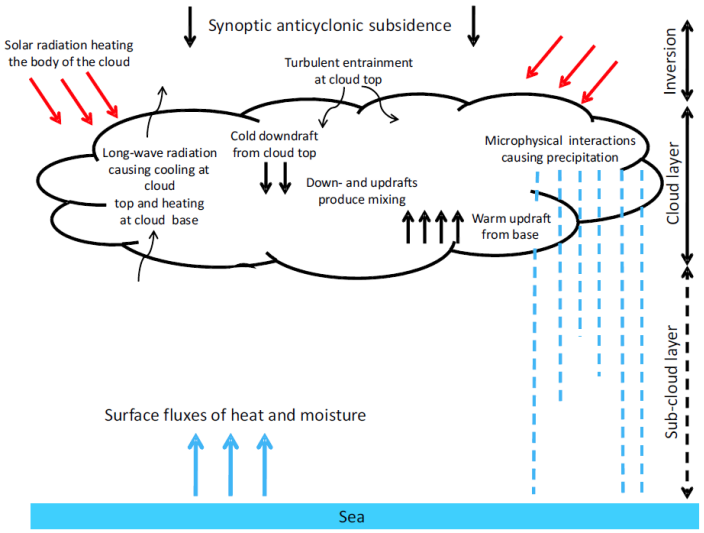

Figure 2.2: Radiative, microphysical and dynamical processes which occur in a mid-latitude stratocumulus topped boundary layer. Reproduced from Holtslag (1998).

the mid-latitudes, and up into the central Arctic ocean (Klein & Hartmann, 1993). They have the most extensive coverage of any cloud type (Wood, 2012), and alongside fair weather cumulus are the most important clouds to influence the development of the BL. Stratocumulus commonly form over regions of high pressure in the sub-tropics and mid-latitudes where synoptic scale anticyclonic subsidence creates a temperature inversion as the descending air warms through adiabatic compression. This capping inversion traps water vapour added to the BL by advection and from surface evaporation causing the BL to moisten until saturation and the formation of cloud.

A boundary layer where the dynamics are controlled by the presence of stratocumulus is called a stratocumulus topped boundary layer (STBL). Measured and idealized vertical profiles of atmospheric variables through a mid-latitude STBL are shown in Figure 2.1. The observed stratocumulus is liquid-phase (liquid condensate only) and non-precipitating. The idealized liquid water mass mixing ratio (henceforth mixing ratio), q_l increases linearly from the height of the cloud base, z_{cb} up to the height of the cloud top, z_{ct}, before rapidly falling to to zero inside the inversion layer. In reality, the entrainment of dry air from above means liquid water mixing ratios near the cloud top are often less than the idealized values. Within the sub-cloud layer, temperature typically decreases at the adiabatic lapse rate of -9.8 K km^{-1} while through the cloud layer latent heat release due to condensation causes temperature to drop off at the saturated adiabatic lapse rate.

Throughout the STBL, the total water mixing ratio, q_t and the equivalent potential temperature, θ_e; which are both conserved under dry as well as moist adiabatic processes, are well-mixed and so their profiles are constant with height. This region is described as

a mixed layer (ML). Above the mixed layer the temperature increases across the inversion, while the water vapour mixing ratio and total water mixing ratios drop of rapidly. While inversions are also commonly present above cloud-free regions, the sharp jump in atmospheric variables at the inversion is a characteristic of the STBL, with vertical mixing due to longwave radiative cooling tending to reduce the potential temperature gradient in the region below cloud top and leaving a sharp jump in temperature at the inversion (Paluch & Lenschow, 1991). Though studies rarely calculate the boundaries of the inversion with any accuracy, the prototypical stratocumulus cloud top is found in the vicinity of the temperature inversion base, z_{ib} and they are often assumed as coincident (e.g. Paluch & Lenschow, 1991; Stevens *et al.*, 2007; Tjernstrom & Rune, 2003).

In Figure 2.1, the observed ML extends from the top of the cloud layer all the way down to the surface, thus the surface and cloud are in a coupled state. However in the sub-tropics and mid-latitude, the STBL typically has a strong diurnal cycle in which the surface and sub-cloud layer sometimes becomes decoupled from the cloud layer by a region of positive stability. Coupled mixed layers such as that observed in Nicholls (1984) are typically found at night time and in the early morning. The deep coupled mixed layer is maintained by turbulence generated from cloud top radiative cooling and from cellular convection (Figure 2.2). After sunrise the absorption of solar radiation heats the cloud. This both destabilises the cloud layer and stabilises the sub-cloud layer below, thus the two regions decouple. Decoupling closes the cloud off from the source of water vapour at the surface which can lead to the cloud thinning and ultimately its break up. In precipitating stratocumulus, latent heating associated with drizzle production within the cloud and evaporative cooling of drizzle below the cloud base can also contribute to the decoupling of the ML. This is often strongest late in the morning when vertical velocities are strongest and drizzle production is at its greatest. If drizzle reaches the surface it can also deplete the BL of water (Stevens *et al.*, 1998).

While the formation of stratocumulus cloud largely depends on the prevailing meteorological conditions, the optical properties of the cloud and its tendency to precipitate depend on both its microphysical and macrophysical properties. In addition to a high relative humidity (low temperature and/or high specific humidity), cloud droplet formation requires the presence of hygroscopic atmospheric aerosol particles known as Cloud Condensation Nuclei (CCN) which are capable of initiating droplet formation at the low supersaturations found in the atmospheric environment; typically supersaturations rarely exceed 10 %, and are often less than 1 % (Pruppacher & Klett, 1997). A strong correlation exists between concentration of CCN particles and the number of cloud droplets, N_l (Twomey, 1959), and the number of droplets over which the liquid water mass is distributed impacts the average size of the cloud droplet with low CCN concentrations leading to a small number of large droplets, while high CCN concentrations leading a large number of small droplets.

The CCN concentration affects the clouds optical properties - with an increase in the CCN concentration, hence droplet number at a fixed liquid water content (LWC) leading to the cloud having a higher shortwave albedo (Twomey, 1977). The distribution of droplet sizes is also broader when CCN concentrations are low and because the growth of droplets to a precipitable size in the warm environment is largely dependent on their collision and coalescence, smaller CCN concentrations are associated with drizzle production (Bretherton *et al.*, 2004; vanZanten *et al.*, 2005). Typically in the marine environment CCN numbers are in the range of 100 cm^{-3} to 1000 cm^{-3} (Raes *et al.*, 2000). Ackerman *et al.* (2004) found that an increase in the cloud droplet number led to an increase in the LWP of sub-tropical stratocumulus. The response of the LWP to droplet number was found to be due to an increase in sedimentation in the region near cloud top. In (Bretherton *et al.*, 2007), sedimentation was found to decrease the entrainment rate by removing liquid water from the EZ, thus reducing evaporative and radiative cooling which are mechanisms which promote the sinking of entrained air into the cloud layer.

2.1.3 Cloud top entrainment

Cloud top entrainment occurs as boundary layer thermals overshoot the top of the mixed layer, capturing non turbulent air from within the temperature inversion before returning to the BL. Entrainment is of central importance to the development of the STBL. It is the primary means of boundary layer growth (Boers *et al.*, 1984), and a major influence on the structure and distribution of stratocumulus clouds. Through a mechanism known as cloud top entrainment instability (CTEI)(Deardorff, 1980; Lilly, 1968), entrainment can also sometimes lead to the thinning and break up of stratocumulus. CTEI occurs if the mixing of warm dry inversion air with saturated BL air causes strong enough evaporation to destabilise the air parcel and make it negatively buoyant. Under the force of buoyancy the parcel sinks leading to a positive buoyancy flux, $\frac{g}{T_v}\overline{w'\theta_v'}$, stronger turbulence and increased entrainment of warm dry air (Yamaguchi & Randall, 2008). Thus the CTEI mechanism has a positive feedback on itself which can lead to the destruction of the cloud.

While entrainment is an inherently local process, with mixing occurring discontinuously across the cloud top interface in discrete events, the rate of entrainment of free tropospheric air into the mixed layer below is by definition a property of the area and time averaged mixing (Stull, 1988). The entrainment rate is usually defined in terms of an entrainment velocity, w_e which is zero when there is no turbulence and positive at any other time. If the rate of atmospheric subsidence, w_s and the height of the boundary layer top, z_i are known accurately then w_e can be calculated simply through (Wood &

Bretherton, 2004):

$$\frac{\partial z_i}{\partial t} + u(z_i) \cdot \nabla z_i = w_e - w_s(z_i) \tag{2.1}$$

where $u(z_i)$ is the horizontal wind velocity. A number of parametrizations also exist to calculate the entrainment rate (see for example Stevens (2002) for a review).

2.1.4 Entrainment zone definition

When calculating the entrainment rate from observations it is convenient to define an interfacial layer over which the mixing occurs known as the entrainment zone (EZ). As entrainment is the mixing of laminar and turbulent air, the entrainment zone is a layer characterised by overshooting thermals, intermittent turbulence and broken cloud. A fundamental definition of the entrainment zone is that it is the region around the top of the ML where $\overline{w'\theta'_v}$ is negative (Figure 2.3)(Driedonks & Tennekes, 1984); denoting the production of potential energy at the expense of turbulent kinetic energy (TKE) i.e. the consumption of turbulent energy in mixing less dense and hence more buoyant air down into the BL. While this definition of the EZ is theoretically correct, in reality it is difficult to determine $\overline{w'\theta'_v}$ from observations, and for this reason a number of other definitions of the EZ have been developed, as yet none of which have become universally excepted.

It is often defined as the region in which the mean profile of some scalar quantity has a significant vertical gradient (Cohn & Angevine, 2000). Example quantities include the potential temperature, θ, the water vapour mixing ratio, q_v or specific humidity, q_{spec}, and the concentration of atmospheric aerosol and hence the lidar backscatter. Deardorff (1980) defines the upper limit of the EZ as greatest height reached by overshooting thermals and the lower limit as the height where mixed layer air occupies 90 - 95 % of the horizontal area. A similar technique commonly used in lidar studies is to define the EZ from the probability density function of a set of spatially or temporally distributed local estimate of the BL top (Flamant *et al.*, 1997; Wilde *et al.*, 1985), where the 5 % and 95 % limits of the distribution are often chosen as the EZ boundaries. These techniques suffer from the varied definition of z_i between studies. In Deardorff (1980) z_i is taken as the height where the mean $\overline{w'\theta'_v}$ is at its minimum while in Cohn & Angevine (2000) it is defined as the mean of gradient estimates of the BL top.

A relatively new method which was developed to find z_i and the EZ boundaries from lidar backscatter profiles is the use of an edge-detecting wavelet technique (Brooks, 2003; Davis *et al.*, 1997; Grabon *et al.*, 2010). The wavelet method is able to determine the upper and lower boundaries of the transition zone; which Brooks (2003) defines as the local region over which an atmospheric scalar changes from its well-mixed BL value to it free-tropospheric value. The transition zone is the gradient region which would be identified from a single radiosonde profile and can vary significantly from the EZ. For

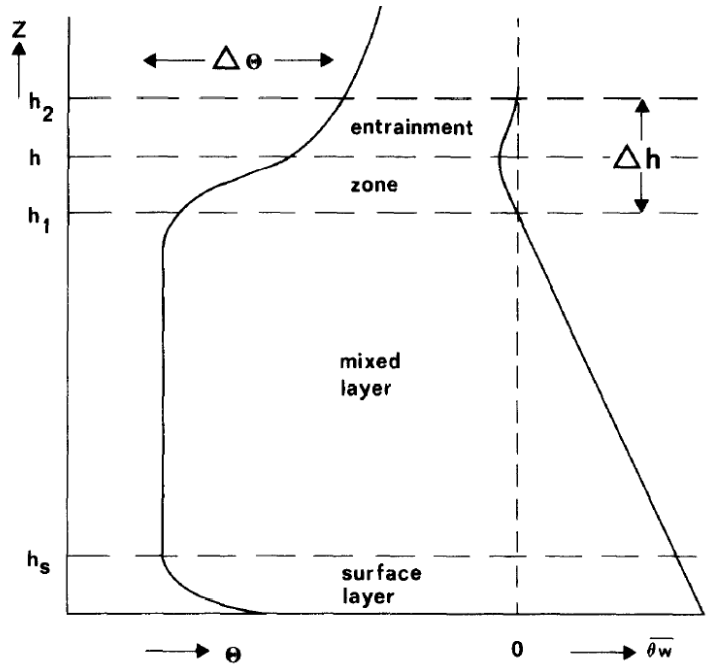

Figure 2.3: Typical structure of the θ and vertical heat flux $\overline{w'\theta'}$ profiles through the convective boundary layer. h_1 and h_2 are the heights of the entrainment zone base and top respectively, h is the height of the mixed layer top, and h_s is the height of the surface layer top. Reproduced from Driedonks & Tennekes (1984).

example estimates of z_i from single radiosonde profiles can produce errors as large as $0.4z_i$ (Stull, 1988). In Brooks (2003) the upper and lower boundaries of the EZ are determined as the area average of the transition zone boundaries, and the BL top is determined to be equal to the base of the entrainment zone. Alternatively, as described in Brooks & Fowler (2012) the BL top is sometimes defined as the area average altitude of the peak in the vertical gradient in the lidar backscatter signal, which is somewhere near the centre of the transition zone. Reviews of the different measures and estimates of z_i can be found in Sullivan *et al.* (1998) and Brooks & Fowler (2012).

To avoid confusion from the different naming conventions, henceforth the inversion will from now on refer strictly to the temperature inversion. The boundaries of the inversion; which is a deep stable layer, are not necessarily the same as the boundaries of the inversion; which is a dynamic layer will may extend only a short distance into the inversion layer. Nevertheless the base of both regions is typically equal and so z_{ib} will also be used to denote both the inversion base and the entrainment zone base. z_{it} will be used exclusively to denote the top of the entrainment zone. z_i will be used exclusively to denote the boundary layer top determined as the area average altitude of the peak in the vertical gradient of the potential temperature profiles.

2.2 Arctic clouds and their climatic significance

Recent observations show that the Arctic is subject to rapid changes. Near-surface temperatures are rising throughout the region (Johannessen *et al.*, 2004), and the sea-ice extent and thickness are decreasing (Lindsay & Zhang, 2005; Rothrock *et al.*, 1999); to the effect that in 2012 the Arctic sea-ice September minimum extent reached a record low of 49 % below the 1979 - 2000 average (NSIDC, 2012). The warming experienced in the Arctic is more pronounced than anywhere else on the earth with near-surface temperatures rising at twice the rate of the global average (Winton, 2006), thereby highlighting the region's sensitivity to rapid climate change (Holland & Bitz, 2003; Serreze *et al.*, 2009) in what is commonly termed "Arctic amplification" (Serreze & Francis, 2006).

Numerous mechanisms have been identified as leading to the amplified global warming in the Arctic region including changes to atmospheric circulations (Graversen *et al.*, 2008; Yang *et al.*, 2010), oceanic circulations (Chylek *et al.*, 2009) or a combination of both (Bengtsson *et al.*, 2004; Wood & Overland, 2010). The impact of these on Arctic climate change is substantial, for instance Yang *et al.* (2010) attribute up to 50 % of the rise in Arctic tropospheric temperatures through the late 1990s to increasing poleward energy transport. Local processes have also been identified as contributing to the amplification. Curry *et al.* (1996) demonstrated how physical feedback mechanisms lead to accelerated warming, for example the sea-ice albedo feedback (Perovich *et al.*, 2007): warming of the Arctic ocean leads to a reduction in sea-ice coverage and increase in the area of open-ocean exposed - as open-ocean has a lower albedo than sea-ice this leads to weaker reflection of downwelling solar radiation back to space, greater solar warming of the surface and an increase in the sea-ice melt. Other causes include the altered heat transport between the lower atmosphere and the retreating sea-ice (Screen & Simmonds, 2010; Serreze *et al.*, 2009), enhanced longwave radiative forcing due to changes in the atmospheric water vapour content and cloud cover (Francis & Hunter, 2007; Graversen & Wang, 2009), and changes to atmospheric aerosol; with Shindell & Faluvegi (2009) suggesting that the reduction in Arctic concentrations of sulphate aerosols and the concurrent increase in the concentration of black carbon has substantially contributed to the increase in tropospheric temperatures over the past three decades. Feedbacks within the climate system can also lead to processes working together and this can exacerbate the Arctic warming (Serreze & Barry, 2011).

Climate modelling studies show that the Arctic amplification is likely to continue into the future with the Intergovernmental Panel on Climate Change Forth Assessment Report (IPCC-AR4) predicting that the Arctic region will experience a 5^{o}C increase in annual-mean air temperatures by the end of the 21st century (Solomon *et al.*, 2007) and the summertime Arctic Ocean predicted to be largely free of sea-ice within the next 40

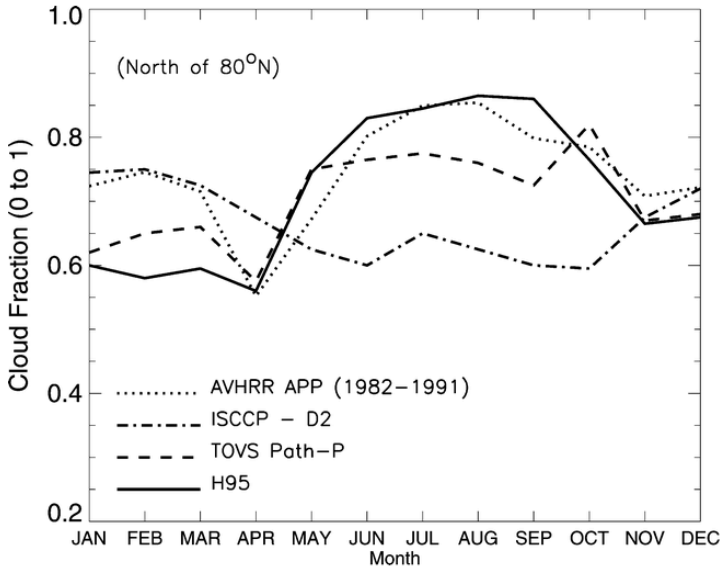

Figure 2.4: Annual cycle of cloud fraction from surface-based observations (H95) and satellite retrievals (ISCCP D2, TOVS Path-P, and APP-x) for the Arctic region north of 80^{o}N over the period 1982-91. Reproduced from Wang & Key (2005).

years (Chapman & Walsh, 2007). Despite climate models agreeing that the region is set to warm, modelling the Arctic climate is a particular problem for General Circulation Models (GCMs) and Regional Climate Models (RCMs) meaning they struggle to reproduce even the current Arctic climate properly (Chapman & Walsh, 2007; Tjernstrom *et al.*, 2005, 2008; Walsh *et al.*, 2009), and show their greatest variability over the Arctic region (Solomon *et al.*, 2007; Tjernstrom *et al.*, 2005; Walsh *et al.*, 2002). The difficultly in simulating the Arctic climate is largely due to the poor understanding of physical mechanisms and feedbacks within the system - which in turn results from a paucity of data (Randall *et al.*, 1998). This leads to model parametrizations of physical processes relying on data from more accessible regions in the lower latitudes where conditions are often very different.

A major concern for climate models is their inability to correctly predict clouds (Solomon *et al.*, 2007), and Arctic clouds are a particular problem (Karlsson & Svensson, 2010; Tjernstrom *et al.*, 2008; Walsh *et al.*, 2002, 2009) which is disconcerting due to their prominence in causing Arctic amplification (Winton, 2006). Arctic clouds are generally characterised by semi-persistent low level stratiform clouds and fog, which are ubiquitous to the region, particularly during the summer months where cloud fractions can be as high as 80 - 90 % (Curry & Ebert, 1992; Liu *et al.*, 2012; Shupe *et al.*, 2011; Wang & Key, 2005). The seasonal distribution of cloud fraction at latitudes above 80^{o}N from a number of ground based and satellite measurements is shown in Figure 2.4. Cloud fraction peaks during the summer and reaches a seasonal low during the spring and autumn - the so

called transition seasons. During the wintertime cloud fraction is typically around 60 %. Curry *et al.* (1996) and Beesley & Moritz (1999) investigated this annual cycle of cloud cover and attributed differences in seasonal cloudiness to a greater presence of clear-sky ice crystal precipitation reducing the cloud lifetime in the colder months, though the reason why the lowest cloud fraction is found in the transitional seasons and not the summer is still unknown.

Fog and stratocumulus have an important influence on the energy balance of the Arctic region; with Intrieri *et al.* (2002b) showing that that low-level clouds are the most significant factor controlling the Arctic surface radiation budget, and Curry *et al.* (1993) demonstrating that the equilibrium thickness of sea-ice may be significantly affected by changes to cloud coverage and optical properties. Clouds regulate the Earth's surface energy budget through their influence on radiation, causing both a reduction in the downward shortwave flux to the surface and enhancement in the downward longwave flux as compared to clear sky conditions; the albedo and greenhouse effects respectively. Low clouds tend to radiate at a similar intensity as the surface which reduces their greenhouse forcing. In the sub-tropics and mid-latitudes this leads to the reflectivity being more important in low clouds, therefore the cloud albedo effect tends to outweigh the greenhouse effect with the net result that they have a negative radiative forcing; thus they cool the surface relative to clear sky conditions (Harrison *et al.*, 1990). However over the Arctic Ocean the incoming shortwave radiation flux is weak and the surface reflectivity is often of a similar magnitude or greater to the cloud albedo, meaning stratocumulus tend to warm the surface throughout the entire year except for a few weeks during the mid-summer where the shortwave flux is at a maximum Intrieri *et al.* (2002b).

The presence of sea-ice is an integral feature of the Arctic climate system with sea-ice affecting the physical relationship between the surface and atmosphere through its large albedo and its insulating of the atmosphere from the relatively warm ocean below the ice. Although Arctic clouds currently warm the surface the relationship between the sea-ice and clouds is complex (Kay & Gettelman, 2009). The cloud radiative forcing depends on the clouds optical properties; which are related to the cloud phase and microphysical properties, and also on the surface albedo and solar zenith angle (Sedlar *et al.*, 2011). Therefore estimating what the cloud radiative forcing will be in the future is made difficult by uncertainty in how cloud cover and its microphysical properties will change. Intrieri *et al.* (2002a) found a much greater difference in the radiative forcing between clear and cloudy skies in the summer as compared to the winter suggesting that changes to summertime cloud will have the greatest effect on the sea-ice energy budget. Observations show only a small increase in summertime cloud cover over the last few decades whereas the winter cloud fraction has decreased over this period and the spring cloud fraction has increased by around 5 % per decade (Figure 2.5). Schweiger (2004) attributes this to an increase in cyclonic activity.

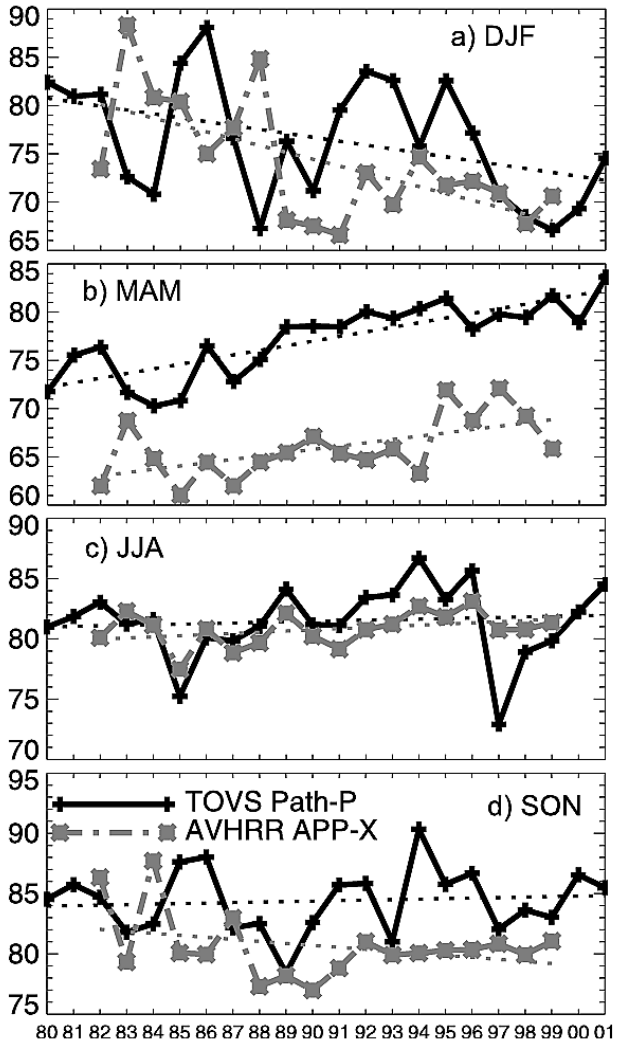

Figure 2.5: Timeseries of the seasonally averaged cloud fraction as detected over the Arctic seas from the TOVS Path-P and AVHRR Polar Pathfinder satellites for the period 1980 - 2001. Cloud fractions are averaged over ocean areas for a) winter, b) spring, c) summer and d) autumn. x-axis is the year, while y-axis is the cloud fraction (%). Reproduced from Schweiger (2004).

2.3 The central Arctic boundary layer

2.3.1 Major Arctic field campaigns

The first major study of Arctic boundary layer clouds was the Arctic Stratus Experiment (ASE)(Herman & Curry, 1984) in June 1980. Before this experiment Arctic stratocumulus had been viewed as dynamically and microphysically similar to sub-tropical marine stratocumulus. ASE made simultaneous measurements of turbulence, radiation and microphysics and provided the fundamental basis for the understanding of Arctic stratocumulus; their formation, multi-layer structure and persistence.

More recently there have been several field campaigns with a primary objective of understanding the Arctic boundary layer. The Beaufort and Arctic Storms Experiment (BASE)(Curry *et al.*, 1997) was carried out in the autumn of 1994 over the South Beaufort Sea with aircraft measurements of the surface and boundary layer cloud properties. The First International Satellite Cloud Climatology Project Regional Experiment (FIRE)(Curry *et al.*, 2000) studied the interaction between Arctic boundary layer cloud and the surface. FIRE took place off the North coast of Alaska during April and July 1998, coinciding with a year-long ice drift program which took place from October 1997 to October 1998 known as The Surface Heat Budget of the Arctic Ocean Project (SHEBA)(Uttal *et al.*, 2002). The broad objective of SHEBA was to understand Arctic feedback processes and improve physical parametrizations in GCMs. Measurements made during SHEBA were extensive and included BL meteorology, remotely sensed dynamical and microphysical cloud properties from cloud radar; and ice and ocean properties. SHEBA is probably the most widely studied dataset of Arctic meteorology and its year long time-line provides a seasonal record of cloud properties at a single location.

The Mixed Phase Arctic Cloud Experiment (M-PACE)(Verlinde *et al.*, 2007) took place during the autumn transitional season of 2004 on the North Slope of Alaska with the objective of characterising Arctic mixed-phase clouds. For one month instrumentation was deployed at four sites in the region, enhancing the ground based instruments already located at the Department of Energy Atmospheric Radiation Measurement site in Barrow and Oliktok Point. Measurements included radiosonde profiles, ground based remote sensing of cloud properties and in-situ cloud measurements through multiple aircraft flights. The Indirect and Semi-Direct Aerosol Campaign (ISDAC)(McFarquhar *et al.*, 2011) took place during April 2008 and was designed as a spring transition season comparison case for the M-PACE campaign; taking place at the same location and with similar instrumentation.

From the European side of the Arctic, four Swedish-led summertime expeditions into the high Arctic Ocean have also been carried out to study the physical and chemi-

cal properties of the central Arctic. The International Arctic Ocean Experiment 1991 (IAOE-91)(Leck *et al.*, 1996) was the first of the Swedish-led field campaigns and had the objective of testing the hypothesis that sulphates derived from marine biogenically produced dimethyl sulphide are a source of CCN in the Arctic, thus influencing Arctic cloud properties. The Arctic Ocean Experiment 1996 (AOE-96)(Leck *et al.*, 2001) and the Arctic Ocean Experiment 2001 (AOE-2001)(Tjernstrom *et al.*, 2004) continued the work of IAOE-91 with the broadened objective of understanding the influence of all aerosol on the regional climate. In AOE-2001 greater emphasis was placed on the structure of the Arctic boundary layer, and a substantially expanded meteorological measurement programme was included to meet the project objectives. The Arctic Summer Cloud Ocean Study 2008 (ASCOS), which was the latest of the field campaigns, was carried out during August and September of 2008. Once again the breadth of the study was expanded to understand the formation and persistence of summertime Arctic clouds. The campaign included a range of measurements encompassing marine biology, atmospheric chemistry and aerosol, oceanography and meteorology so that a number of aerosol-cloud-climate interactions could be studied. ASCOS data forms the basis of the model simulations made in this study; therefore more details on the field campaign will be provided in Chapter 5.

2.3.2 Structure of the lower atmosphere

Due to its high-latitude the central Arctic experiences 24 hours of sunlight a day during the summer months and 24 hours of complete darkness during the winter. Even through the summer months the downwelling flux of solar radiation is small here compared to lower latitudes, and the absence of a strong diurnal variation in the forcing coupled with the presence of persistent low level cloud and the unique sea-ice surface makes the structure of the central Arctic BL distinctively different to the mid-latitude and subtropical marine BL.

Curry *et al.* (1996) defined three types of stratocumulus-topped Arctic boundary layers during summer months: a stable boundary layer with thin patchy cloud possibly in multiple layers; a stable boundary layer with a cloud layer above the BL; and lastly a cloud topped mixed layer extending from the surface. In all cases it is typical for the uppermost cloud layer to be topped by a strong temperature inversion which observations suggest is ubiquitous throughout the year (Kahl, 1990; Kahl *et al.*, 1992; Kahl & Martinez, 1996; Serreze *et al.*, 1992; Tjernstrom & Graversen, 2009) and which Curry *et al.* (1993) found occurred a minimum of 85 % of the time in August and had a median temperature difference across the inversion of 2.8 ^{o}C. Uniquely to the Arctic atmosphere specific humidity inversions are also commonly observed coincident with the temperature inversion (Curry *et al.*, 1996, 2000; Devasthale *et al.*, 2011; Pinto, 1998; Sedlar & Tjernstrom, 2009). These are thought be associated with moisture advection and precipitation

drying the lower atmosphere (Curry *et al.*, 2000).

Measurements of the lower atmosphere made during AOE-2001 characterize the summertime central Arctic boundary layer as shallow (typically around 150 m deep), well-mixed and very moist (Tjernstrom, 2005, 2007; Tjernstrom *et al.*, 2004). The BL was frequently occupied by patchy fog and low level cloud (more than 70 % of the time); with cloud base found below 100 m over 60 % of the time. However strong surface inversion were rarely seen and Tjernstrom (2005) found that although there was a high variability in the near surface stability, vertical gradients were consistently of slightly stable or near-neutral stability in the lowest 100 m of atmosphere (Figure 2.6). Above this layer the observed temperature gradient most frequently followed the moist adiabat until a height of around 400 m which is where the most frequent cloud top was observed during the campaign, i.e. the cloud and sub-cloud layer were well mixed. Beyond cloud top the atmosphere was strongly stable until heights of 1 km. Temperature inversions were commonly found in the lower atmosphere with at least one inversion observed at all times over the entire AOE-2001 expedition and two observed 77 % of the time. Inversions were most frequently situated with their base at 200 m (Tjernstrom, 2005), and typically the temperature decreased by less than 6 ^{o}C over the depth of the inversion, which was most frequently around 400 m. Inversions of specific humidity were also observed to coincide with the temperature inversion, with specific humidities most frequently found to increase by between 0 - 0.5 g kg^{-1}. Typically this resulted in a 0 % change in the relative humidity over the specific humidity inversions depth.

Lower atmospheric conditions as measured during the SHEBA summer, showed a BL structure similar to that observed during AOE-2001. Dai *et al.* (2011) found that the median BL depth was 430, 180 and 320 m in the months of June, July and August respectively, whilst measurements of the vertical potential temperature gradient showed the BL was most commonly of a near-neutral stability (Tjernstrom & Graversen, 2009). Throughout the rest of the year the lower atmospheric stability was also most frequently near-neutral (Figure 2.7), though a higher stability was more commonly encountered during the winter months (Persson *et al.*, 2002), with the result that BL depth was lower here than during any other season with a median value of 100 m (Dai *et al.*, 2011). Surface temperature inversions were found frequently in the winter and autumn (61 and 53 % of the time respectively) but rarely in the spring and summer (15 and 9 %), whilst elevated inversions dominated in the spring and summer months (85 and 91 %), with autumn and winter occurrences less frequent though still significant (39 and 47 %) (Tjernstrom & Graversen, 2009). The occurrence of both surface and elevated inversions around half the time during the winter is indicative of a switch in the structure of the atmosphere which Tjernstrom & Graversen (2009) explain as an effect of a change to BL cloudiness. In all seasons, elevated inversions were most commonly found with their bases capping the BL; an inversion base height of around 200 - 400 m was measured during the spring

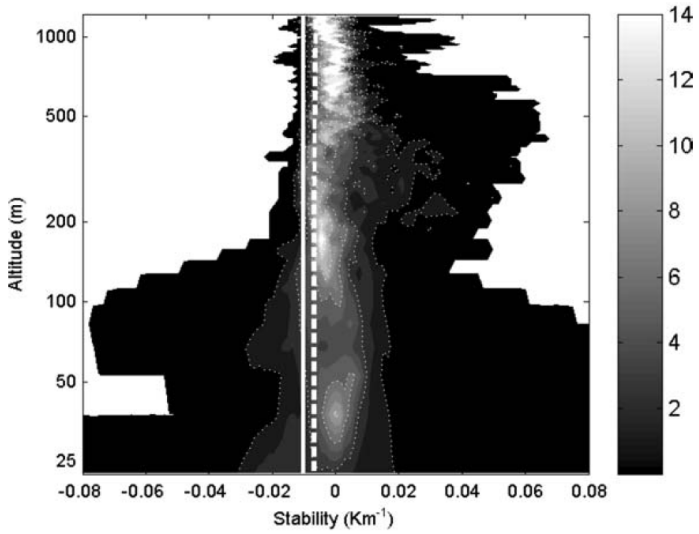

Figure 2.6: Frequency of occurrence in %, of the vertical temperature gradient (K m^{-1}) as a function of height for the entire AOE-2001 expedition north of 85^{o}N. The thick solid and dashed lines are the dry and moist adiabats, respectively. Reproduced from Tjernstrom (2005).

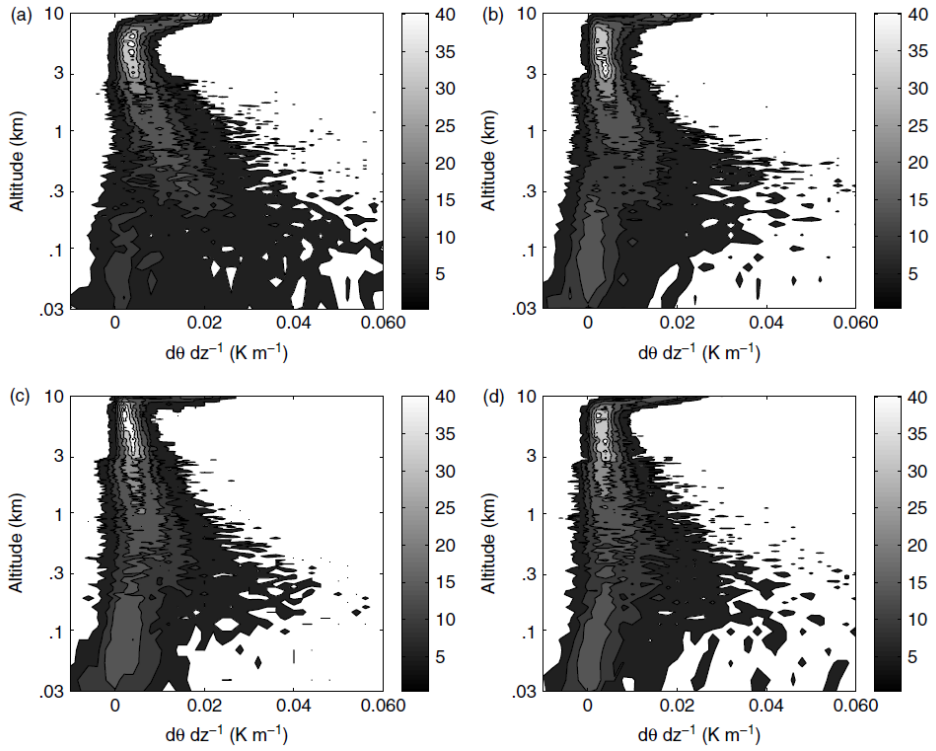

Figure 2.7: Frequency of occurrence in %, of the vertical potential temperature gradient (K m^{-1}) for the SHEBA expedition during (a) December - February, (b) March - May, (c) June - August and (d) September - November. Note the logarithmic scale. Reproduced from (Tjernstrom & Graversen, 2009).

and summer, while in the winter the inversion base was lower (less than 100 m). Inversion depths were thicker during the winter than the summer with the median thickness of 600 - 800 m compared to 200 - 400 m and inversion were also stronger; typically 8 - 10 ^{o}C in the winter compared to 2 - 6 ^{o}C in the summer (Tjernstrom & Graversen, 2009).

Contrary to that found in the sub-tropical and mid-latitude marine STBL, there is no strong diurnal variation of the Arctic BL. However from an analysis of AOE-2001 data, Tjernstrom (2007) found that the small diurnal variation in solar fluxes during the summer led to a statistically significant diurnal cycle in BL properties such as the wind speed, friction velocity and cloud properties, and more weakly for temperature, relative humidity and sensible heat flux. The most pronounced diurnal variability was found in the cloud layer; with cloud-base height at its lowest at noon preceded by enhanced drizzle and elevated cloud top heights in the afternoon, which is the opposite to what is found in mid-latitude stratocumulus. When the capping inversion layer was coolest and least strongly stable in the mid afternoon the cloud layer was at is warmest and most strongly stratified. The opposite was found in the mid morning.

From the surface of the central Arctic Ocean, sea-ice exerts a strong control over the lower BL conditions (Tjernstrom *et al.*, 2004). It can impact cloud coverage (Schweiger *et al.*, 2008), and its presence is a feature which distinguishes a central Arctic BL from the typical marine STBL. While the sea-ice surface of the central Arctic is fairly homogeneous compared to other environments, differences to the amount of snow cover and area of open ocean can have significant consequences on surface properties and to surface-atmospheric exchange. When sea-ice melts, areas of open ocean called open leads form between ice floes, and ponds of freshwater form on the ice; Perovich *et al.* (2002) found meltponds covered up to 25 % of the surface during the SHEBA summer. Meltponds and open leads decrease the albedo of the surface and increase the fluxes of heat and moisture into the atmosphere (Pinto *et al.*, 2003; Sterk *et al.*, 2013). The presence of melt ponds and open leads provides the BL with a near continuous supply of moisture with the result that the near-surface relative humidity with respect to water was always greater than 90 % during AOE-2001 (Tjernstrom *et al.*, 2004), and almost 100 % during the entire SHEBA summer (Andreas *et al.*, 2002). While during the wintertime, the SHEBA relative humidities with respect to liquid water were lower, falling to a minimum of between 60 - 70 %, while the relative humidity with respect to ice was found to be near 100 % or more over the entire year. Latent heat release and storage associated with the melt and freeze of sea-ice and snow also influence near-surface atmospheric temperatures, and during AOE-2001 temperatures were most commonly observed at 0 ^{o}C and -1.7 ^{o}C (which are the freezing points of fresh and salt water respectively) and displayed little sensitivity to heating and cooling higher in the atmosphere (Tjernstrom *et al.*, 2004).

2.3.3 Mixed-phase Arctic stratocumulus clouds

Low-level stratiform clouds are ubiquitous in the Arctic region. However despite their prevalence, the long polar winters and formidable conditions experienced in the region mean that direct measurements of clouds are sparser here than anywhere else on the planet. On account of this observational deficit, relatively little is know about the processes which lead to the formation and persistence of Arctic stratocumulus as compared to the sub-tropical and mid-latitude counterparts (Curry *et al.*, 1996; Morrison *et al.*, 2012). Though observations and modelling studies suggest that the principal physical processes which govern the development of the STBL also govern the development of Arctic stratocumulus topped boundary layer (Figure 2.8). Studies also show that a number of differences in the dynamical, microphysical and radiative properties of the clouds exist.

Large-scale formation of Arctic stratocumulus is thought to be caused by the modification of the local air mass due to the advection of relatively warm and moist air and from radiative cooling (Curry & Herman, 1985b; Herman & Goody, 1976; Herman & Curry, 1984). However, because the Arctic BL is always close to saturation, mesoscale disturbances which cause either the BL temperature to fall or its specific humidity to increase can cause cloud formation on local scales (Wang & Wang, 2004). This can also sometimes lead to the formation of multiple stratiform layers which is a distinctly Arctic phenomenon (Curry *et al.*, 1996; Tsay & Jayaweera, 1984). The relationship of cloud to the large scale environment is complicated, however once formed Arctic stratocumulus are able to persist for a few days or more (Shupe, 2011), under weak synoptic forcing and large-scale subsidence (Pinto, 1998; Zuidema *et al.*, 2005). Local mixing is more important to their maintenance with Curry *et al.* (2000) suggesting that meltponds and open leads act as a source of BL moisture which is critical to their persistence. Where a specific humidity inversion is present above the cloud top, entrainment of air from the inversion into the BL may also support the persistence of the cloud layer Tsay & Jayaweera (1984).

Microphysical properties can impact on Arctic stratocumulus. Annual Arctic aerosol concentrations are typically highest during the winter and spring because of an inflow of anthropogenic pollution from the mid-latitudes at this time of year (e.g. Sirois & Barrie, 1999). However in the summer the Arctic BL can be considered pristine with aerosol concentrations usually less than 150 cm^{-3} (Bigg *et al.*, 1996; Bigg & Leck, 2001; Covert *et al.*, 1996; Heintzenberg & Leck, 2012). These low aerosol numbers are due to the fact that few local aerosol sources exist in the Arctic BL; in the AOE-96 and AOE-2001 field campaigns the surface microlayer of open leads (thin film on the water top) was proposed to be a primary biological source of marine particles (Bigg *et al.*, 2001; Leck *et al.*, 1996, 2002), though its relative importance as a source is as yet undetermined.

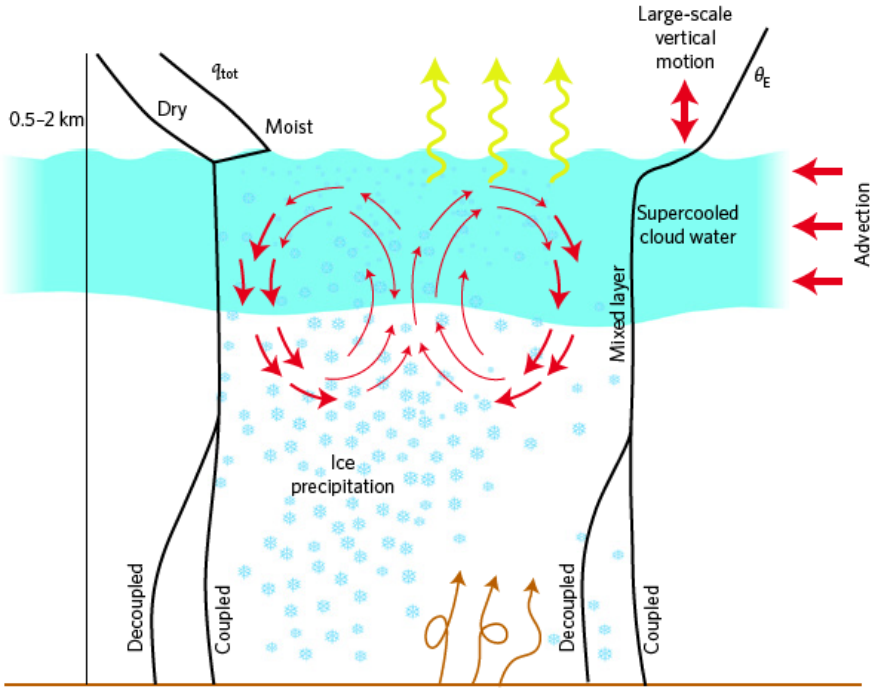

Figure 2.8: Conceptual model to illustrate the structure of mixed-phase Arctic stratocumulus. Reproduced from Morrison *et al.* (2012).

Low concentrations are exacerbated by the high frequency of inversions preventing particle deposition from the free troposphere into the BL. Unusually, the low concentration of CCN aerosol in the lower Arctic atmosphere means that cloud formation is frequently limited by CCN availability (Bigg *et al.*, 1996; Mauritsen *et al.*, 2011) - Mauritsen *et al.* (2011) estimated that such conditions might occur as much as 30 % of the time based on all the CCN measurements from the IAOE-91, AOE-96, AOE-2001 and ASCOS campaigns. Thus the local Arctic BL is sometimes under conditions of what Mauritsen *et al.* (2011) describes as a "tenuous cloud regime"; whereby at typical supersaturations the CCN concentrations are too low for cloud formation (no condensation until around 400 % relative humidity).

A significant difference between Arctic stratocumulus and those found in lower latitudes is the cloud phase. While sub-tropical stratocumulus are exclusively liquid-phase: composed of liquid water, drizzle and/or rain droplets only. Arctic stratocumulus have been observed to be liquid-phase only - possibly at temperatures below 0^oC with cloud in the form of supercooled liquid water; ice-phase only where they are composed of ice, snow and/or graupel; or mixed-phase where they are composed of a mixture of supercooled liquid water droplets and ice crystals. The seasonal frequency of occurrence of cloud phase was calculated by Shupe (2011) at three Arctic locations; Barrow and Oliktok Point in

the north slope of Alaska and from the SHEBA site in the western Arctic Ocean. When considering the annual mean across all sites, ice-phase only clouds were the most prevalent. These were found at least 40 % of the time during each month of the year at each of sites, and between 60 and 70 % of the time as an annual average. Ice clouds were found through the BL and in the free troposphere up to heights approaching the tropopause. Ice cloud temperatures varied between 0^oC and 60^oC.

Mixed-phase clouds were the next most common cloud type with a annual average occurrence of between 25 and 47 % (Shupe *et al.*, 2006). Mixed-phase clouds displayed more of a seasonal cycle than ice clouds, with a minima in winter and maxima in September or October. Liquid-phase only clouds showed the greatest variability of all cloud types with a strong seasonal cycle evident at each measurement site. Liquid cloud occurrences peaked during the summer, with a maximum frequency of occurrence of more than 30 % at SHEBA and Barrow in June and July (Shupe *et al.*, 2006). While winter and spring frequencies were much lower falling to minimums of less than 5 % at all sites. Liquid water was observed down to temperatures as cold as -40^{o}C; which is the temperature at which homogeneous freezing of cloud droplets occurs (Pruppacher & Klett, 1997), though below -24^{o}C liquid water was always in the presence of ice.

The persistence of mixed-phase clouds is surprising as at temperatures below the freezing point of water, the saturation vapour pressure over ice is lower than that over liquid water and this permits ice particles to grow by vapour deposition at the expense of liquid condensate, the so-called Wegener-Bergeron-Findeison mechanism (Bergeron, 1935; Findeisen, 1938; Wegener, 1911). Riming of cloud water onto existing ice particles also contributes to the loss of cloud water and under certain environmental conditions secondary ice multiplication mechanisms can rapidly increase the ice crystal number leading to an increased instability from the Wegener-Bergeron-Findeison mechanism; for instance fragmentation of ice particles (Vardiman, 1978), and rime splintering (Hallett & Mossop, 1974; Mossop, 1985) which occurs between temperatures of -3 and -8^{o}C.

While glaciation of the whole cloud can sometime occur quite rapidly (e.g. Hobbs & Rangno, 1990) the formation of new ice crystals seems to be sufficiently slow in mixed-phase Arctic stratocumulus for liquid water contents to be maintained and the cloud to remain of mixed-phase (Morrison *et al.*, 2012). Nucleation of ice occurs on ice-forming aerosol known as Ice Nuclei (IN) which are found at much lower atmospheric concentrations than CCN - typically between 10^{-5} to 0.1 cm^3 (DeMott *et al.*, 2010; Rogers *et al.*, 2001). Because ice crystal number is critical to the Wegener-Bergeron-Findeison mechanism, low IN concentrations are necessary to support persistent mixed-phase cloud, and model simulations show that modest increases in IN can lead to the rapid glaciation of mixed-phase clouds into ice-phase only clouds (Harrington *et al.*, 1999; Jiang *et al.*, 2000; Pinto, 1998).

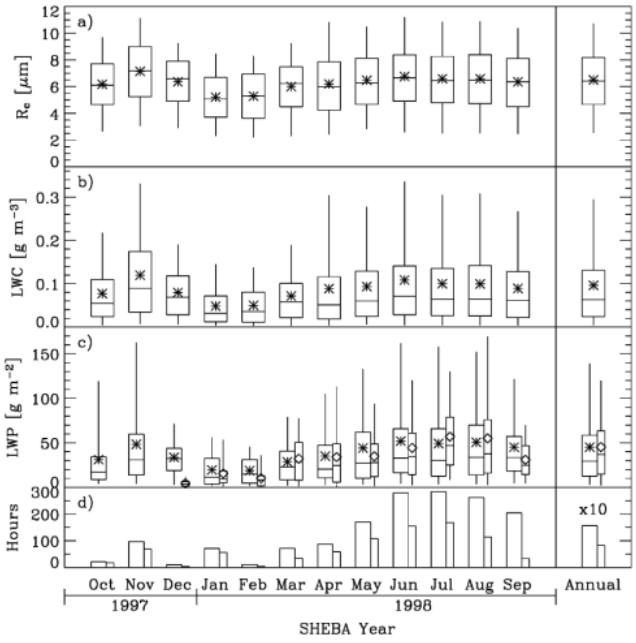

Figure 2.9: Monthly and annual statistics of all-liquid cloud (a) droplet effective radius, (b) liquid water content, (c) liquid water path, and (d) hours of occurrence. The box-and-whisker plots provide the 5th, 25th, 50th, 75th and 95th percentiles of the data, and the mean is given as a symbol. Reproduced from Shupe *et al.* (2006).

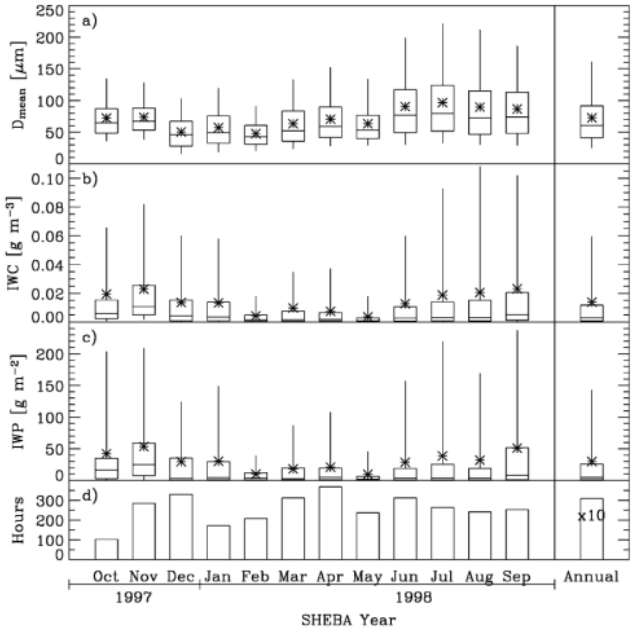

Figure 2.10: Monthly and annual statistics of all-ice cloud (a) ice effective diameter, (b) ice water content, (c) ice water path, and (d) hours of occurrence. The box-and-whisker plots provide the 5th, 25th, 50th, 75th and 95th percentiles of the data, and the mean is given as a symbol. Reproduced from Shupe *et al.* (2006).

It might be possible that the liquid phase may itself regulate the ice concentrations within the cloud (Morrison *et al.*, 2012). Rangno & Hobbs (2001) and Hobbs & Rangno (1985) both found a correlation between the number of large droplets and the ice concentrations in mixed-phase clouds, while de Boer *et al.* (2011) found that despite the greater super-saturation with respect to ice at temperature below 0^oC, ice crystals only occurred once supercooled liquid was present in the cloud. This is supported by observations showing the preference of a mixed-phase over ice-phase only state at temperatures above about -25^{o}C (Shupe, 2011). If indeed the number of large droplets and the ice concentrations are correlated then the conversion of liquid to ice would be self limiting and provided a negative feedback on ice production (Morrison *et al.*, 2012). The spatial distribution of liquid water and ice within the mixed-phase cloud may also contribute to their resistance to full glaciation. The characteristic structure of mixed-phase Arctic stratocumulus is of a thin layer of supercooled liquid water near the top of the cloud which continually precipitates ice through and below the liquid layer (Shupe *et al.*, 2008). The continual loss of ice, restricts its ability to compete with liquid water for the available vapour and supports its maintenance (e.g. Harrington *et al.*, 1999).

Generally the absolute amount of water in Arctic stratocumulus is lower than found in marine stratocumulus, with measurements from ASE finding a maximum liquid water content of 0.5 g m^{-3} and the vertically integrated liquid water content, also known as the liquid water path (LWP) ranging from 11 to 117 g m^{-2} for low clouds. Mean droplet radii were found in the range of 2 - 7 μm (Curry, 1986; Herman & Curry, 1984; Tsay & Jayaweera, 1984). Ground based radar and lidar retrievals of all-liquid and all-ice cloud microphysical properties for the whole SHEBA campaign are shown in Figures 2.9 and 2.10. During the summer months the LWC had an average value of around 0.1 g m^{-3} and the ice water content (IWC) was an average of 0.02 g m^{-3} (Shupe *et al.*, 2006). The LWP and the vertically integrated ice water content, also known as the ice water path (IWP) were observed to be in the range of 30 - 50 g m^{-2} and 20 - 50 g m^{-2} respectively (Shupe *et al.*, 2006).

The mean vertical distribution of LWC observed during SHEBA for single-layer clouds was a linear increase from cloud base until a height of about 60 % of the cloud top, while Tsay & Jayaweera (1984) found maximum LWC near the top of the liquid layer as in typical in sub-tropical stratocumulus. Shupe *et al.* (2006) found that IWC was at a maximum at 25 % of the depth of the cloud from its base to top in all-ice clouds; reflecting ice crystal growth as the particles fall through the liquid cloud, and their rapid sublimation below cloud base. While in mixed-phase clouds a are broader IWC maximum was observed in the upper-middle portion of the cloud. Shupe *et al.* (2006) observed cloud droplet number concentrations of the order of 100 cm^{-3} while in both ASE and M-PACE, droplet number concentrations reached up to 500 cm^{-3} (Curry & Ebert, 1992; Verlinde *et al.*, 2007). Droplet numbers over the Arctic are sensitive to aerosol pollution events and

Garrett & Zhao (2006) found annual mean values of 53 cm^{-3} and 153 cm^{-3}, made during clean and polluted conditions near Barrow, Alaska. The observed droplet size spectra in Arctic stratocumulus appears to be fairly broad and Curry (1986) found the ratio of the standard deviation to the mean radius of the droplet spectrum to be an average of around 0.6 from ASE observations. This is larger than is typically found in sub-tropical clouds (e.g. Noonkester, 1984) which Curry (1986) attribute to turbulence induced by radiative cooling at cloud top causing fluctuations in the supersaturation field. Tsay & Jayaweera (1984) found that the droplet spectra is usually bi-modal at cloud top and mono-modal at cloud base.

The characteristic distribution of a small number of large droplets within Arctic stratocumulus, means the clouds are typically optically thin. Thus they are less effective at reflecting solar radiation back to space (Twomey, 1977) than stratocumulus with a large number of droplets; for summertime Arctic stratocumulus Herman & Curry (1984) determined cloud reflectivities to be between 0.2 and 0.68 compared to typical marine values of 0.5 or greater (e.g. Stephens *et al.*, 1978). Sometimes Arctic stratocumulus may become grey, whereby they emit less thermal radiation than a black body (emission is dependent on temperature only)(Shupe & Intrieri, 2004; Walsh & Chapman, 1998). Cloud thermal radiation emission follows the relationship:

$$F_{LW} = \varepsilon \sigma_{SB} T^4 \tag{2.2}$$

where σ_{SB} is the Stefan-Boltzmann constant, T is the temperature and ε is the emissivity which is given by:

$$\varepsilon = 1 - exp(-k_{abs} LWP) \tag{2.3}$$

where the mass absorption coefficient k_{abs} depends on the wavelength. Clouds start to emit thermal radiation as blackbodies ($\varepsilon \approx 1$) between LWPs of around 30 to 50 g m^{-2} (Garrett & Zhao, 2006; Stephens, 1978). In regions dominated by marine stratocumulus the average LWP is between 40 and 150 g m^{-2} (e.g. ODell *et al.*, 2008; Weng & Grody, 1994) thus low latitude stratocumulus behave like black bodies. However the LWP of Arctic stratocumulus is often less than this value (Shupe *et al.*, 2006), and consequently Curry & Herman (1985a) determined bulk cloud emissivities to range between 0.4 and 1 during the summer months. The low LWP of Arctic stratocumulus means that emission has a greater dependence on the cloud microstructure; temperature, height, droplet number and water content (Shupe & Intrieri, 2004), and makes them particularly sensitive changes to CCN (Garrett & Zhao, 2006).

The cloud emissivity also determines the longwave radiative cooling rate, which as for marine stratocumulus is a dominant term in the local heat budget of the mixed-phase

stratocumulus boundary layer, generating instability which leads to the buoyant production of TKE. In mixed-phase clouds the presence of the ice can reduce the longwave radiative cooling rate over that expected for a liquid-phase only cloud, by limiting the amount of liquid water (Pinto, 1998).

The ice can also affect the depth over which cooling occurs by altering the opacity of the cloud. Opacity is commonly described using the optical depth, τ. For a cloud layer where the mass extinction coefficient, k_{ext} is constant ($k_{ext} = k_{abs} + k_{sca}$, where k_{sca} is the mass scattering coefficient), τ can be determined through the relationship:

$$\tau = k_{ext} \int_0^h LWC dz \tag{2.4}$$

The value of k_{ext} is proportional to the geometrical cross-sectional area of the particle and the extinction efficiency, Q_{ext} which in turn depends on particle size, the frequency of the radiation and the particle distribution. For the extinction of longwave radiation by cloud droplets, Q_{ext} has a complex relationship and must be calculated using Mie theory, however for particles much larger than the wavelength of the radiation, Q_{ext} asymptotes to 2, and so τ can be approximately calculated as (Wood, 2006):

$$\tau = \int_0^h \frac{3}{2} \frac{LWC}{\rho_w r_e} dz \tag{2.5}$$

where h is the cloud thickness, ρ_w is the density of water and r_e is the cloud droplet effective radius; which is the area weighted radius of the cloud droplets, relating the total surface area of the cloud droplets to their combined mass (Hansen & Travis, 1974). Equivalent relationships also exist for ice (e.g. Ebert & Curry, 1992), where an ice effective diameter D_e is used as a measure of the optical size of ice crystals.

While the ice cloud optical depth is relatively small compared to that of supercooled liquid cloud, and therefore ice is less important at preventing the transmission of radiation through the cloud. The presence of ice can indirectly regulate the clouds optical depth with Curry & Ebert (1992) finding that a move to ice-only conditions is associated with a drop in optical depth. As the greatest longwave radiative cooling in a cloud layer occurs around about the level where the optical depth is equal to one (Marshak & Davis, 2005; Wallace & Hobbs, 2006), the presence of ice extends the depth of peak longwave radiative cooling deeper into the cloud. During the SHEBA summer Shupe *et al.* (2006) found r_e and D_e to be mean values of 5 μm and 90 μm respectively (Figures 2.9 and 2.10).

The relationship between local processes; the cloud microphysics, radiation and dynamics in mixed-phase Arctic stratocumulus (Figure 2.8) is key to the sustenance of the cloud (Morrison *et al.*, 2012). As for sub-tropical stratocumulus, turbulence in the Arctic BL is primarily generated through longwave radiative cooling; with peak cooling rates of greater

than 60 K day^{-1} near cloud top (Harrington *et al.*, 1999; Jiang *et al.*, 2000; Pinto, 1998), keeping the BL well-mixed so that θ_e and q_t are nearly constant with height, and forcing condensation in updraughts. Thus the microphysics-radiation-dynamics relationship is a self-maintaining feedback (Morrison *et al.*, 2012).

Large-scale horizontal advection of water vapour into the inversion can also help sustain the clouds (Curry, 1983; Curry *et al.*, 1997; Pinto, 1998), with turbulent transport of water vapour from the specific humidity inversions to the mixed layer providing a source of moisture to balance the almost continual loss from ice precipitation (Solomon *et al.*, 2011). Though the surface fluxes are relatively minor over the sea-ice (e.g. Persson *et al.*, 2002; Tjernstrom, 2007), the source of moisture from the surface can also contribute to the clouds persistence (Zuidema *et al.*, 2005).

Where ice precipitation is particularly strong or the large-scale advection causes the environment to dry, the cloud can sometimes dry enough that the supercooled liquid water is reduced to an amount that the cloud top radiative cooling is too weak to maintain turbulent mixing of the BL, causing the cloud to decouple from the surface (Morrison *et al.*, 2011). Unlike in the sub-tropical BL, the presence of humidity inversions and the feedbacks between local processes makes the cloud less susceptible to break up associated with decoupling (Bretherton *et al.*, 2010).

2.3.4 Cloud encroachment into the inversion

Whilst the prototypical sub-tropical and mid-latitude stratocumulus has a cloud top which is found coincident with the base of the capping inversion. A range of observations have shown that Arctic stratocumulus frequently have a cloud top which extends inside the inversion layer (Sedlar & Tjernstrom, 2009; Tjernstrom, 2005). Using data collected during SHEBA, ASCOS and from an Arctic observation site at Barrow, Alaska, Sedlar *et al.* (2012) recently analysed observations of specific humidity inversions in an attempt to characterize the encroachment of cloud into the inversion layer.

Inversion boundaries were identified from temperature retrievals made by a dual-channel microwave radiometer, while the cloud top was identified from radar reflectivity retrievals from a millimetre cloud radar. Two types of cloud-inversion regimes were identified. The first was the typical marine STBL regime where the cloud is capped by the inversion, which Sedlar *et al.* (2012) distinguished as cloud top being at or below the inversion base by no more than 100 m. The second regime was of a cloud inside the inversion, which was distinguished as a cloud top at least 90 m (two vertical radar gates) above the inversion base, but at a height lower than the inversion top. Only inversion with a depth of more than 40 m and clouds which were below an altitude of 3 km were considered.

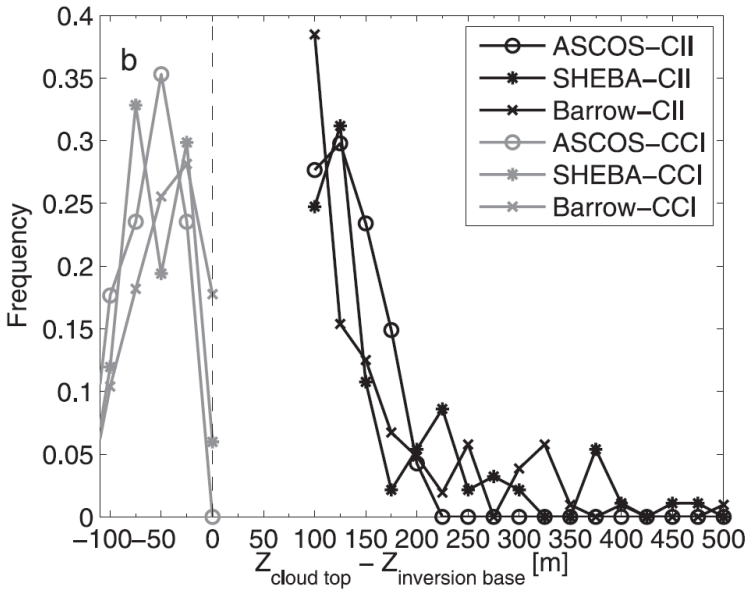

Figure 2.11: Relative frequency of height difference between the inversion base and cloud top for clouds capped by the inversion (grey lines) and clouds inside the inversion (black lines). Reproduced from Sedlar *et al.* (2012).

In each of the datasets the combined prevalence of both of the cloud-inversion regimes was found to be less than 50 % of the total time. During ASCOS the majority (two thirds) of the cloud-inversion collocation was determined to be cloud inside the inversion. While in Barrow, the prevalence of regimes was reversed with cloud capped by the inversion present around two thirds of the time. In SHEBA the relative frequency of both regimes was more equal, with 60 % of collocations being cloud inside the inversion. SHEBA and ASCOS measurement were made over Arctic Ocean while Barrow is based on the north slope Alaska, suggesting a preference for clouds inside the inversion away from land. The magnitude of difference between the cloud top and inversion base heights was typically 50 m or less where cloud was capped by the inversion in ASCOS and at Barrow, while distributed more evenly between heights of -100 to 0 m in SHEBA. In all datasets the greatest frequency of occurrence of cloud encroachment depth was below 150 m, though infrequently the cloud top extended as high as 500 m inside the inversion (Figure 2.11). In general lower clouds with bases below 600 m (300 m for sea-ice sites) were found to be more likely to extend into the inversion, while higher clouds were more likely to be capped by the inversion.

Overall the inversion thickness ranged between 100 and 500 m, and inversion strengths varied between 0 and 14^{o}C. Generally cases where cloud was found inside the inversion were associated with inversions which were stronger by 2 - 4 ^{o}C and deeper by 200 - 300 m. Inversions associated with clouds capped by the inversion were typically weaker with

a strength of less than 2^{o}C. Moisture inversions were found in 85 % of cases where cloud encroached in the temperature inversion and in more than 60 % of cases where the cloud was capped by the inversion. The high frequency of moisture inversions shows that they are widely prevalent, and suggests that they may be an important source of BL moisture, especially where decoupling exists between the cloud and the surface.

Sedlar *et al.* (2012) also examined the longwave emissivity and emission temperature for clouds of both regimes with a radiative transfer model. A number of different profiles using an idealised setup of an inversion layer cloud with varying water contents inside the inversion were examined. The emissivity profiles were found to have a dependence on the fraction of the LWC found inside the inversion which led to longwave cooling occurring over a greater depth of the cloud. Sedlar *et al.* (2012) suggest the change in the cooling depth promotes a rise in the total cloud layer cooling because of increased condensation associate with the change in longwave emissivity. The broadening of the cooling region was also associated with a reduction in the peak of the cooling profile. However in all cases except the most extreme liquid water contents inside the inversion, the position of the peak cooling was determined to be at the inversion base height and so cloud inside the inversion would not necessarily be expected to force an adjustment of the thermodynamic profile.

So far the only modelling study to address the question of how cloud is maintained inside the inversion layer is Solomon *et al.* (2011). The Solomon *et al.* (2011) study modelled an Arctic mixed-phase stratocumulus observed over the Beaufort Sea during the ISDAC field campaign on 8th April 2008. The observed cloud was multi-layered, with a mixed-phase cloud with top at around 1 km precipitating ice and snow from its base into an ice-only layer below. The cloud was largely composed of ice, with the retrieved IWP of 60 g m^{-2} or greater, generally exceeding the retrieved LWP of between 20 and 100 g m^{-2}. Observations suggested that the cloud layer was decoupled from the surface by a stable region of air at cloud base which separated well-mixed layers within the cloud and below the cloud base. Above the cloudy mixed layer a sharp temperature inversion of around 4 K and a humidity inversion where water vapour mixing ratios were found to increase from 1.2 to 1.6 g kg^{-1} across the transition zone were measured. Cloud top was retrieved up to a maximum of 100 m inside the inversion.

Modelling of the cloud was performed using a version of the Weather Research Forecast model (Skamarock *et al.*, 2008), in which several grids of increasing resolution were nested inside each other. The innermost domain had a maximum vertical resolution of 16 m through the cloud-driven mixed layer and 8 m through the upper entrainment zone, allowing the dynamical motions of large eddies to be resolved explicitly. The model was forced with lateral and surface boundary conditions from the European Centre for Medium-Range Weather Forecasts (ECMWF) 4x daily, T255 ERA-Interim dataset.

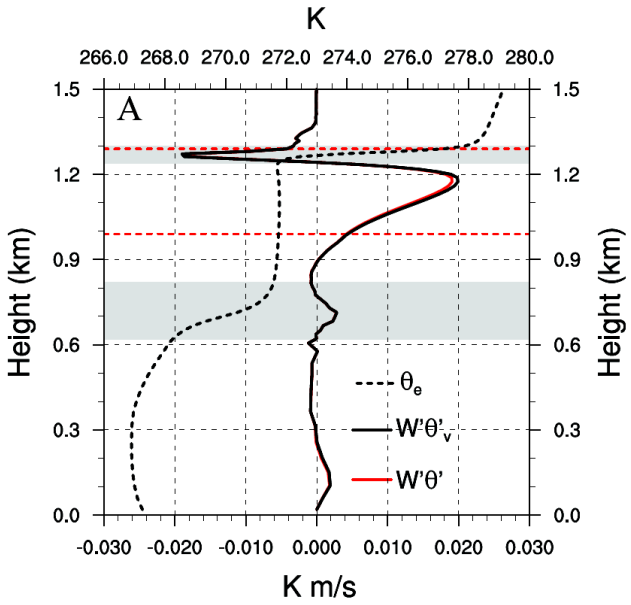

Figure 2.12: Horizontally and temporally averaged profiles of θ_e, $\overline{w'\theta'}$ and $\overline{w'\theta'_v}$ through an inversion encroaching Arctic stratocumulus. The gray shading indicates the position of the entrainment zones and dashed red lines the position of the cloud layer top and base. Reproduced from Solomon *et al.* (2011)

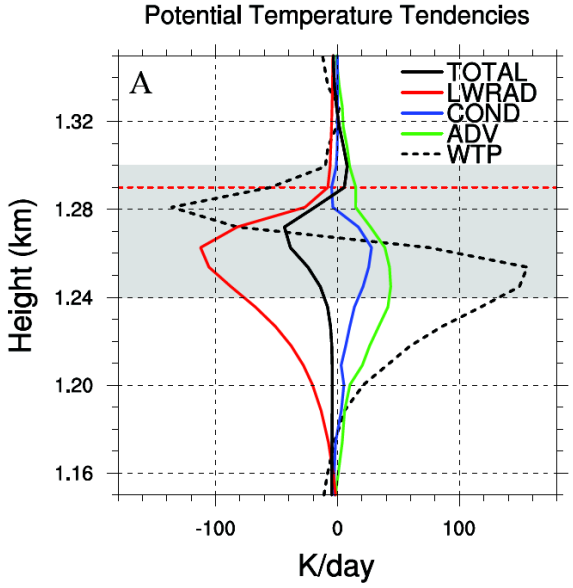

Figure 2.13: Horizontally and temporally averaged potential temperature tendencies in the upper region of the mixed layer and cloud top entrainment zone. TOTAL is the total tendency, COND is the tendency due to condensation/evaporation, LWRAD the tendency due to longwave radiative heating/cooling, ADV the tendency due to total advection and WTP the tendency due to vertical eddy advection. The gray shading indicates the position of the entrainment zones and dashed red lines the position of the cloud layer top and base. Reproduced from Solomon *et al.* (2011)

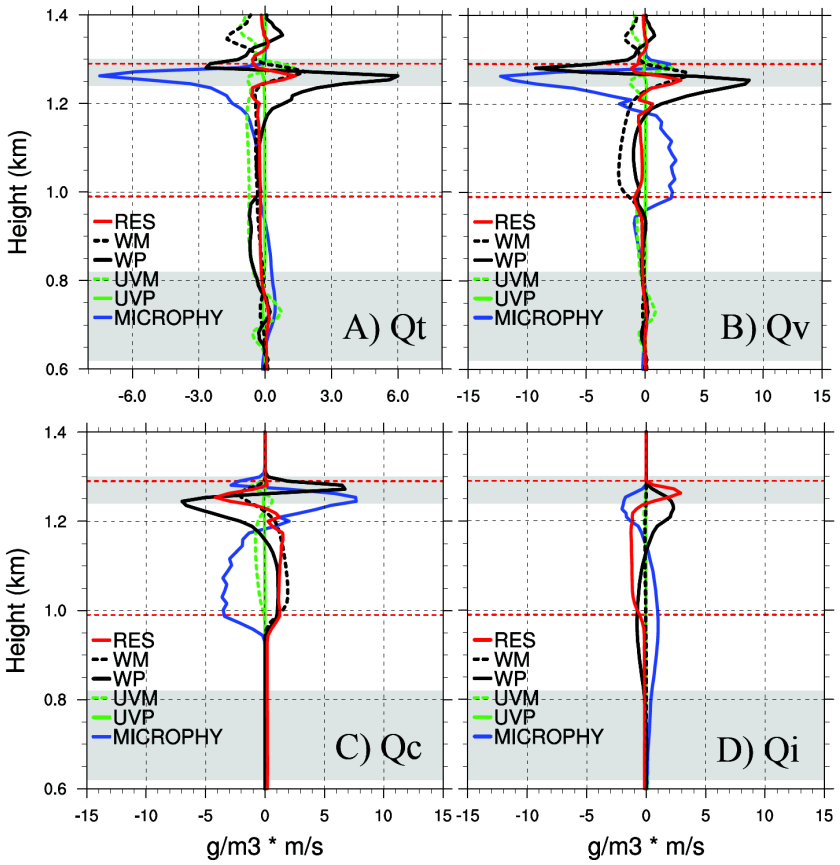

Figure 2.14: Horizontally and temporally averaged tendencies of (A) total water, (B) water vapour, (C) cloud liquid water, and (D) cloud ice water. Note units are printed incorrectly and should read g m^{-3} day^{-1}. MICROPHY is the net tendency due to cloud microphysics and sedimentation. RES is the residual tendency due to sub-grid scale mixing plus diffusion. WM and UVM are the tendencies due to mean horizontal and vertical advection respectively and are calculated by horizontally averaging tendencies. UVP is the tendency due to horizontal eddy advection which is is calculated as the divergence of fluxes across the domain, and WP is tendency due to vertical eddy advection which is calculated from the divergence of the vertical eddy flux. In each of the plots the gray shading indicates the position of the entrainment zones and dashed red lines the position of the cloud layer top and base. Reproduced from Solomon *et al.* (2011)

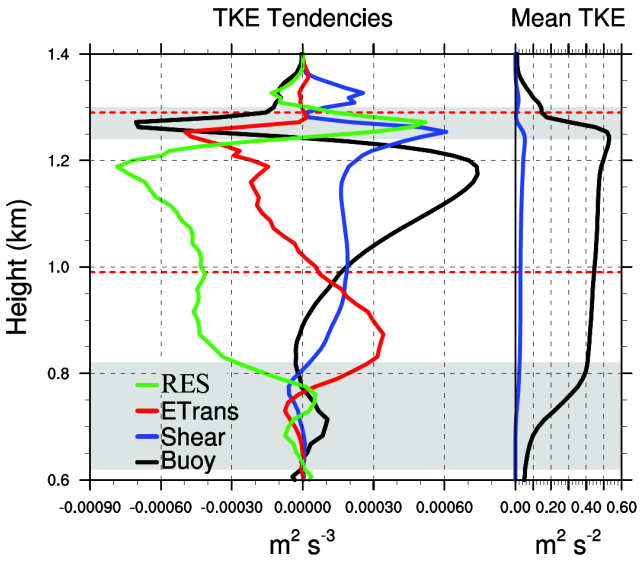

Figure 2.15: (Left) Horizontally and temporally averaged resolved TKE tendencies, where ETrans is tendency due TKE transport, Shear the tendency due to shear production, Buoy the tendency due to buoyancy and RES which is the tendency due to pressure transport plus dissipation. (Right) Mean resolved (black line) and sub-grid (blue line) TKE. The gray shading indicates the position of the entrainment zones and dashed red lines the position of the cloud layer top and base. Reproduced from Solomon *et al.* (2011)

Generally, the simulated BL compared well with the observations although the stable region between the cloud and sub-cloud layer was too deep and the simulated temperature inversion was 1 K too strong.

The time and area averaged profiles of $\overline{w'\theta}$, $\overline{w'\theta'_v}$ and θ_e are shown in Figure 2.12. The entrainment zones which were estimated from the changes in the θ_e slope are also shown. The upper entrainment zone is around 60 m deep and its boundaries are roughly consistent with the area of negative $\overline{w'\theta'_v}$ near the top of the mixed layer. The peak in simulated cloud water was found at the base of the humidity inversion and liquid cloud extended approximately 50 m into the inversion, accounting for 23 % of the total liquid cloud water. The negative peak in $\overline{w'\theta'_v}$; which is identified as the top of the mixed layer, z_i in Deardorff (1980), is located just below the centre of the entrainment zone between 20 and 30 m above z_{ib}.

Figures 2.13, 2.14 and 2.15 show the 15-minute time and area averaged budgets of θ, the water contents and TKE respectively. Prognostic equations for θ and the water

constituents are given by (Stull, 1988):

$$\frac{\partial\overline{\theta}}{\partial t} = \left(\frac{p_0}{p}\right)^{\frac{R}{C_p}} Q_1 - u_i \cdot \nabla\theta - \frac{\partial\overline{w'\theta'}}{\partial z} \tag{2.6}$$

$$\frac{\partial\overline{q_n}}{\partial t} = Q_2^n - u_i \cdot \nabla q_n - \frac{\partial\overline{w'q_n'}}{\partial z} \tag{2.7}$$

where p is the pressure and p_0 the pressure at the surface, C_p is the specific heat capacity at constant pressure, u_i is three dimensional flow velocity; where i denotes the direction, w is the vertical velocity and ' denotes a perturbation from the mean state. The θ budget is a balance of heat storage and tendencies due to diabatic heating/cooling, Q_1; from condensational heating and radiative heating, and from both the horizontal and vertical transport of heat due to the mean winds and the divergence of the vertical heat flux. The water constituent, q_n (where n is the water species) budgets are a balance between water storage and tendencies due to diabatic moistening due to phase changes, Q_2^n; where sedimentation is included in the Q_2^n term for the hydrometeors, and from the transport of water due to the mean winds and the divergence of the vertical water flux.

The TKE budget is given by (Garratt, 1992):

$$\frac{\partial\overline{TKE}}{\partial t} = \left(\frac{g}{\theta_0}\right)\overline{w'\theta_v'} - \left(\overline{u'w'}\frac{\partial\overline{u}}{\partial z} + \overline{v'w'}\frac{\partial\overline{v}}{\partial z}\right) - \frac{\partial\overline{w'TKE}}{\partial z} - \frac{\partial\overline{w'p'}}{\overline{\rho}\partial z} - \epsilon \tag{2.8}$$

where TKE=$0.5(\overline{u'^2} + \overline{v'^2} + \overline{w'^2})$. The first term of the TKE budget is the storage and this is balanced by (from left to right respectively); buoyancy production/consumption, shear production, vertical turbulent transport, pressure transport and viscous dissipation.

Figures 2.13 and 2.14 show that the temperature and humidity inversions are supported by a large scale horizontal advective source of warm moist air into the upper entrainment zone (henceforth entrainment zone) equal to an advective θ tendency of 40 K day^{-1} and water vapour tendency of around 2 g kg^{-1} day^{-1}. Large scale vertical transport of moisture also increases the water vapour tendency in the EZ by up to 3 g kg^{-1} day^{-1}. Longwave radiative cooling is the dominant source of TKE in the cloud-driven mixed layer and the main driver of entrainment (Figure 2.15). Radiative cooling peaks within the EZ with a tendency of around -110 K day^{-1}, though here it is largely offset by condensational heating and the vertical eddy flux of heat from the inversion above, resulting in a net EZ cooling of up to -40 K day^{-1}. A weak but significant eddy flux of water vapour from the humidity inversion also act as a source of moisture to the cloud layer below, offsetting the loss of water vapour from condensation in updraughts and deposition in both updraughts and downdraughts in the mixed-layer.

Overall the mixed layer is a net sink of total water with sedimentation loss of ice and snow to the surface the greatest contributor. The vertical flux of water vapour from the

humidity inversion into the mixed layer is the only source of humidity in the decoupled cloud system simulated in Solomon *et al.* (2011), thus the humidity inversion plays a crucial role in supporting the persistence of the mixed-phase cloud. This highlights a significant difference between Arctic stratocumulus where cloud top encroaches inside the inversion and typical sub-tropical stratocumulus where entrainment dries the BL.

Chapter 3

Large Eddy Simulation model description

Large Eddy Simulation (LES) is a modelling technique used to simulate turbulent flows such as those observed in the BL. The basis of the LES technique is to filter the basic equation set so that the only largest most energetic BL eddies (typically on scales greater than a few metres to about 100 metres, depending on the application) are explicitly modelled, while those eddies which are in the dissipating range of turbulent motions are parametrised. These eddies are unimportant for the mean flow evolution and their statistically self similar and isotropic properties allow them to be parametrised effectively in a sub-grid scale (SGS) turbulence model. Such parametrisation reduces the computational constraints of resolving all scales of BL turbulence, while still allowing the determination of non-mean flow characteristics.

3.1 UK Met Office Large Eddy Model

The LES model used in this study is Version 2.4 of the UK Met Office (UKMO) Large Eddy Model (LEM)(Derbyshire *et al.*, 1999; Gray *et al.*, 2001); though with the inclusion of fully interactive microphysics and radiation schemes within the model, the LEM can more appropriately be described as a Cloud Resolving Model (CRM). Previous applications of the LEM have included the simulation of dry and moist boundary layers including both shallow and precipitating convective clouds, marine stratocumulus, altostratus and cirrus (Hill & Dobbie, 2008; Hill *et al.*, 2008; Marsham *et al.*, 2007a,b; Petch, 2006). It has also been compared against many other CRMs and LES models in several model intercomparisons (Ackerman *et al.*, 2009; Morrison *et al.*, 2009a; Siebesma *et al.*, 2003; Stevens *et al.*, 2005).

3.1.1 Governing equations of the resolved-scale fields

The LEM solves a filtered Boussinesq-type equation set which is applicable for incompressible fluids. The Boussinesq approximation is suitable for buoyancy-driven flows where shallow convection conditions are satisfied - such as in the BL - and assumes that density differences are sufficiently small within the resolved flow so as to be neglected in the momentum equation, except where they appear in terms multiplied by the acceleration due to gravity. The Boussinesq-type equation set takes the following form (in tensor notation):

$$\frac{Du_i}{Dt} = -\frac{\partial}{\partial x_i}\left(\frac{p'}{\rho_s}\right) + \delta_{i3}B' + \frac{1}{\rho_s}\frac{\partial \tau^s_{ij}}{\partial x_j} - 2\epsilon_{ijk}\Omega_j uk \tag{3.1}$$

$$0 = \frac{\partial}{\partial x_i}(\rho_s u_i) \tag{3.2}$$

$$\frac{D\theta}{Dt} = \frac{1}{\rho_s}\frac{\partial h^\theta_i}{\partial x_i} + \left(\frac{\partial \theta}{\partial t}\right)_{MPHYS} + \left(\frac{\partial \theta}{\partial t}\right)_{RAD} + \left(\frac{\partial \theta}{\partial t}\right)_{LS} \tag{3.3}$$

$$\frac{Dq_n}{Dt} = \frac{1}{\rho_s}\frac{\partial h^{q_n}_i}{\partial x_i} + \left(\frac{\partial q_n}{\partial t}\right)_{MPHYS} + \left(\frac{\partial q_n}{\partial t}\right)_{LS}\left(\frac{\partial q_n}{\partial t}\right)_{SED} \tag{3.4}$$

where the subscript s denotes a reference state and $'$ a perturbation from the reference state. In the LEM equation set, u is the resolved flow velocity vector, x the three dimensional position vector, p is the pressure, ρ is the air density, θ is the resolved potential temperature and q_n represents all other resolved scalar variables including the hydrometeors. The terms τ^s, which is the sub-grid stress and h^θ and h^{q_n} which are the sub-grid scalar fluxes of θ and q_n respectively, are the sub-grid contributions to the resolved field and will be described in Section 3.1.2. B' is a buoyancy term given by $B' = g\theta'_v/\theta_s$, where θ_v is the virtual potential temperature and g is the acceleration due to gravity.

The terms $(\partial\theta/\partial t)_{MPHYS}$, $(\partial\theta/\partial t)_{RAD}$, $(\partial\theta/\partial t)_{LS}$, $(\partial q_n/\partial t)_{MPHYS}$ and $(\partial q_n/\partial t)_{LS}$ are the source terms for θ and q_n due to microphysics, radiation and large scale forcing respectively. These will be described in more detail in Sections 3.1.3, 3.1.4 and 3.1.6. $(\partial q_n/\partial t)_{SED}$ represents the tendency due to sedimentation which is equal to the divergence of the particle fallout, $\partial V_{q_l x}/\partial z$, where $V_{q_l x}$ is the terminal particle fall speed. δ_{i3} is the Kroneker delta function, ϵ_{ijk} is the alternating pseudo-tensor and Ω is the Earth's angular velocity. As convention the material derivative, D/Dt is given by:

$$\frac{D}{Dt} \equiv \frac{\partial}{\partial t} + u_i\frac{\partial}{\partial x_i} \tag{3.5}$$

For a Boussinesq system where the mean reference state is given by ρ_s, θ_s and p_s, it is assumed that deviations from the reference state are small throughout the atmosphere and the reference state is constant with height. Such an approximation is only valid

for shallow motions limited to the BL, so instead the LEM uses the so-called quasi-Boussinesq or anelastic approximation whereby the reference state is allowed to change as a function of height only. The anelastic assumption requires the LEM to be setup using an approximately adiabatic reference state, using θ' as the prognostic thermodynamic variable, therefore Equation 3.3 is replaced by:

$$\frac{D\theta'}{Dt} + w\frac{D\theta_s}{Dz} = \frac{1}{\rho_s}\frac{\partial h_i^{\theta'}}{\partial x_i} + \frac{1}{\rho_s}\frac{\partial h_3^{\theta}}{\partial z} + \left(\frac{\partial \theta'}{\partial t}\right)_{MPHYS} + \left(\frac{\partial \theta'}{\partial t}\right)_{RAD} + \left(\frac{\partial \theta'}{\partial t}\right)_{LS} \tag{3.6}$$

where w is the vertical velocity. Although the anelastic approximation is well suited to the atmospheric flow we aim to simulate in this study, the equation set does have intrinsic errors associated with the approximation, though these can be minimised by assuring the deviations from the reference state are small.

3.1.2 Sub-grid motions

The parametrization of sub-grid motion in the LEM is based on an extension of the classical Smagorinsky-Lilly eddy viscosity model (Smagorinsky, 1963). The sub-grid contributions to the resolved flow are provided by the sub-grid stress, τ_{ij}^s, and scalar flux, $h_{n,i}$ which are defined by:

$$\tau_{ij}^s = \rho_s \nu S_{ij} \tag{3.7}$$

$$h_{n,i} = -\rho_s \nu_h \partial q_n / \partial x_i \tag{3.8}$$

where ν is the sub-grid eddy viscosity, ν_h the corresponding diffusivity for scalars, and

$$S_{ij} = \frac{\partial u_i}{\partial x_j}\frac{\partial u_j}{\partial x_i} \tag{3.9}$$

is the rate of strain tensor. Following Smagorinsky (1963), the eddy viscosity and eddy diffusivity are calculated as a function of S_{ij} and a basic mixing length λ_e which filters out motions on scales greater than the grid box size.

$$\nu = \lambda_e^2 S f_m(Ri_p) \tag{3.10}$$

$$\nu_h = \lambda_e^2 S f_h(Ri_p) \tag{3.11}$$

However in the LEM a dependence is also made on the stability of the flow through a pointwise Richardson number dependant function, $f(Ri_p)$, where:

$$Ri_p = \frac{\partial B'/\partial z}{S^2} \tag{3.12}$$

and no more sub-grid contributions to the flow are made when $f(Ri_p)$ is greater than a critical Richardson number, Ri_c.

3.1.3 Cloud microphysics

The standard LEM as described in Gray *et al.* (2001) has an integrated three phase bulk microphysics scheme which has been tested extensively within the model. The approach of the Gray *et al.* (2001) cloud microphysics scheme is to represent cloud droplets using only the prognostic mass mixing ratio of the cloud droplet size distribution; a so called single-moment approach. In single-moment models the number concentration of cloud droplets is constant through the model integration and set to a user defined value.

For this reason the approach taken here has been to use the double-moment cloud microphysics scheme developed in Morrison *et al.* (2005, 2009b). This microphysics model prognoses both the 0th moment (number concentration) and the 3rd moment (mass mixing ratio) of the particle size distribution for five hydrometeor species; cloud droplets, cloud ice, rain, snow and graupel. Cloud droplets and rain particle size distributions are represented by gamma functions:

$$N(D) = \; N_o D^{\mu} e^{-\lambda D} \tag{3.13}$$

where D is the particle diameter, and N_o, λ and μ are the intercept, slope and shape parameters of the size distribution respectively. In turn N_o and λ are derived from the predicted number concentration N, mass mixing ratio q and μ which is defined. For cloud ice and the precipitation species; rain, snow and graupel, $\mu = 0$ and the gamma functions reduce to the Marshall-Palmer (exponential function) distributions. For cloud droplets μ is a function of the predicted number concentration.

Within the Morrison *et al.* (2005) scheme number concentration and mass mixing ratio tendency equations for each hydrometeor are found from:

$$\begin{aligned}\left(\frac{\partial q_i}{\partial t}\right)_{MPHYS} =& \left(\frac{\partial q_i}{\partial t}\right)_{PRO} + \left(\frac{\partial q_i}{\partial t}\right)_{COND/DEP} + \left(\frac{\partial q_i}{\partial t}\right)_{AUTO} \\ &+ \left(\frac{\partial q_i}{\partial t}\right)_{COAG} + \left(\frac{\partial q_i}{\partial t}\right)_{MLT/FRZ} + \left(\frac{\partial q_i}{\partial t}\right)_{MULT}\end{aligned} \tag{3.14}$$

$$\begin{aligned}\left(\frac{\partial N_i}{\partial t}\right)_{MPHYS} =& \left(\frac{\partial N_i}{\partial t}\right)_{PRO} + \left(\frac{\partial N_i}{\partial t}\right)_{EVAP/SUB} + \left(\frac{\partial N_i}{\partial t}\right)_{AUTO} \\ &+ \left(\frac{\partial N_i}{\partial t}\right)_{SELF} + \left(\frac{\partial N_i}{\partial t}\right)_{COAG} + \left(\frac{\partial N_i}{\partial t}\right)_{MLT/FRZ} + \left(\frac{\partial q_i}{\partial t}\right)_{MULT}\end{aligned} \tag{3.15}$$

where subscript i refers to the species. The terms on the right hand side of Equation 3.14 from left to right are primary production (droplet activation or ice nucleation), condensa-

tion/deposition (evaporation/sublimation), autoconversion (transfer of water and ice to snow and rain due to coalescence and diffusional growth), coagulation, melting/freezing, and ice multiplication. On the right hand side of Equation 3.15 from left to right the terms represent primary production, condensation/deposition (evaporation/sublimation), autoconversion, self-collection, collection between hydrometeor species, melting/freezing, and ice multiplication. Details on the parametrisations of all these processes are outlined in Morrison *et al.* (2005, 2009b).

3.1.3.1 Droplet activation

Aerosol activation to cloud droplets is based on the parametrisation of Abdul-Razzak *et al.* (1998) and Abdul-Razzak & Ghan (2000). In this scheme the aerosol number size distribution (subscript a) is represented by a multi-mode log normal size distribution:

$$\frac{dn}{da} = \sum_{i=1}^{I} \frac{N_{ai}}{\sqrt{2\pi}\sigma_i} \exp\left(-\frac{1}{2}\frac{\ln^2(r/\bar{r}_i)}{\ln^2(\sigma_i)}\right) \tag{3.16}$$

with each aerosol mode i described by a number of chemical and physical characteristics of the aerosol species. In the Morrison *et al.* (2005, 2009b) scheme, the geometric mean dry radius $\bar{r}_i$, geometric standard deviation σ_i and total number concentration N_{ai} of mode i is prescribed from observations. The scheme parametrises the maximum supersaturation S_{max} reached under the environmental conditions, and derives a critical size r_{ci} at which all larger particles are activated from:

$$r_{ci} = \bar{r}_i \left(\frac{S_{ci}}{S_{max}}\right)^{\frac{2}{3}} (i = 1, ..., I) \tag{3.17}$$

where S_{ci} is the critical supersaturation of a particle of size $\bar{r}_i$. The potential number of droplets activated over each time step, N_{act} is then calculated from:

$$N_{act} = \sum_{i=1}^{I} N_{ai} \frac{1}{2}[1-\mathrm{erf}(u_i)] \tag{3.18}$$

where:

$$u_i \equiv \frac{\ln(r_{ci}/\bar{r}_i)}{\sqrt{2}\ln\sigma_i} = \frac{2\ln(S_{ci}/S_{max})}{\sqrt{2}\ln\sigma_i} \tag{3.19}$$

and finally the droplet number tendency due to aerosol activation is given by:

$$\left(\frac{\partial N_l}{\partial t}\right)_{PRO} = \frac{N_{act} - N_l}{dt} \tag{3.20}$$

where the number of cloud droplets already present has been taken away from N_l which is used as a proxy for the potential number activated.

3.1.4 Radiation

Radiation in the LEM is treated using the Edwards-Slingo radiation code (Edwards & Slingo, 1996). The Edwards-Slingo scheme uses the two stream Delta-Eddington approximation for both shortwave and longwave regions of the spectrum. The code is flexible in respect to the number and width of spectral bands, which for these simulations are fixed at 6 and 9 for the shortwave and longwave regions respectively. Over all spectral bands the Delta-Eddington approximation computes a solution to the upward and downward net flux density divergence, dF^+ and dF^- over a differential thickness $d\tau$, where τ is the optical depth.

$$\frac{dF^+}{d\tau} = \alpha_1 F^+ \text{ - } \alpha_2 F^- \text{ - } Q^+ \tag{3.21}$$

$$\frac{dF^-}{d\tau} = \alpha_2 F^+ \text{ - } \alpha_1 F^- \text{ + } Q^- \tag{3.22}$$

The weighting functions, α_1 and α_2; and source functions, $Q^{\pm}$ are defined in terms of a diffusivity factor, the forward and backward scattering fractions for diffuse shortwave radiation and the backward scattering fraction for direct shortwave radiation.

Gaseous absorption, and scattering and absorption by aerosol are treated in the model with fixed profiles of species defined by the user at the beginning of the simulation. The optical properties for both water droplets and ice particles are considered grey, i.e. the emissivity is assumed constant for all spectral bands. Single scattering properties for the liquid phase are defined using the liquid water path and effective radius of the droplet size distribution and equivalently for the ice phase following the parametrisation of Slingo (1989). At the surface an emissivity and albedo are also defined by the user at the beginning of the simulation.

3.1.5 Boundary conditions

The LEM uses periodic horizontal boundary conditions for all prognostic quantities. On LES scales the Arctic boundary layer can be assumed as horizontally homogeneous and so periodic boundary conditions are well suited to such a study and shouldn't complicate BL development so long as the domain is large enough to support a reasonable number of mixing length scale eddies. The model domain top and bottom act like rigid lids such that the vertical velocity is set equal to zero at both surfaces. To prevent the spurious reflection of gravity waves off the rigid domain top, the boundary is placed well above the cloud layer and a Newtonian dampening layer is used whereby all prognostic variables in the damping layer are relaxed to their horizontal means.

The surface boundary conditions for the LEM are derived from Monin-Obukhov similarity theory (Monin & Obukhov, 1954) using the Businger-Dyer approximations (Businger

et al., 1971). This bulk formula allows the calculation of the turbulent fluxes of heat, moisture and momentum which then act on resolved fields in the lowest model level. To complete this calculation the LEM supports the specification of either a fixed surface temperature and surface humidity; or fixed surface sensible and latent heat fluxes. In either case, the values are defined as horizontally homogeneous across the domain, and can either be specified as time-varying or constant for the simulation. In the time-varying case, the time dependence of the surface boundary conditions must be specified before initialisation.

3.1.6 Large scale forcing

Dynamical motions in LES are limited to the depth of the BL. In reality the microscale atmosphere is influenced by both local processes and from mesoscale and synoptic systems that develop over scales much greater than those which can be modelled in an LES. For this reason it is usual for LES models (in a Eularian system) to specify terms in their equations set which account for larger scale atmospheric forcing. In the LEM this is done through the specification of large scale sources of heat, $(\partial\theta/\partial t)_{LS}$ and scalars $(\partial q_n/\partial t)_{LS}$ to account for horizontal advection into the model domain, and through the definition of a large scale vertical velocity w_{LS} to account for atmospheric subsidence or ascent. Forcings are specified at each level of the model grid and act uniformly across each horizontal layer of the model domain. While time-varying forcing can be specified, forcing profiles have to be defined at the beginning of the simulation.

3.1.6.1 Wavelet method to determine the mixed layer top

In this study, so as to allow a time-varying forcing which develops in accord with the evolution of the modelled BL depth, a modified version of the algorithm described in Brooks (2003) is used to determine the position of the BL top and the forcing profiles are modified to follow its evolution. The Brooks (2003) algorithm is an edge-detecting wavelet technique developed to find the BL top from the profile of lidar backscatter. The algorithm makes use of a wavelet covariance transform; which was developed as a means of detecting step changes in a signal. The wavelet covariance transform, W_f is equal to (Gamage & Hagelberg, 1993):

$$W_f(a,b) = \frac{1}{a}\int_{z_b}^{z_t} f(z)\, h\left(\frac{z-b}{a}\right) dz \tag{3.23}$$

where a is the spatial extent, or dilation, $f(z)$ is the signal of interest, z_b and z_t are the lower and upper limits of the profile, h is a step function named the Haar function, which

is defined as:

$$h\left(\frac{z-b}{a}\right) = \begin{cases} +1: & b - \frac{a}{2} \leq z \leq b \\ -1: & b \leq z \leq b + \frac{a}{2} \\ 0: & elsewhere \end{cases} \tag{3.24}$$

where b is the location at which the Haar function is centred. The local maximum in the covariance transform of the Haar function identifies a step in $f(z)$, which is equal to a boundary of the transition zone. The choice of the dilation is important, and needs to be large enough to distinguish the transition zone from small scale variability. An example lidar backscatter profile, Haar function and the resulting W_f at a number of different dilations is shown in Figure 3.1.

When $f(z)$ is made equal to the potential temperature, the direction of gradient in the profile is reversed. Consequently the direction of the Haar function is reversed in the inversion finding algorithm. In all results a dilation of 100 m is used as this was found to give the most accurate results without being too sensitive to the small scale variability of the profiles.

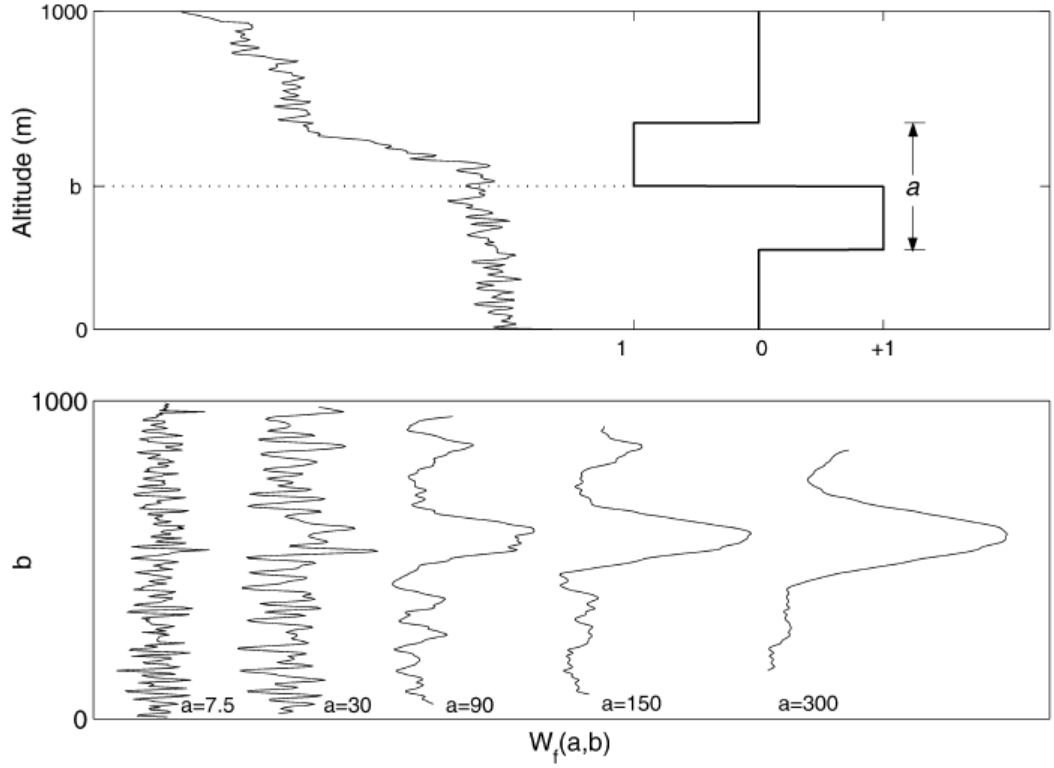

Figure 3.1: Example of a lidar backscatter profile and Haar function (top) and the resulting covariance transform at various values (bottom). Reproduced from Brooks (2003)

Chapter 4

Validation of the LES model

In this chapter, simulations are made to validate that the LEM with Morrison *et al.* (2005, 2009b) cloud microphysics is capable of accurately modelling the radiative, dynamical, and microphysical properties of mixed-phase Arctic stratocumulus. Validating high resolution models such as those used for LES is tricky as observations often lack the spatial or temporal resolution needed for a detailed comparison. The validation problem is made even more problematic by the fact that many physical processes including microphysical ones are almost impossible to measure in the field. This makes it extremely difficult to directly validate model physics. In fact, for this reason the results of LES and CRM simulations are themselves typically used to validate the physics of large scale atmospheric models such as GCMs and RCMs.

A general validation of the model against field observations is usually done through a comparison of few easily measurable atmospheric variables such as the water paths, profiles of water contents and state variables, surface precipitation rates, and velocity and turbulence fields if available. Often the comparison is made using the mean fields of the model. Another complementary approach for validation is to compare the results of several models with each other. While all LES and CRM models are fundamentally similar, differences in the model physics and numerical schemes can have a significant effect on their simulation of atmospheric flows. Comparing results is a useful way of ascertaining the modelling capability as compared to other models.

In this chapter, simulations of a single layer mixed-phase Arctic stratocumulus cloud observed during the M-PACE field campaign are presented. The validation of the LEM will be done through an evaluation of simulations against both observations and a range of LES model and CRM simulations made as part of the Global Water and Energy Experiment Cloud System Study (GCSS) M-PACE B model intercomparison (Klein *et al.*, 2009). General details about the M-PACE field campaign are given in the references of

Table 4.1: Description of simulations made in the M-PACE B validation.

	Microphysics	Hoz. domain	Hoz. res.	Vert. domain.	Vert. res.
val_standard	mixed-phase	20 km	50 m	4 km	50 m
val_no_ice	warm only	20 km	50 m	4 km	50 m
val_high_res	mixed-phase	20 km	50 m	4 km	25 m

Section 2.3.1 and specifics of the case study can be found in Klein *et al.* (2009). For this reason, only a brief discussion of the campaign, participating models and observations made will be given.

4.1 M-PACE B case study

The GCSS M-PACE B study was an model intercomparison with the aim of presenting the state of current models ability to simulate single-layer mixed-phase Arctic stratocumulus clouds. The intercomparison included the participation of 17 single column models and 9 CRMs including a version of the UKMO LEM which used the double-moment cloud microphysics scheme of Ferrier (1994). For this the purpose of the validation we will focus on the results of the CRM simulations only.

Participating models aimed to simulate a cold-air outbreak mixed-phase Arctic stratocumulus observed over the Beaufort sea between 1700 UTC 9 October and 0500 UTC 10 October 2004. Observations of BL properties included measurements from two aircraft flights through the study area and by a range of active and passive remote sensing equipment at locations in Barrow and Oliktok point. More details on the instruments and study area can be found in Klein *et al.* (2009) and references therein.

The observed BL was well-mixed from the surface up to the base of a weak capping temperature inversion of around 2 K at between 1000 and 1500 m. Liquid cloud was observed in the upper half of the BL and ice was observed in the liquid layer and precipitating throughout the sub-cloud layer all the way down to the surface. Liquid mass greatly exceeded ice mass.

4.2 Initial setup and validation design

Participating models made three simulations; a standard simulation with the full warm and cold-phase cloud microphysics, a simulation with no ice, and a high resolution simulation. The model domain and resolution varied between models. The LEM with Ferrier

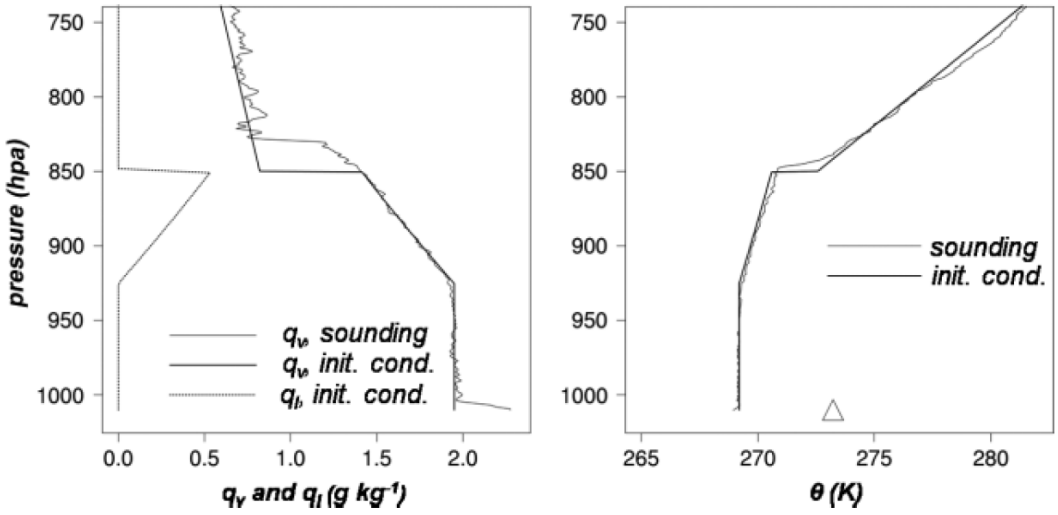

Figure 4.1: Initial model conditions for the potential temperature (right panel, thick line), and the water vapour (left panel, thick line) and liquid cloud water mixing ratios (left panel, dotted line). Also shown are the profiles of θ (right panel, thin line) and q_v (left panel, thin line) from a sounding at Barrow on 1700 UTC 9 October 2004. Figure is taken from Klein *et al.* (2009).

(1994) cloud microphysics used a 3D domain of 6.4 x 6.4 x 4 km and a uniform resolution of 50 m in the horizontal; and 50 and 25 m in the vertical for the standard and high resolution simulations respectively.

In this study, three validation simulations are made using the LEM with Morrison *et al.* (2005, 2009b) cloud microphysics (Table 4.1). The val_standard and val_hi_res simulations use the full two-moment Morrison *et al.* (2005, 2009b) cloud microphysics scheme described in Section 3.1.3. This prognoses the mass and number of liquid cloud droplets, rain, ice crystals, snow crystals and graupel. val_no_ice is a warm-phase simulation where only the liquid water and rain are prognosed. In the Morrison *et al.* (2005, 2009b) cloud microphysics scheme a bi-modal log-normal dry-aerosol size distribution is needed to prognose the activation of aerosol to cloud droplets and an ice nuclei concentration is required to prognose source of ice crystals from heterogeneous nucleation. The ice nuclei concentrations and dry aerosol distribution parameters used in the validation simulations are as described in Klein *et al.* (2009). All validation simulations are made on total 2D domain of 20 x 4 km, where the decision to validate the model in two dimensions was made as 2D is the preferred dimensionality with which we aim to complete ASCOS simulations. In val_standard and val_no_ice both the horizontal and vertical resolution is 50 m, while in val_hi_res the vertical resolution is increased to 25 m.

The initialisation profiles used in each of the CRM simulations and the three validation

Table 4.2: Median LWP and IWP values (4 - 12 hours) simulated in the M-PACE B validation runs and those modelled in the GCSS model intercomparison (Klein *et al.*, 2009). In the table, UKMO refers to the LEM simulations with Ferrier (1994) cloud microphysics, while UKMO2M to the LEM simulations with Morrison *et al.* (2005, 2009b) cloud microphysics. Median CRM is the median of all CRM simulations and Median 2M is the median of all simulations which included double-moment cloud microphysics.

	Liquid water path (g m^{-2})			Ice water path (g m^{-2})	
	Standard	No ice	High resolution	Standard	High resolution
Median CRM	57.3	183.6	63.1	17.1	22.8
Median 2M	100.0	183.6	195.7	19.9	10.3
UKMO	29.7	77.6	36.7	22.7	24.3
UKMO2M	149.1	243.2	153.6	30.9	27.5

simulations is shown in Figure 4.1. The model is initialised using uniform profiles of θ_{il} and q_t the surface up to a pressure of 850 hPa. Above the mixed layer the inversion is represented by a step in θ_{il} and q_t over a single model grid level. In the validation simulations no liquid or ice cloud is specified at initialisation and is instead formed through the cloud microphysics scheme.

Large scale forcings are applied to the models to keep the results from drifting too far from observations. Applied forcings constitute a large scale vertical velocity (subsidence), and horizontal advective sources of water vapour and heat. Profiles of forcings are shown in Klein *et al.* (2009). The surface boundary is specified as an ocean surface with a temperature of 274.1 K. Surface fluxes are kept fixed for the entirety of the simulations at 136.5 W m^2 for sensible heat and 107.7 W m^2 for latent heat.

4.3 val_standard simulation results

Following the method of Klein *et al.* (2009), the model was integrated for a total of 12 hours and results are compared for the 4 - 12 hour time period. The val_standard simulation takes around two hours to spin-up. After spin-up a mixed-phase cloud with a liquid cloud base at around 650 m and top at around 1500 m is present (Figure 4.2). Despite the imposed large scale atmospheric subsidence, the cloud is lifted over the simulations with cloud top reaching 1700 m by 12 hours. The liquid cloud is precipitating rain; and ice, snow and graupel are also simulated from the surface up to the height of the liquid cloud top. Over the 4 - 12 hour period the time-averaged cloud fraction is greater than zero between 0 m and the maximum cloud top of 1700 m. This is over 100 m or more deeper than simulated by the other CRM's, however the result compares

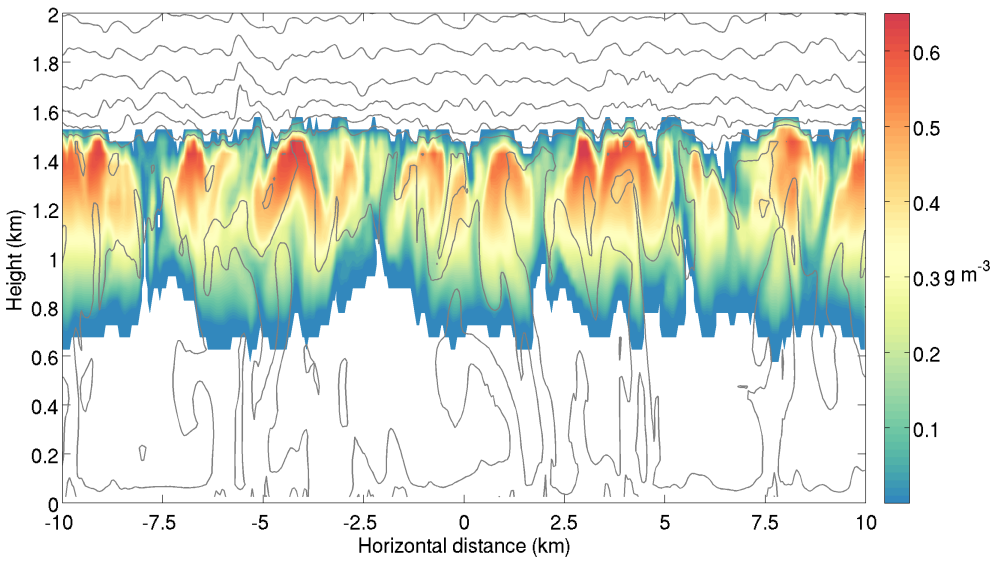

Figure 4.2: val_standard simulation. Instantaneous horizontal cross-section of LWC output at 2 hours of simulation time with 1 K contours of θ_e from between 274 and 302 K overlaid (grey lines).

favourably with the radar observations in which cloud fractions are positive up to around 1750 m.

Observed condensate water paths over the study period varied considerably depending on the platform and region of measurement. Ground based measurements are greater than the aircraft measurements, particularly for the IWP and those collected over Barrow are larger than those collected over Oliktok point. Klein *et al.* (2009) suggest best estimates of 160 ± 50 g m^{-2} for the LWP and in the range of 8 to 30 g m^{-2} for the IWP.

Median condensate water paths for the validation simulations are given in Table 4.2 alongside some results from the model intercomparison. Here the LWP includes the total integrated rain water content where simulated and the IWP the total integrated snow and graupel water contents where applicable. As shown in Table 4.2, the overall performance of the CRM simulations is poor, and although the median IWP falls inside the best estimate of observations, the median LWP is massively underestimated with simulated clouds containing half the lower observed estimate of liquid cloud mass. The condensate water paths simulated in val_standard (labelled as standard UKMO2M in the table) perform better and both the LWP and IWP values are reasonable.

The water paths simulated in val_standard differ considerably from those simulated in the original LEM simulations (labelled as standard UKMO in the table), with the simulated LWP almost five times less than in val_standard. Although both the original standard

LEM simulation and the val_original simulation use double-moment cloud microphysics for rain and the ice species, the original LEM model is only single-moment for liquid water and so uses a fixed cloud droplet number. The simulations also have a different dimensionality and domain size. The improvement in simulated LWP between the median of all CRM's and the median of the double-moment models suggests that the improved microphysical sophistication of the val_original simulation explains the improvement in its LWP representation. However, it should be noted that as explained in Klein *et al.* (2009) the simulations made by the models which use double-moment cloud microphysics were distributed bi-modally with half the models simulating LWP's less than 60 g m^{-2} and half simulating values exceeding 140 g m^{-2}, which suggests that the simulated clouds are dependent on more than just the microphysics scheme.

The time-averaged vertical distribution of the liquid and ice water contents from the median of the CRM simulations and from the val_standard simulation are shown in Figures 4.3 and 4.4 respectively. In these figures water contents are displayed on a normalized height coordinate where -1 is equal to the surface height, 0 to the liquid cloud base height and +1 to the liquid cloud top height. The peak average LWC simulated in val_standard is around 0.34 g m^{-3}. This value is at the upper limit of the range of maximum LWC's simulated by the CRM's, and slightly greater than the peak median LWC of around 0.30 g m^{-3} measured by the aircraft. In the median CRM profile the peak LWC is found between 60 and 70 % of the way through the cloud while in the aircraft observations and val_standard simulation the peak LWC is found 80 % of the way through the cloud layer.

The distribution of ice simulated in val_standard is more similar to the median of the CRM results, and the profiles falls at the uppermost quarter of all CRM simulations. Compared to the liquid, the distribution of ice is much more uniform and extends to the surface. However, peaks in the IWC do exist and as for the LWC's, the peak median IWC is found between 60 - 70 % of the way through the liquid cloud layer in the CRM's and 80 % of the way through the liquid cloud layer in the val_standard simulation. Generally the magnitude and distribution of water contents simulated by val_standard is consistent with the observations and performs well compared to the CRM results. It should be noted however that the variability in the observations and in particular the IWC values is relatively large and this variability is not captured in the model.

Figures 4.5 and 4.6 compares time-averaged vertical distributions of the total water mass mixing ratio and the liquid-ice-water potential temperature respectively from the median of the CRM simulations and from the val_standard simulation. θ_{il} and q_t are both conserved under dry as well as moist adiabatic processes. On initialisation the atmosphere is well mixed from the surface up to the base of the capping inversion at 1300 m. Over the course of the val_standard simulation the inversion lifts so that the 4 - 12 hour average

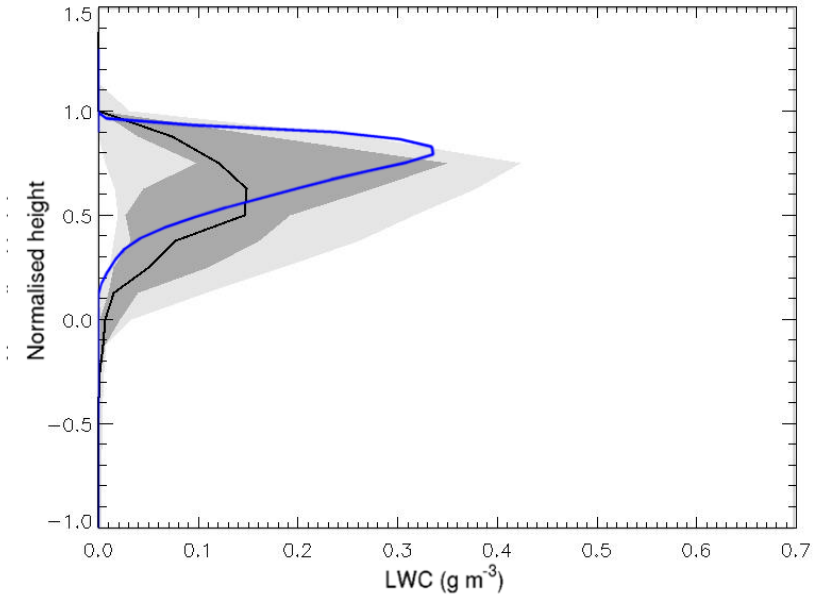

Figure 4.3: Time-averaged LWC from CRM's as a function of normalized height. Black line denotes the median profile of all CRM models, the dark shaded area the innermost 50 % of data and light shaded area the outermost 50 %. The blue line denotes the val_standard profile. Figure is from Klein *et al.* (2009), except edited to include the LEM simulations.

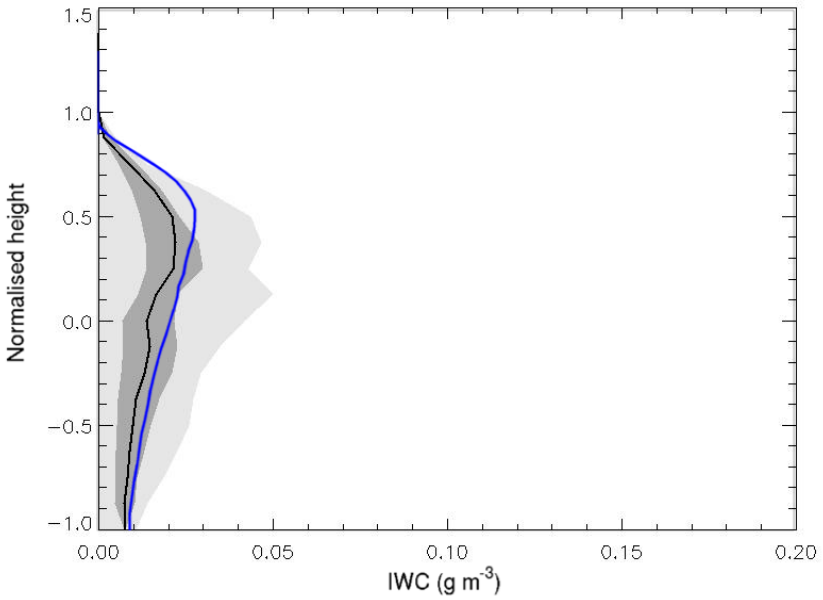

Figure 4.4: As Figure 4.3, except for the IWC. Figure is from Klein *et al.* (2009), except edited to include the LEM simulations.

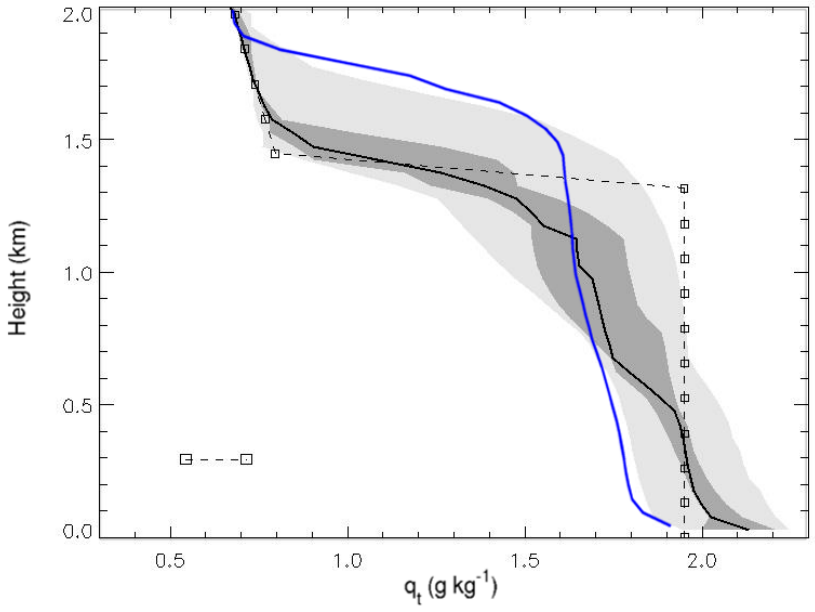

Figure 4.5: As Figure 4.3, except for the total water mixing ratio, q_t. Dot-dash line is the initial condition. Figure is from Klein *et al.* (2009), except edited to include the LEM simulations.

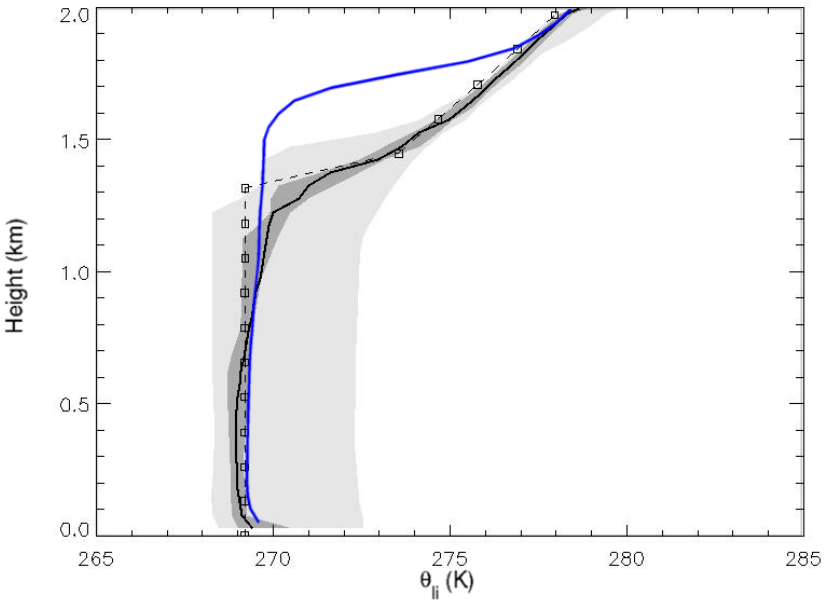

Figure 4.6: As Figure 4.5, except for the liquid-ice-water potential temperature, θ_{il}. Figure is from Klein *et al.* (2009), except edited to include the LEM simulations.

inversion layer base is situated at 1700 m. This is 200 m higher than the median of the CRM simulations and at the outermost range of all simulations. The time-averaged q_t profile is much more uniformly distributed in the val_standard simulation than it is in the median of the CRM simulations. The time-averaged θ_{il} profile is also more well-mixed, with turbulence driven by cloud top radiative cooling and strong surface heat fluxes maintaining a mixed-layer through the whole of the boundary layer. Klein *et al.* (2009) found that the models which predicted the largest LWC's were also the most well mixed and the results of the val_standard simulation support this conclusion. Greater liquid mass driving stronger cloud top radiative cooling and turbulent mixing would also increase the rate of cloud top entrainment and explain the extra 200 m of mixed layer growth in the val_standard simulation.

4.4 Sensitivity studies

4.4.1 No ice microphysics

As shown in Table 4.2, the LWP increased by over 60 % between the val_standard and val_no_ice simulations. While the increase is significant, the fractional change is relatively small as compared to the median of the CRM models which experienced an LWP increase of 220 % between the standard and no ice simulations, and in the original LEM simulation which experienced a increase of 165 %. The results indicate that the inclusion of cold-phase microphysics has a large impact on the total condensate simulated. The change to the LWP from the inclusion of ice is less in the val_no_ice simulation than in the original LEM simulations supporting the conclusion of Klein *et al.* (2009) that models with condensate water paths under 150 g m^{-2} show the greatest sensitivity.

4.4.2 Vertical resolution

As found by Klein *et al.* (2009), there was little sensitivity to vertical resolution between the val_standard and val_high_res simulations and the sensitivity was much less than to the inclusion of ice microphysics. While the vertical resolution was doubled between the simulations, even the val_high_res simulation had a relatively crude vertical resolution of 25 m, and increasing the vertical resolution to 10 or 5 m may have a far greater effect on the simulated cloud.

4.5 Summary and discussion

Simulations of a single layer mixed-phase Arctic stratocumulus observed during the M-PACE field campaign were made to validate the LEM with Morrison *et al.* (2005, 2009b) cloud microphysics. Results were compared with simulations made by seven other CRM's made as part of the GCSS M-PACE B model intercomparison. These included a set of simulations made with a version of the Met Office LEM with Ferrier (1994) cloud microphysics.

The LEM performed favourably compared to results produced by the range of CRM's which participated in the model intercomparison. CRM's had a tendency to produce a cloud which contained too little liquid water, and this resulted in less vertical mixing, a shallower BL and the development of an unrealistic q_t profile. In comparison, the mixed-phase stratocumulus simulated by the LEM was both qualitatively and quantitatively similar to the observed cloud. The simulated liquid and ice water paths were within the bounds of the measurement range, and the profiles of water contents agreed extremely well with the observed quantities. Generally the performance of the LEM with the Morrison *et al.* (2005, 2009b) microphysics scheme is improved over the original model and the results give confidence that the Morrison *et al.* (2005, 2009b) cloud microphysics scheme is sophisticated enough to model mixed-phase stratocumulus clouds with reasonable accuracy.

Chapter 5

Dataset description and analysis

The following chapter gives a description of, and outlines analysis made on the datasets used to setup the model simulations. Data is provided by the Arctic Summer Cloud Ocean Study (ASCOS) and the affiliated Arctic Mechanisms of Interaction Between the Surface and Atmosphere (AMISA) field campaigns. These complementary and concurrent experiments were carried out over the central Arctic Ocean during the summer of 2008. Together they provide one of the most complete sets of observations of summertime BL meteorology collected over the central Arctic region.

A full description of the field campaigns is beyond the scope of this chapter and more details can be found within the references of the relevant sections. Here only a basic overview of the campaign logistics, alongside meteorological conditions experienced and details on any instruments used in the setup or analysis of model simulations are provided. Supplementary to the campaign descriptions, in Section 5.1.3 an analysis of the thermodynamic and cloud fields observed during ASCOS and a comparison with the conditions experienced during other central Arctic field campaigns is presented. Lastly in Section 5.2.1.2 the development of a representative observationally constrained aerosol size distribution which will be used in the large eddy simulations is detailed.

5.1 Arctic Summer Cloud Ocean Study 2008

The Arctic Summer Cloud Ocean Study (ASCOS) was an International Polar Year project aimed at understanding the processes which are important to the formation and lifetime of low-level Arctic clouds in the Arctic Ocean. ASCOS took place between 2 August and 9 September 2008, based aboard the Swedish icebreaker Oden (Figure 5.1) and was the fourth in a series of summer expeditions to this region continuing the experiments carried out during the IAOE-91 (Leck *et al.*, 1996), AOE-96 (Leck *et al.*, 2001)

Figure 5.1: The Swedish icebreaker Oden drifting with a central Arctic ice-flow, and in the foreground, acoustic screens around sodar instrumentation. Courtesy of Ian Brooks.

and AOE-2001 (Tjernstrom *et al.*, 2004) field campaigns. Oden's cruise track is shown in Figure 5.2. For the three weeks (12 August - 1 September) the ship was moored to and drifted with a 3.2 x 5.7 km ice floe, reaching a maximum latitude of 87.5^{o}N. During this period extensive measurements were made both from the ship and at three sites on the ice floe: an ocean site, an open lead site and a surface meteorology site. An aerial photo of the ice floe, with measurement sites labelled is shown in Figure 5.3.

5.1.1 Meteorological instrumentation

ASCOS took an integrated approach to understand the life cycle of Arctic stratocumulus and measurements included physical oceanography, marine biochemistry, gas and particulate chemistry, ocean turbulence and meteorology. In this study our interest is confined to the meteorological instrumentation, which can be divided into: surface based instruments used to measure ground and surface layer properties, ground based remote sensing equipment used to provide indirectly measured profiles of the atmosphere, and radiosonde balloons to provide directly measured atmospheric profiles.

5.1.1.1 Surface layer measurements

An array of both direct and remote sensing surface based meteorological instrumentation was setup to measure ground and surface layer properties. On the sea-ice, instrumentation included a 15 m mast with aspirated temperature sensors, relative humidity sensors and sonic anemometers paired to either fine wire temperature sensors or Licor (LI-7500) open path H_20/CO_2 analysers. Sensors were vertically situated so as to give measurements on an approximately logarithmic scale. A 30 m mast with a single sonic

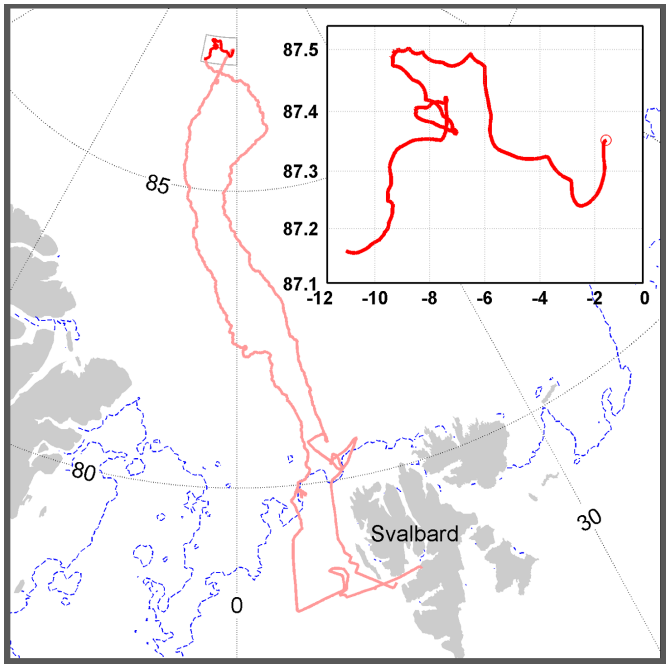

Figure 5.2: Odens track during ASCOS. Inset diagram is the path taken during the ice drift period. Courtesy of Ian Brooks.

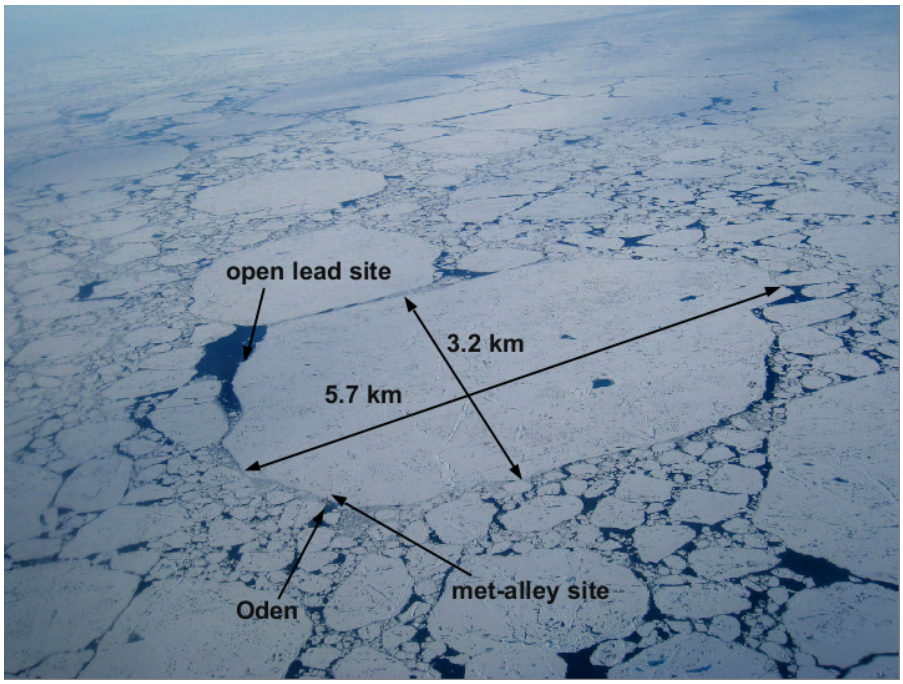

Figure 5.3: The ASCOS ice camp including position of Oden, the open lead, met-alley and ocean measurement sites. Courtesy of Staffan Sjögren.

anemometer at its head was also set up close to the 15 m mast, extending turbulence measurements above the expected surface layer. Near the meteorological masts four Epply radiometers made measurements of upwelling and downwelling shortwave and longwave radiative fluxes, and thermocouples were deployed on the ice surface to measure the skin temperature, and within the ice at depths of 5, 15, 40 and 100 cm to collect a vertical profile of ice temperature. A more detailed description of the surface meteorological equipment is given in Sedlar *et al.* (2011)..

5.1.1.2 Radiosonde balloons

At approximately 0000, 0600, 1200 and 1800 UTC daily for the entire duration of the cruise, Vaisala RS92 radiosondes were released from Oden's helipad. These provided vertical profiles of temperature, relative humidity and wind speed which were later interpolated onto a uniform vertical grid with 5 m vertical resolution in the lowest 1 km degrading to 100 m resolution above 12 km.

5.1.1.3 Remote sensing instruments and derived measurements

On the Oden an array of remote sensing instruments were deployed (Figure 5.4), including a 449 MHz wind profiler and a 60 GHz scanning microwave radiometer, which following the retrieval techniques of Trokhimovski *et al.* (1998) and Westwater *et al.* (1999) provided temperature profiles between 30 m and 1200 m with root-mean-square-errors typically less than 1 K. Laser ceilometers, an S-band cloud and precipitation radar, a dual wavelength (24/31 GHz) microwave radiometer (MWR)(Westwater *et al.*, 2001), and a 35-GHz millimeter cloud radar (MMCR)(Moran *et al.*, 1998) were also deployed to retrieve various cloud and precipitation properties.

Effective radius was determined from the MMCR radar reflectivity (Frisch *et al.*, 2002), while during periods without precipitation, LWP was diagnosed from the MWR (Shupe, 2007) with a root-mean-square-error of around 25 g m^{-2} (Westwater *et al.*, 2001). Using the LWP, vertical temperature profiles from the radiosondes and the radar reflectivity, mean Doppler velocity and spectral width from the MMCR, the cloud phase was determined which allowed a number of liquid and ice phase cloud properties to be derived. Estimates of the liquid cloud base and top made from the ceilometer and MMCR reflectivity measurements respectively can be used with the LWP and radiosonde temperature profiles to determine the LWC, though while the LWP is determined with a reasonable accuracy the distribution of liquid water within the cloud layer is uncertain and assumed to be adiabatic. Ice cloud boundaries and the IWC can be determined based on MMCR radar reflectivity retrievals using an Arctic specific retrieval coefficient (Shupe *et al.*,

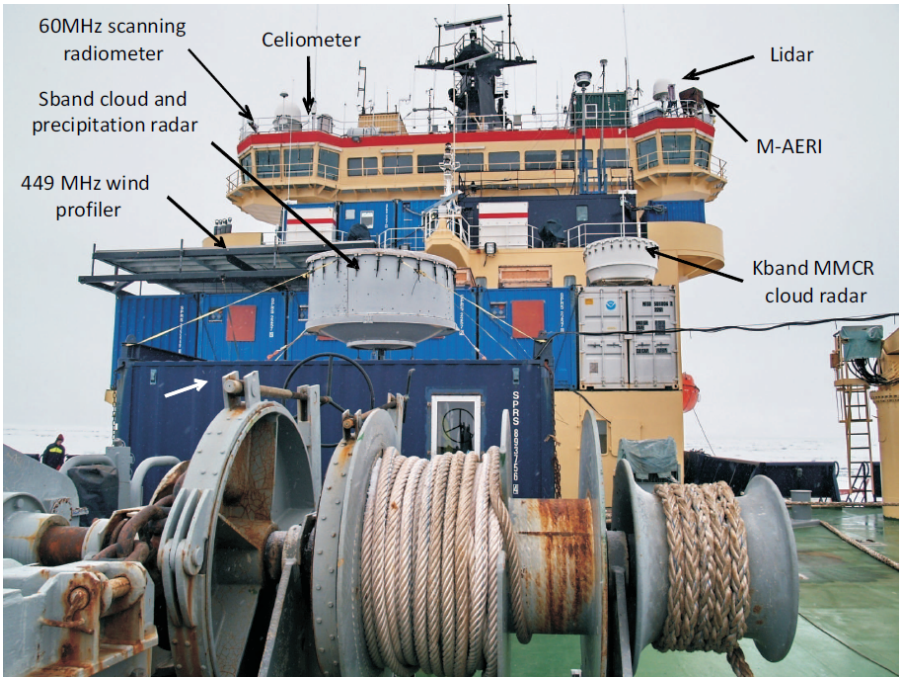

Figure 5.4: Remote sensing instrumentation aboard Oden. Courtesy of Michael Tjernström.

2005, 2006). While the relative vertical distribution of ice is easily quantified from the radar reflectivity, determining IWP is more difficult with random and systematic errors both contributing to an IWP uncertainty factor of two.

5.1.2 Overview of meteorological conditions

The prevailing large-scale atmospheric pattern during the ASCOS campaign was of an anticyclonic circulation over the Arctic ocean, broken by a series a storms systems which brought conditions of strong wind, deep clouds and precipitation into the vicinity of Oden. The conditions experienced during ASCOS were seasonally uncharacteristic and anomalous to the climatological mean (see Tjernstrom *et al.* (2012) for a more detailed explanation). They also differed from the synoptic-scale conditions experienced during previous central Arctic expeditions; AOE-96, AOE-2001 and SHEBA, which were generally more cyclonic.

The synoptic-scale atmospheric conditions varied considerably over the campaign. To illustrate the development of the large-scale meteorology, Figure 5.5 shows ECMWF surface pressure and 10 m wind fields on four days of the ice drift period, with 12-hourly storm tracks of the most dominant weather systems derived from ECMWF analysis also indicated. During Oden's transit to the central Arctic and in the first half of the ice drift

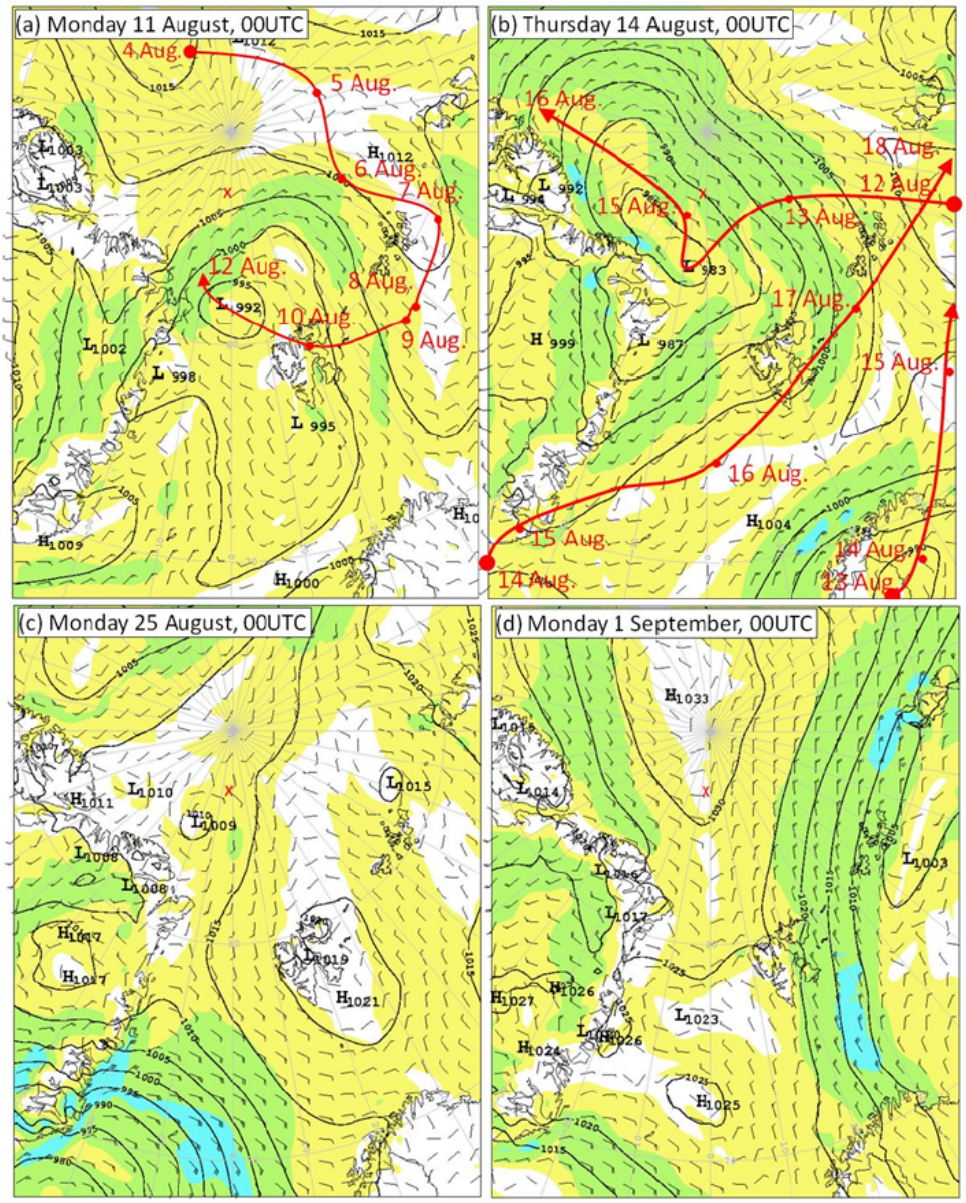

Figure 5.5: Synoptic scale sea-level pressure and 10 m level surface wind from the ECMWF analysis over four days of the ASCOS campaign: (a) 11, (b) 14, (c) 25 August and (d) 1 September, 2008. Red lines show the 12-hour storm tracks of the most significant weather systems encountered in the period around the analysis day, with red dots mark the location of the storm centre at 0000 UTC on each day. The approximate location of the ASCOS ice drift is marked by the red x. Reproduced from Tjernstrom *et al.* (2012).

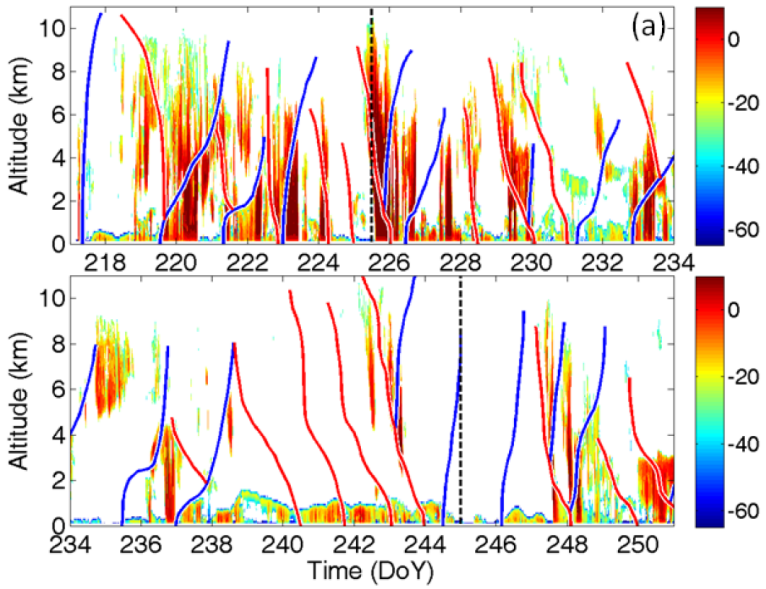

Figure 5.6: Time-height cross section of the MMCR radar reflectivity (dBZ_e) with the positions of major warm (red line) and cold (blue line) frontal zones indicated. For reference; day of year (DoY) 234 is the 21 August. Reproduced from Tjernstrom *et al.* (2012).

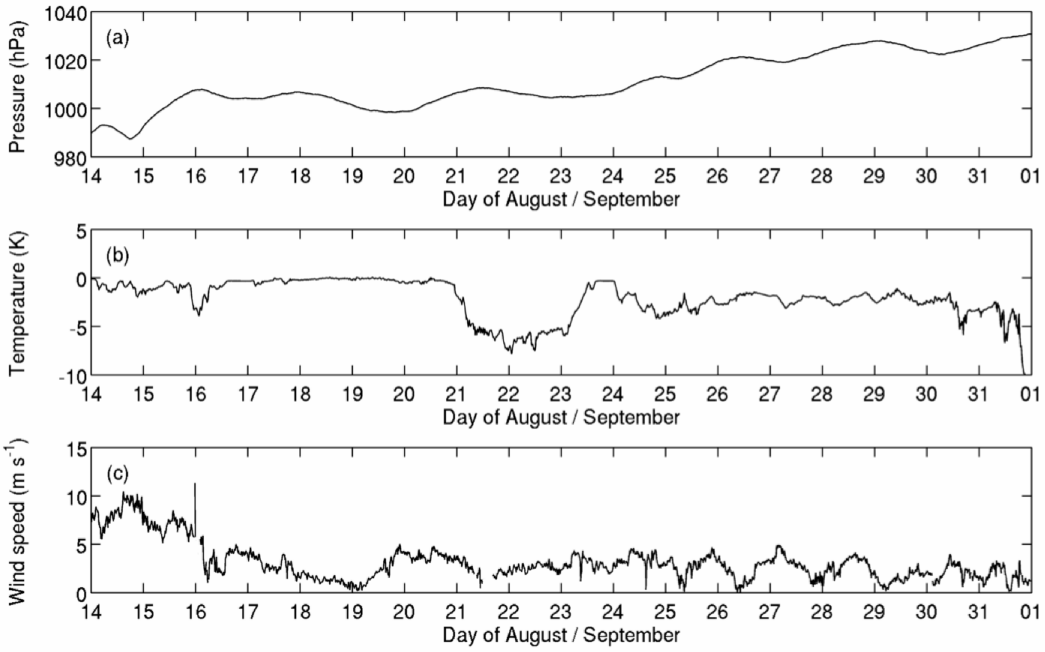

Figure 5.7: Timeseries of measurements made at the surface meteorology site over the ice drift period. (a) Surface pressure, (b) 1 m temperature and (c) 2 m wind speed.

(up until the 24 August), a number of significant low-pressure systems passed over the ASCOS study area. Typically the storm systems moved in from a westerly direction, which is the opposite of the norm but consistent with the anomalous surface pressure fields (Tjernstrom *et al.*, 2012).

Starting from the 4 August, the first storm system moved clockwise around the pole from the Canada basin to Kara Sea which it reached by the 7 August (Figure 5.5 (a)), before passing south over ASCOS on the first day of the ice drift period (12 August). This was followed by another significant weather system which rapidly moved west (Figure 5.5 (b)); from the Kara Sea on the 12 August, south past Oden on 14 and 15 August before moving over the Canadian archipelago. Two further storms the appeared and travelled north-eastwards over the next few days but didn't affect ASCOS. From the 21 August there was a two day break in the synoptic activity, however on 23 August this inactivity was broken by the passing of a further storm system through the Arctic. After the 24 August conditions were more quiescent with large scale meteorology largely governed by a high pressure system which initially developed over Svalbard before moving northwards over the pole, and a second high was positioned over the northern Atlantic (Figure 5.5 (c) and (d)).

The influence of synoptic activity on the development of the vertical structure of clouds in the region around Oden is illustrated in Figure 5.6, which shows a time-height cross section of the MMCR radar reflectivity overlaid with the positions of major frontal zones as determined subjectively by Tjernstrom *et al.* (2012) from the rate of change of the equivalent potential temperature (determined from the radiosondes). As warm air is observed earlier aloft than at the surface, warm fronts are identified as those sloping backwards in time. Cold fronts slope forwards in time for the opposite reason. The most synoptically active conditions were observed in the time period before the 21 August (DoY 234), with a high number of fronts passing over Oden during this period and the cloud radar reflectivity; which is proportional to the particle size to the sixth power, identifying the presence of clouds which were geometrically thick, sometimes in multiple layers and often precipitating ice. Over this period the surface temperature was always between 0 and -1.8 ^{o}C (the freezing points of fresh and saline water respectively), while near-surface wind speeds varied from values typically greater than 5 m s^{-1} before 17 August (DoY 230); when the greater number of fronts pass over Oden, to less than 5 m s^{-1} afterwards (Figure 5.7).

The break in synoptic activity from the 21 August (DoY 234) was marked by a significant drop in surface temperature to -7 ^{o}C and a small rise in the surface pressure. Over this period cloud was tenuous apart from the presence of a cirrus cloud between an altitude of 5 and 9.5 km which passed over Oden on the 22 August (DoY 235). Sedlar *et al.* (2011) attributes the drop in temperature over these days to the loss of warming associated with

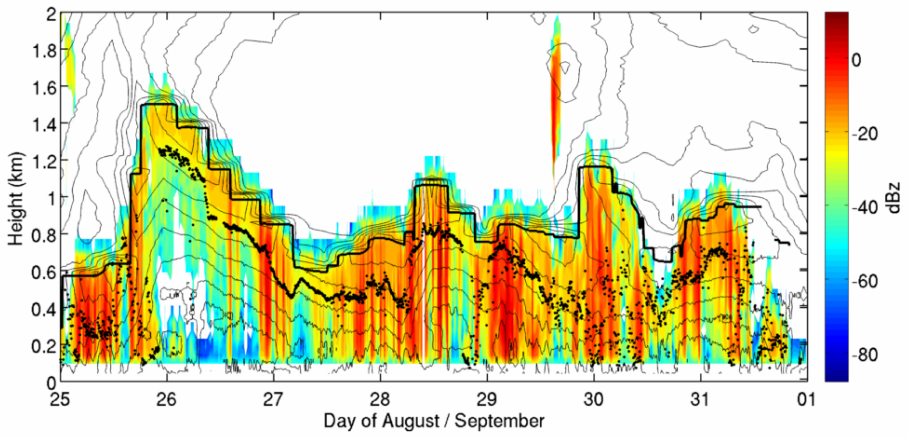

Figure 5.8: Time-height cross section of MMCR reflectivity (filled colour) for the period 0000 UTC 25 August - 0000 UTC 01 September. Ceilometer first cloud base height (black circles), inversion base height (thick black line), and 60 GHz scanning microwave radiometer temperature (thin black line below 1200 m) and interpolated radiosonde temperature (thin black line above 1200 m) measurements overlaid.

the longwave radiative forcing from low level cloud. This was interrupted between the 23 August (DoY 236) and 24 August (DoY 237) when a further depression passed over Oden bringing a brief period of deeper cloud activity and a drop in the surface pressure, although near-surface winds remained low. After 24 August high pressure brought cooler and drier air to the region around Oden and quiescent conditions of low near-surface winds. Low level stratiform cloud dominated from this time onwards and over the next week near-surface temperatures remained between -4 and -2 ^{o}C until a drop in surface temperatures late on the 1 September which saw the onset of the freeze. The freeze onset date is most commonly found between the 2nd week of August and 1st week of September (Belchansky *et al.*, 2004), and Sedlar *et al.* (2011) argue that without the presence of stratiform cloud to warm the surface, onset of freeze could have occurred any time from 21 August onwards. Cloudiness during this period was determined largely by the large scale circulation, demonstrating the complex interplay between the synoptic conditions, cloud cover and sea-ice in the region (Kay & Gettelman, 2009).

A number of different meteorological regimes can be identified from the cloud fields and surface measurements (Birch *et al.*, 2012; Sedlar *et al.*, 2011), with the most significant change in conditions occurring after 24 August. This change saw a major shift from a synoptically dominated system with deep precipitating clouds to a stratocumulus driven regime, which is more characteristic of that expected in the central Arctic during the summer. As the focus of this study is on stratiform BL clouds, henceforth analysis will only consider measurements from the latter half of the ice drift; 0000 UTC 25 August - 0000 UTC 01 September.

5.1.3 Characteristics of the lower atmosphere

5.1.3.1 General conditions

A time-height cross section of the cloud radar reflectivity for the stratocumulus dominated period is shown in Figure 5.8. Also shown are the positions of the first cloud base as determined from the laser ceilometer, and the temperature; which was provided from 60 GHz scanning microwave radiometer below 1200 m and from the interpolated radiosonde measurements above. The height of the inversion base as determined using the Brooks (2003) algorithm is also shown.

A first-order impression of the period is of a lower atmosphere dominated by the presence of a persistent stratocumulus cloud, which is a single layer except for a brief time at the start of the 25 August and for a few hours on the evening of 29 August. A cloud radar reflectivity greater than -17 dBZ is characteristic of targets which are bigger than cloud droplets (Shupe, 2011). Within the observed BL these targets are confined to heights below a shallow layer of liquid water near the cloud top and are identified as ice. Sometimes the ice signal extends down to the surface, thus ice is precipitating through the cloud and sub-cloud layer with a vertical distribution which is typical of mixed-phase Arctic stratocumulus (Shupe *et al.*, 2008). On first impressions the cloud deck is elevated as compared to that observed during the AOE-2001 campaign and maximum height of the reflectivity signal is higher than the inversion base over much of the analysis period, suggesting the clouds are mostly of the cloud inside the inversion regime identified by Sedlar *et al.* (2012).

Timeseries of the LWP and IWP over the stratocumulus dominated period are shown in Figures 5.9 and 5.10 respectively. The LWP is greater than zero over 97 % of the time during this period while the IWP is greater than zero more than 99 % of the time. Therefore cloud is most often characterized as mixed phase. Observed LWP's are typically in the order of 50 to 150 g m^{-2} with a median value of 59 g m^{-2}. The median IWP is 5 g m^{-2}. The IWP shows considerable variability (two orders of magnitudes) over hourly time scales, with background IWP's of less than 10 g m^{-2} broken up with icing events where the IWP increases by up to 250 g m^{-2}.

Without detailed measurements of the ice particle numbers it is impossible to properly explain these events, however changes to IN concentration would be one possible mechanism whereby rapid glaciation would occur (Harrington *et al.*, 1999; Pinto, 1998). As BL temperatures are always sub-freezing, small changes to IN concentrations can lead to rapid ice growth through the Wegener-Bergeron-Findeison mechanism as explained in Section 2.3.3, which would rapidly remove the liquid water and possibly lead to an ice-only cloud (e.g. Harrington *et al.*, 1999; Jiang *et al.*, 2000). Interestingly the linear

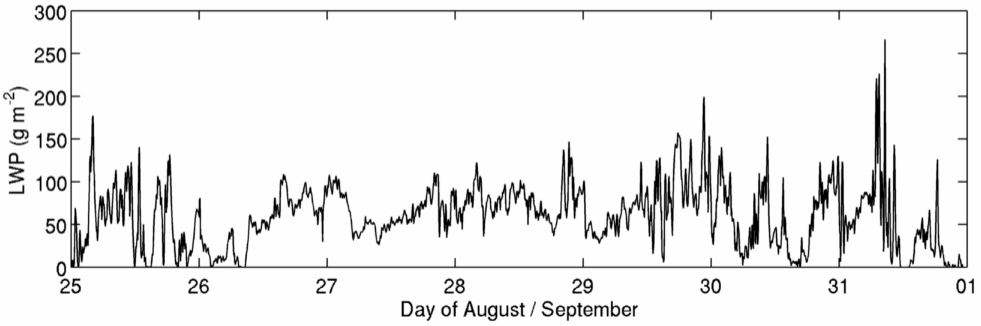

Figure 5.9: Timeseries of LWP over the period 0000 UTC 25 August - 0000 UTC 01 September.

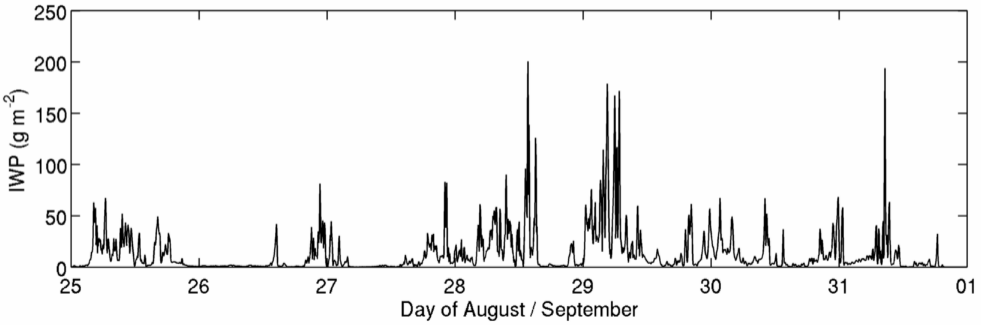

Figure 5.10: As Figure 5.9 except for the IWP.

correlation between the LWP and IWP is small (the coefficient of determination, $r^2 = 0.08$) therefore rapid icing events don't have much of an impact on the liquid water. It is possible that the vertical distribution of liquid and ice prevents full glaciation after rapid icing (Morrison *et al.*, 2012; Shupe *et al.*, 2008).

Figure 5.11 shows the thermodynamic structure of the lower atmosphere as captured by measurements made during the approximately 6-hourly radiosonde ascents. The boundaries of the cloud are also shown, where the cloud top is determined from the maximum height of return of the 5-minute averaged MMCR reflectivity and the cloud base is determined as uppermost cloud base below the MMCR cloud top as determined from the laser ceilometer. Note the differences in the two measurement procedures; the radiosonde observations are measurements from a single ascent through the atmosphere while the cloud boundaries are remote retrievals whose signal is the average of that collected over a wider geographical extent.

Profiles of the lower atmosphere show a variety of structures. At least one temperature inversion is present below 2 km in each of the radiosonde profiles and specific humidities

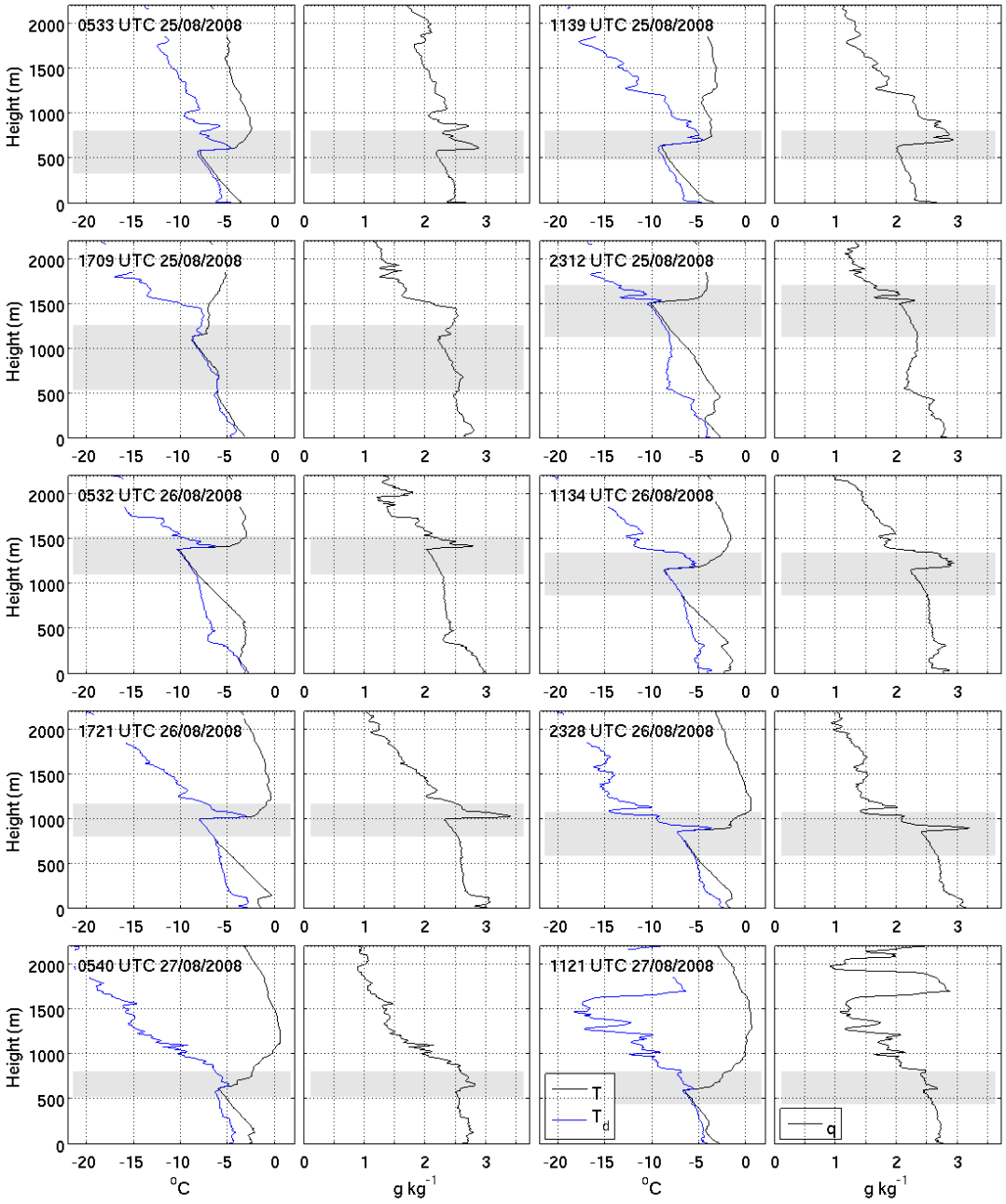

Figure 5.11: (a) 6-hourly radiosonde thermodynamic profiles over the stratocumulus analysis period. For each radiosonde ascent the left pane shows profiles of temperature (black line) and dew point temperature (blue line) and right pane shows specific humidity (black line). The grey shaded regions represent cloud boundaries, with cloud top determined from 5-min averaged MMCR reflectivity profiles and cloud base from laser ceilometer within 5 min of the radiosonde release time. 0533 UTC 25th August 2008 - 1121 UTC 27th August 2008.

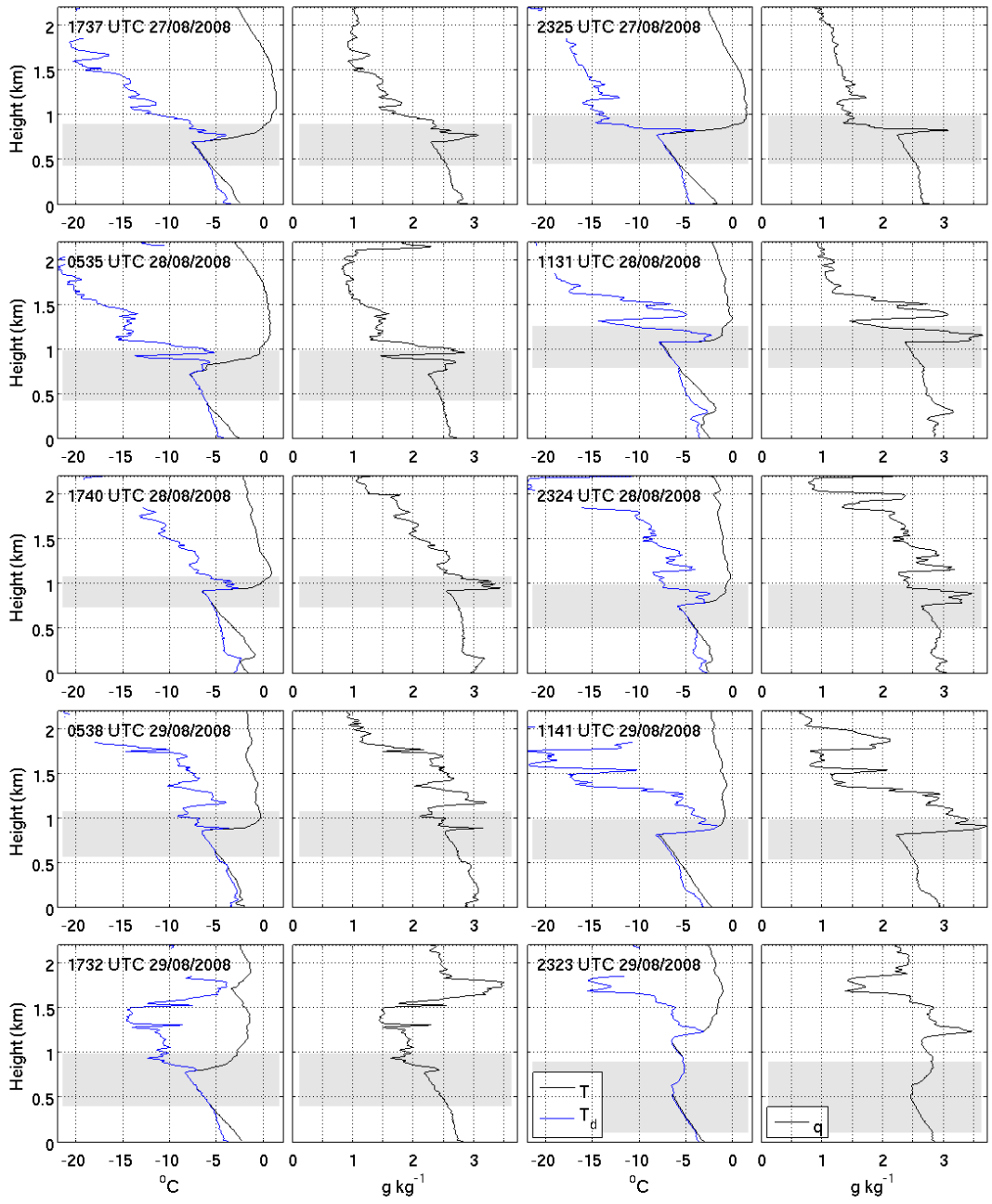

Figure 5.11: (b) 1737 UTC 27th August 2008 - 2323 UTC 29th August 2008.

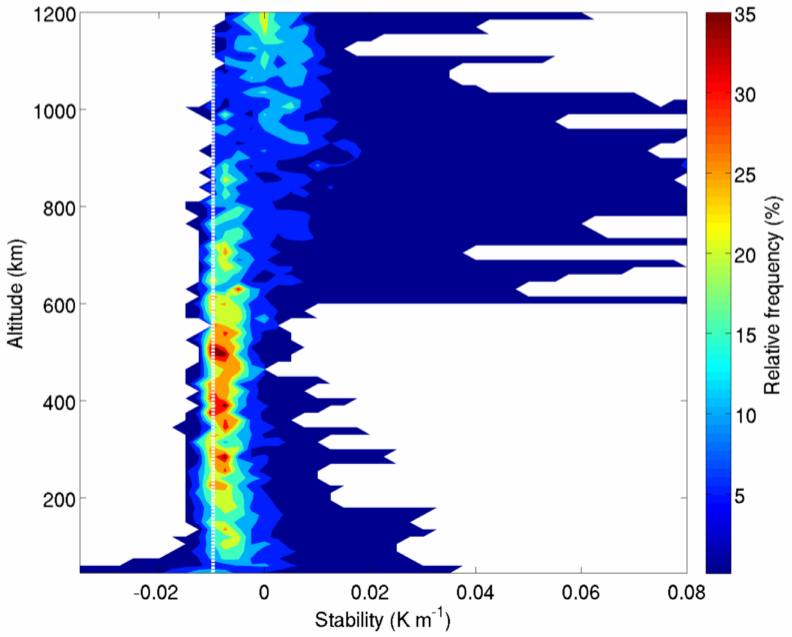

Figure 5.12: Frequency of occurrence (%), of the vertical temperature gradient (K m^{-1}) for the entire stratocumulus dominated period. Temperature gradients are calculated from the 60 GHz scanning microwave radiometer measurements. Also shown is the position of the dry adiabat (white dotted line).

are often observed coincide with the main temperature inversion. Despite the differences between the two measurement procedures the cloud base determined by the laser ceilometer is largely coincident with the first vertical height at which saturation is predicted from the thermodynamic profiles. In most of these profiles the temperature gradient above cloud base falls off vertically at the moist adiabat. Clouds are typically around 400 - 500 m deep and in all of the profiles the cloud top extends into the temperature inversion. The temperature and dew point profiles also show the atmosphere to be saturated above the base of the inversion on some occasions. However the extension into the inversion predicted from the thermodynamic profiles is modest (less than 100 m) compared to the that found from the MMCR cloud top estimates (up to 400 m). The difference between these estimates of cloud top could be attributed to a local variation in the supersaturation field above the inversion. However because of errors in the dew point temperature due to the hygrometer instrument freezing during the radiosonde ascents, it is difficult to ascertain how important local variability is to the measured differences.

Directly below the cloud base a variety of temperature structures are observed, however the temperature profile most commonly falls off vertically at the dry adiabat from an altitude of 100 - 200 m until cloud base. The 100 - 200 m altitude most often denotes the

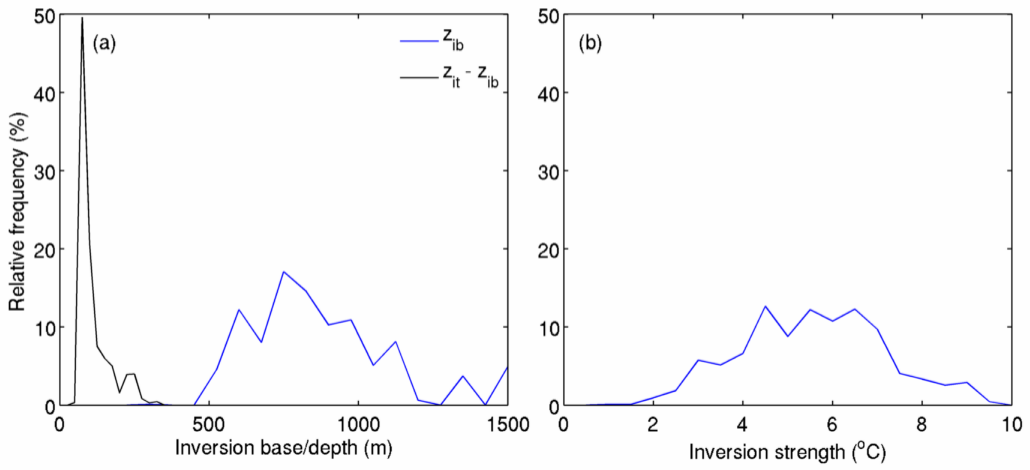

Figure 5.13: Frequency of occurrence (%) of the main temperature inversion analysed from the scanning microwave radiometer, showing (a) the height to the main inversion base and the depths of the main inversion (m), and (b) the strength of the inversions (^{o}C).

height of the BL top, with the BL either stable, or of a near-neutral stability and capped by a shallow region where the temperature increases (by less than 0.3^{o}C) at its uppermost. Though the true BL is shallow, the cloud-driven mixed layer has characteristics of a STBL which has been elevated above the true BL. Mostly this region is well mixed, however a stable region below cloud base sometimes separates the cloud from the sub-cloud layer indicating decoupling.

5.1.3.2 Vertical atmospheric structure

Figure 5.12 shows the frequency of occurrence of the lower atmospheric stability for the stratocumulus dominated period. Stability is determined as the vertical gradient of the 60 GHz scanning microwave radiometer temperature with height. Within the lowest 900 m of the atmosphere the stability was most frequently found to have a gradient between the moist and dry adiabats. The high frequency of this gradient demonstrates the influence of the cloud on the lower Arctic atmosphere during this period of ASCOS, and is consistent with the stability observed at lower levels during the AOE-2001 (Figure 2.6) and SHEBA field campaigns (Figure 2.7).

Despite the preference for neutral stability in the lower atmosphere, the temperature gradient of the lowest 100 m was variable and sometimes very stable conditions were measured. This situation of a near neutral but sometimes stable surface was also observed during AOE-2001 (Tjernstrom, 2005) and results suggest that this surface regime may

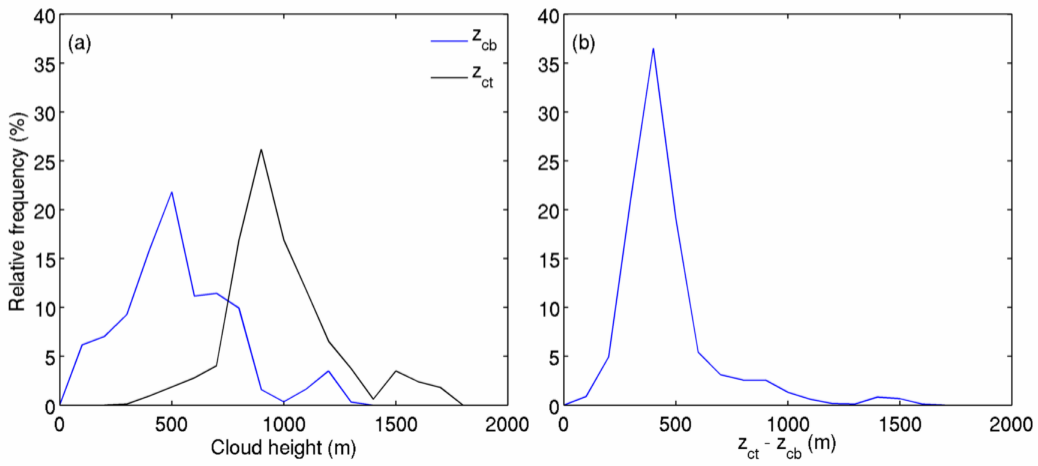

Figure 5.14: As Figure 5.13 except for the (a) cloud base and cloud top heights and (b) cloud depth.

be common to the Arctic summer. Above 600 m the vertical temperature gradient was also frequently positive, while above 900 m, positive stability is the most frequently occurring thermal structure. The high stability in these regions indicates the presence of the inversion layer at these heights.

The frequency of occurrence of the inversion base height as determined by applying the Brooks (2003) algorithm to the 60 GHz scanning radiometer data is shown in Figure 5.13. At least one inversion was found in over 90 % of the radiometer profiles during the stratocumulus period, which is close to the 91 % occurrence of elevated temperature inversion found over the SHEBA summer (Tjernstrom & Graversen, 2009). Like in AOE-2001 and during the SHEBA summer, there is a preference during the ASCOS stratocumulus dominated period for elevated inversions over surface inversions. However the peak inversion base is found at around 750 m (Figure 5.13 (a)) compared to 200 m during AOE-2001 (Tjernstrom, 2005) and between 200 - 400 m during the SHEBA summer (Tjernstrom & Graversen, 2009).

The inversion top was also determined from the radiometer data. Inversion top was identified subjectively, though for the majority of the analysis period was found equal to the height of the greatest temperature above the inversion base and below 2 km. The peak frequency of the inversion top height was found at around 900 m. Inversion depths were most frequently less than 100 m (Figure 5.13 (a)) and had strengths of 4 - 8^{o}C (Figure 5.13 (b)) making them narrower and sharper than those experienced during both AOE-2001 and in the SHEBA summer.

Stratocumulus clouds were also elevated during ASCOS as compared to that observed

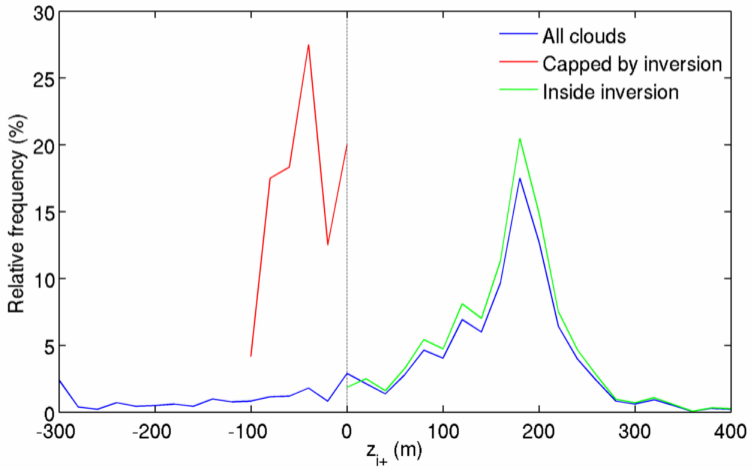

Figure 5.15: As Figure 5.13 except for height difference (m) between the cloud top and the inversion base, z_{i+}.

during AOE-2001 and SHEBA. Figure 5.14 (a) shows the frequency of occurrence of the cloud base measured by laser ceilometer and cloud tops from determined by the MMCR reflectivity for the stratocumulus dominated period. Cloud bases ranged between the surface and around 1.4 km over the analysis period with a peak occurrence at 500 m. While the peak cloud top was situated at around 950 m and the most frequent cloud depth was 500 m (Figure 5.14 (b)), which is narrower than found in the previous summer campaigns.

5.1.3.3 Cloud-inversion properties

Analysis of the ASCOS observations will now be directed at the focus of this study - the encroachment of cloud top into the temperature inversion. Following the methodology of Sedlar *et al.* (2012), observations of cloud and thermodynamic fields are utilised to determine whether cloud was situated inside the inversion layer, or cloud was capped by the inversion. During the period of ASCOS which was dominated by stratocumulus, the inversion encroachment depth, z_{i+}, which is given by:

$$z_{i+} = z_{ct} - z_{ib} \tag{5.1}$$

was greater than zero in 86 % of the profiles where cloud was observed. Thus cloud inside the inversion were the most prevalent cloud-inversion regime. The relative frequency of occurrence of z_{i+} is shown in Figure 5.15. Typically the cloud encroached less than 180 m inside the inversion though a small number of profiles measured z_{i+} values of more than 300 m, with the maximum around 500 m. Of the 14 % of profiles where z_{i+} was less than

zero, 45 % were within 100 m of the inversion; which is the definition of a cloud capped by the inversion given by Sedlar *et al.* (2012). This amount is equal to around 6 % of the total profiles in which cloud was observed. Of the clouds capped by the inversion the cloud top was most frequency observed within 50 m of the inversion (Figure 5.15).

z_{i+} values for low level clouds were also calculated by Sedlar *et al.* (2012) from ASCOS observations; however in their study cloud was analysed over the entire ice drift and their determination of the inversion boundaries also differed to this study (see Section 2.3.4). Because the analysis of Sedlar *et al.* (2012) included time-periods in which non-stratocumulus-dominated conditions prevailed, the collocation of cloud inside the inversion was reduced to two thirds in their study. However despite the difference in the chosen analysis period and the inversion finding method, the most frequent z_{i+} value as determined by Sedlar *et al.* (2012), and in this study were within 25 m of each other (Figure 2.11). This supports the use of the Brooks (2003) algorithm to determine the inversion base height, and furthermore suggests that the stratocumulus dominated period chosen in this study is an appropriate time-period for a detailed analysis of the cloud encroachment mechanisms.

While cloud-inversion collocations for the SHEBA campaign and at the Arctic observation site at Barrow, Alaska, differed to those found during the stratocumulus dominated period of ASCOS; with cloud capped by the inversion typically more prevalent at these sites. As discussed in Section 2.3.4, analysis of the cloud encroachment depth at these locations also showed a preference for clouds inside the inversion to have a z_{i+} of 150 m or less, with maximum cloud encroachment depths of up to 500 m occurring much less frequently. The approximate agreement of the z_{i+} distribution found during the stratocumulus dominated period of ASCOS and at the other Arctic locations, suggests that for clouds with tops inside the inversion, the encroachment depth is relatively independent of location. Furthermore the preference for z_{i+} values of 150 m or less may be indicative of limit to the encroachment depth under the most frequently encountered atmospheric conditions.

Physically it may be expected that z_{i+} is limited by a feedback from the clouds presence inside the inversion; such as a thermal adjustment caused by strong radiative cooling inside the layer. However, although z_{i+} is a useful reference for the state of the cloud-inversion, knowledge of the cloud and inversion layer boundaries exclusively is not indicative of the underlying physical processes which control the encroachment. To predict the influence of the encroachment on the physics of the cloud - for instance through its alteration of radiative fluxes - observations of cloud water mass and cloud microphysical properties; and their vertical distribution through the cloud are needed.

Although high-resolution cloud microphysical measurements were not recorded during ASCOS. The influence of z_{i+} on cloud thermodynamics can be qualitatively estimated

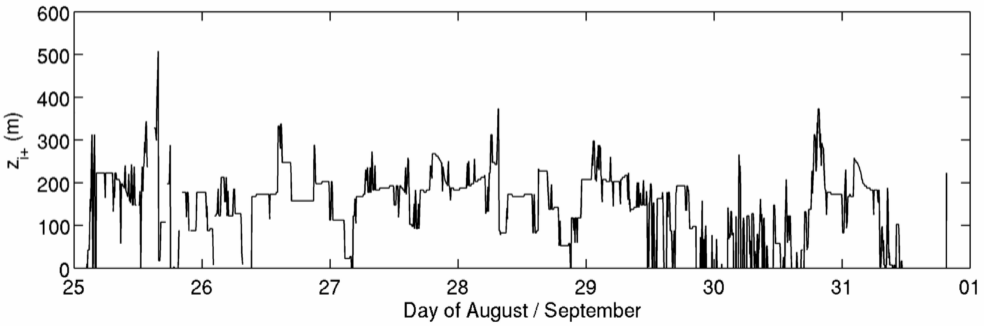

Figure 5.16: Timeseries of z_{i+} over the period 0000 UTC 25 August - 0000 UTC 01 September.

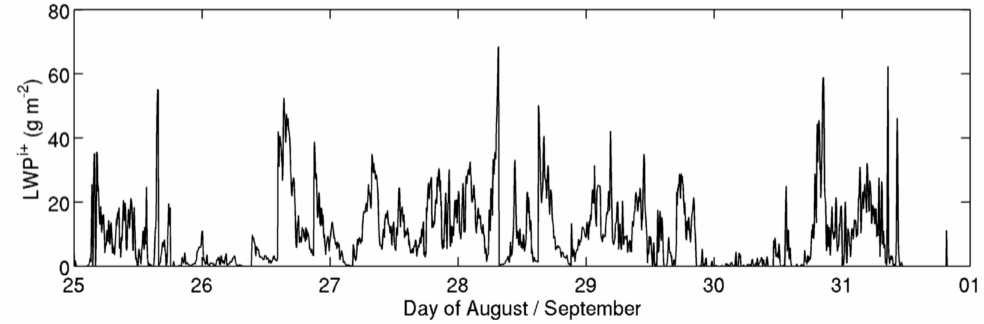

Figure 5.17: As Figure 5.16 except for LWP^{i+}.

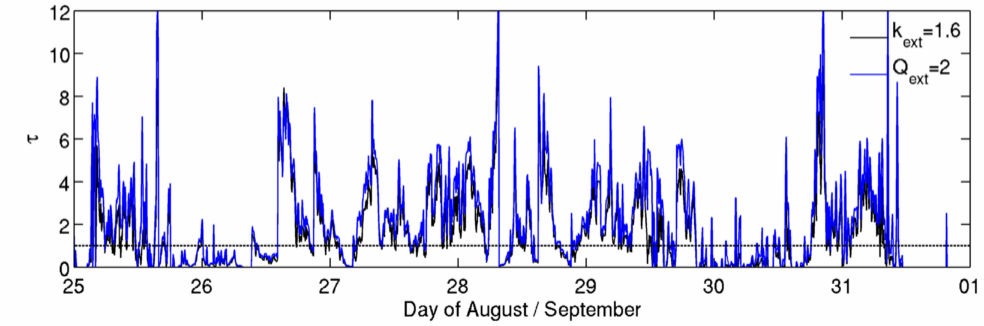

Figure 5.18: As Figure 5.16 except for the τ values of the inversion layer calculated using a k_{ext} of 0.16 m^2 g^{-1} (black solid line) and using a Q_{ext} of 2 (blue solid line). Also shown is the line of unity optical depth (dashed black line).

from the effect that the liquid cloud mass inside the inversion has on the optical depth. The absolute integrated mass of liquid cloud water inside the inversion is given by:

$$LWP^{i+} = \int_{z_{ib}}^{z_{ct}} LWC dz \tag{5.2}$$

Computing the optical depth of the liquid layer inside the inversion using Equations 2.4 and 5.2 requires the calculation of k_{ext} through Mie theory, however its calculation is complex and so to reduce the computational expense, two estimates of the optical depth using simplified assumptions are used instead. The first estimate of τ makes the assumption of a constant k_{ext} equal to a value of 0.16 m^2 g^{-1} - which is a reasonable value for stratocumulus clouds (Stephens, 1978). The second estimate assumes that cloud droplet are much larger than the wavelength of radiation, thus Q_{ext} can be made equal to two and τ can be calculated from the vertical distribution of the LWC and r_e through Equation 2.5. This assumption usually only holds true for the extinction of shortwave radiation by cloud droplets, though provides a limit to the longwave optical depth value.

Timeseries of z_{i+} (>0 only), LWP^{i+} and τ for the analysis period are shown in Figures 5.16, 5.17 and 5.18 respectively. While none of the timeseries of the cloud-inversion properties follow a trend over the analysis period, over time scales of half a day or less, LWP^{i+} fluctuates between values less than 10 g m^{-2} and greater than 20 g m^{-2}; and z_{i+} fluctuates between values of 50 m or less and values of 150 m or more. The temporal development of z_{i+} has a step like appearance suggesting that the transition from shallow to deep inversion encroachment depths is rapid, occurring over less than 60 minutes or so. However this is likely to be artificial and the transition between shallow and deep inversion encroachment depths more gradual. The step like development results from the rapid change in the inversion base height, which is caused by the inversion being detected in the upper part of the 60 GHz scanning radiometer retrieval. In the upper region of the radiometer retrieval, the retrieval method uses time-interpolated radiosonde temperature profiles as a first guess to derive the radiometer temperatures, and the step-like appearance is most likely an artefact of the interpolation. Nevertheless the fluctuation between relatively deep to shallow and relatively moist to dry inversions over short time-scales demonstrates that the cloud-inversion system is not quasi-static.

Because of its dependence on LWP^{i+}, the optical depth also fluctuates rapidly over short time-scales; the opacity of the cloud inside the inversion varying between values close to zero and a maximum of 16 ($Q_{ext} = 2$). Despite the different assumptions made in the two τ approximations, the temporal development of both timeseries is generally equivalent. However the $Q_{ext} = 2$ method produces larger optical depths and the root-mean-square error of the τ approximations is 0.92. Although there is uncertainty in the exact magnitude of τ, the frequency that the optical depth is greater than or equal to one is approximately the same using both assumptions; with $\tau \geq 1$ for 48 % and 58

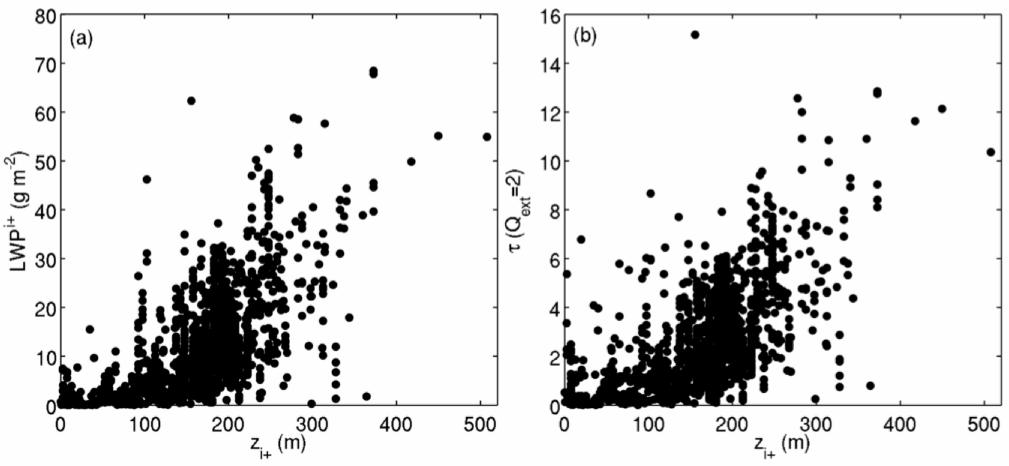

Figure 5.19: Scatter plot of (a) z_{i+} against LWP^{i+}, and (b) z_{i+} against τ as calculated using the $Q_{ext} = 2$ assumption.

% of the analysis period as calculated using the $k_{ext} = 0.16$ and $Q_{ext} = 2$ assumptions respectively. Thus the results suggest that inversion is commonly opaque to longwave radiation.

The relationship between z_{i+} and LWP^{i+}; and between z_{i+} and τ as calculated using the $Q_{ext} = 2$ assumption is shown in Figures 5.19 (a) and (b) respectively. Despite a large amount of scatter, a weak positive relationship between both z_{i+} and LWP^{i+}; and z_{i+} and τ is evident, with the largest masses of liquid water and highest optical depths generally found in the deepest cloudy-inversion layers. From a physical perspective, the high temperature and stability of the inversion acts as a barrier to the condensational growth of cloud droplets in the layer. Therefore it might be expected that the LWC decreases proportional to z_{i+}, leading to a functional relationship between LWP^{i+} and z_{i+}. However, while the shape of the relationship between z_{i+} and LWP^{i+} suggests a weak linear relationship between the variables, an r^2 value of 0.39 indicates that less than half the variability of LWP^{i+} can be explained by a linear dependence on z_{i+}. Thus other variables must contribute significantly to the mass of liquid water inside the inversion.

The proportionality of τ and LWP^{i+} using the $k_{ext} = 0.16$ assumption means that Figure 5.19 (a) also indicates the relationship between these variables. Comparing the scatter between Figures 5.19 (a) and (b), there is little difference, thus despite the different assumptions made in calculating the two τ values, the linear dependence on z_{i+} is relatively similar with r^2 equal to 0.35 for $Q_{ext} = 2$. This results from the high linear dependence of τ (found using $Q_{ext} = 2$) on LWP^{i+}, with r^2 equal to 0.90.

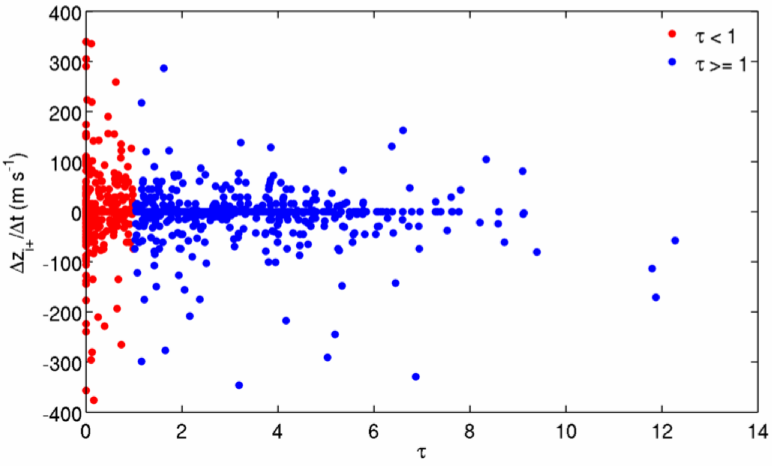

Figure 5.20: Scatter plot of τ as calculated using the $Q_{ext} = 2$ assumption against $\Delta z_{i+}/\Delta t$. Red dots indicate τ values below one, and blue dots τ values greater than or equal to one.

As discussed in Section 2.3.3, the position of maximum longwave radiative cooling is found about where the optical depth is equal to one. Therefore Figure 5.18 suggests that during the stratocumulus dominated period of ASCOS, the position of maximum longwave radiative cooling was commonly inside the inversion layer. Assuming that the radiative cooling is the dominant term in the upper cloud heat budget, then the absolute cooling of the inversion relative to the boundary layer should lead to the inversion layer experiencing a thermal adjustment to the presence of the cloud. Such an adjustment wasn't simulated by Solomon *et al.* (2011); with radiative cooling instead balanced by the heat from condensation and large scale advection. Sedlar *et al.* (2012) also found that despite cooling occurring over a greater depth, the maximum radiative cooling was only positioned above the inversion base when the mass of liquid water inside the inversion was large. While under smaller instances of the LWP^{i+}, the maximum cooling was positioned coincident with z_{ib}.

Unfortunately the errors associated with the radiometer retrieval method, means that it isn't possible to determine whether a cooling response of the atmosphere to the presence of inversion layer cloud is directly evident in the ASCOS dataset with any certainty. Despite this limitation, adjustment of the inversion boundaries should be evident in the timeseries of z_{i+}, with cooling of the cloud-inversion region causing z_{i+} to fall as z_{ib} equates with the base of the cooled layer.

To examine whether this was found over the analysis period, the τ ($Q_{ext} = 2$) and z_{ib} timeseries were temporally averaged to remove short time-scale fluctuations, and the relationship between τ and $\Delta z_{ib}/\Delta t$ was examined. A number of averaging periods

between 12.5 and 50 minutes were tested, and because the thermal adjustment might not respond quickly enough to cause a reduction in z_{i+} over the same time period, time lags varying between zero minutes and maximum of 50 minutes were applied to $\Delta z_{ib}/\Delta t$. For each of the averaging periods and lags, the relationship between τ and z_{i+} was found to be very weak. The shape of the relationship between the variables was similar for each determinations, and is illustrated in Figure 5.20 for an averaging period of 25 minutes and zero minutes time lag. Generally $\Delta z_{ib}/\Delta t$ is scattered around a change of 0 m s^{-1} and both increases and reductions in z_{i+} are found across the range of optical depths. Figure 5.20 suggests that thermal adjustment of the inversion due to the presence of cloud was not experienced in the analysis period. However, the use of a τ approximation as a proxy for the radiative cooling potential of the layer means that the result is not conclusive.

The examination of the thermal adjustment mechanism demonstrates the limitation of direct analysis of the ASCOS dataset in providing a detailed understanding of the underlying physical process which control the encroachment. Nevertheless, the clear positive relationship between z_{i+} and LWP^{i+} (Figure 5.19 (a)) suggests that characterization of the encroachment may be possible using simple parameterizations. Although the formulation of such parameterizations is beyond the scope of this analysis, and would benefit from a more detailed understanding of the physics beforehand. The relationships between a few atmospheric variables which would be expected to influence the encroachment will now be examined.

The relationship between z_{i+}, and the percentage of the total liquid cloud mass found inside the inversion, q_l^{i+}, as calculated from:

$$q_l^{i+} = 100\frac{LWP^{i+}}{LWP} \tag{5.3}$$

is shown in Figure 5.21 (a). The dependence between the variables indicates the weighting of the cloud mass inside the inversion, to the mass in the BL at different inversion encroachment depths; small values indicating a well mixed cloud with an approximately adiabatic liquid water profile, and high values a cloud which deviates from the typical stratocumulus profiles described in Section 2.1.2. The dependence of q_l^{i+} on z_{i+} is positive and non-linear and the variability of q_l^{i+} below 150 m is smaller than at encroachment depth above this value, suggesting a transition to less uniform cloud layers as z_{i+} increases.

Normalising z_{i+} by the total cloud depth, $z_{ct} - z_{cb}$ reduces the scatter of the variables, while retaining the approximate shape of the relationship (Figure 5.21 (b)). Without a detailed understanding of the mechanisms which lead to the encroachment, it is not necessarily clear which way the dependence between these variables lies, however q_l^{i+} has

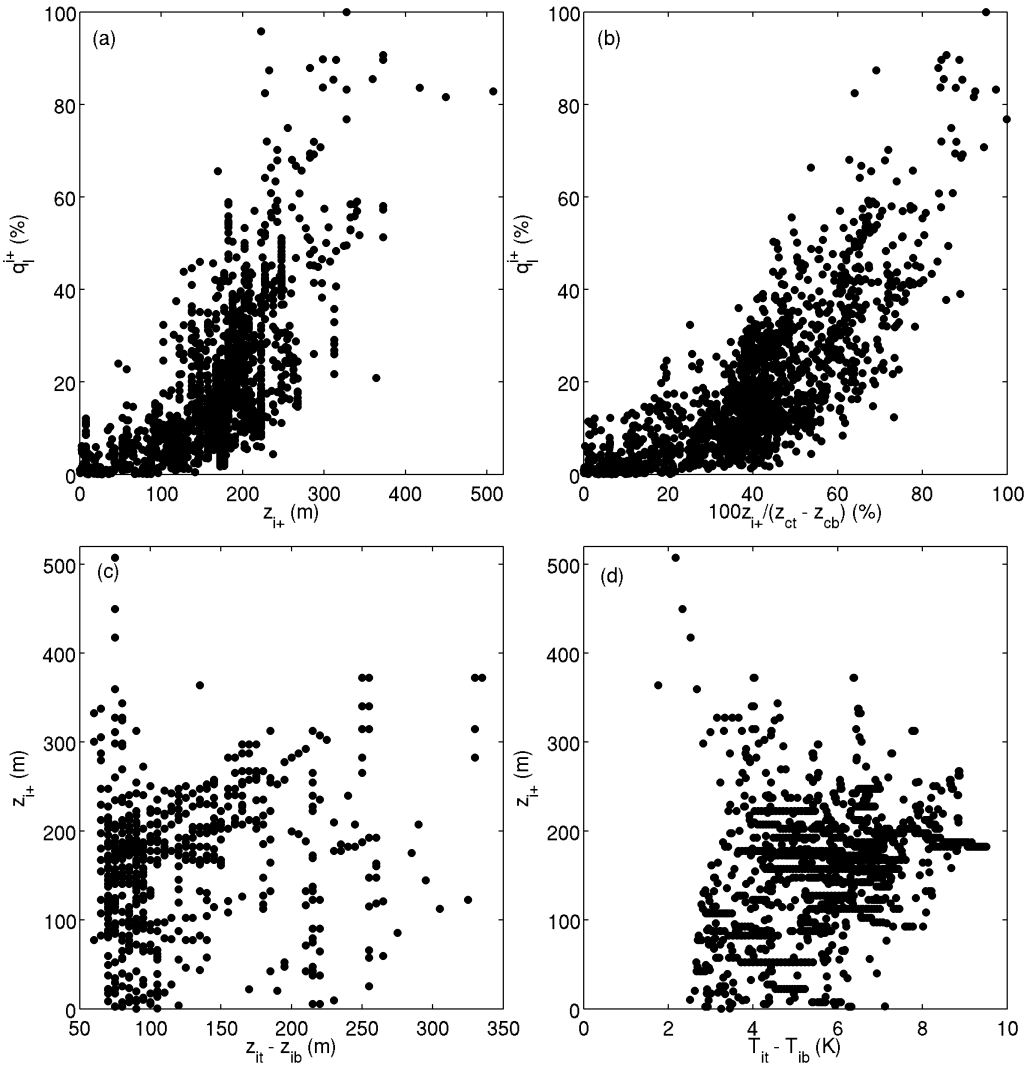

Figure 5.21: Scatter plot indicating the relationship between (a) z_{i+} (m) and q_l^{i+} (%), (b) $100z_{i+}/(z_{ct}$ - $z_{cb})$ (%) and q_l^{i+} (%), (c) z_{it} - z_{ib} (m) and z_{i+} (m), and (d) T_{it} - T_{ib} (K) and z_{i+} (m).

been chosen as the response variable in (Figure 5.21 (b)) as its determination is probably the most useful to predict. While the depth of encroachment is most likely influenced by both the cloud properties and the background atmospheric state, if z_{ib} can be related to the background atmospheric state with confidence, Figure 5.21 (b) would give an indication of the mass inside the inversion, and allow the possibility of determining its influence on the clouds heat budget and dynamics.

The depth of the inversion layer $z_{it} - z_{ib}$, and strength of the temperature inversion, $T_{it} - T_{ib}$ are two atmospheric quantities which might be expected to influence the depth of encroachment. Unfortunately, there is weak if any dependence of z_{i+} on these variables (Figures 5.21 (c) and (d)). The dependence of z_{i+} on number of other quantities were also tested, though the relationship was always weak. However one variable which the dependence wasn't determined for, because of a lack of measurements, is strength of the humidity inversion. Simulations made by Solomon *et al.* (2011) indicate the importance of the specific humidity inversion in maintaining the cloud inside the temperature inversion, and if there is a strong dependence between the humidity inversion strength and z_{i+}, a parameterization of LWP^{i+} would be made possible.

5.2 Arctic Mechanisms of Interaction Between the Surface and Atmosphere

The Arctic Mechanisms of Interaction Between the Surface and Atmosphere (AMISA) field campaign was an aircraft-borne field campaign with the objective of studying Arctic clouds and mapping sea-ice extent. AMISA was carried out aboard a NASA DC-8 aircraft, with flights taking place concurrently with ASCOS so as to supplement the extensive surface based observations with in situ measurements of cloud and aerosol properties; instruments aboard the aircraft remotely sensed the sea ice and various meteorological properties, and a number of instruments made direct measurements of physical and chemical aerosol properties.

In total seven DC-8 flights were made between 8 August and 28 August. Besides the first and last flights which made the transit between the USA and Kiruna, Sweden, all other flights began and ended in Kiruna. Five of the flights (including the first transit) passed over the Oden so as to allow cross examination of observations from the different platforms. Table 5.1 gives details of the flight logistics and their scientific mission.

Table 5.1: Description of AMISA flights.

Flight	Date	Description
1	08/08/2008	Transit. Palmdale, USA - Kiruna, Sweden (Oden overpass)
2	12/08/2008	Mapping radiation, microphysics near Oden
3	15/08/2008	Mapping radiation, microphysics near Oden
4	22/08/2008	Ice edge mapping
5	23/08/2008	Mapping radiation, microphysics near Oden
6	25/08/2008	Mapping radiation, microphysics near Oden
7	28/08/2008	Transit. Kiruna, Sweden - Bangor, USA

5.2.1 AMISA aerosol number-size distribution

As explained in Section 3.1.3.1, an aerosol number size distribution is needed in the LEM Morrison *et al.* (2005, 2009b) microphysics scheme to model the activation of aerosol particles to cloud droplets. In this study, measurements made during AMISA are analysed to construct an aerosol number size distribution which is representative of that found in vicinity of Oden during the stratocumulus dominated period. As the focus of this study is on low level central Arctic stratiform cloud, data collected on the transit flights and during the stormy conditions is unsuitable for the analysis. Therefore analysis will be limited to flight 6.

During AMISA flight 6, the DC-8 left Kiruna, Sweden at 0710 UTC, flying at high altitude until 1400 UTC when the plane descended below 2 km. Over the next four and a half hours the plane was in the vicinity of the Oden flying racetrack patterns at fixed and varying altitudes around the ship (Figure 5.2.1 so as to collect vertical measurement of cloud and aerosol properties). Aerosol number size distributions are derived from measurements collected during flight 6 between 1400 and 1630 UTC on the 25 August.

5.2.1.1 Instrumentation

Typically aerosols which activate to become cloud droplets are particles from the accumulation or coarse mode particles. Particles of these sizes have diameters of 0.01 μm or greater (Raes *et al.*, 2000). To cover as wide a range of particle sizes as was possible from the measurements, aerosol number size distributions are constructed from a combination of measurements made using a Particle Measurement Systems (PMS) Passive Cavity Aerosol Spectrometer Probe (PCASP) and a NASA Langley TSI Scanning Mobility Particle Sizer (SMPS). The PCASP instrument is an optical particle counter which measures aerosol size distribution in the nominal range 0.1 to 3 μm (diameter), by exposing each particle to laser radiation and measuring the amount of light scattered.

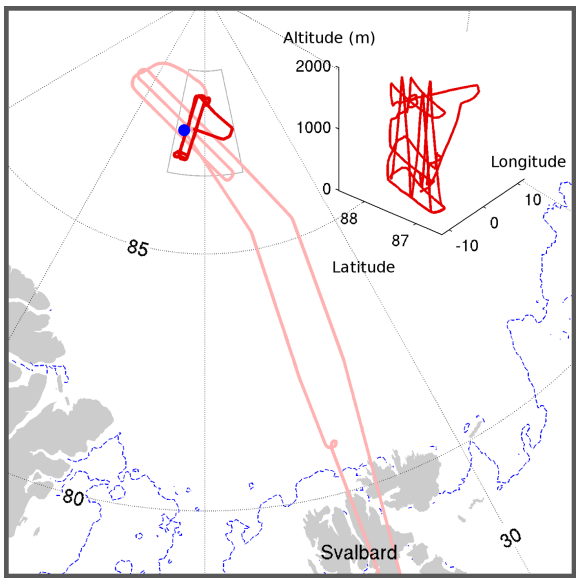

Figure 5.22: AMISA flight track on 25/08/2008. The blue marker shows Oden's location. Inset diagram is the 3D flight path over the analysis period.

The instrument is fitted to the aircraft in one of the PMS canisters under the aircraft wings. The SMPS instrument separates and identifies particles in the size range 0.01 - 0.2 μm by their differential mobility when exposed to an electrical field, the instrument was based inside the aircraft and aerosol was collected through a Clarke probe inlet.

5.2.1.2 Aerosol size distribution

Aerosol particles found within the central Arctic may be either local; for instance from the surface microlayer of open leads (Bigg *et al.*, 2001), or transported into the region (Sirois & Barrie, 1999). In both cases, for the CCN aerosols to form droplets, vertical transport of the particles; either from the surface, or from the free troposphere has to be able to move them to a region of the atmosphere which is saturated. For particles advected into the free troposphere a barrier to their movement is the frequent occurrence of temperature inversions. As explained in Section 2.1.1, the rapid increase of temperature across the inversion makes it is highly stable. Therefore turbulent motions are dampened inside the inversion and transport of scalars such as aerosol particles across the interface is limited. For particles who's source is at the ground, surface inversions and decoupling of the cloud layer cause a similar barrier. Observations show that cloud formation is frequently limited by CCN availability in the central Arctic (Bigg *et al.*, 1996; Mauritsen *et al.*, 2011), and the presence of frequent inversions may contribute to the low CCN numbers.

Table 5.2: AMISA flight 6 aerosol number-size distribution parameters; mean and standard deviation of the aerosol concentration and number of measurement bins used to compute the statistics.

Position	SMPS (cm^{-3})			PCASP (cm^{-3})		
	Mean	St.dev	No.	Mean	St.dev	No.
Above-Cloud	161.73	86.89	20	14.95	20.26	162
Below-Cloud	67.05	83.51	21	6.57	6.66	128
In-Cloud	85.28	0.00	2	1.90	1.21	24

Temperature profiles from the ascending/descending portions of flight indicate that the observed cloud was in the vicinity of a temperature inversion during the analysis period, suggesting that the vertical distribution of aerosol isn't uniform through the atmosphere. To allow the examination of the effect of location on aerosol spectrum, observations were classified by whether the aircraft was flying in-cloud, above cloud or below the cloud layer.

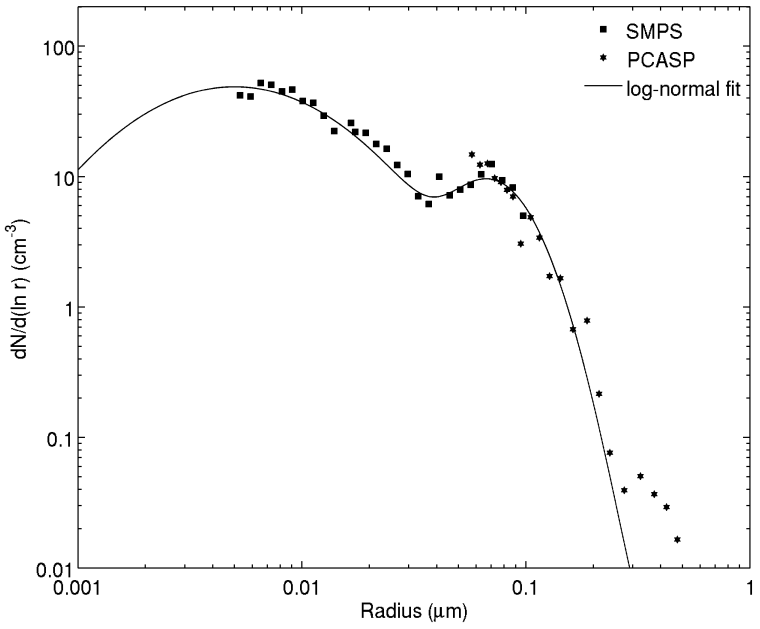

Figure 5.23: Temporally and spatially averaged SMPS (square markers) and PCASP (hexagon markers) aerosol number-size measurements and their fitted log-normal distribution (solid line).

Table 5.3: AMISA flight 6 log-normal aerosol number-size distribution fitting parameters.

Position	Mode 1			Mode 2		
	$\bar{r}_1$ (μm)	σ_1 (μm)	N_{a1} (cm^{-3})	$\bar{r}_2$ (μm)	σ_2 (μm)	N_{a2} (cm^{-3})
Above-Cloud	161.73	86.89	20	14.95	20.26	162
Below-Cloud	67.05	83.51	21	6.57	6.66	128
In-Cloud	85.28	0.00	2	1.90	1.21	24

Cloudiness was classified by liquid water relative humidities of 100 % or more. The above/below position classification was then inferred from the altitude, relative humidity and temperature records. As static temperature and humidity profiles at the plane's location are unavailable, it was assumed in the classification of above-cloud and below-cloud that observed stratocumulus is a single cloud layer and has a uniform cloud top height over small horizontal distances. Above-cloud was associated with measurements inside or above the inversion layer.

To construct the categorised distributions, a single spectrum was generated from the SMPS and PCASP measurements every 15 minutes. As both instruments didn't operate continuously over the analysis period, those bins in which either of the instruments didn't make measurements were then discarded to remove bias. From these 15 minute spectra, in-cloud, above-cloud and below-cloud mean size distributions for the whole analysis period were produced. Table 5.2 gives concentration statistics for each classification. Particle numbers of both instruments are largest above the cloud suggesting an above-cloud aerosol source. In-cloud PCASP concentrations are smaller than those found in clear-sky, which is consistent with the largest particles forming cloud droplets. SMPS concentrations are smaller below the cloud than inside.

Differences in the SMPS and PCASP measurement techniques mean that the two distributions don't fit perfectly in the overlap size range. To ensure PCASP and SMPS distribution consistency in the overlap region, PCASP number concentrations across the whole PCASP distribution were adjusted so that the PCASP and SMPS number concentrations in the overlap region were equal. Bimodal log-normal distributions were then fitted to the three mean aerosol distributions. Table 5.3 details the fitting parameters. As temperature inversion were so frequently observed during period dominated by stratocumulus cloud, the below-cloud distribution was chosen to best represent the background aerosol. The fitted log-normal curves for the below cloud distribution are shown in Figure 5.23.

5.3 Summary and discussion

This chapter introduced the Arctic Summer Cloud Ocean Study (ASCOS) and compared observations made during ASCOS with measurements collected during previous central Arctic field campaigns. ASCOS was carried out during the summer of 2008 under seasonally uncharacteristic large-scale atmospheric conditions, which differed to those experienced during AOE-96, AOE-2001 and SHEBA where the central Arctic was commonly dominated by high pressure. During the fist half of the ASCOS ice-drift, synoptic-scale conditions were characterized by the passing of a series of frontal systems over the central Arctic bringing deep convective storms clouds to the vicinity of Oden. While in the latter half of the ice-drift, conditions became more typical for the central Arctic summer and were characterized by quiescent conditions and Arctic stratocumulus cloud dominating the lower atmosphere. In support of the aims of the thesis, analysis was directed at the stratocumulus-dominated period, 25 August - 1 October.

Overall the thermodynamics conditions showed similarities with previous summer campaigns; a slightly stable or near-neural BL around 100 - 300 m deep, followed vertically by a layer of near-neutral stability until the height of the cloud top. However the depth of the sub-cloud layer was often much deeper during ASCOS, with the cloud elevated as compared to those observed during AOE-2001 and SHEBA by an average amount of around 500 - 600 m. The stratocumulus deck observed during ASCOS was nearly always mixed-phase with a characteristic vertical structure of a thin layer of liquid water - typically around 500 m deep - which was continually precipitating ice through the cloud down to the surface. Clouds were mostly decoupled from the surface. LWP's were in the order of 50 to 150 g m^{-2} and the IWP had a median value of 5 g m^{-2}. However, ice concentrations varied considerably over the latter ice-drift and measurements were unable to explain the rapid growth of the IWP by up to two orders of magnitude. Correlation between the ice and liquid was weak and ice events never caused the cloud to become ice-only. Results suggest that the rapid glaciation of cloud through the Wegener-Bergeron-Findeison mechanism may be inhibited by the vertical distribution of hydrometeors in the cloud.

To allow an examination of the encroachment of cloud into the temperature inversion, the Brooks (2003) algorithm was used determine the location of the temperature inversion base. Elevated temperature inversions were identified in 90 % of atmospheric temperature profiles during the analysis period, which is consistent with their identification over 91 % of the SHEBA summer. In keeping with previous summer campaigns, ASCOS data showed a preference for elevated over surface inversions, however inversion bases were found most commonly located a height of around 750 m, compared to 200 m during AOE-2001 and between 200 - 400 m during SHEBA. Thus despite ASCOS sharing a similar

vertical structure of the lower atmosphere to previous campaigns: shallow stable or neutral BL, followed by a well-mixed cloud-driven layer up to the base of the temperature inversion, the depth of the lower atmosphere was much greater during ASCOS.

To help understand how the prevalence of inversion encroaching clouds during ASCOS compared to that found at other Arctic locations, cloud-inversion collocations were used to identify the periods where the cloud was situated inside the inversion layer and those where cloud was capped by the inversion layer. Over the analysis period, cloud was determined to be inside the inversion for 86 % of the observed profiles, which was found to be approximately representative of collocations evaluated over the entire ASCOS ice-drift. The high prevalence of the cloud inside the inversion regime is also similar to observations of cloud-inversion encroachment during SHEBA, where cloud inside the inversion was observed around 60 % of the time. And while clouds capped by the inversion are found to be the most frequent cloud-inversion collocation over the Arctic measurement site at Barrow, Alaska, the site is situated closer to a land mass. Therefore the high collocation of cloud inside the inversion observed during ASCOS and SHEBA was identified as being characteristic of the regimes prevalence over the central Arctic sea-ice.

When cloud was found inside the inversion, the most frequently found encroachment depth z_{i+}, was 150 m into the temperature inversion. The observation of z_{i+} most commonly occurring below 150 m at other Arctic locations suggested a possible feedback in the cloud which limited the encroachment depth. To examine whether z_{i+} was limited by a thermal adjustment of the inversion layer from strong radiative cooling at cloud top, the integrated mass of the inversion layer liquid cloud, LWP^{i+} and an approximation of the longwave optical depth of the layer, τ were found to help describe the radiative cooling potential of the layer. Approximations of τ were made using the assumption that the cloud either had a constant mass extinction coefficient of 0.16 $\mathrm{m}^2\ \mathrm{g}^{-1}$; meaning τ was proportional to LWP^{i+}, or that the cloud particles were much larger than the wavelength of the radiation, allowing the calculation τ using an extinction efficiency of two. This approximation is usually only strictly valid when examining the shortwave optical depth.

The temporal development of z_{i+}, LWP^{i+} and τ showed considerable variability over short timescales, however for between 48 % and 58 % of the analysis period, τ was found to be greater than one. Because the position of peak cloud top radiative cooling is expected about the region where τ is equal to one, this suggested that peak radiative cooling was located inside the inversion layer approximately half of the time cloud was found inside the inversion. Although this suggested a potential for thermal adjustment from cloud top radiative cooling, analysis of the correlation between τ and the change in z_{i+} over time showed no adjustment of z_{i+} proceeding periods where τ was large and thermal adjustment would be expected. While this analysis was not conclusive, this

result suggests that radiative cooling within the inversion layer is probably balanced by condensational heating and heat transport into the layer as found by Solomon *et al.* (2011), leading to the peak absolute cooling of the layer occurring coincident with the inversion base (Sedlar *et al.*, 2012).

Both LWP^{i+}, and the fraction of the total liquid water cloud mass found inside the inversion, q_l^{i+} were identified as has having a non-linear functional dependence on z_{i+}. Despite a large amount of scatter, the relationship between z_{i+} and these variables demonstrates the possibility for parameterization of the encroachment mechanism with the intention of calculating the mass of water inside the inversion. For such a parameterization, z_{i+} would need to be found within the model, however from the limited ASCOS observations, z_{i+} was to found to have little dependence on other atmospheric parameters including the strength and depth of the temperature inversion. Nevertheless, ASCOS observations didn't allow the dependence of z_{i+} on the humidity inversion strength to be calculated and it is expected from Solomon *et al.* (2011) that a relationship between these variables exists.

Next aerosol number-size distributions measured during the Arctic Mechanisms of Interaction Between the Surface and Atmosphere (AMISA) field campaign were analysed to derive aerosol activation parameters for the LEM model. Only one flight made during AMISA was suitable for modelling the low level Arctic stratocumulus clouds. Using flight data of meteorological conditions to determine where the measurement was made in relation to the cloud and inversion, average aerosol distributions were composed using the PCASP and SMPS instruments. Distributions were determined for above-cloud, in-cloud and below-cloud conditions and log-normal approximations fitted to the three datasets. The below-cloud distribution was chosen as the most suitable in representing the background aerosol.

In reference to the aims of thesis, results show that despite the seasonally uncharacteristic large-scale atmospheric conditions and greater preference for clouds situated higher in the atmosphere, the prevalence of cloud inside the inversion was similar in ASCOS to that found during previous summer campaigns, particularly SHEBA. Cloud encroachment into the inversion was found to occur frequently during ASCOS, with a significant mass of liquid water present inside the inversion suggesting a potential influence on development of the lower atmosphere. While analysis of cloud-inversion properties was unable to determine any relationships which could directly be used to determine the depth cloud encroaches into the inversion, the mass of water inside the inversion was determined to have a function dependence on z_{i+}, implying that parameterizations of encroachment may be possible. Although ASCOS observations suffered from a lack of coverage and absence of measurement of several properties which would be useful in understanding the mechanisms which control the encroachment, simulations using the LEM in the next

chapters should be able address these issues and provide a more detailed mechanistic understanding of the cloud encroachment.

In summary, the results in this chapter suggest that the encroachment of cloud into the temperature inversion is widely prevalent in Arctic stratocumulus and despite the seasonally uncharacteristic conditions experienced during the campaign, indicate the suitability of ASCOS data to investigating the encroachment mechanism.

Chapter 6

Stratocumulus encroachment into the inversion layer: Large Eddy Simulations

In Chapter 4 a number of the simulated cloud properties were found to quantitatively agree with the M-PACE observations, and results demonstrated the LEM's ability to simulate mixed-phase Arctic stratocumulus and the complex dynamical-microphysical-radiative interactions which influence the development of the Arctic BL. The dynamics of the cloud observed in the M-PACE B case study were driven by cloud-top radiative cooling, and from the strong surface fluxes of heat and moisture found over the Beaufort Sea. As is found in sub-tropical marine stratocumulus, the total water mixing ratio observed in the M-PACE B case was conserved through the BL and dropped off rapidly through the transition zone. Consequently cloud top was observed to be coincident with the top of the boundary layer.

The mean conditions observed during the ASCOS field campaign differed to those observed during M-PACE. Over the sea-ice surface of the central Arctic much weaker forcings act on the BL. Specific humidity inversions are also frequently observed coincident with the capping temperature inversion, and cloud top is often observed to encroach into the transition zone (Sedlar *et al.*, 2012; Tjernstrom *et al.*, 2012). The mechanisms which allow cloud to persist inside the temperature inversion have been examined by Solomon *et al.* (2011), who demonstrated that inversion layer cloud could be supported so long as a source of inversion layer water vapour was maintained to balance sedimentation loss. Solomon *et al.* (2011) also provided an explanation of why the temperature inversion doesn't adjust to the presence of cloud, with condensational heating, vertical eddy advection and zonal advection of heat balancing the cloud top radiative cooling in the

Table 6.1: Description of simulations made to investigate the encroachment of cloud into the inversion layer. Setup parameters described in text.

Simulation	Domain	q_t^{bl} (g kg^{-1})	q_t^{inv} (g kg^{-1})	N_{in} (L^{-1})	$(\partial q_v/\partial t)_{LS}$ (g kg^{-1} day^{-1})	$(\Delta z)_{LS}$ (m)
control	2D	2.78	1.00	1.7	-	-
control_N_{in}x2	2D	2.78	1.00	3.4	-	-
control_N_{in}x3	2D	2.78	1.00	5.1	-	-
control_N_{in}x4	2D	2.78	1.00	6.8	-	-
control_dry	2D	2.08	1.00	3.4	-	-
control_3D	3D	2.78	1.00	3.4	-	-
ls2g150m	2D	2.78	1.00	3.4	2.0	150
ls2g150m_3D	3D	2.78	1.00	3.4	2.0	150

inversion layer. While the modelling study was able to provide a detailed description of these processes, the model setup used in Solomon *et al.* (2011) was inadequate to study the sensitivity of the cloud and BL properties to temperature and specific humidity inversions with different attributes. In this chapter the LEM is employed to study the observed encroachment using an idealised framework, with analysis focusing on the radiative, dynamical and microphysical relationships which exist in inversion encroaching clouds and the differences they have to stratocumulus whose cloud top is found below the inversion.

6.1 Initial setup and simulation design

The dynamic and thermodynamic conditions used to setup the control simulations are developed from the radiosonde launches at 1121 and 1737 UTC on 27 August. The LEM is initialised using profiles of liquid water potential temperature, θ_l (Deardorff, 1976):

$$\theta_l = \theta - \left(\frac{L_v \theta}{C_p T}\right) \cdot q_l \tag{6.1}$$

and the total water mixing ratio, q_t, which are both conserved through phase changes of water (Figure 6.1). Here L_v is the latent heat of vaporization. Neither liquid nor ice cloud are prescribed at initialisation but are instead formed through the model microphysics. Throughout the model domain the specification of θ_l and q_t approximate the observed radiosonde profiles with an idealised linear fit, with the minor inversion at 200 m and the main inversion above the boundary layer defined by steps in θ_l over a single grid box level. Vertically uniform zonal and meridional horizontal winds of -8 m s^{-1} and -3.5 m s^{-1} respectively are prescribed at initialisation, with nudging employed throughout the model domain. To prevent the spurious reflection of gravity waves off the rigid top, a

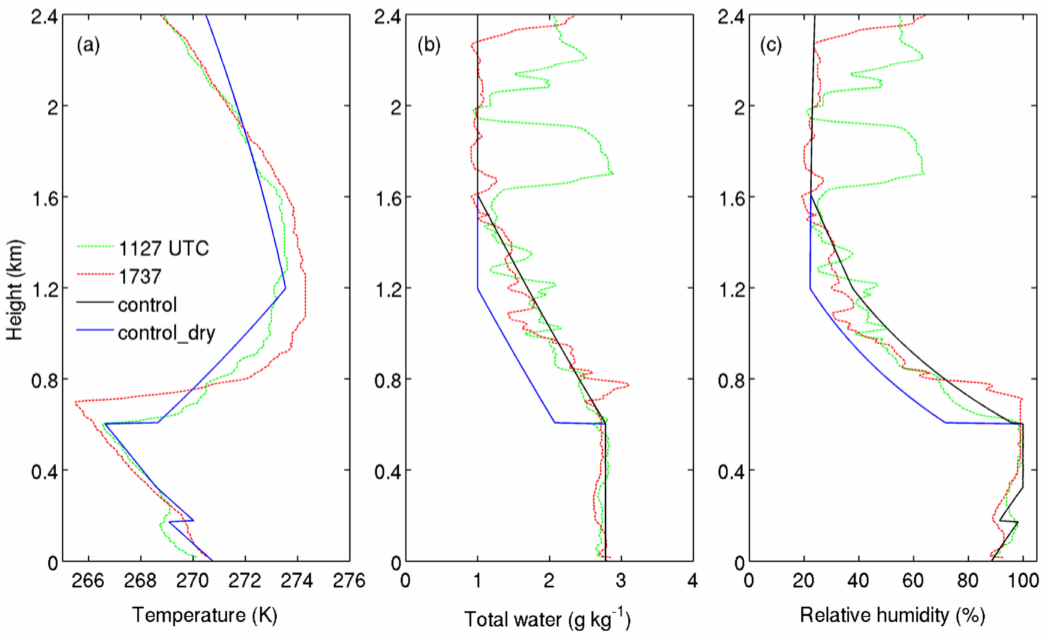

Figure 6.1: Profiles of (a) temperature, (b) total water mixing ratio and (c) relative humidity, from radiosondes launched at 1127 (green dashed line) and 1737 UTC 27 August (red dashed line) and from the control initialisation (black solid line) and control_dry initialisation (blue solid line).

Newtonian dampening layer is employed between 1.8 and 2.4 km, and to instigate model turbulence, θ_l and q_t are randomly perturbed between 0.3 and 0.6 km.

In total eight simulations are presented in this chapter. The control runs are setup so that a total water inversion is not present in the simulation; they are used to test the sensitivity of the model to microphysical parameters and in the case of control_dry, the sensitivity of the initial setup to inversion moisture. Two further simulations use the exact setup of the control run except prescribe a water vapour forcing so that an inversion in total water forms in the region above the mixed layer. Most simulations are made in 2D for computational efficiency. However two 3D simulations are included to test the sensitivity to model dimensionality. 2D simulations are made on a model domain of 4.8 km in the horizontal by 2.4 km in the vertical, using a grid spacing of 10 m in the horizontal and a staggered grid in the vertical with 5 m resolution between the surface and 1.2 km, and 10 m resolution above. 3D simulations use a horizontal domain of 4.8 x 4.8 km.

Details of the initial specification of simulations is shown in Table 6.1, where q_t^{bl} and q_t^{inv} are the initial total water mixing ratios at the BL top and top of the temperature inversion respectively, and N_{in} is the number of ice nuclei available for primary ice nucleation.

Table 6.2: Value of the fixed LEM model parameters.

Parameter	Value
Latitude (^{o})	87.35
Longitude (^{o})	-8.55
Surface Temperature (K)	271.0
Surface Pressure (hPa)	1020.5
Sensible Heat Flux (W m^{-2})	-0.08
Latent Heat Flux (W m^{-2})	2.06
Albedo	0.84
Roughness Length Heat (m)	5x10^{-5}
Roughness Length Momentum (m)	5x10^{-4}
Effective Radius (μm)	7.3
Effective Radius Ice (μm)	25.3

As no measurements of N_{in} were collected during ASCOS, here we apply the same primary ice nucleation conditions as specified in the GCSS SHEBA model inter-comparison (Morrison *et al.*, 2011), where at temperatures below 273.15 K, and at supersaturation with respect to ice of greater than 5 %:

$$\left(\frac{\partial N_i}{\partial t}\right)_{PRIMNUC} = \frac{N_{in} - (N_i + N_s + N_g)}{\partial t} \tag{6.2}$$

In control an N_{in} of 1.7 L^{-1} is used following Morrison *et al.* (2011), while in the other simulations multiples of this value are used to test the sensitivity to ice specification. Surface boundary conditions are defined by fixed fluxes of sensible and latent heat. Their prescribed values and that of various other parameters used in the model are shown in Table 6.2. These values are all means of ASCOS observations on 27th August 2008 except the roughness lengths which are prescribed following Birch (2009). The bi-modal aerosol distribution described in Section 5.2.1 is used by the Morrison *et al.* (2005, 2009b) microphysics scheme to model the activation of aerosol particles to cloud droplets. Aerosol composition is assumed to be ammonium bisulphate with an insoluble fraction of 30% (Klein *et al.*, 2009).

Large scale advective forcing of water vapour is applied to the ls2g150m and ls2g150m_3D simulations to produce a total water inversion, and omitted from the control simulations. Large scale forcing of heat and other scalars are omitted from all simulations, as is the specification of w_{LS}. While subsidence and the large scale advection of heat contribute to the development of the central Arctic BL, these parameters are usually assimilated from field measurements, none of which were made during ASCOS. Another technique used to estimate their values is from the output of GCM model simulations, though because there is often a large uncertainty in their exact magnitude (Stevens *et al.*, 2003) and

because models often display a high sensitivity to their value (see for instance Chlond *et al.* (2004)), this approach was not taken in this study. The consequence of omitting w_{LS} is that the simulated atmosphere is likely to deviate from the observed atmosphere over time. Under conditions of strong subsidence which often accompanies sub-tropical stratocumulus, this may be particularly pronounced. However, because large scale subsidence is typically weak in the Arctic and has a weak influence on the development of mixed-phase Arctic stratocumulus, its omission should not alter the evolution of the cloud much in these simulations. It also is important to note that the aim of these simulations is not to reproduce the case study exactly but rather to understand the physical processes controlling intrusion of the cloud into the inversion. Therefore some deviation of the model from the observations isn't of concern so long as the general characteristics of the case are simulated.

As there are no observations which can be used to provide the advective forcings of water vapour in the LEM model, the magnitude of the advective source of inversion layer water vapour in the ls2g150m and ls2g150m_3D simulations is made equal to the mean advective source modelled in the Solomon *et al.* (2011) study. Over their analysis period, Solomon *et al.* (2011) simulated a 2 g m^{-3} day^{-1} advective source of water into the entrainment zone (Figure 2.14). Following this, in the ls2g150m and ls2g150m_3D simulations a uniform forcing of 2 g m^{-3} day^{-1} is applied to the model grid between z_{ib} and a height 150 m above, where the Brooks (2003) algorithm is used during the model integration to determine z_{ib}. To ensure that the large scale forcing doesn't influence the BL development during the spin-up, the prescribed forcing is only applied after four hours of simulation time.

6.2 Control simulations

The following simulations are chosen as the basis to compare further model runs against. In the control setup, no total water inversion or large scale inversion layer moisture source is specified and the initial profiles are as would be expected for Arctic stratocumulus clouds where cloud top is found coincident with the inversion base. The control simulations are designed so as to facilitate a more meaningful comparison between BL development in situations where cloud top extends a significant distance into the temperature inversion against cases where it is situated close to the inversion base. However, because observations were unable to give a background measure of the central Arctic ice nuclei concentration, the control setup is also used to test the sensitivity of simulations to N_{in} and determine a suitable value to use in further simulations.

In the following results unless otherwise stated, profiles refer to vertical profiles; and timeseries and vertical profiles of selected cloud properties are averages of the entire

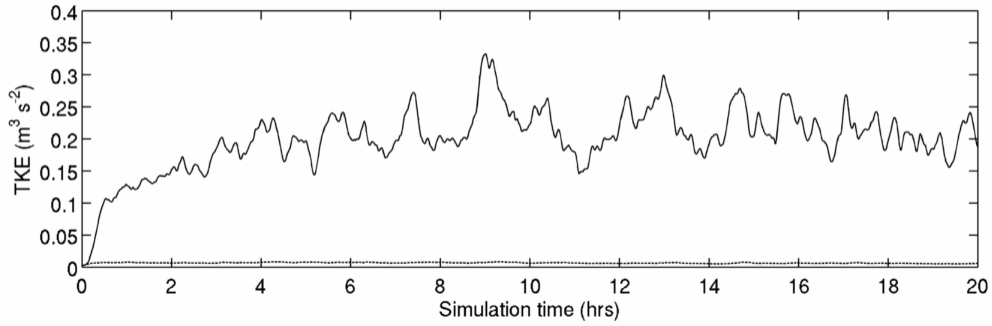

Figure 6.2: control simulation. Timeseries of instantaneous integrated sub-grid TKE (dashed line) and integrated sub-grid + resolved TKE (solid lines).

horizontal domain (layer averages) made over a five minute time-period. Where no time averaging has been performed, results are described as instantaneous.

6.2.1 Time development of the control simulation

The model is integrated in time for a total of 20 hours. In the first few hours spin-up is evident with BL turbulence initially generated from instabilities which develop from the perturbations of the θ_l field and TKE restricted to sub-grid scales. Then after 10 minutes, cloud top radiative cooling starts to drive convective instability generating resolved scale eddies and a rapid increase in TKE (Figure 6.2). After four hours integrated TKE reaches a quasi-stable value of around 0.20 m^3 s^{-2} indicating the simulation is fully spun-up.

A cloud forms within the first model time step with a mixed-phase layer between 300 and 600 m which is precipitating ice and snow into a sub-cloud layer below. During the model spin-up the cloud base falls as turbulence increases and buoyant eddies mix moist air further down into the BL, until four hours of simulation time where the mixed-phase layer reaches a quasi-stable depth of between 450 and 500 m. Over the remainder of the simulation the cloud top lifts at a rate of 0.41 cm s^{-1}, reaching 800 m after 12 hours. The mixed-phase cloud is predominantly composed of liquid water with the peak domain average LWC equal to around 0.4 g m^{-3} and peak domain average IWC equal to 0.026 g m^{-3}, where from here onwards the IWC will be used to refer to the ice + snow water content, and the IWP will refer to the ice + snow water path.

The BL is well mixed from the surface up to the base of the temperature inversion, z_{ib}, which has a strength of around 4 K just preceding the model spin-up, strengthening to more than 6 K by the end of the simulation. These values are typical of that observed during stratocumulus dominated period of ASCOS (see Figure 5.13). The mean (4 - 20 hours) entrainment zone depth is 77 m and the mixed layer top z_i is located 43 m above

the lower limit of the EZ. The peak in the LWC is found to coincide with z_{ib} and the layer maximum cloud top, z_{ct} is found 46 m above z_{ib} which roughly coincides with z_i. The layer average cloud top is found 29 m above z_{ib}. Despite the absence of a large scale moisture source within the inversion layer, the location of both the layer mean and maximum cloud tops with respect to z_{ib} suggests that the cloud is not capped by the inversion. While the depth of the extension into the inversion is relatively small compared to inversion encroachment depths found during ASCOS (Figure 5.16)and other at other Arctic sites (Sedlar *et al.*, 2012), it is not insignificant, and the depth is quasi-constant for the entire duration of the simulation suggesting that the vertical distribution of cloud in the inversion is stable.

The instantaneous 2D cross-sections of LWC and the vertical velocity output at 12 hours are shown in Figure 6.3 and 6.4. Cloud top is situated in the vicinity of the temperature inversion which is marked by a sharp θ_e gradient. LWC is greatest in the region below cloud top reaching a maximum of 0.57 g m^{-3}. Near cloud top the variability in LWC is large and entrainment is evident in the areas where the mixing of dry free-tropospheric air and saturated mixed layer air leads to a greatly reduced water content. The bottom of the liquid layer is less well defined than top with cloud base situated between 350 and 600 m.

The variation in θ_e below cloud top is small and the entire cloud and sub-cloud layer can be considered well-mixed. Different scales of motion are evident at different altitudes, with the largest most dominant eddies occurring in the mixed layer. Within the liquid cloud, the largest eddies have a diameter of around 400 m and vertical motions range from -3.5 to 2.5 m s^{-1}. Within the mixed-layer downdraughts are stronger than updraughts and are limited to a narrower horizontal extent which is consistent with turbulence caused by longwave radiative cooling at cloud top. Condensation is confined to the updraughts and evaporation to the downdraughts; therefore at any level within the cloud the LWC is greater in the updraught than the downdraughts, and the peak LWC's are found at the top of updraughts (Wood, 2012). This asymmetry is also reflected in the difference between the cloud base for upward and downward moving branches of the circulation (Wood, 2012).

Figures 6.5 and 6.6 compare timeseries of the LWP and IWP from the control simulation against ASCOS retrievals over the same period. So as to allow a better comparison between the observations where cloud top extended deep into the inversion and the control simulation where cloud top and z_i are much closer together, Figures 6.5 and 6.6 also compare the LWC and IWC retrievals vertically integrated from the cloud base up to the height of z_{ib}, $\int_{z_{cb}}^{z_{ib}}$LWC dz and $\int_{z_{cbi}}^{z_{ib}}$(IWC) dz respectively. As the first four hours of simulation were marked by model spin-up, in Figures 6.5 and 6.6 and henceforth observations are shifted so that 1137 UTC 27th August corresponds to four hours of

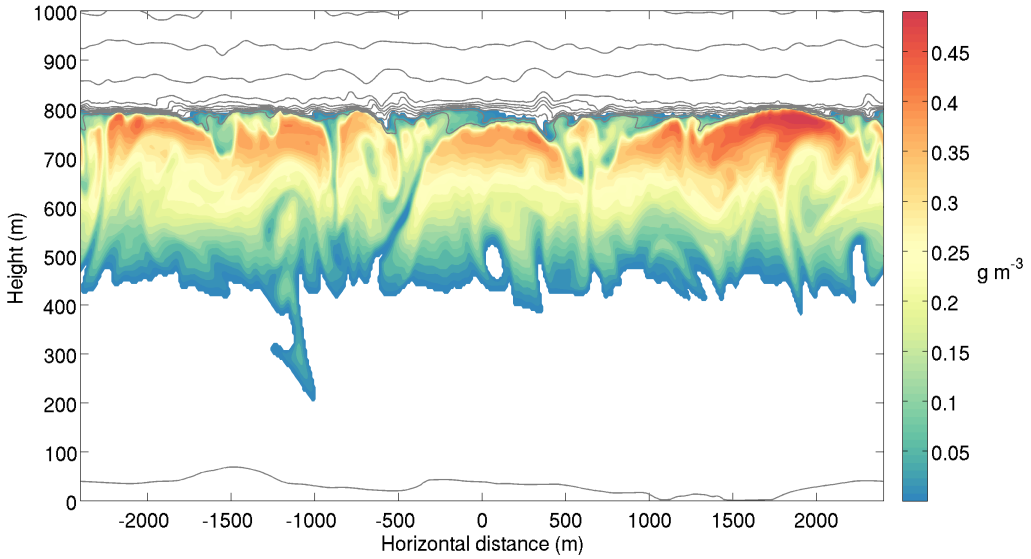

Figure 6.3: control simulation. Instantaneous horizontal cross-section of LWC output at 12 hours of simulation time with 1 K contours of θ_e from between 275 and 285 K overlaid (black lines).

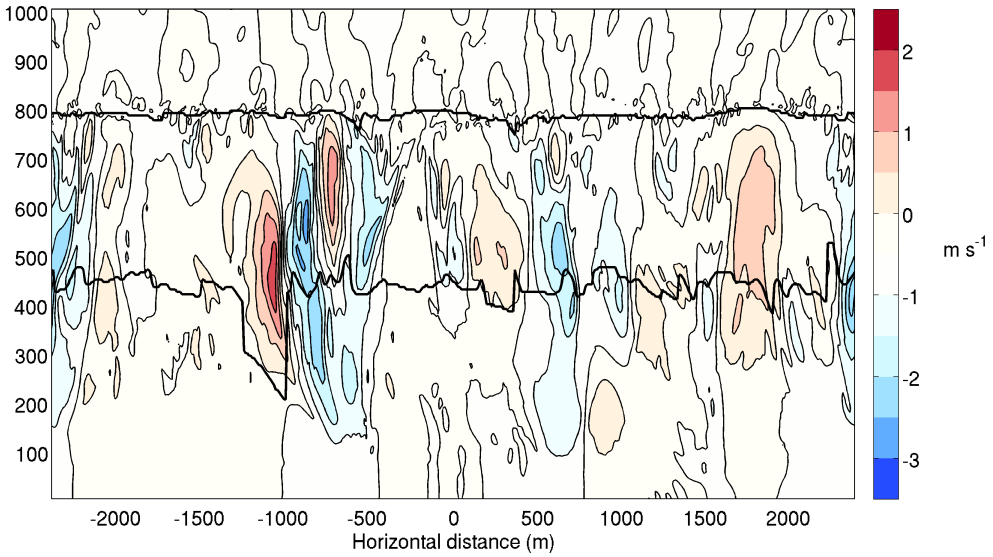

Figure 6.4: control simulation. Instantaneous horizontal cross-section of vertical velocity output at 12 hours of simulation time. Also shown are the liquid cloud base and top (thick black lines).

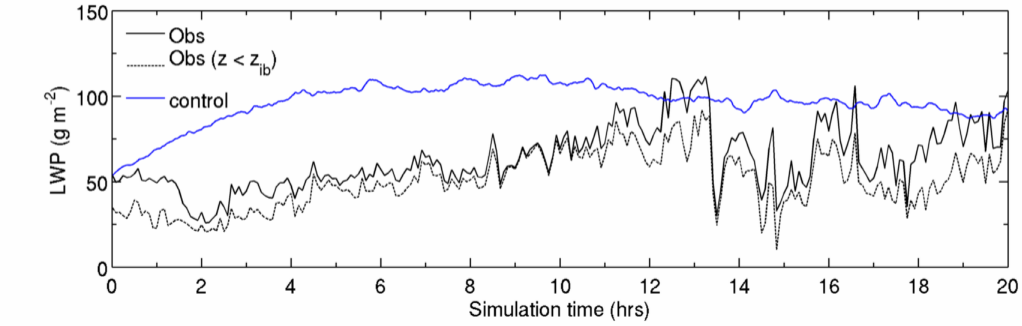

Figure 6.5: control simulation. Timeseries of LWP.

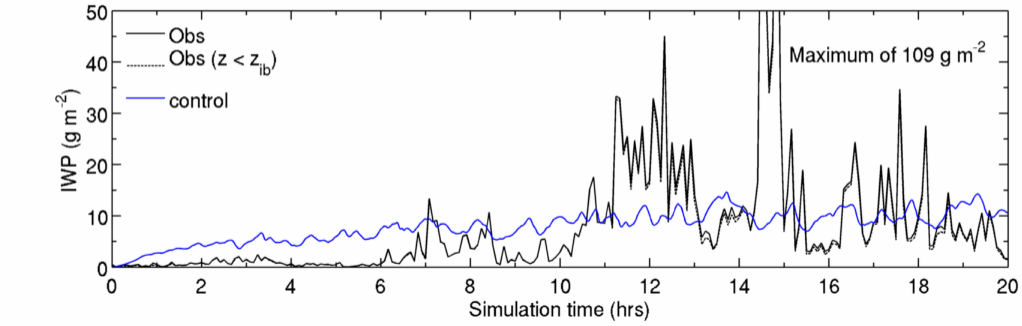

Figure 6.6: control simulation. As Figure 6.5 except for the IWP.

simulation time and the 4 - 20 hour simulation period corresponds to 1137 UTC 27th - 0337 UTC 28th August.

It is evident from Figures 6.5 and 6.6 that while a significant fraction of the retrieved liquid cloud is frequently situated above the base of the temperature inversion, very little of the ice and snow mass is situated there. Initially after model spin-up the control simulation significantly overestimates the integrated mass of liquid cloud water with the simulated LWP up to twice that observed, then after 10 hours the LWP is similar to the upper limit of observations. The simulated liquid cloud is also deeper extending over an average depth of 501 m between the cloud base and inversion base compared to a depth of 395 m in the observations.

The average IWP is slightly underestimated in the control simulation, noting that as described in Section 5.1.1.3 the relative errors in the determination of IWP may be up to a factor of two. Observations display considerably more variability than captured in the model with values ranging by a factor of 100, however some of the difference is likely explained by the fact that the observational retrievals are single column measurements as the cloud advects past, while model results are domain averages thus some of the

small-scale variability is smoothed out. Correctly representing the phase composition of clouds is a common struggle for modelling studies (Harrington *et al.*, 1999; Luo *et al.*, 2008a; Morrison *et al.*, 2003), especially where the atmosphere is supercooled meaning ice microphysical mechanisms such as the Wegener-Bergeron-Findeison instability can lead to the rapid glaciation of the cloud. The reasonable simulation of both the absolute and relative magnitudes of the liquid and ice cloud and their persistence throughout the simulation suggests that the model does a reasonable job at simulating the microphysical processes.

6.2.2 The sensitivity of the control simulation to the ice nuclei concentration

A number of runs were made to test the sensitivity of the control simulation to the concentration of ice nuclei, N_{in}. The development of these simulations was generally consistent with development of the control run, however the increase in N_{in} led to higher ice and lower liquid water contents. Table 6.3 compares cloud water statistics for the range of control simulations. Between control and control_N$_{in}$x2 the increase of N_{in} from 1.7 to 3.4 L^{-1} leads to an average increase in the $\int_{z_{cbi}}^{z_{ib}}$(IWC) dz of over 20 % and a decrease in $\int_{z_{cb}}^{z_{ib}}$(LWC) dz of more than 30 %, which is consistent with the findings of Prenni *et al.* (2007) and Morrison *et al.* (2008). This is also accompanied by an 10 % decrease in the depth of the liquid layer and slight increase in the depth of the ice layer. The entrainment rate, w_e, which in the absence of a large scale subsidence forcing is calculated as:

$$w_e = \frac{\Delta z_i}{\Delta t} \tag{6.3}$$

is found to decrease as N_{in} is increased (Table 6.4). All values are reasonable for stratocumulus clouds (e.g. Stevens *et al.*, 2003). Both the magnitude of the domain minimum and maximum vertical velocities and of the integrated TKE also decrease as N_{in} is increased. This decrease in turbulence is associated with a reduction in the magnitude of the buoyancy production of TKE, which in turn is due to a fall in the longwave cooling rate as a greater amount of water is distributed away from the liquid into the ice phase. The drop in the entrainment rate is consistent with the fall in ML turbulence and has been simulated in Fridlind *et al.* (2012).

Figures 6.7 and 6.8 compare profiles of the layer average LWC and cloud droplet density; and IWC and ice + snow crystal density respectively from the each of the control simulations. Profiles are temporally averaged over 4 - 20 hours and have been normalised before the time averaging is carried out so that the liquid or ice cloud base height is equal to zero and the inversion base height is equal to one. Within the ice layer, crystal

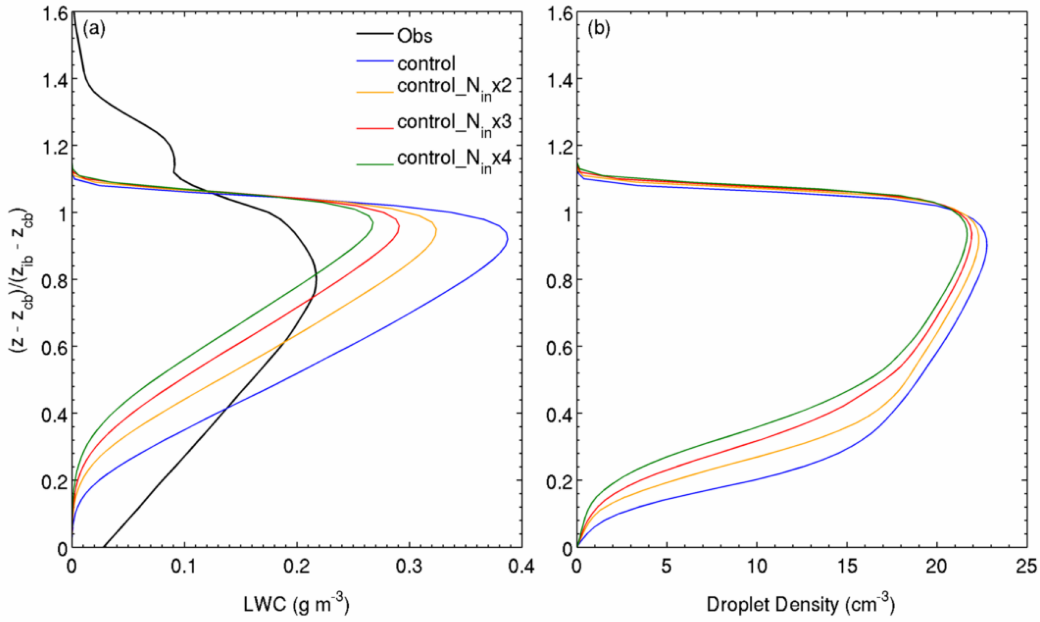

Figure 6.7: Comparison of profiles of liquid cloud properties with height normalised so inversion base height is equal to one and cloud base zero, for the control simulations. Solid lines are the time-averaged (4 - 20 hours) profiles of (a) LWC, and (b) droplet density. Dashed lines are the ± 1 standard deviations.

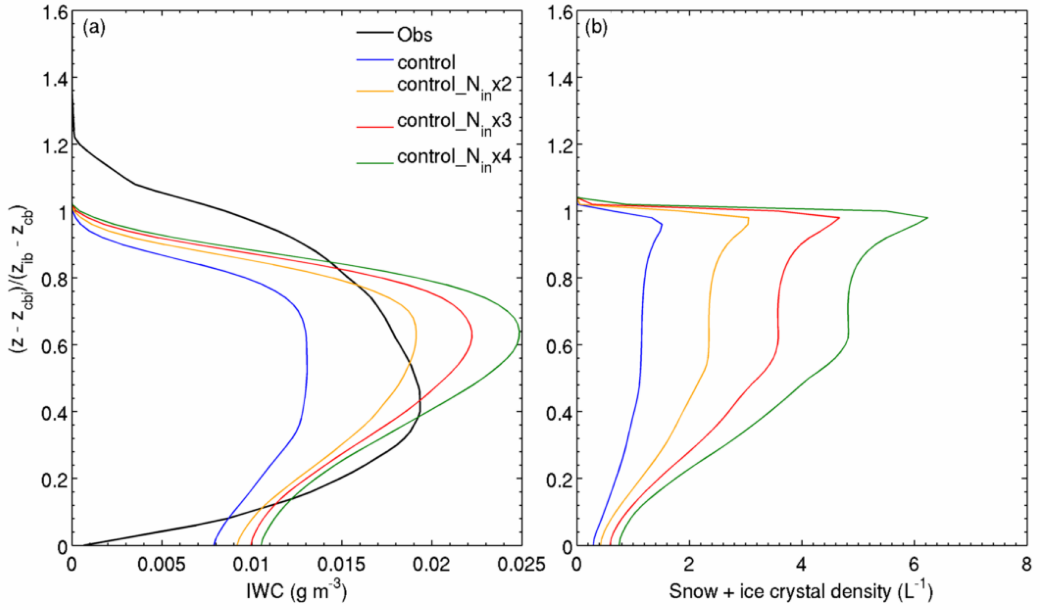

Figure 6.8: As for Figure 6.7 except for the (a) IWC, and (b) ice + snow crystal density. Profiles normalised by the inversion base and the ice cloud base.

Table 6.3: Comparison of the time-averaged cloud water statistics of the control simulations (4 - 20 hours).

Data	$z_{ib} - z_{cb}$ (m)		$\int_{z_{cb}}^{z_{ib}}(LWC)dz$ (gm^{-2})		$z_{ib} - z_{cbi}$ (m)		$\int_{z_{cbi}}^{z_{ib}}(IWC)dz$ (gm^{-2})	
	μ	σ	μ	σ	μ	σ	μ	σ
Observations	395	82	57.17	14.17	618	68	9.59	13.38
control	501	29	92.97	5.97	713	72	8.94	2.20
control_N$_{in}$x2	448	41	62.18	4.97	729	53	10.95	1.41
control_N$_{in}$x3	433	54	48.27	6.69	737	55	11.99	1.45
control_N$_{in}$x4	419	60	39.68	6.43	726	51	12.60	1.18

numbers increase upwards through the cloud with the maximum number densities found slightly below the ice layer top, which is situated roughly coincident with the base of the inversion. Approximately two thirds of the total number is made up of ice crystals and in all simulations primary ice nucleation in the major source of crystal number. Ice and snow mass peaks at 60 % of the way up the ice cloud layer. This is higher than the observations where the peak was found 40 % of the way up the cloud, however agrees with the surface-base retrievals of mixed-phase cloud made during SHEBA where the peak was a broad maximum in the upper-middle of the cloud (Shupe *et al.*, 2006).

Nucleation and deposition of water vapour onto the growing ice crystals are the largest microphysical sources of ice, while sublimation reduces ice in the sub-cloud layer. Snow is primarily formed from the deposition of water vapour onto the growing particles, though droplet accretion and ice-to-snow autoconversion also contribute to its microphysical source above the liquid cloud base. As for ice, sublimation leads to a net microphysical loss of snow in the sub-cloud layer. The increase in N_{in} over the range of control simulations leads to a linear increase in the ice + snow crystal density and in the mixed-phase region of the cloud. The increase in N_{in} also causes a change in the ice mass which is greatest as N_{in} is doubled from 1.7 to 3.4 L^{-1}. Comparing the retrieved IWC profile to the simulations, the best agreement with the peak IWC is found from the control_N$_{in}$x2 run.

Above the lowest 20% of the liquid cloud; where the layer average LWC is small due to variability in the cloud base, the LWC increases linearly with height until its peak at z_{ib}. Within the inversion the LWC drops off rapidly. This distribution of liquid cloud matches that found by Sedlar *et al.* (2012) from an analysis of inversion encroaching clouds observed at the ASCOS, SHEBA and Barrow sites. Condensation in cloudy updraughts is the major microphysical source of liquid droplets and evaporation in downdraughts the largest microphysical sink. In the main body of the cloud the droplet number density is approximately constant with height and so droplets increase in size upwards through the

Table 6.4: As in Table 6.3 except for the time-averaged dynamical statistics.

Data	TKE ($m^2\ s^{-3}$)		w_{max} ($m\ s^{-1}$)		w_{min} ($m\ s^{-1}$)		w_e ($cm\ s^{-1}$)	
	μ	σ	μ	σ	μ	σ	μ	σ
control	0.21	0.04	2.04	0.28	-2.44	0.33	0.41	0.02
control_N_{in}x2	0.16	0.03	1.90	0.24	-2.33	0.25	0.37	0.02
control_N_{in}x3	0.15	0.02	1.79	0.22	-2.27	0.26	0.33	0.02
control_N_{in}x4	0.13	0.02	1.73	0.21	-2.25	0.26	0.30	0.02

liquid layer. Mean simulated droplet number concentrations were in the order of 15 - 20 cm^{-3} which is low for marine clouds but within the range of Arctic observations (Gultepe *et al.*, 2004; Morrison *et al.*, 2008; Shupe *et al.*, 2006). The maximum LWC and droplet number decreases as N_{in} is multiplied, however the height of the peak LWC is always located in the top 10 % of the liquid layer (Tsay & Jayaweera, 1984). In the retrievals the LWC is distributed more evenly through the cloud and the maximum LWC is found slightly lower in the liquid layer. Each of the simulations overestimates the maximum LWC.

Overall the simulations show reasonable agreement with the observed liquid and ice cloud properties. The vertical structure of the cloud water contents follows a typical distribution of Arctic mixed-phase stratocumulus (Shupe *et al.*, 2008), and this is reproduced in each of the simulations. The liquid cloud simulated in the control_N_{in}x4 run has the closest mean depth and peak LWC to the observations however $\int_{z_{cb}}^{z_{ib}}$LWC dz is only around two thirds of the observed value. The control_N_{in}x2 run has the closest agreement with the $\int_{z_{cb}}^{z_{ib}}$LWC dz observations and the best agreement to the retrieved cold-phase cloud.

6.2.3 Mean profiles of fluxes and tendencies in the control_N_{in}x2 simulation

The control_N_{in}x2 simulation was found to have the closest agreement to the observed cloud, and so henceforth will be considered as the standard reference simulation against which to compare further simulations. As was detailed in the previous section the development of the control_N_{in}x2 simulation was similar to that found in control run except that the change in cloud microphysics led to a redistribution of cloud between the liquid and ice phases, and weaker turbulence led to a shallower liquid layer. Within the control_N_{in}x2 simulation the vertical distribution of the LWC was consistent to that found in the control run and z_{ct} was located an average of 47 m above z_{ib}. Thus despite no large scale water vapour advection the control_N_{in}x2 run also cloud top encroachment into the inversion layer. So that a detailed comparison can be made between control_N_{in}x2 and

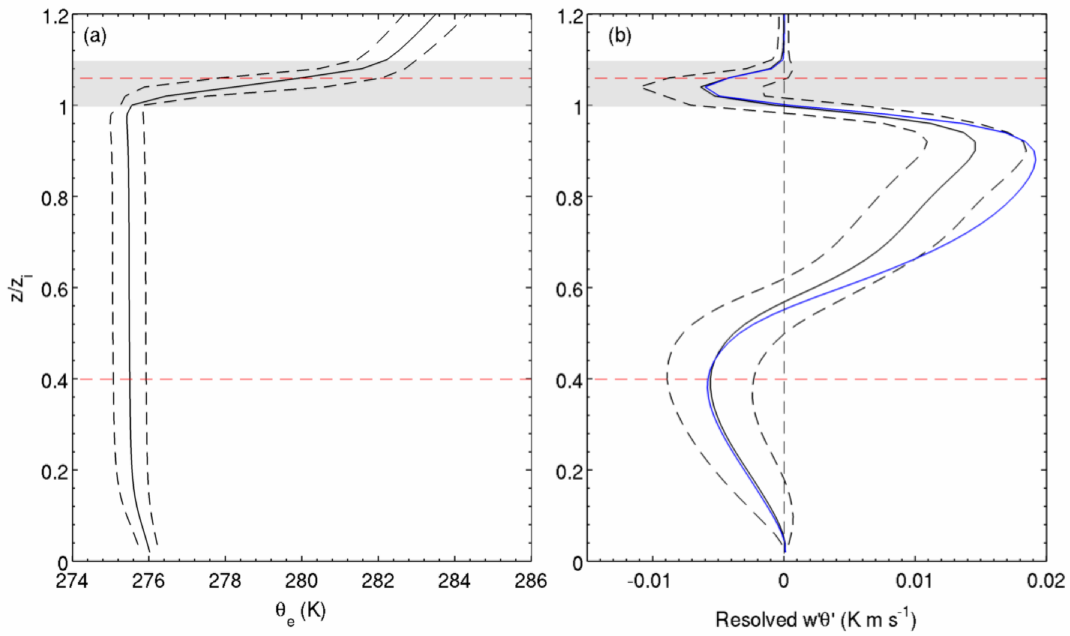

Figure 6.9: control_N$_{in}$x2 simulation. Profiles of (a) θ_e, (b) the resolved $\overline{w'\theta'_v}$ (black line) and the resolved $\overline{w'\theta'}$ (blue line) with height normalised so that the surface height is equal to zero and the inversion base height, z_{ib} is equal to one. Solid lines are the time-averaged (4 - 20 hours) profiles and dashed lines are the $\pm$ 1 standard deviations. The grey shaded area denotes the mean entrainment zone and the horizontal red lines the liquid cloud boundaries.

subsequent simulations, profiles of the $\overline{w'\theta'_v}$ as well as the budgets of θ, TKE and the hydrometer species will now be examined.

6.2.3.1 Buoyancy fluxes

Figure 6.9 shows profiles of equivalent potential temperature, θ_e, the resolved vertical heat flux, $\overline{w'\theta'}$ and the resolved vertical flux of virtual potential temperature, $\overline{w'\theta'_v}$ averaged over 4 - 20 hours, where profiles have been normalised before the time averaging is performed so that the surface height is equal to zero and the inversion base height, z_{ib} is equal to one. These values are the standard heights used to normalise the STBL (Stull, 1988). The layer maximum/minimum cloud boundaries and the entrainment zone are also marked.

θ_e is conserved under both dry and moist adiabatic processes and its vertical derivative gives a measure of the stability of an atmospheric column. A constant θ_e profile indicates a well mixed layer while an increasing θ_e profile with height indicates a stable region. The

resolved $\overline{w'\theta'_v}$ is a measure of eddy transport of heat over vertical layers, with motions in regions of positive $\overline{w'\theta'_v}$ increasing the stability of the layer while motions in regions of negative $\overline{w'\theta'_v}$ decreasing the stability of the layer. In Figure 6.9 the layer minimum cloud base is found at a normalised height of 0.4 while the layer mean cloud base (not shown) is found at normalised depth of 0.5. As is typical for stratocumulus the maximum $\overline{w'\theta'_v}$ value is found within the cloud layer (Nicholls & Leighton, 1986). Above the layer mean cloud base the sharp increase in $\overline{w'\theta'_v}$ is associated with latent heat release (Bretherton & Wyant, 1997), while the layer of negative $\overline{w'\theta'_v}$ below the cloud base makes the sub-cloud layer a sink for turbulence. Negative $\overline{w'\theta'_v}$ is associated with decoupling (Bretherton & Wyant, 1997; Turton & Nicholls, 1987), though the mean θ_e profile is well mixed in the sub-cloud layer suggesting the ML extends from the surface up to the base of the inversion (bottom of the entrainment zone).

Above z_{ib}, the equivalent potential temperature sharply increases by a mean value of 6 ^{o}C over the depth of the entrainment zone. The EZ has an average thickness of 75 m while z_{ct} and the region above the inversion base contains around 10 % of the liquid cloud. Generally the boundaries of the EZ as determined by the Brooks (2003) algorithm are consistent with the region of negative $\overline{w'\theta'_v}$; a fundamental definition of the entrainment zone (Driedonks & Tennekes, 1984) - signifying the consumption of TKE at the expense of entraining less dense inversion layer air into the mixed layer below. The negative peak in $\overline{w'\theta'_v}$ roughly corresponds to the height of the layer maximum cloud top. In the cloud driven mixed layer $\overline{w'\theta'_v}$ is up to 30 % greater than the vertical heat flux, $\overline{w'\theta'}$ indicating that moisture differences contribute significantly to $\overline{w'\theta'_v}$.

6.2.3.2 Potential temperature tendency

Figure 6.10 show the time-averaged θ budget in which the averaging and normalisation of profiles has been performed as for Figure 6.9. In Figure 6.10, TOTAL refers to the net θ tendency, $D\theta/Dt$; RAD is the tendency due to radiative heating/cooling, $(\partial\theta/\partial t)_{RAD}$; MPHYS is the tendency due to cloud microphysics, $(\partial\theta/\partial t)_{MPHYS}$; and EDDY is the tendency due to vertical turbulent transport which is calculated from the divergence of the vertical heat flux, $\partial\overline{w'\theta'}/\partial z$. The θ budget is give in Equation 2.6.

Longwave radiative cooling is the dominant forcing in stratocumulus, generating instabilities which lead to turbulent mixing and driving cloud top entrainment. Longwave cooling dominates the radiative contribution to the θ budget in the uppermost third of the liquid cloud and peaks at the base of the inversion with a minimum tendency of around -70 K day^{-1}. In the bottom two thirds of the liquid cloud the radiative heating rate is positive. This is mostly due to longwave heating which occurs because the absorption of upwelling longwave radiative emitted from the relatively warm surface is greater

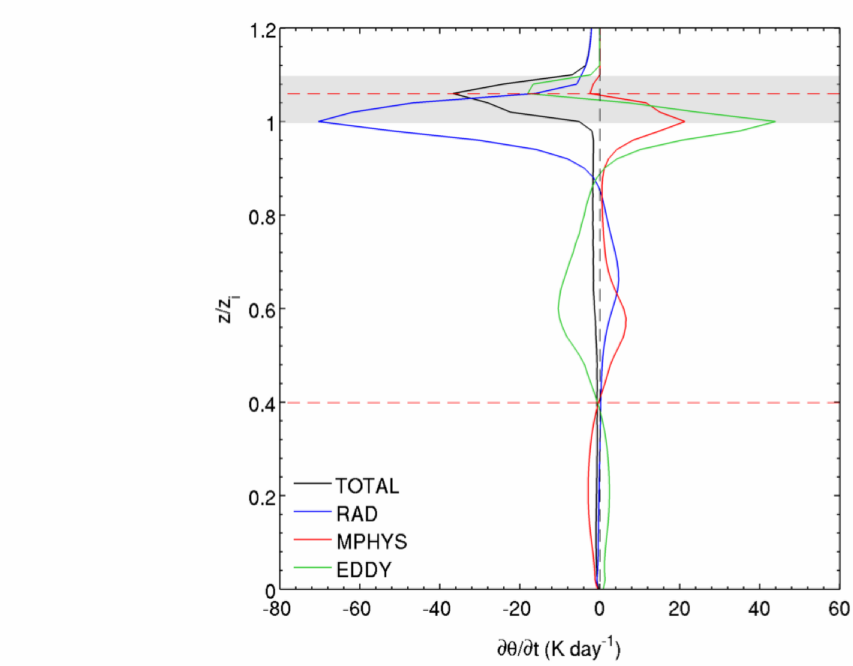

Figure 6.10: control_N$_{in}$x2 simulation. As for Figure 6.9 except for the θ budget. Terms described in text.

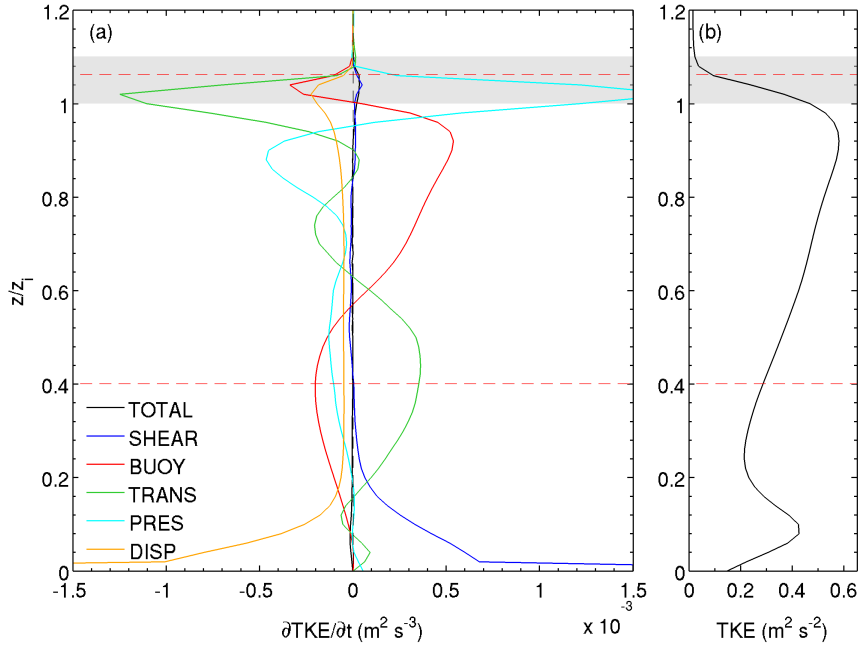

Figure 6.11: control_N$_{in}$x2 simulation. As for Figure 6.9 except for the (a) TKE budget and (b) total TKE. Terms described in text.

than emission from the lower region of the cloud. Throughout the cloud the contribution of the shortwave radiation to the net radiative heating rate is minor with a maximum tendency of less that 5 K day^{-1} found near cloud top.

While the peak in the longwave radiative cooling occurs in the lower EZ, the flux of cooled air downwards away from the layer and the heat from condensation partially balance the radiative cooling here and the largest net cooling of θ occurs coincident with the cloud top in the upper part of the EZ, where radiative cooling is negligible. Here the net θ tendency is a cooling of slightly less than 40 K day^{-1} which peaks at the height of the layer maximum cloud top. Cooling in this region is mostly due to the entrainment of heat away from here into the layer below. Within the cloudy well mixed layer the net θ tendency is slightly negative, close to zero with the diabatic heating terms balanced by cooling from eddy transport.

6.2.3.3 Turbulent kinetic energy tendency

Figure 6.11 (a) and (b) shows the normalised, time-averaged TKE budget and total TKE profiles where TOTAL refers the net TKE tendency, $DTKE/Dt$; SHEAR is the tendency due to shear production, $(\partial TKE/\partial t)_{SHEAR}$; BUOY is the tendency due to buoyancy, $(\partial TKE/\partial t)_{BUOY}$; TRANS is the tendency due to vertical transport of TKE, $(\partial TKE/\partial t)_{TRANS}$; PRES is the tendency due to pressure, $(\partial TKE/\partial t)_{PRES}$; and DISP the loss in TKE due to dissipation, $(\partial TKE/\partial t)_{DISP}$. The TKE budget is given in Equation 2.8.

Total TKE increases with height through the BL and reaches a maximum near the top of the cloud layer, while a secondary maxima is present in the total TKE profile in the sub-cloud layer, close to the surface. The peak in total TKE near the cloud top coincides with the height where the buoyancy production of TKE is greatest indicating that turbulence in the cloud is mostly driven by instability generation from cloud processes; longwave radiative cooling near cloud top and latent heating/cooling. This distribution is typical for Arctic mixed-phase stratocumulus (e.g. Pinto, 1998).

The TKE maxima near the surface is shear-driven. Despite the shear-driven TKE peak near the surface, over the averaging period shear generation is less than turbulent dissipation, leading to a net TKE loss of up to -0.0017 m^2 s^{-3}. Hence the region close to the surface is a net sink of TKE over the averaging period. Within the EZ, negative $\overline{w'\theta'_v}$ due to entrainment leads to the consumption of TKE. A local maxima in the dissipation rate is also found here and there is a net transport of TKE from the EZ and upper cloud, towards the liquid cloud base and the sub-cloud layer below which also reduces the TKE. The pressure term is a positive source of TKE in the EZ and overbalances the other terms leading to peak tendency of 4x10^{-5} m^2 s^{-3}. The pressure term is also positive in the top

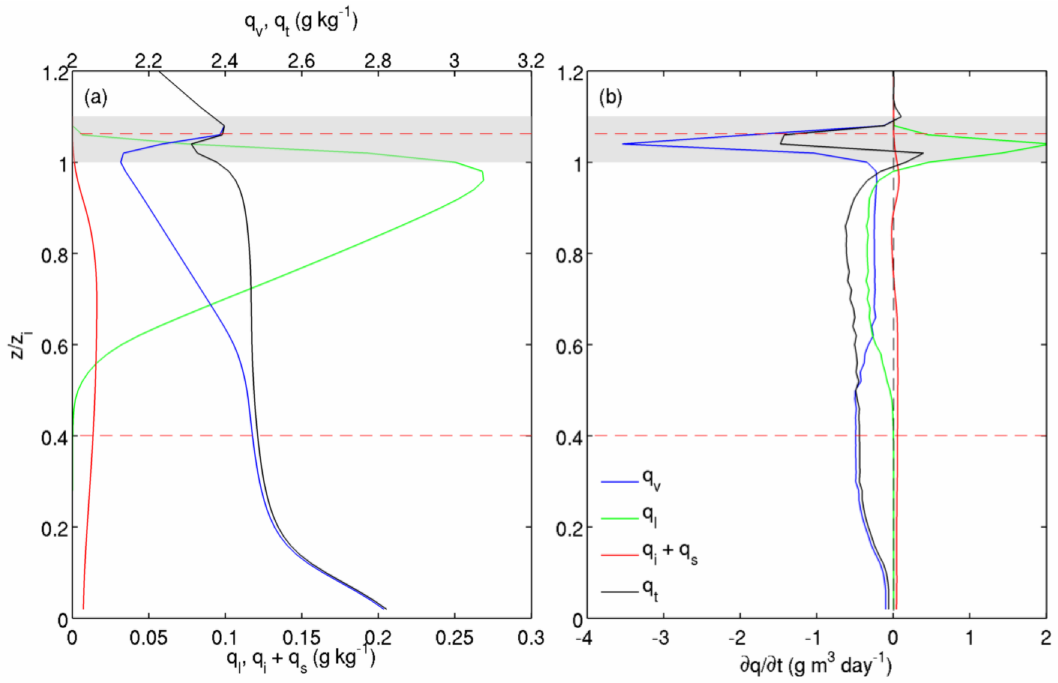

Figure 6.12: control_N$_{in}$x2 simulation. As for Figure 6.9 except for (a) the mean water species mixing ratios and (b) the mean water content tendencies. Note that in (a) the upper x-axis is for the water vapour and total water mixing ratios and the lower x-axis the liquid water and ice + snow water mixing ratios.

5 % of the mixed layer and contributes with the buoyancy to a net source of TKE here. Through the rest of the mixed layer the net TKE tendency is a loss of -3x10^{-6} m^2 s^{-3}.

6.2.3.4 Water content tendencies

Figure 6.12 shows profiles of the time-averaged water constituent mixing ratios and the net water content tendencies normalised in height as for the previous figures. Because ice + snow water mixing ratios are small relative to the liquid and water vapour mixing ratios, the total water mixing ratio is primarily composed of liquid water and water vapour within the cloud and water vapour elsewhere. The vertical distribution of the total water mixing ratio is uniform between the mixed layer, but falls by almost 0.1 g kg^{-1} within the lower EZ, before returning to its mixed layer value at cloud top. Through the cloud layer water vapour decreases until a minimum at the height of the peak LWC. Above this height water vapour increases to a value comparable to that found at cloud base. This significant positive gradient of water vapour across the lower part of the EZ is the result of the initialisation - the falloff of q_t above the inversion base wasn't sharp enough to prevent q_v increasing above the cloud top. The difference of q_v across the

gradient is large enough to be considered a humidity inversion. It might be expected that the excess of water vapour in this region would have been rapidly transported into the BL and a more typical STBL water vapour profile would have formed (Figure 2.1), however the presence of the humidity inversion in the average profiles between 4 -20 hours demonstrates that the dynamical-cloud microphysical interaction within the BL are able to support the humidity even where no large scale advection of moisture is present.

From Figure 6.12 (b) it can be seen that the entire BL is a sink of total water except in shallow regions at the base and top of the EZ. The greatest loss of total water occurs between these layers, with the negative water vapour tendency of more than -3.5 g m^{-3} day^{-1} overbalancing the positive liquid water tendency of around 2 g m^{-3} day^{-1} and leading to a loss of total water of -1.5 g m^{-3} day^{-1}. Water vapour is being lost throughout the EZ, however the loss is not distributed evenly and instead peaks at a height slightly below the centre of the EZ where the minima of the water vapour profile is found. This unequal drying centred around the humidity inversion base, supports the maintenance of the humidity inversion. Liquid water loss is greatest within the cloud layer with the tendency equal to -0.25 g m^{-3} day^{-1} here, while only slightly negative in the sub-cloud layer below. Water vapour loss is also around -0.25 g m^{-3} day^{-1} throughout the entire mixed layer and this results in mean water vapour and total water mixing ratio profiles being nearly 0.2 g kg^{-1} drier than at initialisation. Ice isn't found above z_{ib}, however a net tendency of 0.07 g m^{-3} day^{-1} is found in the region below EZ and of 0.05 g m^{-3} day^{-1} in the bottom half of the cloud, whilst the layer in-between is losing ice and snow at a rate of 0.025 g m^{-3} day^{-1}.

Normalised time-averaged water content tendency terms are shown in Figure 6.13 where TOTAL refers the net water content tendency, Dq/Dt; MPHYS is the tendency due to cloud microphysics, $(\partial q/\partial t)_{MPHYS}$; EDDY is the tendency due to vertical turbulent transport which is calculated from the divergence of the vertical moisture flux, $\partial\overline{w'q'}/\partial z$; and SED is the tendency due to sedimentation of particles, $(\partial q/\partial t)_{SED}$. The water content budget are given in Equation 2.7. The tendency due to cloud microphysics in the LEM is a balance between number of processes as described in Equation 3.14. The microphysical tendency of q_l depends on the activation of aerosol to cloud droplets, condensation/evaporation, and the parametrized autoconversion of liquid droplets to rain droplets, ice and snow. The tendencies for the ice and snow mass depend on ice nucleation, deposition of water vapour onto ice and snow/sublimation, freezing and melting and autoconversion.

The positive liquid water tendency in the lower EZ is primarily due to eddy transport from the mixed layer below, with microphysics also increasing the water content here and at the cloud base. Fallout of cloud droplets from the EZ is significant, removing liquid water from the EZ and transporting it uniformly across the region below. Generally the

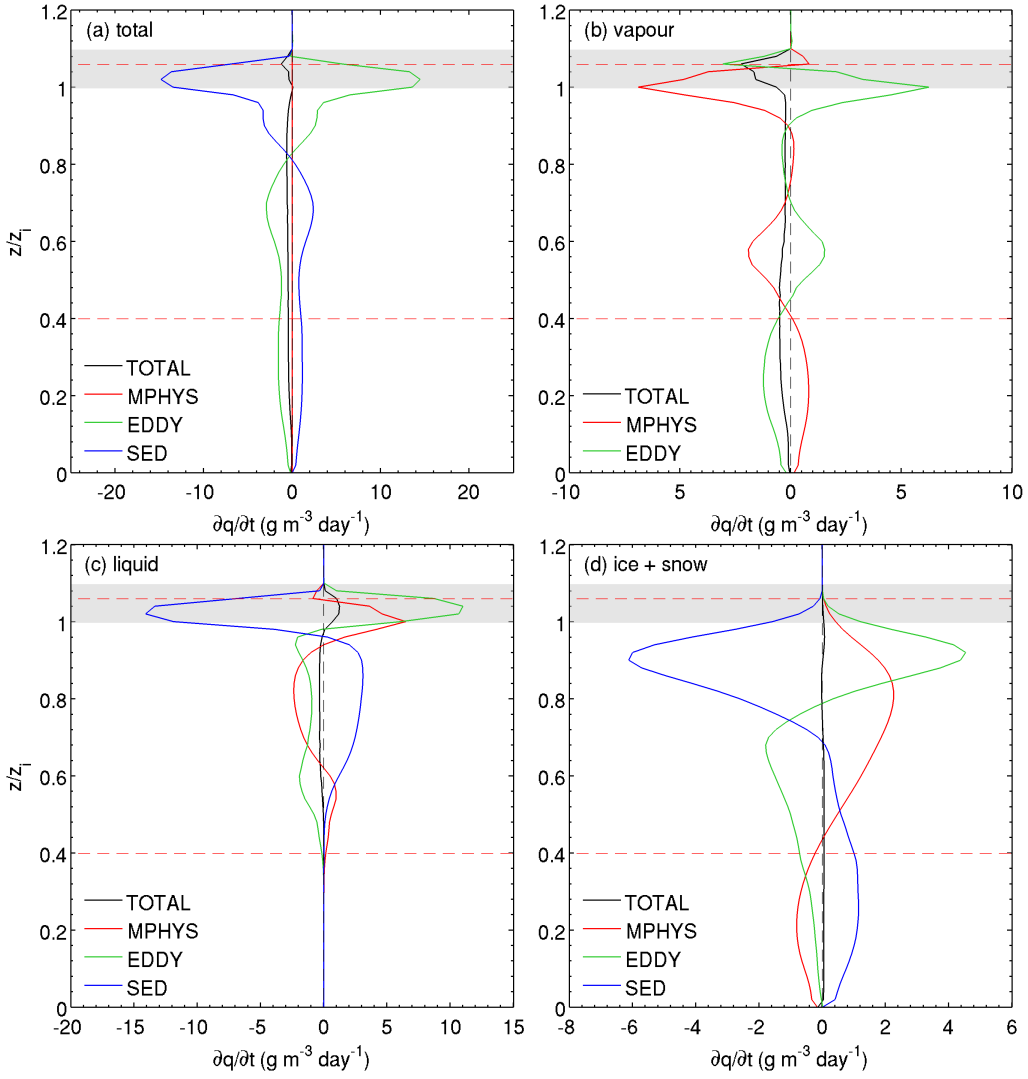

Figure 6.13: control_N$_{in}$x2 simulation. As for Figure 6.9 except for the (a) q_t budget, (b) q_v budget, (c) q_l budget and (d) $q_i + q_s$ budget. Terms described in text.

ice budget terms follow similar profile shapes to the LWC terms, except that in the ice cloud the profiles are skewed to extend through the sub-cloud layer towards the base of the ice layer at the surface. Fallout of ice crystals and snow from the upper cloud to the bottom is mostly offset by eddy transport upwards through the cloud and a net microphysical source of snow and ice above the liquid cloud base and microphysical sink below.

The water vapour budget is only dependent on the cloud microphysical sources/sinks and from eddy transport. In the upper part of the entrainment zone (above z_{ct}), there is net evaporation while through the rest of the EZ condensation leads to a water vapour loss. Eddy transport has the reversed distribution - a down-gradient transport of water vapour from the humidity inversion top to its base (negative $\overline{w'q'_v}$) depletes the upper EZ of water vapour while moistening the cloudy part. The combined sources/sinks contribute to the negative water vapour tendency shown in Figure 6.12 (b). Vertical profiles of the water vapour tendency terms illustrate that condensation below the cloud top is strong enough to overbalance the eddy source of water vapour and produce the vertically unequal drying profile which maintains the humidity inversion. As liquid water is lost from the EZ by sedimentation, and because the only source of water vapour to the cloudy region of the EZ is from the top of the humidity inversion, this means that the humidity inversion also maintains the cloud in this layer. Therefore the system is self-sustaining so long as the eddy transport of water vapour can replenish the lower EZ with enough water vapour for the region to stay saturated.

Dominant cloud microphysical processes are the sublimation of ice and snow which lead to a net microphysical source of water vapour in the sub-cloud layer and evaporation which is a source of water vapour in the centre of the cloud. Condensation and deposition lead to a net microphysical loss of water vapour near the liquid cloud base and near cloud top. Eddy transport partially balances the microphysical loss/gain throughout the cloud. Microphysical terms sum to zero when considering the total water tendency and the largest contribution to the budget comes from the fallout of moisture from the top third of the liquid cloud to the atmosphere below.

6.2.4 Sensitivity of the control setup to EZ moisture

Although it is rare for observations and modelling studies to explicitly calculate the boundaries of the inversion layer exactly, it is often often assumed in sub-tropical and mid-latitude marine stratocumulus that the cloud top is roughly coincident with the base of the inversion layer (e.g. Paluch & Lenschow, 1991; Stevens *et al.*, 2007; Tjernstrom & Rune, 2003). While Arctic stratocumulus differ from low-latitude marine stratocumulus in several ways; including the presence of ice and snow rather than drizzle, weak synoptic

Table 6.5: Time-averaged dynamical statistics of the control_dry simulation (4 - 20 hours).

Data	TKE ($m^2\ s^{-3}$)		w_{max} ($m\ s^{-1}$)		w_{min} ($m\ s^{-1}$)		w_e ($cm\ s^{-1}$)	
	μ	σ	μ	σ	μ	σ	μ	σ
control_N$_{in}$x2	0.16	0.03	1.90	0.24	-2.33	0.25	0.37	0.02
control_dry	0.18	0.04	1.96	0.26	-2.42	0.28	0.37	0.03

subsidence and a much weaker solar radiation flux. In Arctic stratocumulus the cloud top is only expected to encroach into the temperature inversion when a strong specific humidity inversion is present (Sedlar & Tjernstrom, 2009; Sedlar *et al.*, 2012), else the cloud top and inversion base heights are also expected to be equal. Despite the absence of a total water inversion in the control setup, in each of the control simulations presented so far the time-averaged layer maximum cloud top, z_{ct} was found to be situated more than 40 m above z_{ib} at a height which was found to be roughly consistent with z_i. Whilst the layer average cloud top was situated around 30 m above z_{ib}.

Profiles of the water vapour budget terms in Figure 6.13 suggest that the sustainment of the humidity inversion in the absence of moisture advection into the inversion layer, is dependent on the condensation-sedimentation removing water vapour from the lower part of the EZ, thus maintaining the vertical gradient in the water vapour and the eddy transport of water vapour down the inversion. As described in briefly Section 6.2.3.4, the initial specification of the q_t profile leads to the formation of the water vapour inversion. The initial setup employed in the control simulations was of θ and q_t profiles which were well mixed below z_{ib}, while above the inversion base there is a step up of θ, followed by a gradual increase through the rest of the model domain. Above the inversion base, q_t is gradually reduced from its mixed layer value (Figure 6.1). These setup profiles are similar to those used in other large-eddy simulations of stratocumulus (e.g. Stevens *et al.*, 2005), except that in other studies q_t is typically stepped down at z_{ib}.

To examine whether the encroachment of cloud into the inversion in the control simulations is entirely dependent on the presence of the specific humidity inversion, a further simulation - control_dry is presented. The control_dry simulation is initialised using the exact conditions specified in the control_N_{in}x2 run, except that q_t is reduced above the top of the mixed layer (Figure 6.1). In the control_dry run the value of q_t at the mixed layer top is 0.7 g kg^{-1} less than specified in control_N_{in}x2 simulation, which results in a step loss in the relative humidity by around 25 % over a single grid box. Above the top of the mixed layer, the vertical gradient in q$_t$ is equal in both simulations, falling to a minimum of 1 g kg^{-1} at heights of 1.2 and 1.6 km in the control_dry and control_N_{in}x2 simulations respectively.

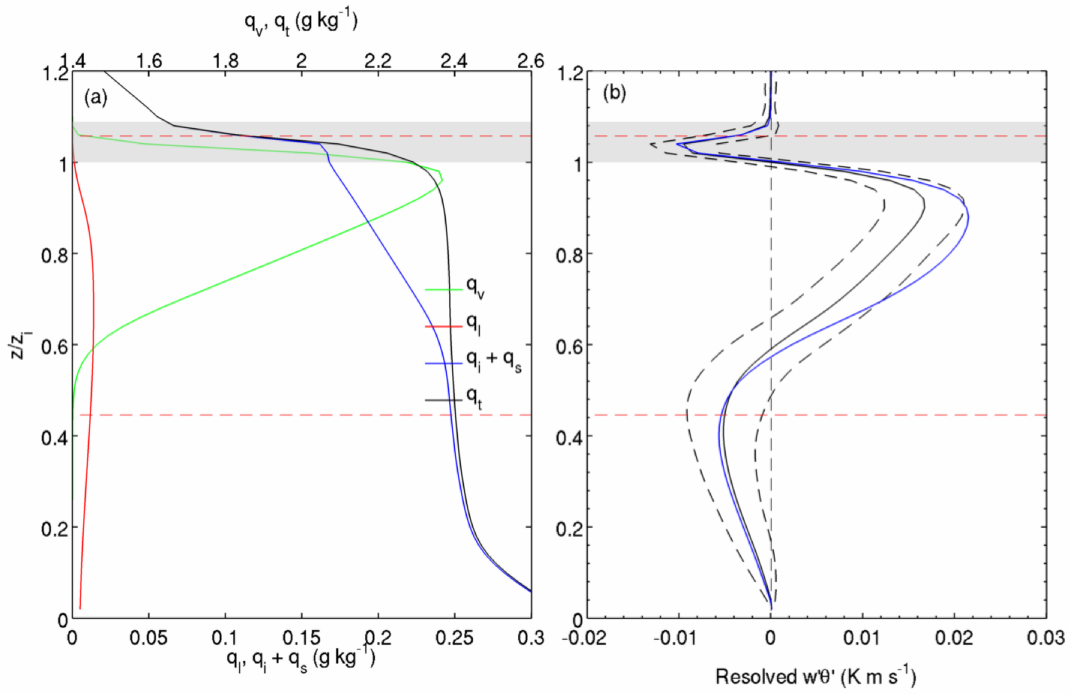

Figure 6.14: control_dry simulation. As for Figure 6.9 except for the (a) mean hydrometeor mixing ratios and (b) $\overline{w'\theta'_v}$ (solid black line) ± 1 standard deviations (dashed black lines) and vertical heat flux (solid blue line). Note that in (a) the upper x-axis is for the water vapour and total water mixing ratios and the lower x-axis the liquid water and ice + snow water mixing ratios.

Although there is a small increase in the integrated TKE, the dynamics of the control_dry run are otherwise generally consistent with that found in the control_N_{in}x2 simulation, with vertical velocities of a similar magnitude and the mean entrainment rate unchanged (Table 6.5). The cloud layer simulated in the control_dry run is also similar to that found in the control_N_{in}x2 simulation, however the liquid layer is slightly shallower with a mean depth of 429 m and this results in a smaller mean LWP of 58.4 g m^{-3}. The alteration of the initial q_t profile in the control_dry run means that the vertical distribution of water vapour and the hydrometeors more closely resembles that found in a prototypical sub-tropical stratocumulus; q_t well-mixed through the cloud layer up until the base of the inversion and q_v decreasing upwards through the cloud layer then more dramatically through the temperature inversion above (Figure 6.14 (a)). However, even though the water vapour decreases through the entire inversion, its fall directly above z_{ib} is not particularly sharp.

Similarly to the control_N_{in}x2 simulation, z_{ib} coincides with the peak in the LWC and liquid water is found above z_{ib}. Thus even without a humidity inversion, liquid cloud is able to extend into the temperature inversion. Over the entire 4 - 20 hour averaging

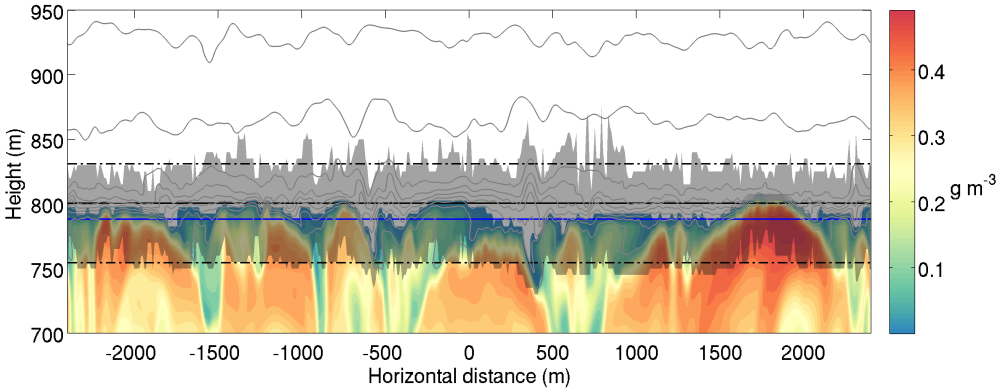

Figure 6.15: control_N$_{in}$x2 simulation. Instantaneous horizontal cross-section of LWC in the vicinity of the entrainment zone, output at 12 hours of simulation time and overlaid with 1 K contours of θ_e. Also shown are the layer average entrainment zone boundaries (black dot-dash lines), z_i (black solid line), the layer average cloud top (black solid line), and the local transition zone region (grey shaded area).

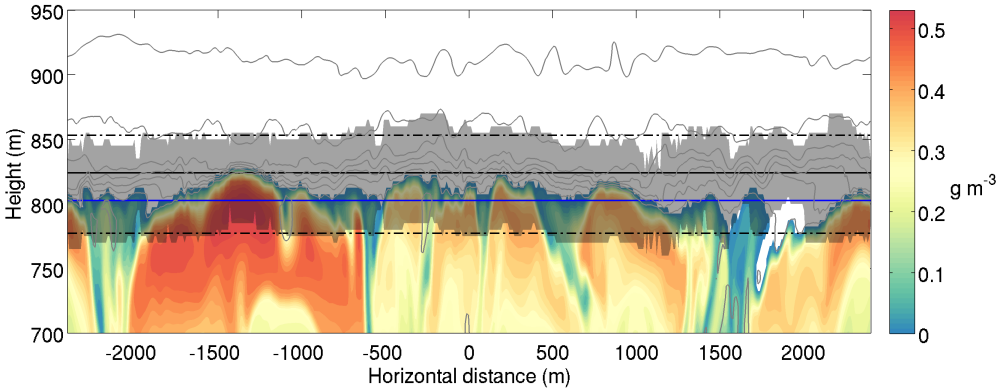

Figure 6.16: control_dry simulation. As for Figure 6.15 except for the control_dry simulation.

period, the mean depth that the layer maximum cloud top encroaches into the inversion is 41 m while the depth that the layer average cloud top encroaches above z_{ib} is 21 m. The layer average depth is around two thirds of the value found in the control_N_{in}x2 run, suggesting the change to the thermodynamic profiles has impacted on the cloud top encroachment depth, though the drying of the initial profiles isn't significant enough for the cloud to be capped by the inversion.

As was found in the control_N_{in}x2 simulation, the time-averaged normalised $\overline{w'\theta'_v}$ is negative between the boundaries of the EZ (Figure 6.14 (b)). As discussed in Section 2.1.4, the EZ is the region in which non-turbulent free tropospheric air is mixed with turbulent air from the mixed layer below, which is the region where $\overline{w'\theta'_v}$ is less than zero (Driedonks & Tennekes, 1984). This supports the validity of the Brooks (2003) algorithm

in its determination of the EZ boundaries.

The structure of the entrainment zone differs between the two simulations as shown in the 2D cross-sections of the instantaneous LWC output at 12 hours and overlaid with contours of θ_e in Figures 6.15 and 6.16. The local transition zone boundaries are also marked in each figure by the grey shaded region, while the layer average cloud top height, z_{ct}, the area average altitude of the peak in the vertical gradient of the potential temperature, z_i and the height of the EZ base, z_{ib} and top, z_{it}; which are calculated as the layer average of the transition zone boundaries, are marked by horizontal lines. As discussed in Section 2.1.4 the transition zone is the local boundary over which mixing occurs. Comparing the output of the two simulations it is noticeable that there is less variability in the position of the cloud top in the control_N_{in}x2 simulation, with the layer mean and maximum cloud tops closer together. Both simulations also illustrate that z_i is almost equal to the layer maximum cloud top, suggesting it is useful as a measure of the BL top.

Figure 6.17 shows the normalised time-averaged water content budgets for the control_dry simulation. Comparing the time-averaged water content tendencies to those found for the control_N_{in}x2 run in Figure 6.13, a change in the vertical profile of the moistening/drying is evident with both the liquid water and water vapour tendencies increasing through most of the EZ. The increasing liquid water content in the EZ is due to liquid water overshooting the top of the mixed layer but only evaporating in the upper part of the EZ - where the humidity gradient has the largest magnitude. In the lower part of the EZ, sedimentation of liquid returns some water back to the ML but the overall tendency is positive. This evaporation causes the water vapour content to increase in the layer.

Net condensation is able to occur in this region as gradient of both the temperature and water vapour profiles directly above the inversion base is relatively small. The normalised θ tendency for the control_N_{in}x2 run in Figure 6.18 shows that this profile shape is due to peak cooling of the EZ occurring above z_{ib}. This is despite the peak in the longwave radiative cooling occurs at the inversion base. With the combination of evaporative and radiative cooling; and the down gradient eddy transport of heat from inversion top to base, causing the peak loss of around 80 K day^{-1} to be found towards the top of the EZ at a height coincident with z_{ct}. In the region directly above z_{ib} where there is net condensational heating, the cooling is weaker at less than 10 day^{-1}.

The extension of z_{ct} an average of 41 m above z_{ib}, and the layer average cloud top 21 m above z_{ib} demonstrates that under certain circumstances cloud is able to encroach into the inversion layer even when a humidity inversion is not present. The height at which cloud is able to encroach into the inversion is dependent on the relative humidity of the EZ; which on a macrophysical scale depends on how sharply the water vapour profile drops off above z_{ib}, how sharply the temperature increases across the inversion,

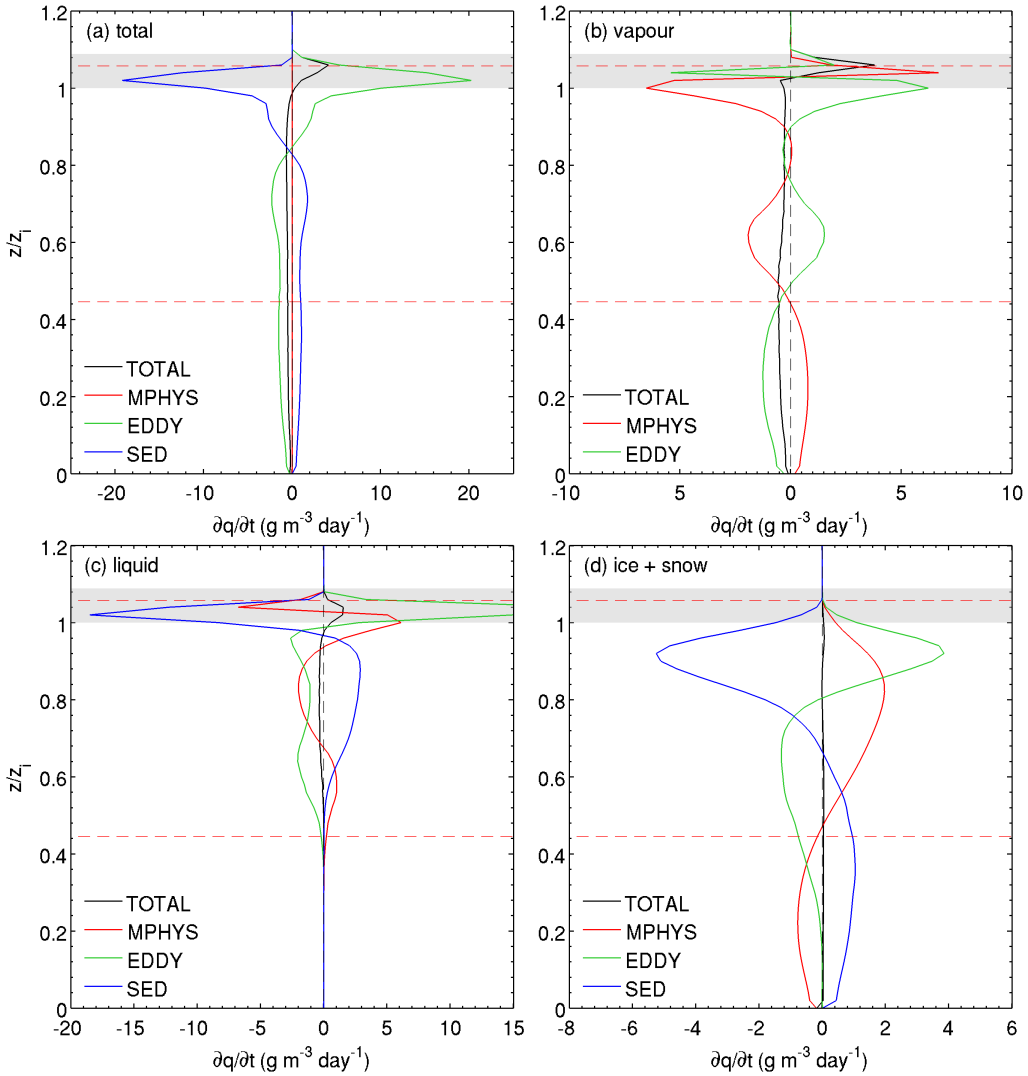

Figure 6.17: control_dry simulation. As for Figure 6.13 except for the (a) q_t budget, (b) q_v budget, (c) q_l budget and (d) $q_i + q_s$ budget in the control_dry simulation.

and on the absolute water vapour and temperatures in the ML. The relatively smooth transition from the ML to the EZ in the control_dry simulation supports an extension of cloud top into the inversion layer; though it is smaller than where a humidity inversion is also present, and suggests that the assumption that the mean cloud top height (in a horizontal sense) and the inversion base are always coincident within the STBL may be erroneous.

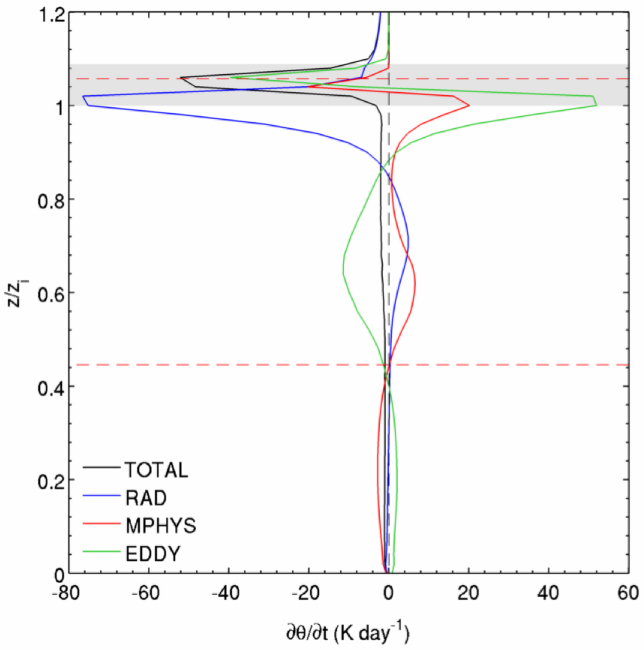

Figure 6.18: control_dry simulation. As for Figure 6.10 except for the control_dry simulation.

6.3 Simulation of cloud top encroachment into the inversion

6.3.1 Time development of the ls2g150m simulation

As in the control simulations the model is integrated in time for a total of 20 hours. The first four hours of simulation are marked by model spin-up and the integration of ls2g150m is identical to the control_N_{in}x2 simulation. After four hours the large scale advective source of water vapour is applied to the model domain in the region between z_{ib} and z_{ib} + 150 m. Between 5 and 10 hours the advected water vapour increases the relative humidity inside the temperature inversion to saturation, and the cloud top rises further into the temperature inversion from its initial quasi-stable height coincident with z_i. The time development of the depth cloud top rises into the inversion, z_{i+} and the percentage of liquid water mass inside the inversion, q_l^{i+} are shown in Figures 6.19 and 6.20 respectively for both the control_N_{in}x2 and ls2g150m simulations. The cloud top was an average of 44 m inside the inversion in the control_N_{in}x2 simulation and this height roughly coincided with the height of z_i. In the ls2g150m simulation it takes 10 hours for the cloud top to reach a quasi-stable depth inside the inversion. Over the 4 - 20 hour comparison period the average z_{i+}, and q_l^{i+} simulated in ls2g150m is 74 m and

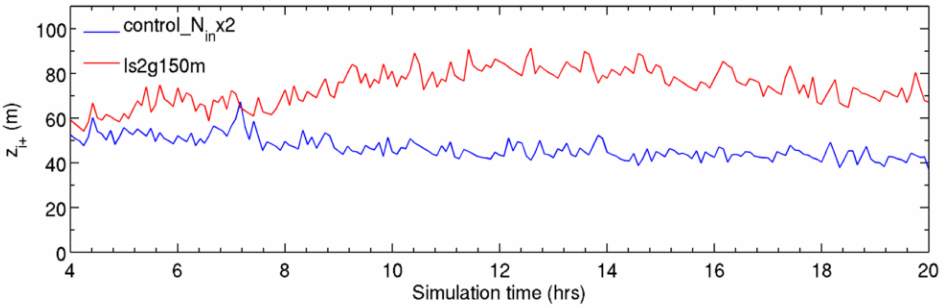

Figure 6.19: ls2g150m simulation. Timeseries of z_{i+}.

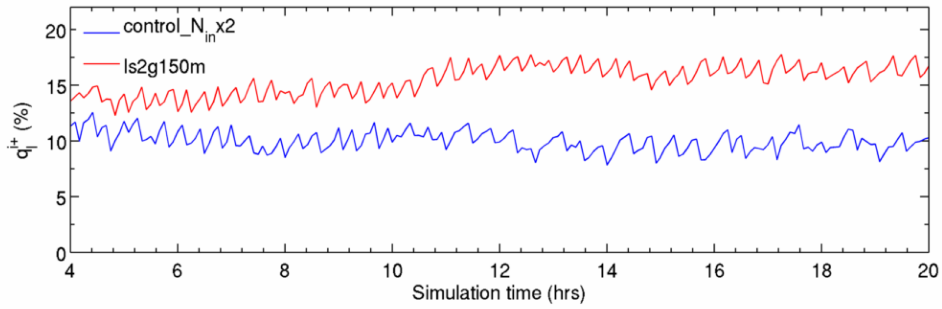

Figure 6.20: ls2g150m simulation. As Figure 6.19 except for q_l^{i+}.

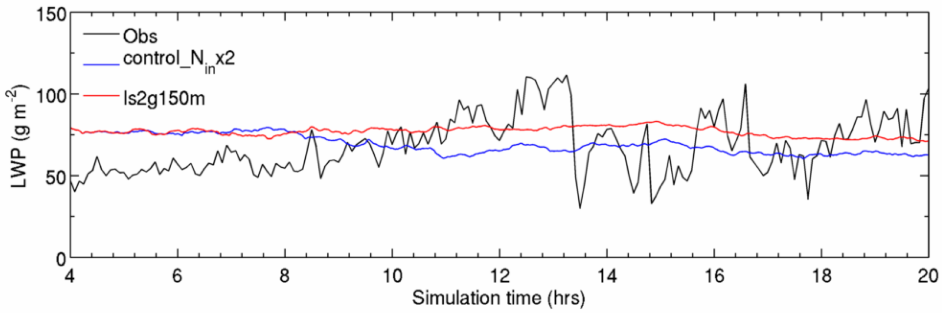

Figure 6.21: ls2g150m simulation. As Figure 6.19 except for LWP.

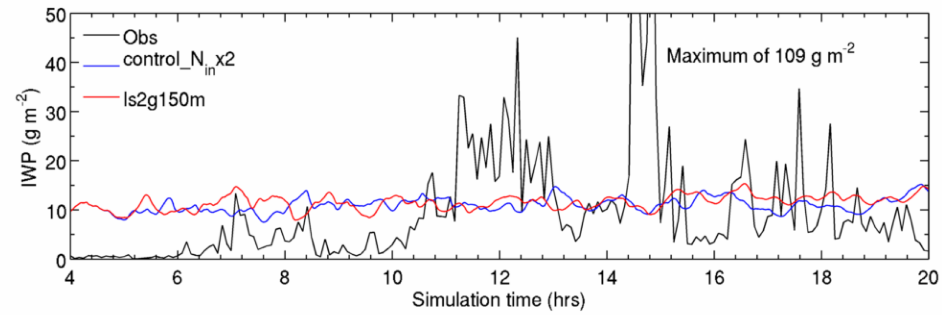

Figure 6.22: ls2g150m simulation. As Figure 6.19 except for IWP.

Table 6.6: Time-averaged cloud water statistics of the ls2g150m simulation (4 - 20 hours).

Data	$z_{ib} - z_{cb}$ (m)		$\int_{z_{cb}}^{z_{ib}}$LWC dz (gm^{-2})		$z_{ib} - z_{cbi}$ (m)		$\int_{z_{cbi}}^{z_{ib}}$(IWC) dz (gm^{-2})	
	μ	σ	μ	σ	μ	σ	μ	σ
Observations	395	82	57.17	14.17	618	68	9.59	13.38
control_N$_{in}$x2	448	41	62.18	4.97	753	61	10.97	1.42
ls2g150m	495	160	65.02	2.56	756	71	11.47	1.48

15 % respectively which is 27 m and 5 % more than simulated in control_N$_{in}$x2. The layer average cloud top is located at a mean depth of 54 m above z_{ib}, and z_i is found at a mean depth of 49 m above z_{ib}.

The well mixed region of the liquid cloud simulated in ls2g150m is also deeper than that simulated in control_N$_{in}$x2 and contains more liquid mass; which is consistent with the entrainment of moist humidity inversion air into the mixed layer (Table 6.6). The combination of a deeper well-mixed liquid layer and the extra inversion layer cloud growth results in an LWP which is an average of 10 % greater than in the control_N$_{in}$x2 simulation (Figure 6.21). As in each of the control simulations, ice and snow is precipitated from the mixed-phase cloud between z_{ib} and z_{cb} and in the sub-cloud layer below down to the surface. The difference between the IWP simulated in ls2g150m and control_N$_{in}$x2 is small (Figure 6.21). w_e is 15 % greater than in the control_N$_{in}$x2 run with a mean value of 0.42 cm s^{-1}. In Figure 6.23 (a) and (b), normalised profiles of the simulated and retrieved LWC and IWC are compared as for Figures 6.7 (a) and 6.8 (a) respectively. Despite a larger peak LWC in the ls2g150m simulation, the shape of the normalised profile throughout the mixed layer and inside the inversion is consistent with that simulated in control_N$_{in}$x2. The peak IWC is also greater in the ls2g150m simulation and is situated slightly lower inside the mixed layer, which is closer to the observed profile.

Despite the extra growth of cloud inside the inversion the time development of the ls2g150m simulation is generally consistent with the control_N$_{in}$x2 simulation. However one interesting difference in the development of the simulation is illustrated in Figure 6.24 which shows the timeseries of integrated TKE. In the control_N$_{in}$x2 simulation integrated TKE is quasi-stable after the model spin-up with an average value of 0.17 m^3 s^{-2}. However in the ls2g150m simulation integrated TKE falls between 5 to 10 hours as the cloud top rises further into the temperature inversion, before reaching a quasi-stable value of around 0.11 m^3 s^{-2} after 10 hours of simulation time. This quasi-stable value is over a third less than mean value simulated in the control_N$_{in}$x2 run, and so marks a significant drop in turbulence which is associated with cloud encroaching into the inversion layer. This suppression of TKE in the ls2g150m simulation marks a change in the dynamics of the cloud system and will be explored over subsequent sections.

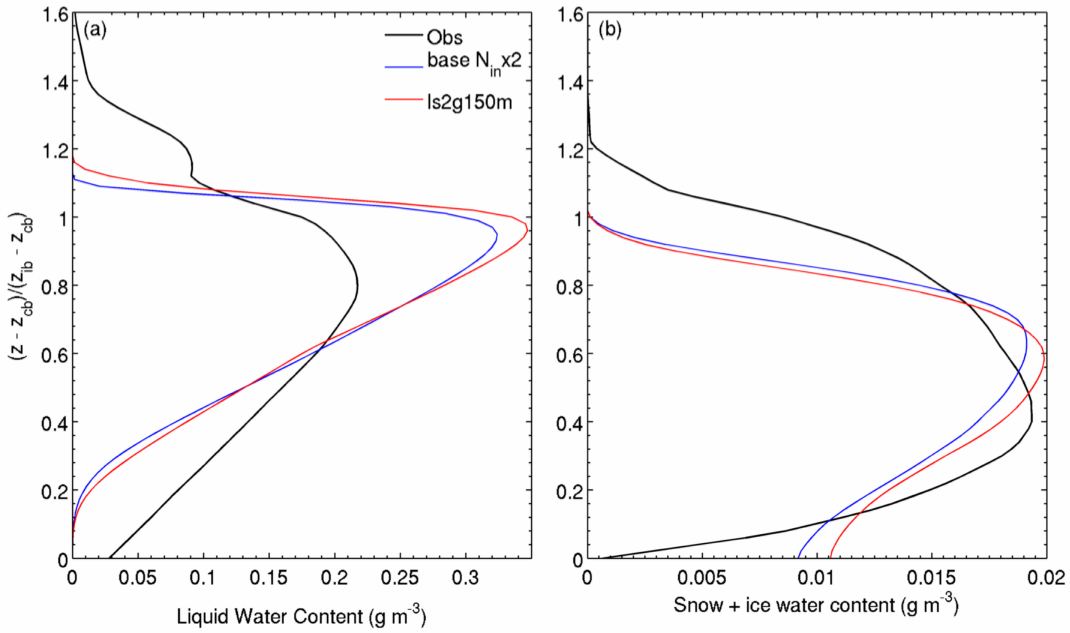

Figure 6.23: ls2g150m simulation. Time-averaged (4 - 20 hours) profiles of the (a) LWC and (b) ice + snow water content. Profiles are normalised so inversion base height is equal to one and cloud base zero.

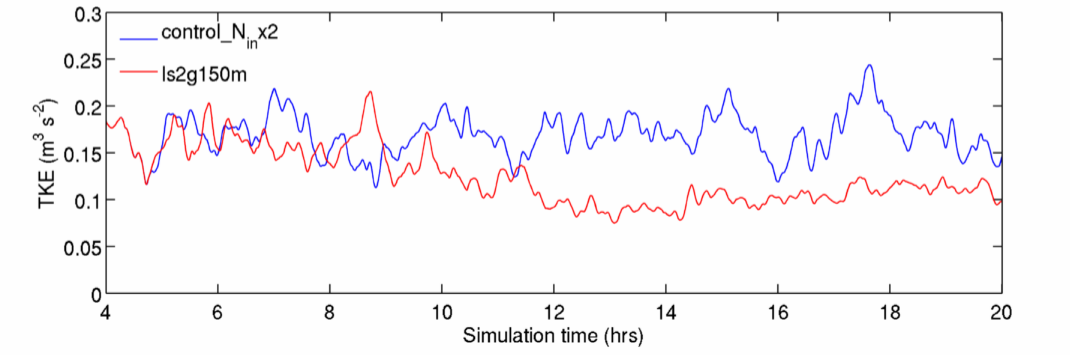

Figure 6.24: ls2g150m simulation. Timeseries of instantaneous integrated sub-grid + resolved TKE.

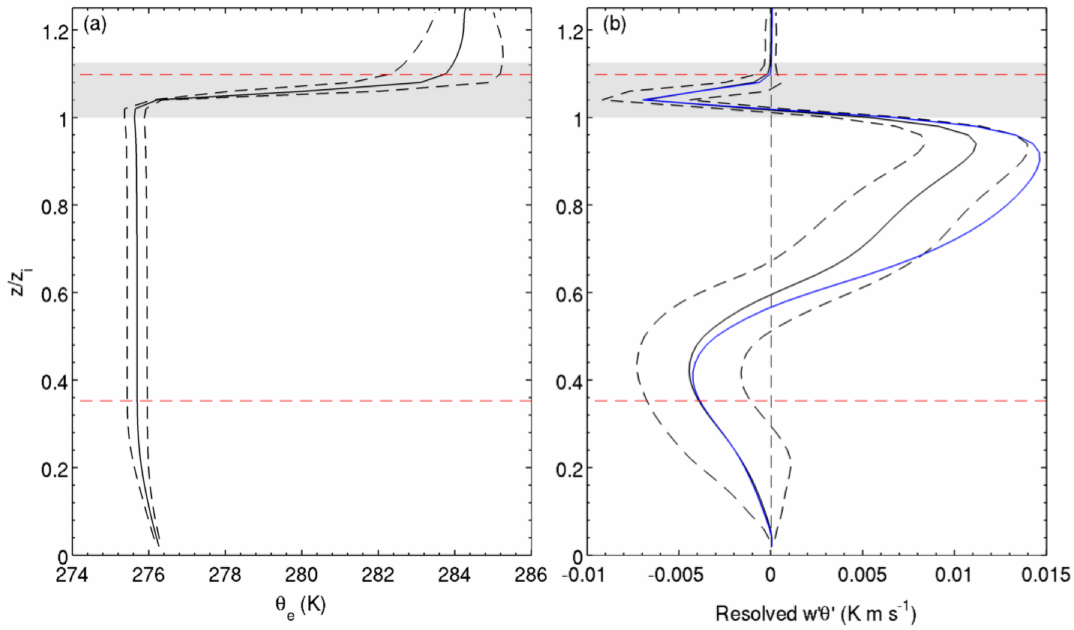

Figure 6.25: ls2g150m simulation. Profiles of (a) θ_e, (b) the resolved $\overline{w'\theta'_v}$ (black line) and the resolved $\overline{w'\theta'}$ (blue line) with height normalised so z_{ib} is equal to one and the surface zero. Solid lines are the time-averaged (4 - 20 hours) profiles and dashed lines are the $\pm$ 1 standard deviations. The grey shaded area denotes the mean entrainment zone and the horizontal red lines the liquid cloud boundaries.

6.3.2 Mean profiles of fluxes and tendencies in the ls2g150m simulation

6.3.2.1 Buoyancy fluxes

Figure 6.25 shows the 4 - 20 hours time-averaged profiles of normalised θ_e, $\overline{w'\theta'}$ and the resolved $\overline{w'\theta'_v}$ where the profiles are normalised as in Figure 6.9 so that the surface height is equal to zero and inversion base height is equal to one. As in the control_N$_{in}$x2 simulation the average θ_e profile is uniform from z_{ib} down to the surface indicating that despite the negative $\overline{w'\theta'_v}$ below the cloud base the entire region is well mixed. The strength of the temperature inversion is greater than simulated in the control_N$_{in}$x2 simulation due to the cloud extending higher up into the free troposphere, and above the EZ there is greater variability in the θ_e profile. The EZ has an average depth of around 93 m, and is defined by the region of negative $\overline{w'\theta'_v}$ near cloud top, however unlike that found in the control_N$_{in}$x2 simulation the cloud top is not coincident with the negative peak in $\overline{w'\theta'_v}$. The magnitude of both $\overline{w'\theta'}$ and $\overline{w'\theta'_v}$ are less than in the control_N$_{in}$x2 simulation suggesting a reduction in the contribution of $\overline{w'\theta'_v}$ to the generation of TKE.

6.3.2.2 Potential temperature tendency

As for the control_N$_{in}$x2 simulation, longwave cooling dominates the radiative contribution to the θ budget in the uppermost third of the liquid cloud and peaks in the EZ (Figure 6.26). The peak longwave radiative cooling is greater than simulated in control_N$_{in}$x2 at around -90 K day^{-1}, compared to around 60 K day^{-1}. As discussed in Section 2.3.4; in radiative transfer calculations through Arctic stratocumulus, Sedlar *et al.* (2012) found that the peak condensational heating always occurred coincident to z_{ib}. however in the ls2g150m simulation the extra liquid cloud mass above z_{ib} leads to the peak cooling occurring slightly inside the EZ. The peak condensational heating is of a slightly larger magnitude to that found in the control_N$_{in}$x2 simulation (around 30 K day^{-1} compared to 20 K day^{-1}) and occurs in the EZ, however because entrained air is relatively moist in ls2g150m no cooling associated with evaporation is found near cloud top. Eddy heat transport of heat is roughly of a similar magnitude to that simulated in control_N$_{in}$x2 causing a peak cooling of around -20 K day^{-1} in the upper EZ, just below the cloud top. This height is coincident with the peak diabatic heating/cooling and contributes to the peak net θ cooling tendency of slightly more than 60 K day^{-1}. This peak cooling in the EZ is 20 K day^{-1} stronger than in the simulation with a humidity source. Below the EZ the profiles of all tendency terms match that found in control_N$_{in}$x2 simulation except that the magnitude of the eddy term is less.

6.3.2.3 Turbulent kinetic energy tendency

The TKE budget in Figure 6.27 (b) shows that there is a reduction in the magnitude of the TKE buoyancy production/consumption term, with production in the upper two thirds of the cloudy mixed layer reduced by around a fifth compared to that simulated in the control_N$_{in}$x2 run, while in the EZ the buoyancy consumption is reduced by around a quarter. The TKE transport and pressure terms are reduced accordingly and the overall effect on the net TKE tendency is a reduction in its magnitude by a quarter in the EZ, with DTKE/DT peaking at 3x10^{-5} m^2 s^{-3}. As in the control_N$_{in}$x2 simulation the total TKE profile has two maxima; one near the surface which is shear-driven and one below z_{ib} which is generated by buoyancy production from longwave radiative cooling (Figure 6.27 (b)). Both maxima are reduced in the ls2g150m simulation with the peak near cloud top almost 30 % less than the equivalent peak found in the control_N$_{in}$x2 run. This reduction accounts for the loss of integrated TKE of around a third between the control_N$_{in}$x2 and ls2g150m simulations (Figure 6.24) and suggests the fall in turbulence is associated with a change to the buoyancy production from longwave radiative cooling as the cloud encroached higher into the inversion.

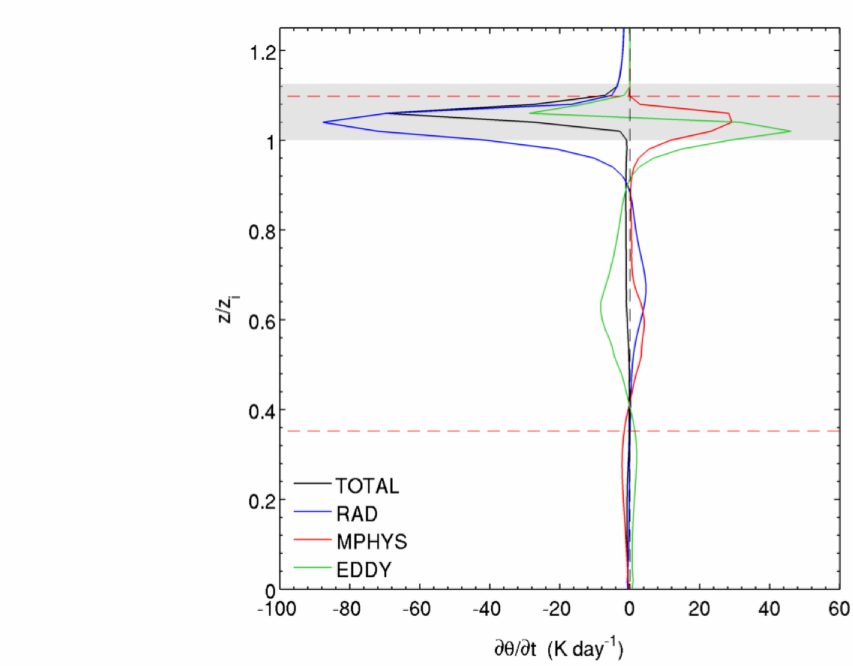

Figure 6.26: ls2g150m simulation. As for Figure 6.25 except for the θ budget. Terms described in Section 6.2.3.2.

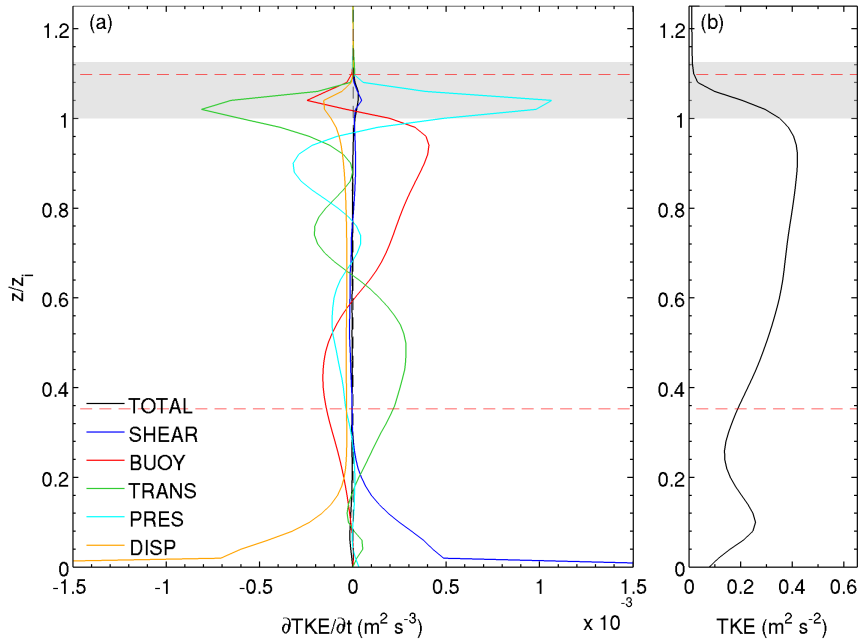

Figure 6.27: ls2g150m simulation. As for Figure 6.25 except for (a) the TKE budget and (b) the total TKE. Terms described in Section 6.2.3.3.

6.3.2.4 Instability generation

The peak radiative cooling was of a similar magnitude in both the control_N$_{in}$x2 and ls2g150m simulations, however in the ls2g150m run the region of net radiative cooling was found to be situated higher in the EZ. To explain why the vertical shift of the cooling profile reduced the buoyancy production of TKE it is useful to examine the generation of instability in the simulated cloud. Instability is incited by longwave radiative cooling when (Dobbie & Jonas, 2001):

$$\frac{\partial H}{\partial z} < 0 \quad and \quad \left|\frac{\partial \theta_v(z,t)}{\partial z}\right| < \left|\frac{\theta_v(z,t)}{T_v}\frac{\partial H}{\partial z}\delta t\right| \tag{6.4}$$

where H is the radiative heating or cooling rate equal to $\partial\theta_{RAD}/\partial t$, T_v is the virtual temperature and $\theta_v(z,t)$ is the virtual potential temperature. From Equation 6.4 a non-dimensional parameter known as the radiative-heating stability number, R_{sn} can be defined as:

$$R_{sn} = \frac{(\partial\theta_v(z,t)/\partial z)}{-(\theta_v(z,t)/T_v)(\partial H/\partial z)\,\delta t} \tag{6.5}$$

where to incite radiative instability it is required that:

$$0 < R_{sn} < 1 \tag{6.6}$$

δt is defined by Dobbie & Jonas (2001) as "the time-scale over which radiation is able to heat or cool the layer before the layer appreciably (dynamically) adjusts". Similarly, by replacing H with the latent heating or cooling rate, L the generation of instability by latent cooling is described and a latent-heating stability number, L_{sn} can be defined. By combining both heat sources a combined radiative and latent stability number, C_{sn} is defined:

$$C_{sn} = \frac{(\partial\theta_v(z,t)/\partial z)}{-(\theta_v(z,t)/T_v)\{(\partial H/\partial z) + (\partial L/\partial z)\}\,\delta t} \tag{6.7}$$

where for instability to be initiated, C_{sn} must satisfy the condition:

$$0 < C_{sn} < 1 \tag{6.8}$$

Figure 6.28 (a) shows profiles of θ_v and the radiative and latent heating rates from the ls2g150m simulation with averaging and normalisation performed on the profiles as done in the previous figures. The regions which are most important in terms of initiating instability are where the vertical gradients of H and L are negative. For H this is between a normalised height of 0.7 and 1.04 with the strongest gradient found in the region of longwave radiative cooling above 0.9. For L this is between 0.6 and 0.7 (though

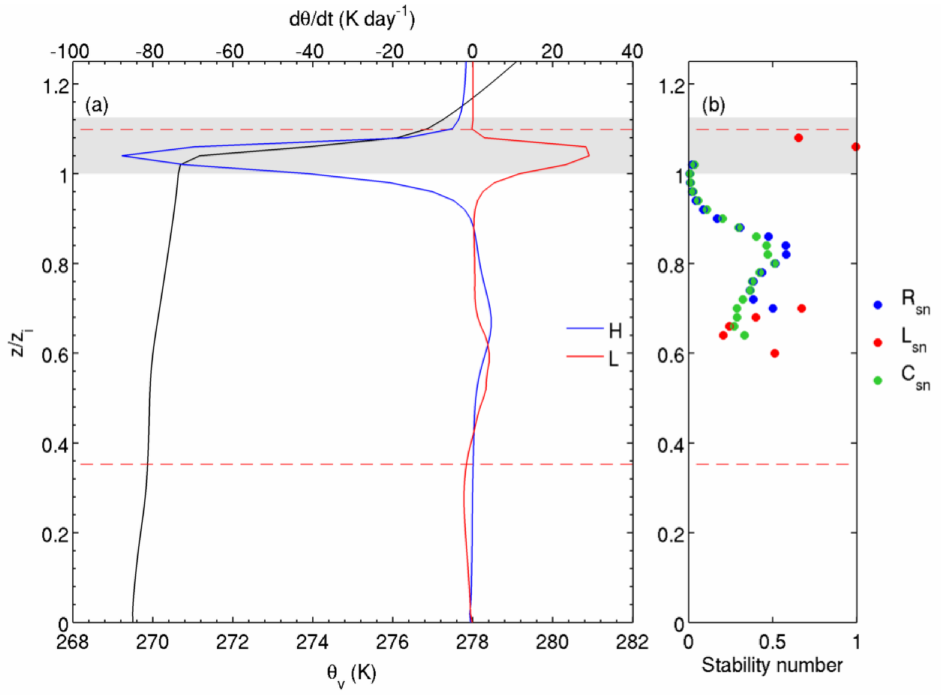

Figure 6.28: ls2g150m simulation. As for Figure 6.25 except for the (a) gradient in radiative (H, blue line) and latent (L, red line) heating rates, and (b) the radiative-heating (R_{sn}, blue), latent-heating (L_{sn}, red) and combined (C_{sn}, green) stability numbers.

$\partial L/\partial z$ is only slightly negative here) and between 1.04 and 1.1 The vertical gradient of the virtual potential temperature, $\partial\theta_v/\partial z$ gives a measure of the stability of the column and its resistance to destabilisation from the production of buoyant parcels of air. $\partial\theta_v/\partial z$ is positive through the entire BL, however its value is much smaller in the ML than in the EZ, meaning diabatic processes are more easily able to overcome the thermal stratification and induce instability. $\partial\theta_v/\partial z$ peaks near the centre of the EZ.

Figure 6.28 (b) shows values of the radiative, latent and combined stability numbers between zero and one, where the numbers are calculated from the normalised time-averaged profiles in Figure 6.28 (a). Instability is incited by latent heating/cooling in two regions: at the top of the EZ, and near the centre of the cloud. Instability is incited by radiative heating/cooling in top of the ML and around the base of the EZ where the gradient in θ_v is relatively small. C_{sn} is between zero and one between 0.64 and 1.04 of the depth of z_{ib}, which is almost the same region as where R_{sn} is between zero and one, and latent heating/cooling is less important than radiative heating/cooling in inciting instability in the uppermost part of the cloud.

A comparison of the normalised heights within cloud that instability is incited at in the control_N$_{in}$x2 and ls2g150m simulations is given in Table 6.7. Instability is incitable by

Table 6.7: Comparison of the stability number statistics of the control_N$_{in}$x2 and ls2g150m simulations. z$_{max}$ is the maximum normalised height within the cloud where instability is incited and % is the percentage of the cloud depth where instability can be incited.

Simulation	$0 < R_{sn} < 1$		$0 < L_{sn} < 1$		$0 < C_{sn} < 1$	
	z$_{max}$	%	z$_{max}$	%	z$_{max}$	%
control_N$_{in}$x2	0.91	50	0.98	30	0.91	62
ls2g150m	0.89	48	0.98	26	0.89	58

latent heating/cooling through a greater fraction of the cloud simulated in the ls2g150m simulation, and incitable by radiative heating/cooling through a greater fraction of the cloud simulated in the control_N$_{in}$x2 simulation. Overall instability is incitable through 62 % and 58 % of the depths of the cloud in the control_N$_{in}$x2 and ls2g150m simulations respectively. The max height of instability generation from radiation in the control_N$_{in}$x2 simulation is at normalised height of 0.91 which is coincident with z_{ib}. In the ls2g150m simulation the maximum height of radiative generation is at 0.89 which is above the z_{ib} at 0.87. In both simulations the uppermost normalised height where $\partial H/\partial z$ is greater than zero is 0.92, thus a greater fraction of the depth where the first condition for instability generation (first terms of Equation 6.4) is satisfied is in a region of strong thermal stratification in the ls2g150m simulation, leading to a decrease in the incitement of instability by the cloud. This reduction in the depth over which instability is incited explains why the encroachment of cloud top further into the EZ in the ls2g150m simulation leads to a reduction in $\overline{w'\theta'_v}$ and the TKE.

6.3.2.5 Mean water contents and tendencies

Figure 6.29 shows profiles of the time-averaged water contents and the net water content tendencies normalised in height as for the previous figures. As in the control_N$_{in}$x2 simulation, the ice mixing ratios are relatively small and the total water mixing ratio is primarily composed of liquid water and water vapour. In the mixed layer the water vapour and total water ratios are consistent to those simulated in the control_N$_{in}$x2 run with an average profiles exhibiting a drying of almost 0.2 g kg^{-1} compared to the initialised profiles. In the EZ a water vapour inversion with a mean strength of 0.8 g kg^{-1} is present, stretching from its base coincident with z_{ib} up to the top of the cloud layer. The relatively large magnitude of the water vapour inversion also causes the total water mixing ratio to increase rapidly through the EZ, though the strength of the q_t inversion is reduced to 0.6 g kg^{-1} because of the presence of liquid water. As in the control_N$_{in}$x2 simulation the total water mixing ratio at the base of the inversion is drier than in the mixed layer.

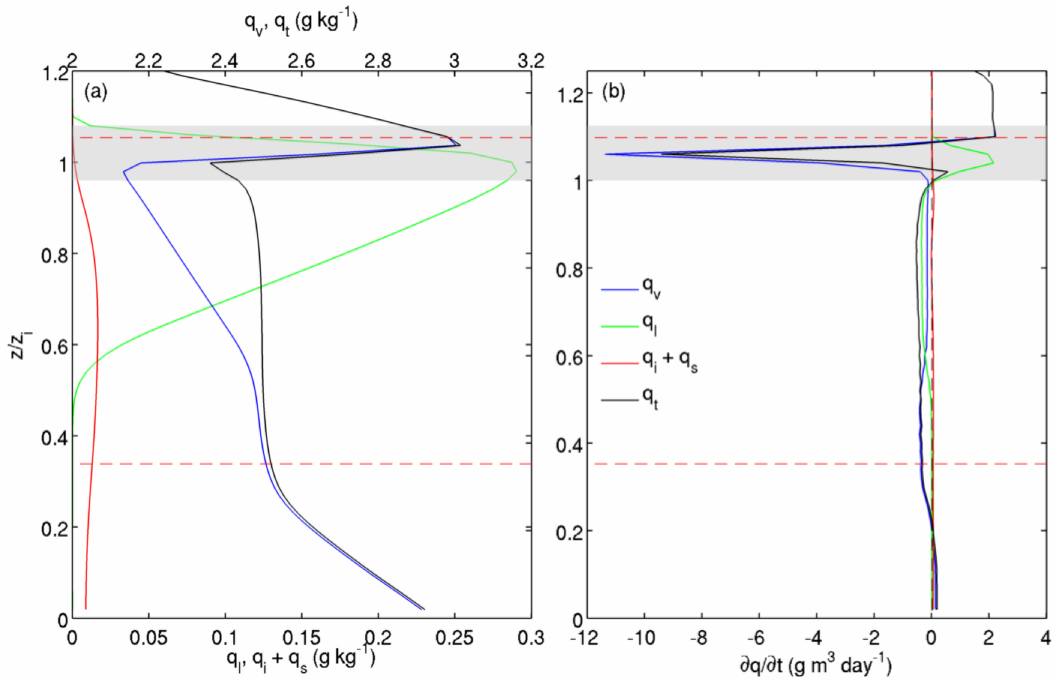

Figure 6.29: ls2g150m simulation. As for Figure 6.25 except for (a) the mean water species mixing ratios and (b) the mean water content tendencies. Note that in (a) the upper x-axis is for the water vapour and total water mixing ratios and the lower x-axis the liquid water and ice + snow water mixing ratios.

As in the control_N$_{in}$x2 simulation, liquid water is increasing at a rate of around 2 g m^3 day^{-1} in the EZ (Figure 6.30 (b)). However the magnitude of the water vapour and total water tendencies is much greater here with the peak q_v loss more than -10 g m^{-3} day^{-1}, which is almost three times the peak tendency found the control_N$_{in}$x2 run. The negative tendency at z_{ib} strengthens the humidity inversion by reducing the water vapour mixing ratio at its base. Above the cloud top a positive water vapour tendency of around 2.5 g m^3 day^{-1} is found, and this also contributes to the strengthening of the humidity inversion from its top. Through the mixed layer net hydrometeor tendencies are roughly consistent with those found in the control_N$_{in}$x2 simulation.

Normalised time-averaged water content budgets are shown in Figure 6.30, where LS is the tendency due to large scale forcing, $(\partial q/\partial t)_{LS}$ and the other terms are as described in Section 6.3.2.5. The liquid and ice water content budgets are generally consistent with those found in the control_N$_{in}$x2 simulation except for a reduction in the eddy transport which results from the drop in the strength of the BL turbulence; and greater sedimentation of liquid cloud droplets from the EZ into the mixed layer below which results from the increase in the cloud's LWC. Examining the water vapour budget, the positive net water vapour tendency above cloud top can be explained by the prescribed

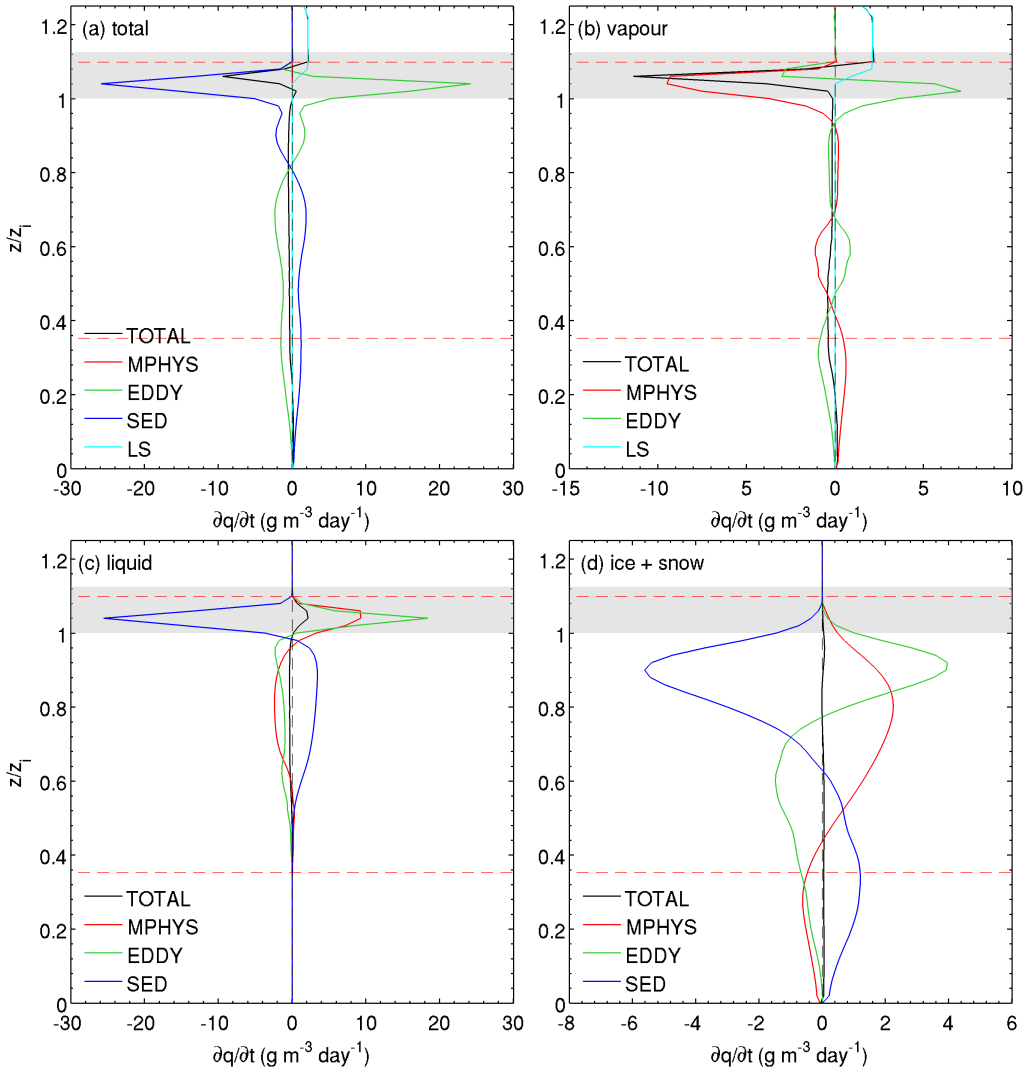

Figure 6.30: ls2g150m simulation. As for Figure 6.25 except for the (a) q_t budget, (b) q_v budget, (c) q_l budget and (d) $q_i + q_s$ budget. Terms described in Section 6.2.3.4 except LS, which is the source of water from large scale forcing, $(\partial q/\partial t)_{LS}$.

Table 6.8: Mean (± one standard deviation) contribution of the budget terms to the 4 - 20 hours time-averaged vertically integrated water content tendencies in the entrainment zone. In units of g m^{-2} day^{-1}.

Entrainment zone	MPHYS	EDDY	SED	LS	TOTAL
Total water	0±0	628±283	-858±358	83±38	-147±145
Water vapour	-424±196	107±52	0±0	83±38	-234±145
Liquid water	413±192	510±231	-837±350	0±0	86±72
Ice water	11±5	11± 9	-21±12	0±0	1±1

Table 6.9: As in Table 6.8 except for the mixed layer budget.

Mixed layer	MPHYS	EDDY	SED	LS	TOTAL
Total water	0±0	-584±266	374±194	0±0	-211±184
Water vapour	-70±169	-63±37	0±0	0±0	-133±177
Liquid water	-417±244	-510±231	820±343	0±0	-108±170
Ice water	487±218	-11±9	-446±219	0±0	30±149

large scale water vapour forcing. While the increased magnitude of the water vapour loss within the EZ can be explained by a change to the tendency due to cloud microphysics. The magnitude of the water vapour loss due to cloud microphysical processes is similar to that modelled in the control_N_{in}x2 simulation except that in ls2g150m simulation the increased cloud-inversion encroachment depth shifts the condensation region near cloud top vertically in relation to z_{ib}, so that its peak is coincident with the peak loss due to eddy transport. This also explains the increased loss of total water in the EZ.

6.3.2.6 Layer Budgets

In Tables 6.8 and 6.9 the mean ± 1 standard deviation of the time-averaged (4 - 20 hours) vertically integrated layer budgets for each hydrometeor are compared for the entrainment zone and mixed layer respectively. There is a mean net decrease in the total water content in the EZ with sedimentation away from the layer greater than combined source of moisture from the large scale forcing and from the eddy transport into the layer. Because the ice water contents in the EZ are relatively small, sedimentation loss from the layer is almost entirely due to liquid water (-837 g m^{-2} day^{-1} of a total -858 g m^{-2} day^{-1}). Eddy transport into the layer is also primarily liquid water, with the mean integrated tendency of 510 g m^{-2} day^{-1} almost five times greater than for water vapour. A net microphysical source of liquid water of 413 g m^{-2} day^{-1} is found in the EZ which combined with the eddy source is greater than the sedimentation by 86 g m^{-2} day^{-1}. Liquid water is the only hydrometeor with a positive net tendency in the layer, with the loss of water vapour due to cloud microphysics (condensation and deposition)

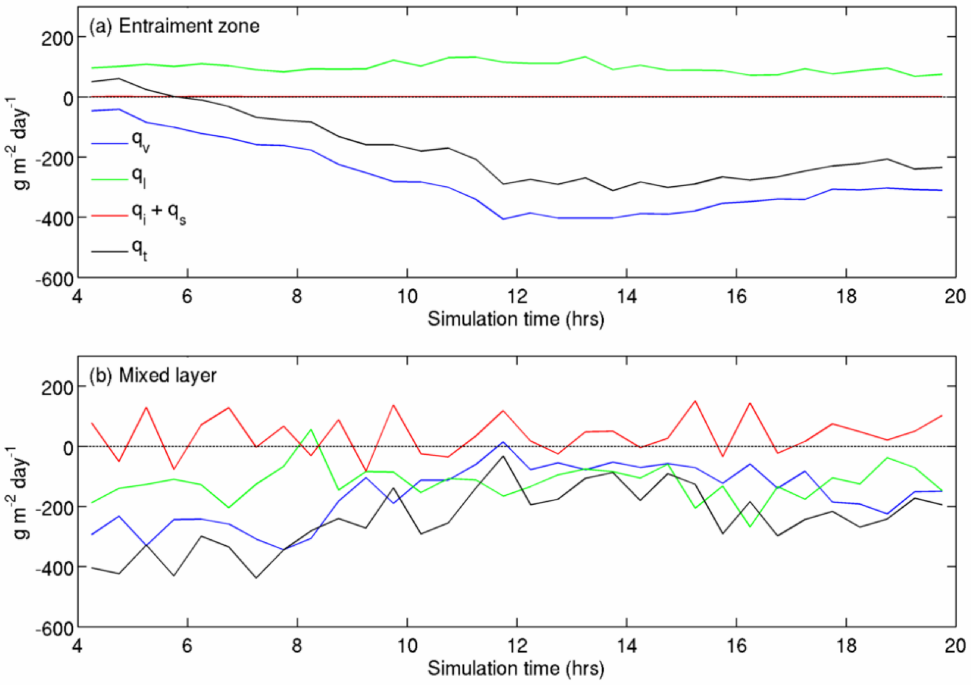

Figure 6.31: ls2g150m simulation. Timeseries of the 30 minute averaged water content tendencies integrated through the (a) entrainment zone and (b) mixed layer.

dominating the water vapour budget and leading to a net loss of -234 g m^{-2} day^{-1}. The ice budget in the EZ is relatively small and almost in balance. Comparing the integrated EZ tendencies to those simulated in the control_N_{in}x2 run, the sign of each of the net hydrometeor tendencies is the same however the magnitude of the integrated tendencies is greater with the liquid tendency equal to 86 g m^{-2} day^{-1} compared with to 64 g m^{-2} day^{-1} in the control_N_{in}x2 simulation and the water vapour tendency equal to -133 g m^{-2} day^{-1} compared to -100 g m^{-2} day^{-1}.

In the ML there is also a mean net decrease in the total water content with eddy transport to the EZ (primarily as liquid water) in excess of the sedimentation source in the layer by 211 g m^{-2} day^{-1}. A mean net decrease in the integrated liquid water content is also found with the source of liquid from sedimentation unable to balance the eddy transport to the EZ and the net microphysical loss from evaporation. Deposition of water vapour onto ice and snow is greater than its evaporative source leading to a net microphysical loss of water vapour of -70 g m^{-2}. Eddy transport of water vapour with a tendency of -63 g m^{-2} also contributes to an integrated water vapour content tendency which is negative. The eddy transport tendency in the ML is 44 g m^{-2} less than the total eddy transport into the EZ meaning the excess is sourced from above the EZ. The integrated

ice water tendencies are much larger in the ML than in the EZ with the net integrated tendency equal to 30 g m^{-2}, with the source from cloud microphysics mostly offset by sedimentation loss to the surface. The net integrated ML tendencies of liquid water and ice in the ls2g150m simulation are comparable to those simulated in the control_N_{in}x2 run, while the net integrated water vapour and total water tendencies are roughly double the size of those simulated in the control_N_{in}x2 run.

Timeseries of the mean water content tendencies averaged across the entrainment zone and the mixed layer (Figure 6.31), show that throughout almost the entire duration of the ls2g150m simulation the EZ is a source of liquid water while the mixed layer is a sink. Though there is variation in the magnitude of the gain/loss of liquid water in these regions, the temporal dependency is minimal, which suggests that the layer average tendencies are independent of the depth cloud top encroaches above the inversion base (Figure 6.19, which rises steadily between 4 and 12 hours. Both the EZ and ML are sinks for water vapour and total water and their layer average tendencies appear to show greater dependence on the depth of z_{ct} - z_{ib}. This can be explained by the vertical shift in the water vapour loss associated with condensation which was described in Section 6.3.2.5. The ice tendency in the mixed layer shows little temporal dependence and switches between being slightly positive to slightly negative which suggest that the ML can be both a source or sink of ice at different times.

6.3.3 Comparison with the Solomon *et al.* (2011) simulation

Despite the differences in both the modelling framework used; model dimensions, grid size and resolution, model forcings etc, and the differences between the simulated case studies; surface-cloud coupling, liquid/ice phase distribution - both the ls2g150m run and the simulation made in the Solomon *et al.* (2011) study were able to model the encroachment of cloud top into the inversion layer. Furthermore, the processes which allow the stratocumulus cloud to encroach into the inversion in the ls2g150m simulation is consistent with those described in Solomon *et al.* (2011), giving confidence to the results of this chapter.

Comparing the potential temperature tendencies in Figures 6.26 and 2.13 it is apparent that even with the absence of an advective heat source in the ls2g150m simulation, the simulated θ budget inside the EZ is qualitatively similar in both simulations with condensational heating and a net heat transport from the upper part of the EZ to the lower part balancing the cooling from longwave emission. Although the LWC's are smaller in the Solomon *et al.* (2011) simulation, the magnitude of the peak longwave radiative cooling is larger than modelled in the ls2g150m run, most likely reflecting a greater droplet number near cloud top which causes the cooling to be concentrated in a shallower layer.

The condensational heat source is of similar magnitude in both simulations, whilst the warming from eddy transport in the ls2g150m simulation is less that a third of size of that simulated in the Solomon *et al.* (2011) study, with the difference reflecting a reduction in $\overline{w'\theta'}$. Overall the difference in the peak net tendency is roughly 20 K day^{-1}.

The net TKE distribution is similar in both of the simulations with a peak found near the top of the mixed layer which has a magnitude of 0.4 m^2 s^{-2}. Buoyancy production is the largest contributor to the TKE tendency in both the simulations, though the tendency is larger in the Solomon *et al.* (2011) run. Shear is also an important source of TKE in the Solomon *et al.* (2011) simulation, through the cloud and in the EZ especially where it balances TKE consumption from the dampening effect of the stable layer. The setup of vertically uniform horizontal velocities at initialisation and the constraint on their development from the model nudging means that shear is less important in the ls2g150m simulation except near the surface.

Although water contents are greater in the ls2g150m run, in both of the simulations the distribution of water contents within the ML and EZ is similar, with total water well mixed up to the base of the inversion, liquid cloud increasing linearly from its base to z_{ib} before dropping off through the EZ, and ice precipitating through the whole BL below z_{ib}. Profiles of the water content budgets and their vertically integrated values in the EZ and ML also share similarities. In both simulations condensation in cloudy updraughts is greater than evaporation inside the EZ leading to a microphysical source of liquid water, while sedimentation of liquid droplets depletes the EZ of liquid water. The magnitude of the sedimentation is larger in the ls2g150m simulations, suggesting larger cloud droplets and a smaller droplet concentration which is consistent with the difference in the radiative cooling described above. In both simulations there is a net eddy transfer of liquid water from the ML to the EZ which offsets the net loss from the sedimentation and contributes with the microphysical liquid source to a positive liquid water tendency in the EZ.

In both simulations there is down gradient eddy transfer of water vapour from the top of the entrainment zone towards it base. The eddy flux dries the upper part of the EZ, whilst moistening the lower part where the loss due to condensation is greatest. In the Solomon *et al.* (2011) simulation, mean and turbulent horizontal advective source of water vapour also moisten the EZ with the net effect of the water vapour tendency being positive in the region of EZ below the cloud top. In the ls2g150m simulation the advective sources of moisture are parametrized by a large scale forcing of water vapour. The net effect of the large scale forcing is to moisten the EZ and the region of inversion layer above (up to an average of around 70 m higher than z_{ct}). Below the cloud top the contribution from the large scale forcing is too small to offset the net water vapour sink from condensation and there is a negative water vapour tendency, while above the cloud top the forcing leads to a positive water vapour tendency.

6.3.4 Comparison of 2D and 3D simulations

To test the sensitivity of the control setup to the dimensionality of the model domain, two 3D simulations were also made. control_3D and ls2g150m_3D were ran using the exact specifications of the control_N$_{in}$x2 and ls2g150m simulations except that they included a second horizontal dimension (Table 6.1). The spin-up of the 3D simulations mirrors that found in the 2D runs with TKE increasing rapidly over the first ten minutes before gradually increasing to a quasi-stable value after fours hours (Figure 6.32).

After spin-up, the magnitude of the integrated TKE is only around a third of that found in the 2D simulations with a mean value of 0.051 m^3 s^2 in the control_3D run and 0.038 m^3 s^2 in the ls2g150m_3D run. Stronger turbulence is a characteristic of 2D simulations (Moeng *et al.*, 1996), however the reduction in integrated TKE of a quarter between the two 3D simulations is consistent with that found in 2D and so gives confidence that the change in the cloud dynamics as the cloud encroaches into the inversion is retained. The mean encroachment depths simulated in the 3D run were almost equal to the 2D values with the domain maximum cloud top situated 47 m above z_{ib} in the control_3D run and 65 m above z_{ib} in the ls2g150m_3D run. Compared to ls2g150m, there was less variability in the cloud top height in the ls2g150m_3D simulation and the layer average value was at around 60 m, which is 10 m higher than in 2D.

Domain average maximum and minimum vertical velocities are reduced in the 3D simulations, dropping to -1.76 m s^{-1} and 1.41 m s^{-1} respectively in the control_3D simulation and -1.41 m s^{-1} and 1.31 m s^{-1} respectively in the ls2g150m simulation. Weaker turbulence in the 3D simulation leads to a reduction in w_e, with the mean value of 0.16 cm s^{-1} less than half that simulated in the control_N$_{in}$x2 run. In the ls2g150m_3D simulation the reduction is less significant, with the mean w_e equal to 0.4 cm s^{-1} which is only 10 % less than simulated in the ls2g150m simulation. The difference in the reduction of the entrainment velocity between the two setups demonstrates that in simulations where the cloud top encroaches into the inversion, z_{ib} is not solely dependent on the intensity of the turbulence. Between the 2D and 3D simulations there is a significant increase in the net amount of condensate and a redistribution of water between the warm and cold phases. In both 3D simulations the mean LWP is around a third greater and the mean IWP a third less than in the 3D run. Overall much less variability of the domain average properties was found in the 3D simulations than in 2D (Grabowski *et al.*, 1998).

A comparison of the time-averaged 2D and 3D θ_e and q_l profiles which are normalised in height so that the cloud top is equal to one and the surface zero is shown in Figure 6.33, while profiles of the TKE, and vertical heat and total moisture fluxes normalised equivalently are shown in Figure 6.34. The peak LWC is greater in the 3D simulations and the liquid cloud fills a greater depth of the BL. Overall the mean depth of the liquid layer

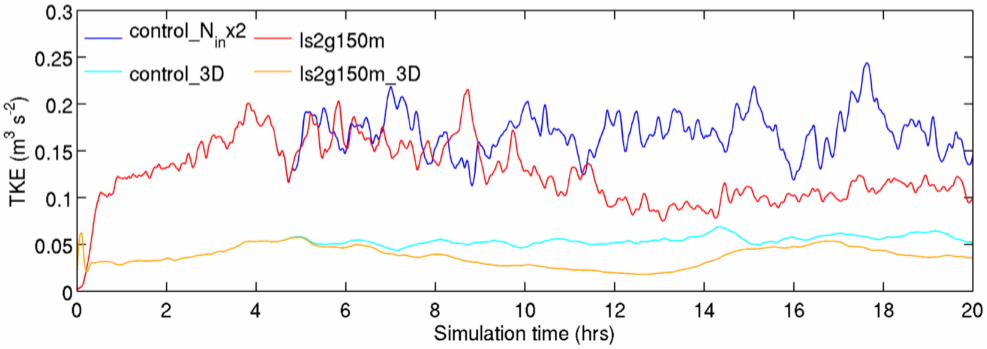

Figure 6.32: Comparison of timeseries of instantaneous integrated sub-grid + resolved TKE in the control_N$_{in}$x2 and control_3D simulations.

is a 575 m in the control_3D simulation and 729 m in the ls2g150m simulation, meaning depths increased by more than 100 m and 200 m respectively over the 2D simulations. In the control_3D run the greater liquid water contents near cloud top leads to a larger peak in the radiative cooling which drives stronger eddy heat and moisture fluxes. While in the ls2g150m and ls2g150m_3D simulations the peak in the radiative cooling and in the eddy heat flux is of an equal magnitude. Despite the increase in the magnitude of $\overline{w'\theta'}'$ in the control_3D simulation the net TKE profile is smaller throughout the BL than in the 2D run. Near cloud top the negative eddy flux associated with entrainment is reduced in the 3D simulations suggesting that dynamics in stably stratified regions are handled differently in the 2D and 3D models. Entrainment has the effect of drawing warm air down into the ML and its reduction in the 3D simulations, coupled with greater longwave cooling causes the temperature in the mixed layer to fall.

Despite the change to the magnitude and shape of the eddy flux profiles, the heat budget in the ls2g150m and ls2g150m_3D simulations are similar with longwave radiative cooling peaking in the EZ where it is partially offset by condensational heating, and in the lower part of the EZ eddy transfer of heat; with an overall effect of a net cooling throughout entrainment zone. The moisture budgets are also equivalent in the 2D and 3D simulations with net source of liquid water in the EZ, and a net loss of water vapour in the EZ and source in the region of the inversion layer above. Overall there is a noticeable difference in the eddy structure of the 2D and 3D simulations and a significant change to the domain integrated water contents and TKE. However, despite the differences, the cloud structure and simulation of cloud top encroachment inside the inversion is relatively consistent.

The differences between the 2D and 3D simulations are significant enough that 3D simulations would be preferable on physical terms. However the total length of time need to run the 3D simulation over 160 processors was more than three weeks for a 20 hour

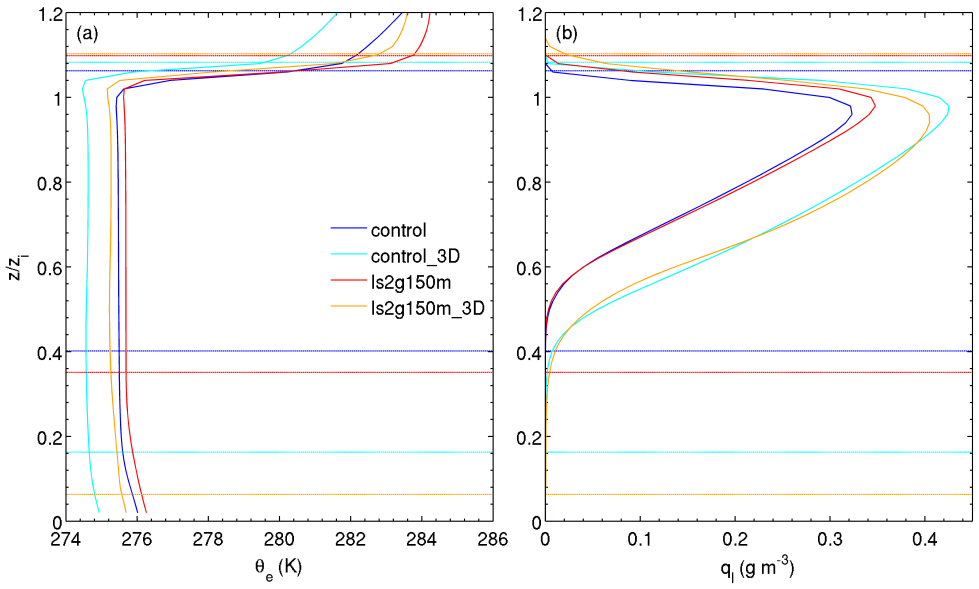

Figure 6.33: Comparison of the control_N$_{in}$x2 and control_3D simulations. Profiles of the time-averaged (a) θ_e and (b) q_l normalised so liquid cloud top is equal to one and the surface zero. The black horizontal line marks the cloud top and coloured horizontal lines the cloud bases.

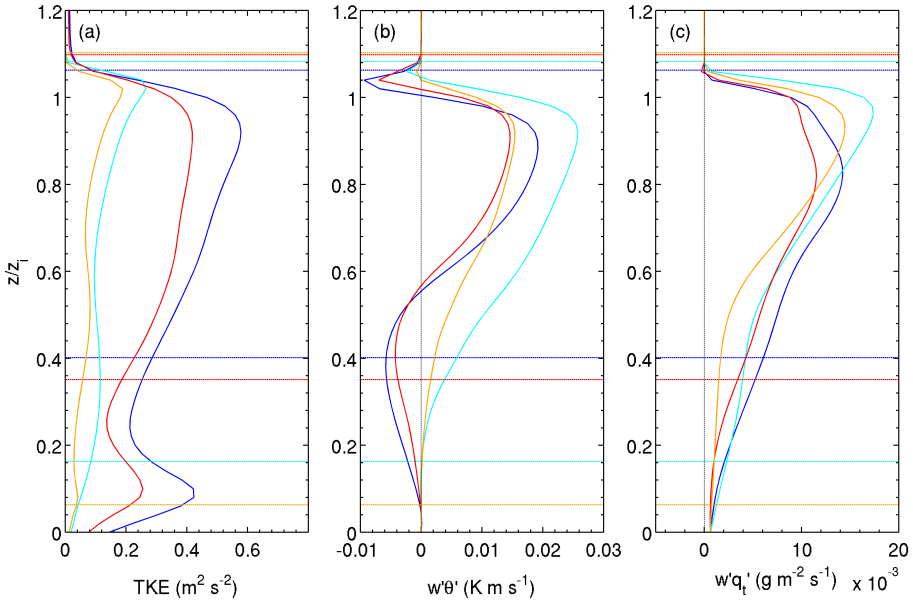

Figure 6.34: Comparison of the control_N$_{in}$x2 and control_3D simulations. Profiles of the time-averaged (a) TKE, (b) $\overline{w'\theta'}$ and (c) $\overline{w'q_t}$ normalised so liquid cloud top is equal to one and the surface zero. The black horizontal line marks the cloud top and coloured horizontal lines the cloud bases.

model integration at the specified resolution. This compares to two day running length for the equivalent 2D simulation when ran on a single processor. For this reason, the simulations in this study are primarily made in two dimensions.

6.4 Summary and conclusions

In this chapter a mixed-phase Arctic stratocumulus observed on 27th August 2008 during the ASCOS field campaign was simulated using the Met Office LEM. Observations of cloud and thermodynamic fields showed a well-mixed Arctic stratocumulus topped BL, which was capped by an inversion in both temperature and specific humidity. As observed in similar Arctic stratocumulus in the presence of the specific humidity inversion (Sedlar *et al.*, 2012), the cloud top was found to extend into the inversion by as much as 400 m over the observation period (Figure 5.15). Until very recently there has been little effort to understand the physical mechanisms which control cloud encroachment into the inversion, however from modelling a mixed-phase Arctic stratocumulus observed over the Beaufort sea, Solomon *et al.* (2011) found that inversion layer cloud could be supported in the presence of a humidity inversion, as long as a source of inversion layer moisture - such as horizontal advection of water vapour (Curry *et al.*, 1997; Pinto, 1998) - was present to replenish the liquid and ice which is lost from sedimentation (Solomon *et al.*, 2011).

To examine the physical processes which support the extension of cloud top in the inversion, and understand how it influences the development of the BL, a number of two-dimension large eddy simulations were made in this chapter. The control_N$_{in}$x2 simulation was setup using idealised profiles of θ_l and q_t, with profile shapes similar to that expected in a sub-tropical STBL; well-mixed until cloud top height with θ_l rising rapidly above and q_t dropping off. The simulation omitted any large scale sources of water vapour, however despite the lack of moisture sources above the base of the inversion, the layer maximum cloud top was found over 47 m inside the EZ - which was coincident to the height that the minimum $\overline{w'\theta_v'}$ was found. The layer average cloud top was found to be at 29 m above z_{ib}. The extension of cloud into the inversion layer initially occurred because the drop in the total water mixing ratio at the model initialisation was gradual enough that a specific humidity inversion formed after the initial condensation in the model. The persistence of the cloud in the inversion was supported by radiative-dynamical-microphysical mechanisms within the cloud.

The cloud was mixed-phase and persistent with a steady LWP and cloud depth. Though mixed phase, the ice mass concentration of the cloud was relatively small, and while it rose steadily over the simulation the cloud didn't glaciate to an ice-only cloud, as other models have simulated (Harrington *et al.*, 1999; Luo *et al.*, 2008a; Morrison *et al.*,

2003). The vertical layering of the cloud was typical for that found in mixed-phase Arctic stratocumulus with a shallow layer of liquid near the cloud top precipitating ice through the cloud below through the sub-cloud layer down to the surface (Shupe *et al.*, 2008). As indicated by Morrison *et al.* (2012), this may have contributed to the persistence of the liquid water. As is typical for both sub-tropical marine Arctic stratocumulus and mixed-phase Arctic stratocumulus, instability generated from radiative cooling was found to be the most significant source of turbulence (e.g.Lilly (1968) and Moeng *et al.* (1996) for marine stratocumulus and Jiang *et al.* (2000) and Luo *et al.* (2008b) for Arctic stratocumulus).

Buoyancy generated from radiative cooling was found to create strong downdraughts in the cloud and narrow updraughts in which condensation occurred. Nucleation and deposition were found to be the largest sources of ice mass, and although sublimation in the sub-cloud layer returned some water vapour back to the atmosphere, the constant precipitation of ice made the BL a net sink of water vapour. However, the drying of the atmosphere wasn't significant enough that liquid water content fell below the amount needed for strong radiative cooling, buoyancy generation and further condensation. Thus the water contents were stable.

The lower part of the entrainment zone/inversion layer was saturated and an analysis of the cloud water content budgets showed that liquid water which overshot the base of the temperature inversion didn't evaporate in this region. Condensation and eddy transport maintained cloud in the lower EZ despite the constant fallout of water droplets to the mixed-layer, and while condensation-sedimentation lead to the lower EZ being a net sink for water vapour, down gradient transport of water vapour from the top of the humidity inversion to its base replenished the water vapour mass. The vertical distribution of condensation supported the humidity inversion structure, thus the humidity inversion with cloud extending into it was self sustaining. However in the absence of moisture advection to the inversion layer it would be expected that the inversion would dry out too much to support cloud top encroachment and the specific humidity inversion would be removed. An analysis of the heat budget showed that the peak radiative cooling was coincident with z_{ib}, which agreed with radiative heating/cooling profiles of an idealised inversion-encroaching cloud as determined by Sedlar *et al.* (2012), however the peak in the net cooling was positioned higher in the cloud because of eddy transport and condensational heating near the inversion. This meant that cooling didn't lead to an adjustment of the temperature inversion boundaries, which would have lead to cloud top being readjusted so it was coincident with the inversion.

Next the control_dry simulation was made to examine what effect a reduction of the initial water vapour mass at cloud top would have on cloud top encroachment into the inversion. In this simulation the initial profile of q_t was made much drier above z_{ib}. Despite the

inversion layer being much drier, the layer maximum cloud top was still found to encroach into the inversion by around 40 m, however the variability in the spatial cloud top height was much larger and the layer mean cloud top height was only around 20 m above the inversion base. As in the control_N_{in}x2 simulation the peak longwave radiative cooling coincided with the inversion base, but the peak cooling occurred higher in the cloud.

The gradual transition from the mixed layer to the inversion was found to be the reason the cloud encroachment was supported. This result is surprising as the top of a stratocumulus cloud is usually assumed to be coincident with the base of the temperature inversion (e.g. Paluch & Lenschow, 1991; Stevens *et al.*, 2007; Tjernstrom & Rune, 2003). The control_dry simulation suggests that even in the absence of a humidity inversion, stratocumulus clouds may encroach inside the inversion a significant depth so long as the temperature increase and/or moisture loss across the inversion isn't too sharp, i.e. the relative humidity loss isn't too large. Because the relative humidity depends on the absolute temperature and specific humidity, it would be expected that the encroachment would happen more readily in the Arctic where the low temperature means that saturation is reached at a lower water vapour contents. Cloud microphysical parameters; droplet number and size, effective radius - may also affect the encroachment depth because of their impact on microphysical process rates and the clouds optical depth.

A further simulation was made using the same initial conditions as the control_N_{in}x2 simulation, except that after the model spin-up a source of water vapour was prescribed to act on the domain in a 150 m deep region above the inversion base. The time development of the ls2g150m simulation, saw the layer maximum cloud top rise more than 90 m into the inversion layer with the time-averaged layer mean cloud top found at over 54 m above z_{ib}. While the profile shapes of the θ, water content and TKE budgets were found to be generally consistent to those modelled in the control_N_{in}x2 simulation, the increase of the liquid water content inside the EZ lead to a greater proportion of the longwave radiative cooling occurring in the stability stratified EZ, reducing the depth over which instability could be incited from longwave radiative cooling. Consequently a reduction in the magnitude of $\overline{w'\theta'_v}$ was found which led to a drop of around a third in the intensity of boundary layer turbulence. Although Sedlar *et al.* (2012) predicted that an increase in the mass of liquid water inside the inversion would cause the depth over which radiative cooling occurs to increase, in their radiative transfer calculation the peak radiative cooling was always coincident with z_{ib}. Although their model only considered radiative transfer, the distribution of radiative cooling they predict as cloud top encroaches into the inversion would not impact on instability generation as instability is only incited where the divergence of the cooling is negative (below the peak cooling). Thus the turbulence reduction in the ls2g150m simulation is in contradiction to their result.

A comparison the ls2g150m simulation with the results of Solomon *et al.* (2011), showed that the idealised setup used in this experiment reproduces the physical mechanisms which Solomon *et al.* (2011) demonstrated to be important in supporting cloud inside the inversion layer. However in the ls2g150m simulation the source of inversion layer moisture was found to increase the water vapour tendency above the cloud only, whereas in the Solomon *et al.* (2011) simulation, a vertical flux of water vapour resulting from advection of water vapour by the mean wind and a horizontal flux of water vapour by the mean wind increased the water vapour throughout the EZ.

A comparison of both the control_N_{in}x2 and ls2g150m simulations with equivalent 3D runs showed differences in the profiles of the TKE and the heat and moisture fluxes through the cloud, and a change in the dynamics resulted in clouds which were deeper, had larger LWP's and smaller IWP's and in the case of the control_N_{in}x2 simulation, much weaker subsidence. Despite the differences between the two and three dimensional simulations, in both cases cloud top were found to extend a similar height into the inversion layer and in both 2D and 3D there was a reduction in the integrated TKE as this height was extended.

Overall the simulations made in this chapter demonstrate the sensitivity of mixed-phase Arctic stratocumulus to the distribution of humidity and temperature in the lower Arctic atmosphere. Cloud top was found able to encroach into the inversion in a number of situations; in the presence of a humidity inversion or a dry entrainment zone, with or without moisture advection above the inversion. And these results represent a departure from the previous assumption of two distinct states of the cloud top-inversion interface; a cloud capped by a temperature inversion, and a cloud encroaching into the temperature inversion.

The aim of this chapter is to understand the mechanisms which control the encroachment of cloud into the temperature inversion and characterize the features which distinguish them from sub-tropical marine stratocumulus. Simulations made in this chapter show that the assumption that sub-tropical stratocumulus (or at least clouds with a similar morphology) always have cloud top coincident with the base of the inversion is not necessarily correct. The simulation of shallow, though not insignificant encroachment of cloud into a dry humidity inversion is a new result, however a detailed examination of the cloud-inversion interface under more typical sub-tropical conditions is needed to understand the magnitude of encroachment in these clouds. Even if a small amount of inversion encroachment is determined to occur frequently at the top sub-tropical stratocumulus, results in this chapter have shown that the effect on BL development is likely to be very small as the distribution of cloud top cooling; and therefore the dynamics of the cloud, is similar to that found in a proto-typical stratocumulus layer. Therefore the assumption that cloud top is coincident with base of the inversion in sub-tropical stratocumulus may

be untrue, but it is likely this has little impact on parameterizations of these clouds.

The mechanisms which control encroachment into the dry inversion were described in this chapter and found to be different to that under conditions where a specific humidity inversion is present. The processes which lead to the maintenance of cloud inside the inversion in this situation was generally shown to be in a agreement with those found by Solomon *et al.* (2011). And while this supports the modelling approach used in this study, simulations made in this chapter and in Solomon *et al.* (2011) are of only very shallow encroachment and it is unclear whether the physics of the system is the same at the larger encroachment depth found in observations.

A significant result of this chapter and a major step in understanding the encroachment is the finding that even relatively modest encroachment can lead to a change in the amount of BL turbulence. This effect is important as cloud-driven turbulence is the largest source of vertical mixing within the central Arctic. As discussed in Section 2.3.3, the Arctic is a CCN-limited environment and so the rate of vertical mixing of aerosol from the surface and/or free troposphere is important to the both the persistence of cloud, its phase and microphysical properties. The finding that encroachment leads to a reduction in the BL turbulence budget is so far the only significant feedback which has been determined from clouds encroaching into the temperature inversion and highlights the need for cloud-inversion encroachment to be represented in parameterizations of Arctic cloud.

Chapter 7

Sensitivity of cloud encroachment to water vapour forcing

In Chapter 6, simulations made using an LES model were used to understand the physical mechanisms which allow mixed-phase Arctic stratocumulus to extend into the Arctic temperature inversion. Using observations from the ASCOS field campaign, a modelling setup was specified for the simulations which both reproduced the general meteorological properties of the case study, whilst also remaining idealised enough for the physical mechanisms of cloud-inversion encroachment to be analysed without unnecessary reference to the specific meteorological state. Whilst the simulations made in Chapter 6 were able to model cloud top encroachment into the Arctic inversion, the depth of encroachment was relatively shallow compared to that measured by a range of observations presented in Chapters 2 and 5.

Although results showed cloud encroachment into the inversion even in the absence of a specific humidity inversion, the greatest encroachment was found where a humidity inversion was maintained by large scale advection of water vapour. In the ls2g150m simulation the advective forcing of water vapour was informed by the Solomon *et al.* (2011) modelling study of an Arctic stratocumulus observed during the ISDAC field campaign as described in Section 2.3.4, while in reality moisture advection into the Arctic depends on the synoptic scale dynamics and can vary considerably (e.g. Pinto, 1998). Due to the importance of the advective moisture source in forming the humidity inversion, and its influence on encroachment in the ls2g150m simulation, it is reasonable to expect that a change to the specification of the water vapour advection would impact on the encroachment depth. Therefore in this chapter simulations are made which test the sensitivity of the modelled encroachment to the large scale forcing.

Table 7.1: Description of simulations made to investigate the sensitivity of encroachment to water vapour forcing. Setup parameters described in Section 6.1.

Simulation	Domain	q_{bl} (g kg^{-1})	q_{inv} (g kg^{-1})	N_{in} (L^{-1})	$(\partial q_v/\partial t)_{LS}$ (g kg^{-1} day^{-1})	$(\Delta z)_{LS}$ (m)
control_N_{in}x2	2D	2.67	1.00	3.4	-	-
ls2g050m	2D	2.78	1.00	3.4	2.0	50
ls2g100m	2D	2.78	1.00	3.4	2.0	100
ls2g150m	2D	2.78	1.00	3.4	2.0	150
ls2g200m	2D	2.78	1.00	3.4	2.0	200
ls3g050m	2D	2.78	1.00	3.4	3.0	50
ls3g100m	2D	2.78	1.00	3.4	3.0	100
ls3g150m	2D	2.78	1.00	3.4	3.0	150
ls3g200m	2D	2.78	1.00	3.4	3.0	200
ls4g050m	2D	2.78	1.00	3.4	4.0	50
ls4g100m	2D	2.78	1.00	3.4	4.0	100
ls4g150m	2D	2.78	1.00	3.4	4.0	150
ls4g200m	2D	2.78	1.00	3.4	4.0	200

7.1 Initial setup and simulation design

In total 11 new simulations are made in this chapter. These are used in addition to the control_N_{in}x2 and ls2g150m simulations to understand how the specification of the large scale water vapour forcing impacts on the cloud encroachment into the inversion layer; and how this feedbacks on the cloud and the BL dynamics.

Details of all the simulations undertaken in this chapter are given in Table 7.1. Each of the forced simulations is based on the setup used in the control_N_{in}x2 simulation, except that a large scale forcing is applied to the model above the inversion base. The forcing specification is as described for the ls2g150m simulation except that two properties of the forcing are varied: the rate of forcing and the depth over which the forcing is applied. A combination of three forcing rates: 2, 3 and 4 g kg^{-1} day^{-1}; and four forcing depths: 50, 100, 150 and 200 m are used in the range of simulations. Once again the Brooks (2003) algorithm is used to find the base of the inversion; which is used as the height at which forcing is applied above. As in the previous chapter, simulations are made in two dimensions to reduce the computation constraint. The purpose of the simulations made here is not to recreate the case study exactly rather to use the observations as a guide for the analysis.

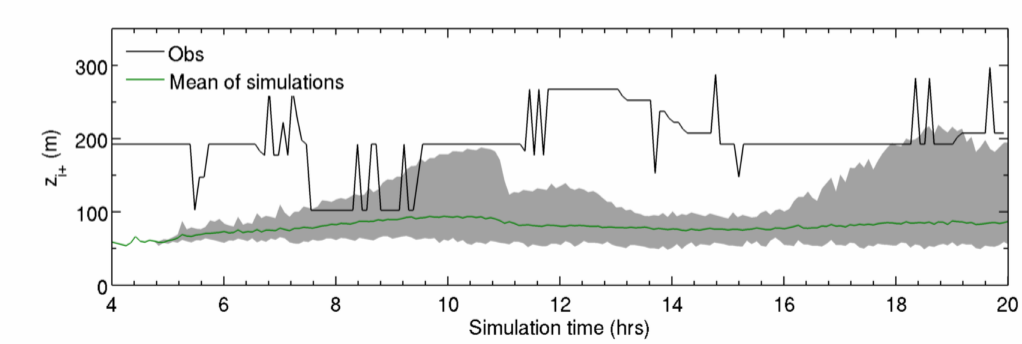

Figure 7.1: Forcing simulations. Timeseries of z_{i+}. Green line is the mean and grey-shaded area denotes the range.

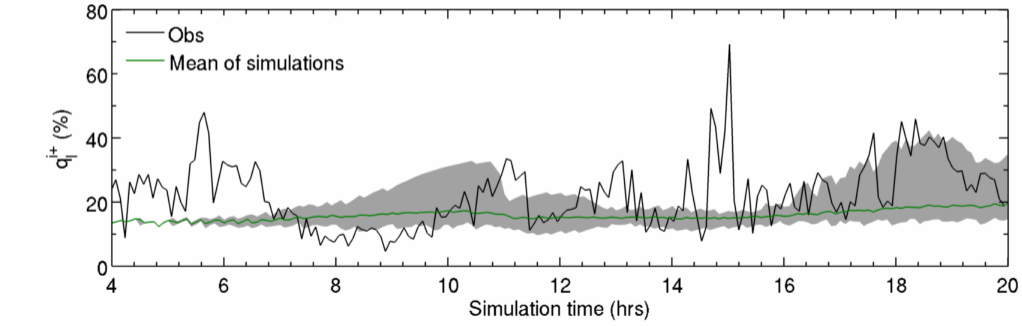

Figure 7.2: Forcing simulations. Timeseries of q_l^{i+}. Green line is the mean and grey-shaded area denotes the range.

7.2 Sensitivity to the q_t inversion strength

7.2.1 Time development of the forcing simulations

As for the ls2g150m simulation, the spin-up of all the forcing simulations is marked by a rise in integrated TKE, a slight deepening of the liquid cloud layer and almost a doubling of the LWP. The setup of each of these simulations is consistent with the control_N$_{in}$x2 run except for the water vapour forcing which is only activated after four hours; therefore as in the control_N$_{in}$x2 simulation the initial specification of q_v is an increase at the base of the temperature inversion (Figure 6.12 (a)). Consequently, over the first four hours the cloud encroaches into the inversion by around 50 m through the mechanisms described in Sections 6.2.3.2 and 6.2.3.4.

After four hours of simulation time the water vapour forcing is switched on and begins to raise the humidity of the sub-saturated region of the inversion layer. The differential forcing rate means that the inversion layer is brought to saturation in the forcing simula-

Table 7.2: Comparison of the time-averaged cloud-inversion layer statistics (4 - 20 hours) of the forcing simulations. $\overline{z_{ct}}$ is the layer average cloud top, while z_{ct} is the layer maximum cloud top.

Data	$\overline{z_{ct}} - z_{ib}$ (m)		$z_{ct} - z_{ib}$ (m)		$\int_{z_{cb}}^{z_{ib}}(LWC)dz$ (gm^{-2})		q_l^{i+} $(\%)$	
	μ	max	μ	max	μ	max	μ	max
Observations	-	-	190	288	15.14	35.21	24.4	69.2
control_N_{in}x2	29	33	47	67	6.88	9.57	10.0	12.5
ls2g050m	41	44	59	74	9.74	11.55	13.5	15.6
ls2g100m	48	52	67	83	10.97	12.75	14.6	17.0
ls2g150m	54	66	74	91	11.88	14.23	15.4	17.7
ls2g200m	60	80	79	101	12.38	15.62	15.6	19.0
ls3g050m	46	48	66	88	10.71	12.47	14.1	17.2
ls3g100m	57	68	75	93	12.56	14.81	15.6	18.4
ls3g150m	65	87	83	111	13.43	17.93	16.0	19.9
ls3g200m	74	120	91	139	15.07	24.65	16.5	27.6
ls4g050m	50	54	68	84	11.60	13.30	15.1	17.4
ls4g100m	63	79	80	101	13.67	17.24	16.2	19.7
ls4g150m	78	116	96	133	16.04	26.31	16.6	27.2
ls4g200m	102	197	121	219	22.67	49.27	21.5	42.4

tions with 4 g kg^{-1} day^{-1} most quickly. This begins after five hours. Over the next few hours, the cloud top begins to encroach further into the inversion (Figure 7.1) and the fraction of the cloud inside the inversion rises steadily in each of the simulations (Figure 7.2).

Time-averaged (4 - 20 hours) cloud-inversion statistics are shown in Table 7.2. The time-averaged encroachment depth and both the absolute and relative mass inside the inversion, increase by both a greater forcing rate at a fixed depth; or a greater forcing depth at fixed rate. Therefore the smallest encroachment occurs in the ls2g050m simulation - this has both the weakest forcing rate and shallowest region over which the water vapour is added. Whilst the greatest encroachment is found in the ls4g200m simulation - this has the combination of the strongest forcing rate and the greatest depth over which water vapour is added.

The encroachment of cloud into the inversion in this simulation is considerable with cloud top extending a maximum of 219 m above z_{ib}, which equates to almost half the liquid mass of the cloud residing inside the inversion. However both the mean and maximum encroachment depths are around 70 m shorter than the respective observations for the comparable time-period. The mean and maximum integrated water contents are greater in the ls4g200m simulation than the observations, while the mean and maximum fractional liquid water cloud masses are less. Thus the real atmosphere exhibits

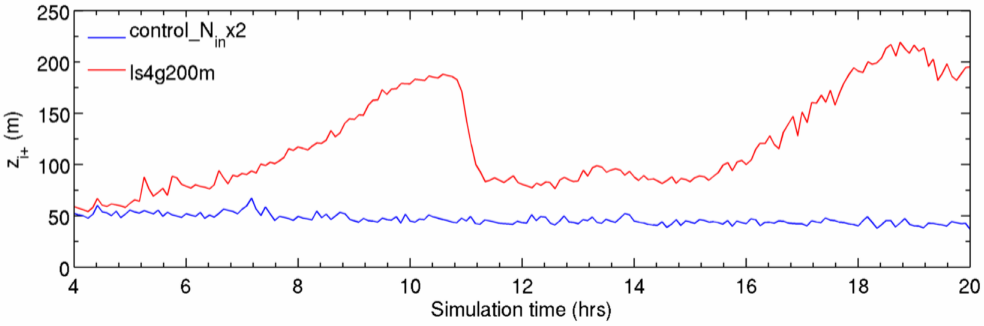

Figure 7.3: ls4g200m simulation. Timeseries of z_{i+}.

a much greater variability in the inversion layer cloud depth-mass relationship over the comparison period than is captured in the range of simulations.

In the majority of the simulations, z_{i+} is relatively constant through the averaging period, with the difference between the mean and the maximum less than 35 m. Thus the cloud encroachment into the inversion is quasi-stable. However the simulations which experience the greatest encroachment; ls3g200m, ls4g150m and the ls4g200m, have a much larger variability in the encroachment depth and the relative and absolute mass inside the inversion. In these simulations rather than the cloud top encroaching to a quasi-stable depth inside the inversion, z_{i+} has a marked temporal development. For the ls4g200m run this is illustrated in Figure 7.3.

In the ls3g200m, ls4g150m and ls4g200m simulations the z_{i+} initially increases as the cloud top encroaches further into the inversion, then z_{i+} is rapidly reduced as the inversion base rises to a height closer to the cloud top. After a period where z_{i+} is quasi-stable the cycle is repeated. Although none of the simulations capture the variability of the observations over the comparison period, the temporal cycle simulated in the ls4g200m simulation is consistent with the general development of the observations presented in Figures 5.16. However, as discussed in Section 5.1.3.3, the cycle in z_{i+} in the observations may only be an artefact of an interpolation of radiosonde temperatures which were used to determine the radiometer temperature; and hence the inversion boundaries.

As was presented for the ls2g150m simulation in the Section 6.3.1, each of the forcing simulations experiences a drop in integrated TKE relative to the control_N_{in}x2 simulation after the water vapour forcing is applied (Figure 7.4). However the scatter of the simulations is substantial, with integrated TKE simulated between a range of 0.02 - 0.22 m^3 s^{-2}. A subsequent rise in the LWP is also found in each of the simulations (Figure 7.5), while the affect of the forcing on the IWP is more complex (Figure 7.6).

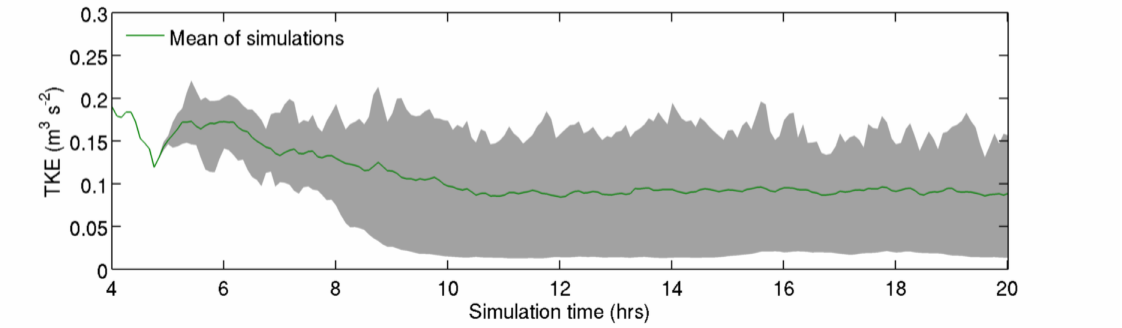

Figure 7.4: Forcing simulations. Timeseries of instantaneous integrated sub-grid + resolved TKE for the forcing simulations. Green line is the mean and grey-shaded area denotes the range.

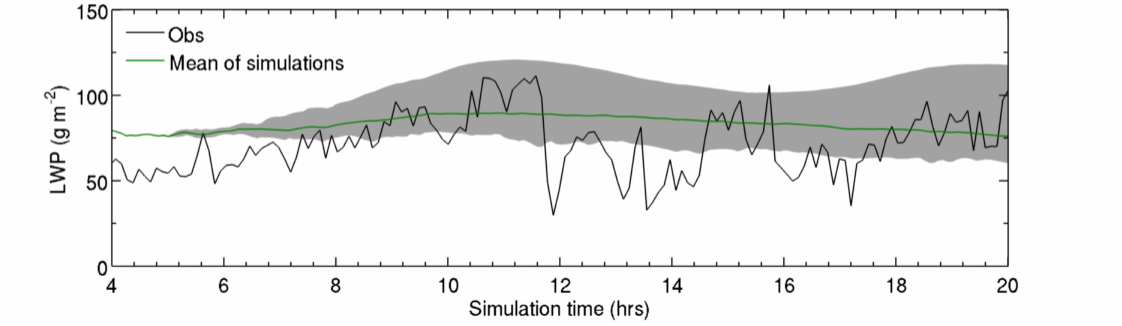

Figure 7.5: Forcing simulations. Timeseries of LWP for the forcing simulations. Green line is the mean and grey-shaded area denotes the range.

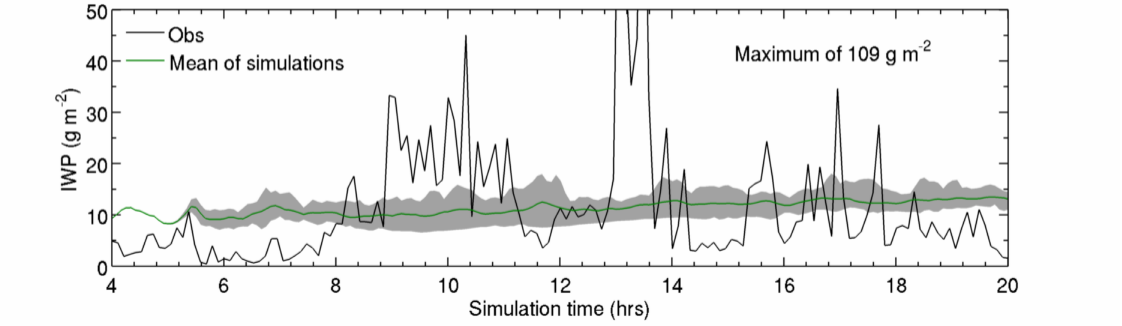

Figure 7.6: Forcing simulations. Timeseries of IWP for the forcing simulations. Green line is the mean and grey-shaded area denotes the range.

Table 7.3: As in Table 7.2 except for the time-averaged cloud water and dynamical statistics.

Data	$z_{ib} - z_{cb}$ (m)		$\int_{z_{cb}}^{z_{ib}}(LWC)dz$ (gm^{-2})		$z_{ib} - z_{cbi}$ (m)		$\int_{z_{cbi}}^{z_{ib}}(IWC)dz$ (gm^{-2})		TKE $(m^2\ s^{-3})$		w_{max} $(m\ s^{-1})$		w_{min} $(m\ s^{-1})$		w_e $(cm\ s^{-1})$	
	μ	σ	μ	σ	μ	σ	μ	σ	μ	σ	μ	σ	μ	σ	μ	σ
Observations	395	82	57.17	14.17	618	68	9.59	13.38	-	-	-	-	-	-	-	-
control_N_{in}x2	448	41	62.18	4.97	753	61	10.97	1.42	0.16	0.03	1.90	0.24	-2.33	0.25	0.37	0.02
ls2g050m	444	45	62.40	6.20	746	60	11.87	2.20	0.15	0.02	1.84	0.21	-2.28	0.25	0.36	0.02
ls2g100m	469	109	64.36	3.42	749	63	12.03	1.91	0.14	0.02	1.78	0.22	-2.22	0.24	0.38	0.02
ls2g150m	495	160	65.02	2.56	756	71	11.47	1.48	0.13	0.03	1.73	0.26	-2.14	0.27	0.42	0.02
ls2g200m	435	54	67.01	3.97	762	78	11.13	1.73	0.12	0.04	1.68	0.33	-2.02	0.40	0.46	0.01
ls3g050m	454	54	65.52	4.62	749	62	12.03	1.91	0.15	0.02	1.81	0.21	-2.26	0.24	0.37	0.02
ls3g100m	577	198	68.14	3.50	761	72	11.80	1.98	0.12	0.03	1.67	0.24	-2.09	0.27	0.43	0.01
ls3g150m	507	158	70.88	5.78	775	85	11.14	1.91	0.11	0.05	1.59	0.34	-1.90	0.44	0.49	0.01
ls3g200m	491	101	76.36	10.30	784	96	10.95	2.53	0.10	0.06	1.51	0.47	-1.78	0.60	0.50	0.05
ls4g050m	485	135	65.42	3.33	751	64	12.03	1.60	0.14	0.02	1.75	0.21	-2.19	0.25	0.39	0.02
ls4g100m	562	201	70.68	4.25	774	81	11.51	1.89	0.10	0.04	1.61	0.29	-1.93	0.36	0.47	0.01
ls4g150m	475	57	80.51	9.06	791	96	10.45	2.26	0.09	0.06	1.41	0.48	-1.65	0.64	0.51	0.09
ls4g200m	483	74	79.90	12.07	792	98	10.15	1.56	0.09	0.07	1.34	0.58	-1.57	0.75	0.49	0.16

Mean cloud water statistics for each of the forced simulations and the control_N_{in}x2 run are presented in Table 7.3. LWP increases with forcing depth and forcing rate, though for the majority of the simulations the change to the LWP is largely the result of the extra liquid water above z_{ib}, with mean integrated water contents in the BL mostly within 20 % of the mean value of the control_N_{in}x2 run. The only simulations where the mean integrated water content of the BL exceed this are the ls3g200m, ls4g150m and the ls4g200m simulations. These also experience the largest liquid mass increase inside the inversion. The relationship between the integrated mass of BL liquid water and the cloud depth is not straightforward and while these simulations have the largest integrated masses, their BL cloud depths are only 10 % greater than in the control_N_{in}x2 run. In contrast the ls3g100m simulation has a mean cloud depth below z_{ib} of 577 m (over 30 % greater) while the mass is only 68.14 g m^{-2} (10 % greater). The difference illustrates a change to the distribution of liquid water below the inversion base. The overall range in cloud depths - from base to top is between values of around 500 - 700 m.

In all of the simulations, less than 2 % of the cloud ice is found inside the inversion layer at any time during the simulation. The IWP has a negative relationship to the water vapour forcing, with values dropping as the forcing rate is increased and also as the forcing depth rises; except between the ls2g050m and ls2g100m simulations where the IWP rises slightly. Despite the drop as forcing increases, all of the simulations but the two with the largest encroachment (ls4g150m and ls4g200m) have mean IWPs which are greater than the control_N_{in}x2 run. The depth of the ice layer - which because of the very small IWC in the inversion layer is equivalent to the depth of the BL - also increases as the forcing depth and strength increase, and apart from a few simulations with weak forcing over a shallow depth, the values are greater than in the control_N_{in}x2 simulation. The combination of an increasing ice cloud depth and decreasing IWP demonstrates that in addition to a change to the LWC distribution, increased cloud-inversion encroachment must also lead to a change to the IWC distribution.

Comparing the BL cloud statistics to the observations, the simulated clouds are deeper and contain a greater mass of liquid water; and although the vertically averaged LWC is relatively close to the observations in the simulations with weak forcing, simulations with larger forcing have larger average LWCs. The ice layer are also deeper in the simulations and have a greater IWP. Mean dynamical quantities for the range of simulations are also shown in Table 7.3. The drop in TKE experienced with increasing encroachment is also found to be dependent on both the forcing depth and strength, as is a reduction in the magnitude of the mean upward and downward vertical velocities. The entrainment rate also generally increases as the forcing rate and strength are increased with the maximum mean value of 0.51 m s^{-1} simulated in the ls4g150m run. This value is almost 40 % greater than in the control_N_{in}x2 simulation.

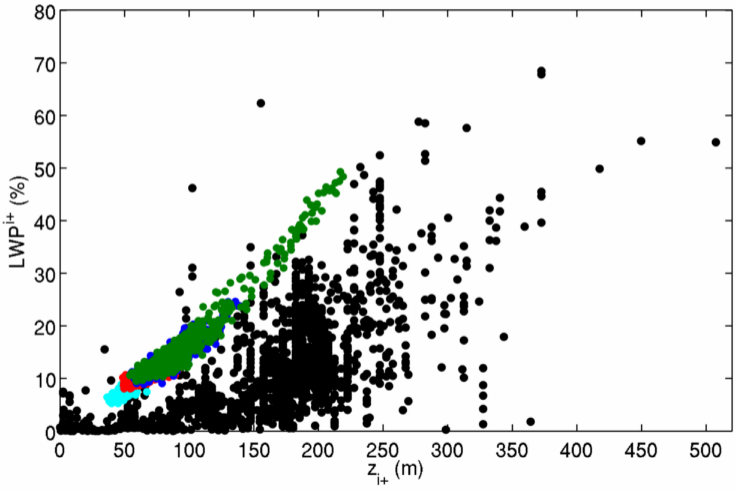

Figure 7.7: Forcing simulations. Comparison of z_{i+} against LWP^{i+} for the forcing simulations. Colours are used to differentiate between the $(\partial q_v/\partial t)_{LS}$ value applied in the simulation with red, blue and green colour representing simulations with a 2, 3 and 4 g kg^{-1} day^{-1} forcings respectively. The cyan markers are the values simulated in the control_N$_{in}$x2 simulation and black markers are the ASCOS measurements described in Section 5.1.3.3.

7.2.2 Relationship between cloud-inversion properties

In Section 5.1.3.3, the ASCOS dataset was analysed to determine whether any statistical relationships were apparent between the encroachment parameters. In this section, the LEM simulations made in this chapter will used in the same manner. Firstly the relationships determined in Section 5.1.3.3 will be tested to see how well the simulated encroachment statistics fit the ASCOS measurements.

Figure 7.7 shows the dependence of LWP^{i+} on z_{i+} for the range of simulations listed in Table 7.1 and from the ASCOS measurements. In Figure 7.7, colours are used to differentiate between the $(\partial q_v/\partial t)_{LS}$ value applied in the simulation with red, blue and green colour representing simulations with a 2, 3 and 4 g kg^{-1} day^{-1} forcings respectively. The cyan markers are the values simulated in the control_N$_{in}$x2 simulation and black markers are the ASCOS measurements. Simulations are 5 minute averages.

Across the simulations there is general increase in z_{i+} and LWP^{i+} as the large-scale water vapour forcing is decreased, and the largest scatter is found from the ls4g200m simulation. A clear dependence of LWP^{i+} on z_{i+} is found in the simulations and the linear correlation is high with the coefficient of determination, r^2 = 0.78. While this suggests that a large

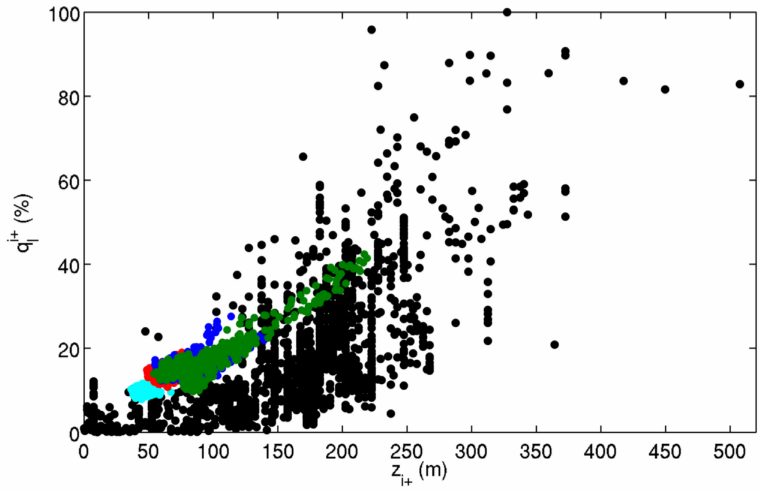

Figure 7.8: Forcing simulations. As for Figure 7.7 except for the z_{i+} against q_l^{i+}. Markers described in the caption of Figure 7.7.

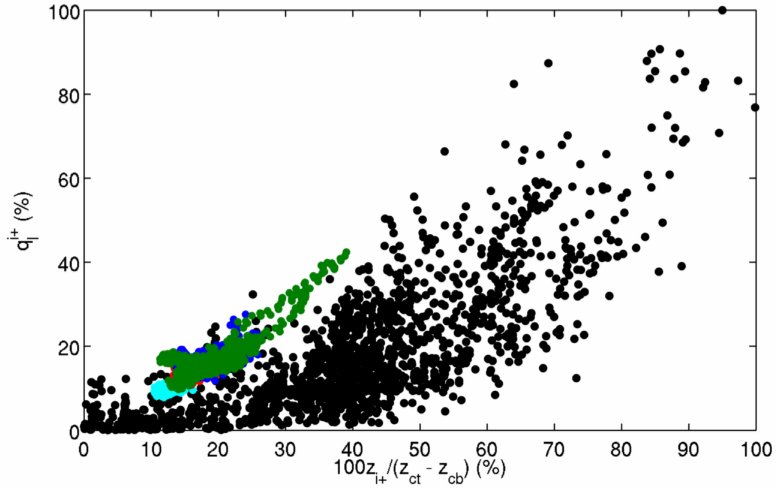

Figure 7.9: Forcing simulations. As for Figure 7.7 except for the $100^* z_{i+}/(z_{ct} - z_{cb})$ against q_l^{i+}. Markers described in the caption of Figure 7.7.

proportion of the variation of the LWP^{i+} is explained by its linear relationship to z_{i+} the non-linear functional relationship apparent in the ASCOS measurements suggests that the linear dependence of the simulated variables might break down at greater values of z_{i+}.

The scatter of the ASCOS observations is much larger than found in the simulations and simulations are grouped at an extremity of the measurements; with the simulated LWP^{i+} values greater than the measured values for a given z_{i+}. The larger scatter of the ASCOS measurements in Figure 7.7 is understandable, as the range of atmospheric conditions experienced during the ASCOS stratocumulus period was much higher than the conditions imposed on the LEM simulations. Model runs presented in this chapter have a varied magnitude of large-scale water vapour forcing into the inversion layer, and the depth over which the forcing was applied differs. However, although this created humidity inversions with different strengths and depths, which in turn resulted in changes to the cloud morphology, water paths and temperature inversion characteristics. The range of conditions experienced in the atmosphere isn't uniquely constrained by a simplistic water vapour forcing and the resulting atmospheric development caused by feedback of the cloud layer. In reality atmospheric dynamics and thermodynamics show a high spatial and temporal variability due to both synoptic scale development and local atmospheric processes.

The dependence of q_l^{i+} on z_{i+}, and q_l^{i+} on $100{*}z_{i+}/(z_{ct} - z_{cb})$ for the simulations and ASCOS measurements is shown Figures 7.8 and 7.9 respectively. As in Figure 7.7 the largest q_l^{i+} values are found in the simulations with the greatest large-scale water vapour forcing and the ls4g200m simulation has the largest scatter. The ASCOS observations again have a much greater scatter than the simulations, with simulations grouped at the upper extremity of the measured data points as in Figure 7.7. Although the linear correlation between simulated variables is also high for both the dependence of q_l^{i+} on z_{i+}, and q_l^{i+} on $100{*}z_{i+}/(z_{ct} - z_{cb})$, with $r^2 = 0.91$ and 0.73 respectively. The fit of the simulations to the ASCOS measurements is only approximate.

Despite the simulated dependencies between the encroachment variables not covering as wide a parameter space of the dependence's suggested by the observations, the shape of the dependence between the variables is relatively similar and the grouping of simulated dependencies within the limits of the measurements, gives confidence that encroachment regime simulated in the LEM bears some relation to that found in the real Arctic atmosphere. A better approximation for the dependence between these variables might found from completing more simulations in which model profiles, parameters and forcings were varied to cover a wider range of atmospheric conditions. If these simulations were be able to capture a greater portion of the variability found in the ASCOS dataset, this could be used to develop a parameterization of LWP^{i+} from z_{i+} which is applicable under a

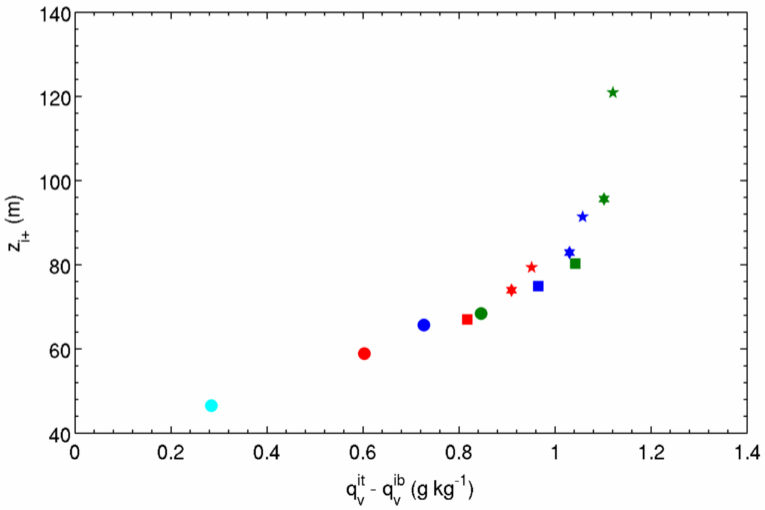

Figure 7.10: Forcing simulations. Comparison of the time-averaged humidity inversion strength, q_v^{it} - q_v^{ib} against LWP^{i+} for the forcing simulations. Colours and markers are used to differentiate between simulations with red, blue and green colour representing simulations with 2, 3 and 4 g kg^{-1} day^{-1} forcings respectively. While circle, square, six-pointed star and five-pointed star shaped markers are used to represent the simulations with forcing depths of 50, 100, 150, 200 m respectively, e.g. the green five-pointed star is the value from the ls4g200m simulation. The cyan circle is the value from the control_N$_{in}$x2 simulation.

variety of conditions. Unfortunately this was not possible to complete in this study.

In Section 5.1.3.3, it was suggested that the dependence of q_l^{i+} on 100*$z_{i+}/(z_{ct}-z_{cb})$ could be used to give an approximate estimate of LWP^{i+} if the dependence of z_{i+} on other atmospheric properties could be determined. Furthermore it was postulated that z_{i+} would likely have a dependence on the strength of the humidity inversion, q_v^{it} - q_v^{ib}, where q_v^{it} is the water vapour mixing ratio at the humidity inversion top and q_v^{ib} is the water vapour mixing ratio at the humidity inversion base. Figure 7.10 shows the dependence of the time-averaged q_v^{it} - q_v^{ib} on z_{i+} for the range of simulations. Although a strong non-linear dependence between the parameters is apparent, the fit of the simulations to the ASCOS data in Figures 7.7 - 7.9 suggests that the simulated dependence is only valid under restricted atmospheric conditions and the exact same dependence isn't likely to be found if the model was setup differently. Nevertheless such a relationship points the way for parameterization of the encroachment in the future.

In Chapter 6 it was shown than the encroachment of cloud into the inversion had a significant effect on the generation of TKE from cloud top radiative cooling in the ls2g150m simulation and that this caused a reduction in BL turbulence. This was demonstrated

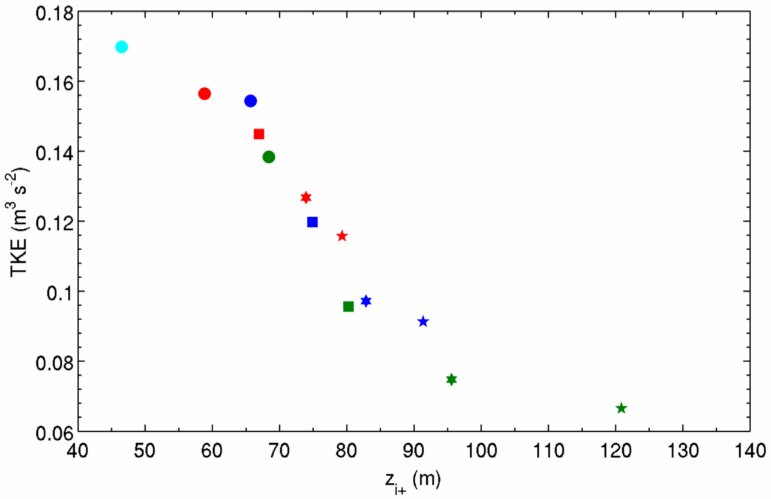

Figure 7.11: Forcing simulations. As for Figure 7.10 except for the time-averaged z_{i+} against the vertically integrated TKE. Markers described in the caption of Figure 7.10.

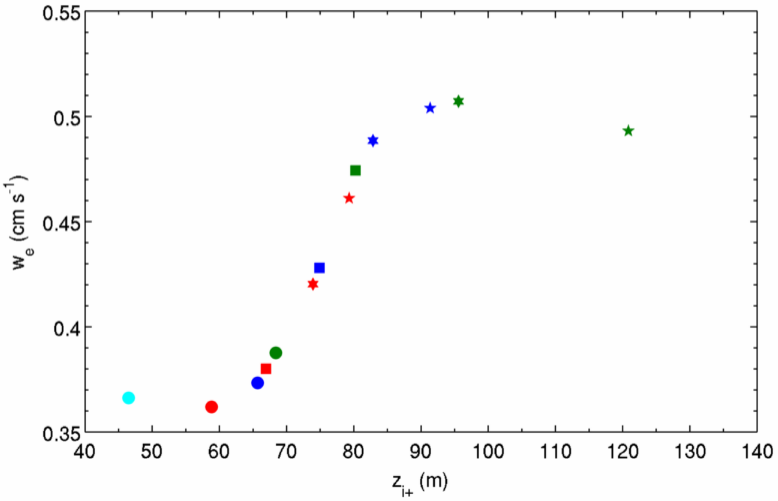

Figure 7.12: Forcing simulations. As for Figure 7.10 except for the time-averaged z_{i+} against w_e. Markers described in the caption of Figure 7.10.

under a number of simulations in Figure 7.6, with the integrated TKE falling to as low as 10 % of the value found in the control_dry run. To determine the relationship between the encroachment depth and the magnitude of atmospheric turbulence, Figure 7.11 shows the correlation between z_{i+} and the magnitude of the integrated TKE. As discussed in Section 7.2.1 strong negative dependence between the variables is evident. As the values plotted in Figure 7.11 are time-averages over the whole analysis period there is no scatter in the individual simulations. The relationship between the time-averaged variables is best described by a negative linear relationship with $r^2 = 0.88$. However, because the drop in TKE occurs from a reduction in buoyancy generation as the cloud extends into the strongly stable inversion (Section 6.3.2.4), it would be expected that the reduction in integrated TKE for a given increase in z_{i+} would eventually flatten out as the buoyancy generation is reduced to zero. This would suggest a non-linear relationship over a wider parameter space.

A reduction in BL turbulence would be expected lead to a fall in the entrainment velocity, w_e, with the weaker turbulent updraughts leading to less overshooting thermals entraining free tropospheric air into the BL. However a positive non-linear relationship between z_{i+} and w_e is found (Figure 7.12). At encroachment depths below 60 m or above 90 m, encroachment seems to have little effect on w_e, however between the depths of 60 and 90 m, w_e increases at an approximate rate of around 0.005 m s^{-1} for every extra meter of encroachment. w_e is calculated from Equation 6.3 in the LEM simulations, therefore Figure 7.12 actually shows the average change in z_i over time at different values of z_{i+}. This indicates that the strongest large-scale water vapour forcings applied in the simulations cause the greatest rise in the inversion base through the atmosphere, and suggests that w_e is an invalid measure of the entrainment rate where encroachment of cloud into the inversion occurs.

The relationship between z_{i+} and w_e as found through a usually correct approximation, shows the difficulty of relating simulated variables to their true atmospheric counterparts. Nevertheless, the high correlation between z_{i+} and the integrated TKE demonstrates the usefulness of the LEM simulations in determining dependencies between encroachment variables and atmospheric properties which are altered by the encroachment, and suggests that a parameterization of the effect encroachment has on the BL is possible.

7.2.3 Vertical distribution of water contents

The time-averaged vertical distribution of LWC for the range of forcing simulations, where the profiles are normalised in height so the cloud top is equal to one and cloud base is equal to zero is shown in Figure 7.13 (a). The greatest variability in the LWC is found above the inversion base, with the largest mean inversion layer LWC found in the

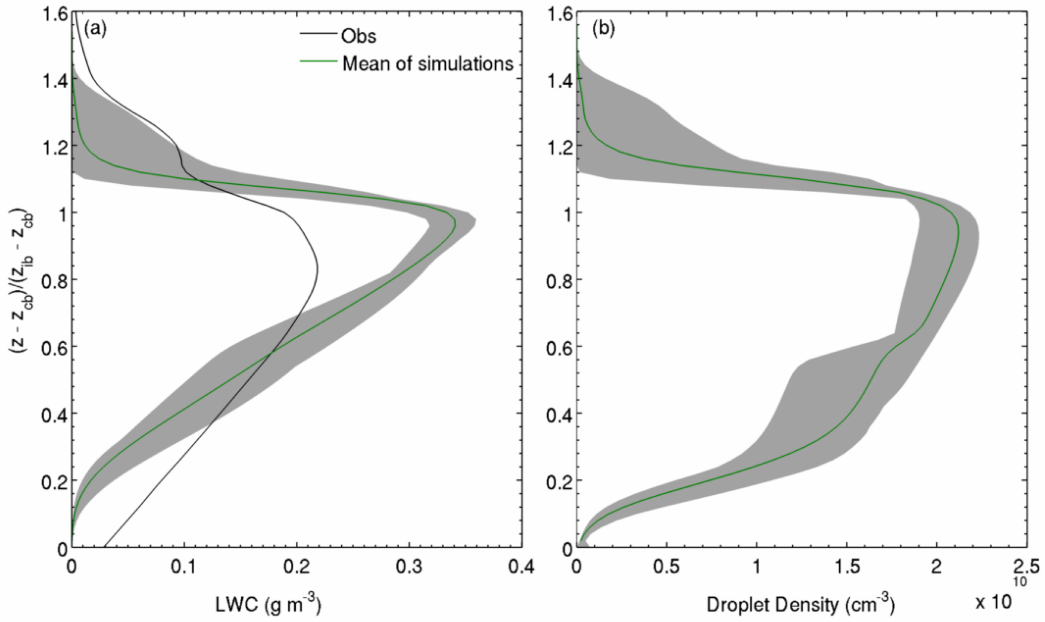

Figure 7.13: Profiles of time-averaged (4 - 20 hours) liquid cloud properties with height normalised so inversion base height is equal to one and cloud base zero. Green solid lines are the mean (a) LWC, and (b) droplet density of simulations. Grey-shaded area denotes the range of observations.

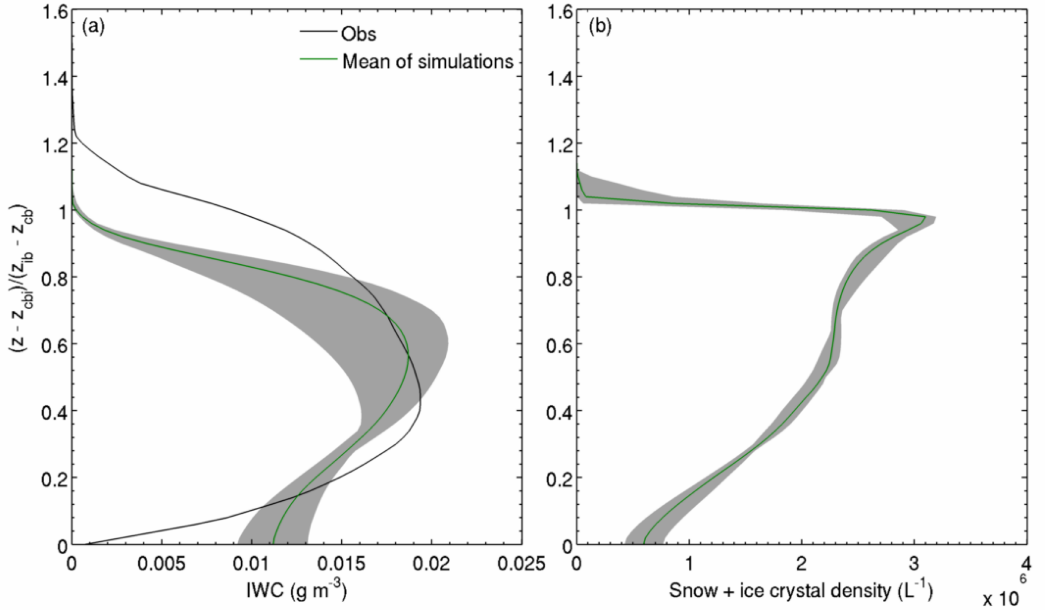

Figure 7.14: As for Figure 7.13 except for the (a) IWC, and (b) ice + snow crystal density. Profiles normalised by the inversion base and the ice cloud base.

ls4g200m simulation. The mean shape of the profile above z_{ib} in the ls4g200m simulation is relatively similar to that found in the observations. As described in Section 5.1.1.3 the vertical distribution of liquid water is difficult to assign properly from the retrievals made using the MMCR reflectivity; therefore the similarity, at least on a mean sense, supports the LWC determination.

In the majority of the simulations (all except the ls3g200m, ls4g150m and ls4g200m runs) the maximum LWC is below z_{ib} through the entire simulation - supporting the results of the Sedlar *et al.* (2012) analysis of vertical water content through profiles of inversion encroaching clouds. These runs simulated a cloud with a top which is always at a quasi-stable depth above the z_{ib}. Consequently the normalised vertical distribution of LWC doesn't change very much through the simulation. The vertical structure of LWC in each of these simulations is similar to the typical stratocumulus distribution with liquid water increasing through the cloud, and a roughly constant cloud droplet number with height is also simulated (Figure 7.13 (b)).

In the ls3g200m, ls4g150m and ls4g200m runs, the cloud growth into the inversion followed by readjustment of the inversion base leads to a temporal variation in the vertical structure of the cloud and the maximum LWC is sometimes determined to be above the inversion base. This is demonstrated in Figure 7.15 which shows vertical profiles of the LWC and temperature from the ls4g200m simulation at half hour intervals between 6 and 15.5 hours of simulation time. Growth of the liquid cloud inside the inversion initially proceeds slowly and with the peak LWC below the base of the inversion and the LWC dropping off linearly above z_{ib}. After 8.5 simulation hours condensation in the inversion layer is more significant and the vertical distribution of the LWC develops a less typical structure with a secondary maxima inside the inversion layer, then after ten hours the mass of the liquid inside the inversion begins to force a cooling of the layer. The LWC inside the inversion continues to rise until the peak is situated above z_{ib}. At this point the vertical distribution of the LWC is almost uniform through the main body of the cloud. By 15 hours the liquid water inside the inversion layer has cooled the inversion enough for the temperature to be well mixed up to the new height of peak LWC, thus z_{ib} has adjusted to the cloud. The LWC now increases linearly through the cloud.

The influence of the cloud-inversion development in the ls3g200m, ls4g150m and ls4g200m simulations is apparent in Figure 7.13 (a) through the variability of the LWC in the centre of the cloud (range of 0.06 g m^{-3}). The lower range of the LWC in Figure 7.13 (a) is the mean LWC profile from the ls4g200m simulation. The cloud-inversion development also leads to a reduction the cloud droplet number. In all of the simulations made in this chapter, condensation occurs in updraughts and evaporation in downdraughts with the layer average sum equal to a net condensation near the top of the cloud and evaporation through the rest of the cloud.

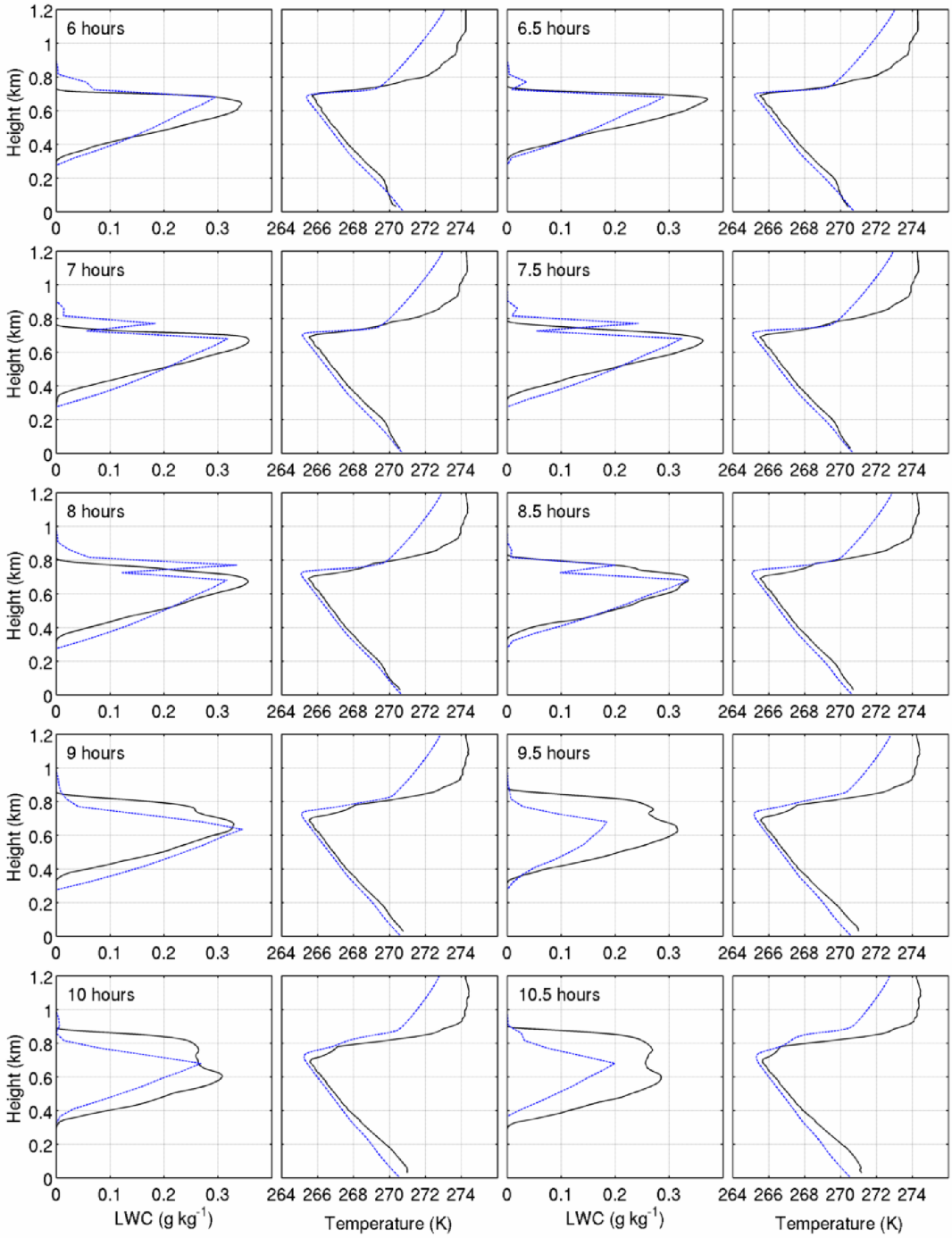

Figure 7.15: (a) ls4g200m simulation. Profiles of simulated 5-minute averaged LWC (blue dashed line) and temperature (solid blue line); and the MMCR reflectivity derived LWC (black dashed line) and radiometer temperature (solid black line). 6 - 10.5 simulation hours.

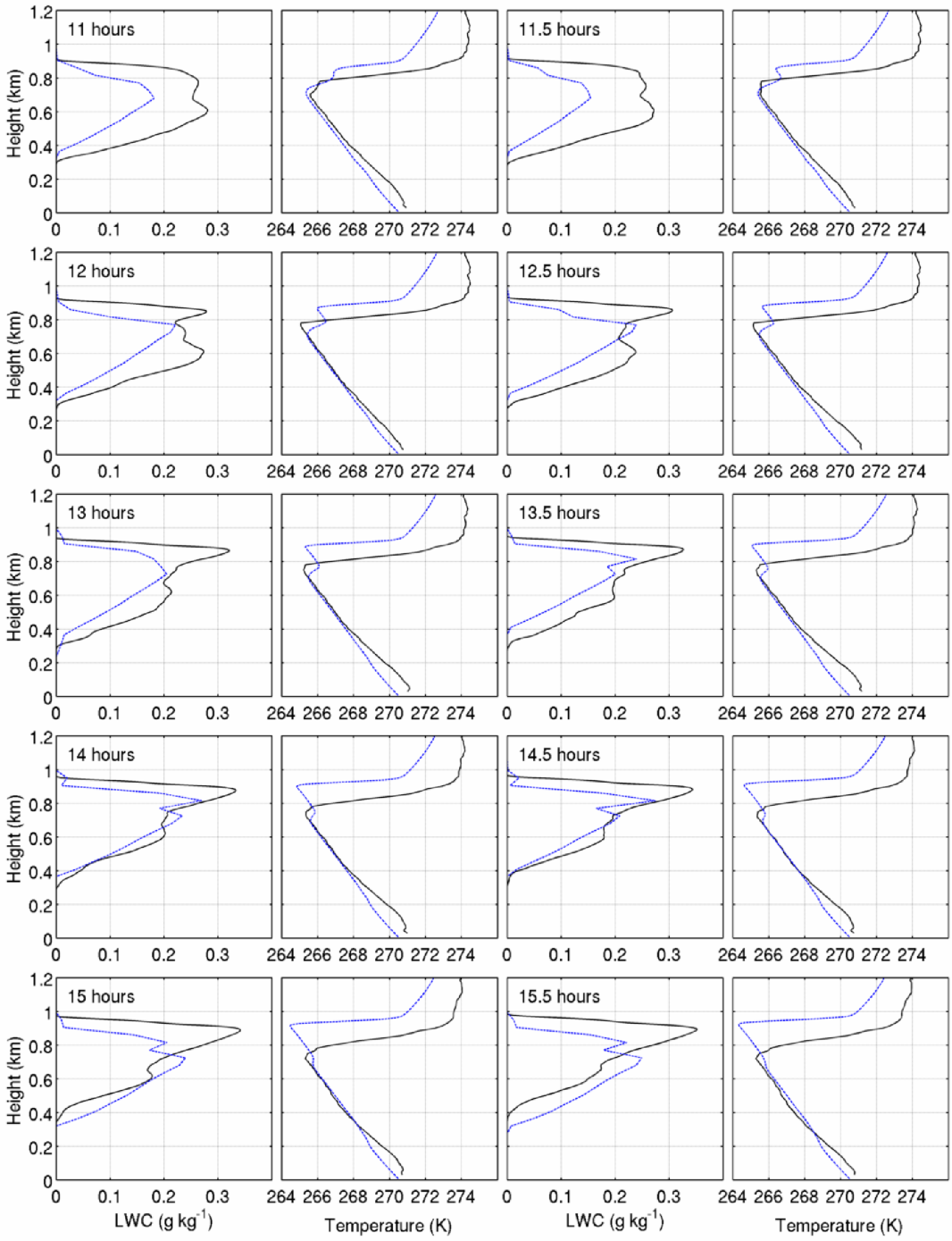

Figure 7.15: (b) 11 - 15.5 simulation hours.

The vertical distribution of ice within the BL is approximately similar in each of the simulations (Figure 7.14), with the height of the peak IWC roughly equal in an absolute sense. However the normalised height of the peak IWC differs between simulations due to changes to the depth of the ML.

Overall the simulations match the magnitude of the observed profile reasonably well. As for the ls2g150m simulation nucleation and deposition of water vapour are the largest microphysical sources of ice and snow, while sublimation reduces ice and snow in the sub-cloud layer. Within the inversion, ice is predicted in the observations, however in all the simulations including the ls4g200m run (where the LWC profile was reasonably well prognosed), ice was limited to the BL only. Ice crystal numbers show little variability between simulations.

7.2.4 Mean profiles of fluxes and tendencies in the ls4g200m simulation

Next the ls4g200m simulation is examined in more detail so that the mechanisms which control the cloud encroachment-inversion adjustment can be understood. As in previous chapters this is done through an examination of time-averaged profiles of $\overline{w'\theta'_v}$, and the budgets of heat, moisture and the TKE. Profiles are normalised in height by z_{ib}.

7.2.4.1 Buoyancy fluxes

Figure 7.16 shows the profile of the time-averaged normalised θ_e profile alongside profiles of the resolved $\overline{w'\theta'}$ and $\overline{w'\theta'_v}$. The mean θ_e profile shows a greater variability than was found in the ls2g150m simulation (Figure 6.25), and while the mixed layer extends down to the surface as in all of the previous simulations examined, in the region directly below z_{ib} (between normalised heights of 0.8 and 1) the mean θ_e profile increases by 0.2 K.

The EZ has a time-averaged depth of 127 m which is around 50 m larger than the depth found in the ls2g150m simulation. Across the EZ the strength of the θ_e increase is also slightly greater by around 1 K, however because the magnitude of the depth increase is much larger - the gradient of the mean inversion in the ls4g200m simulation is less. In the ls2g150m simulation the greatest variability in the θ_e profile was found above the EZ however in the ls4g200m simulation variability of an equal size is also found across the EZ and in the region directly below. The difference is because the cloud top in the ls2g150m simulation is always at a quasi-static depth above the z_{ib} meaning the structure of the EZ is relatively constant through the simulation while in the ls4g200m run, z_{i+} changes over time and as shown in Figure 7.15 the structure of the EZ changes as the layer cools.

As for the previous simulations examined the EZ is marked by negative $\overline{w'\theta'_v}$. The peak

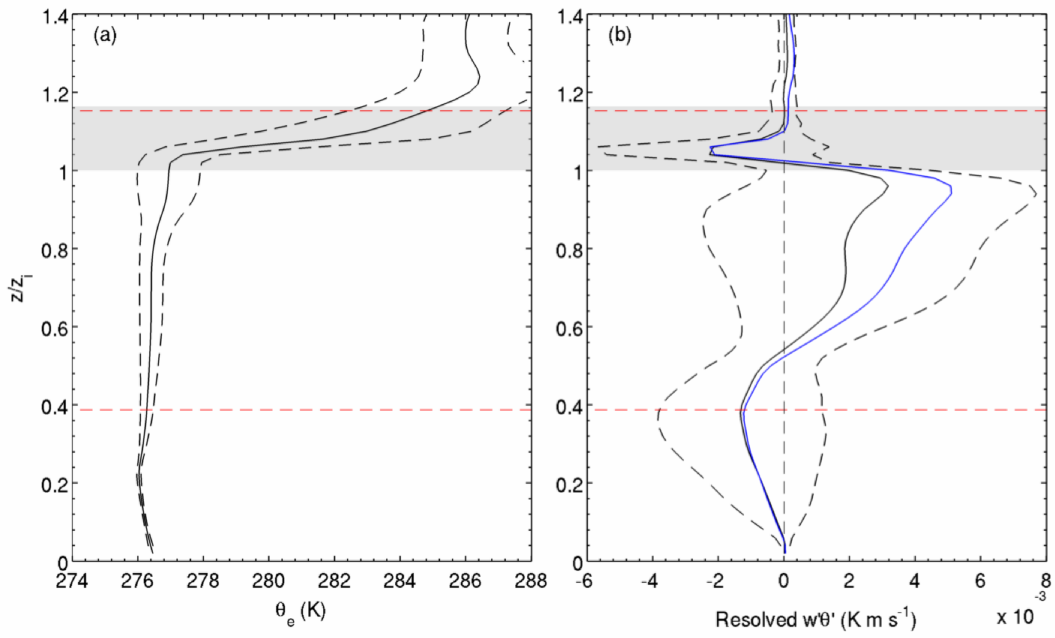

Figure 7.16: ls4g200m simulation. Profiles of (a) θ_e, (b) the resolved $\overline{w'\theta'_v}$ (black line) and the resolved $\overline{w'\theta'}$ (blue line) with height normalised so z_{ib} is equal to one and the surface zero. Solid lines are the time-averaged (4 - 20 hours) profiles and dashed lines are the $\pm$ 1 standard deviations. The grey shaded area denotes the mean entrainment zone and the horizontal red lines the liquid cloud boundaries.

negative $\overline{w'\theta'_v}$ is found towards the bottom of the EZ and has a magnitude of around -2x10^{-3} K m s^{-1}, which is less than half of the peak negative value found in the ls2g150m simulation and around a quarter of the value simulated in the control_N$_{in}$x2 simulation (Figure 6.9). The peak $\overline{w'\theta'_v}$ is found within the mixed layer below z_{ib} at a normalised height of around 0.9, which is above the normalised height of 0.8 where it is located in the previously analysed simulations. Compared to the ls2g150m simulation $\overline{w'\theta'_v}$ is also reduced by around two thirds with the peak value equal to 5x10^{-3} K m s^{-1}.

7.2.4.2 Potential temperature tendency

Due to the cloud-inversion adjustment the heat budget terms have a very different profiles to that found in either the control_N$_{in}$x2 simulation (Figure 6.10) or the ls2g150m simulation (Figure 6.26). Longwave cooling still dominates the radiative contribution to the θ budget, and the radiative cooling is still the largest of all the budget terms, however peak cooling is reduced by a quarter to around -60 K day^{-1} and the cooling is spread over a greater depth (from normalised heights of 0.9 - 1.3 compared to 0.9 -

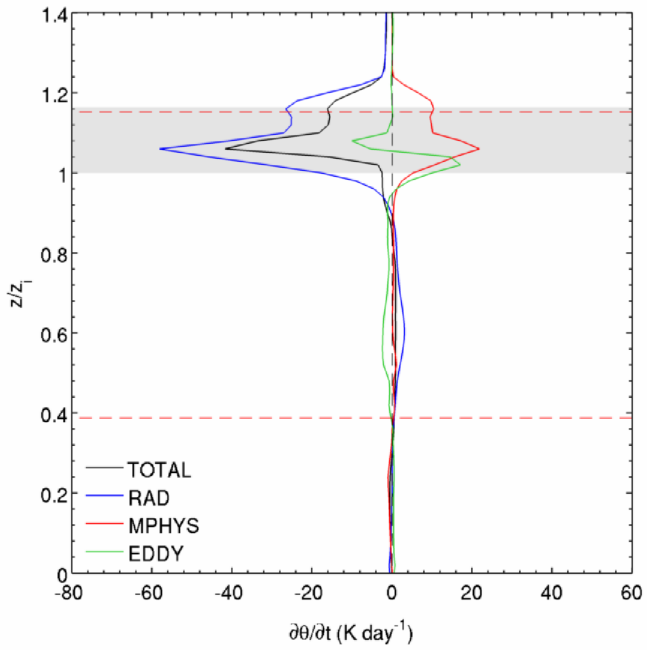

Figure 7.17: ls4g200m simulation. As for Figure 7.16 except for the θ budget. Terms described in Section 6.2.3.2.

1.1). The peak cooling is located at a normalised height of 1.1 which is further above z_{ib} than it was in ls2g150m simulation (normalised height of 1.05) or in the control_N$_{in}$x2 simulation (normalised height of 1), therefore a greater fraction of the cooling is inside the EZ. Because of the cloud-inversion adjustment the radiative heating/cooling profile also has a second minor peak at a normalised height of 1.2.

The condensational heating is of a similar magnitude to that found in the control_N$_{in}$x2 simulation with a peak value of around 20 K day^{-1}, and although the profile shape is very different due to the cloud-inversion adjustment, the height of peak condensational heating is coincident with the height of peak radiative cooling which is consistent with that found in the other simulations. The eddy heating/cooling profile is also consistent with the ls2g150m and control_N$_{in}$x2 simulations with a down gradient transport of heat simulated, except the magnitude is reduced by over 50 % compared to the ls2g150m run. In the ls2g150m simulation eddy transport reduced the net cooling at the height of peak radiative cooling, however the reduction of turbulent transport in the ls4g200m simulation means the combined budget is a peak cooling of -40 K day^{-1} coincident with the peak radiative cooling. Despite this difference the upward shift in the peak radiative cooling means the net cooling is above z_{ib}. A secondary peak cooling of around -25 K day^{-1} is also present at the height of the EZ top.

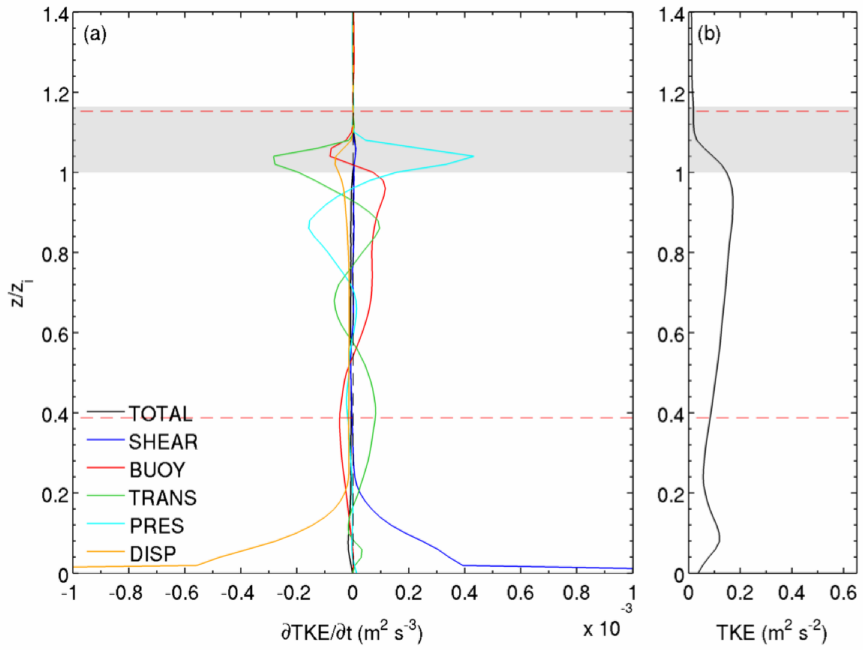

Figure 7.18: ls4g200m simulation. As for Figure 7.16 except for (a) the TKE budget and (b) the total TKE. Terms described in Section 6.2.3.3.

7.2.4.3 Turbulent kinetic energy tendency

Figure 7.18 (a) and (b) shows the normalised, time-averaged TKE budget and total TKE profiles. Both the total TKE and the tendency terms have the same vertical distribution as found in the previous simulations except the magnitude of all of the profiles is reduced. The maximum total TKE directly below z_{ib} is equal 0.18 m^2 s^{-2} which is half that found in the ls2g150m simulation (Figure 6.27) and a third of that found in the control_N$_{in}$x2 simulation (Figure 6.11). As discussed in Section 6.2.3.3, buoyancy production is the greatest generator of turbulence within the cloud and the reduction in the TKE tendency terms is consistent with the reduction in $\overline{w'\theta'_v}$ discussed in Section 7.2.4.1.

7.2.4.4 Mean water contents and tendencies

Figure 7.19 shows profiles of the time-averaged water contents and the net water content tendencies normalised in height as for the previous figures. The ice mixing ratio is relatively small and the total water mixing ratio is primarily composed of liquid and water vapour as in the previous simulations. The liquid cloud top extends higher into the inversion than found in the ls2g150m simulation, while the water vapour and total water profiles are generally similar to that found in the ls2g150m simulation except that

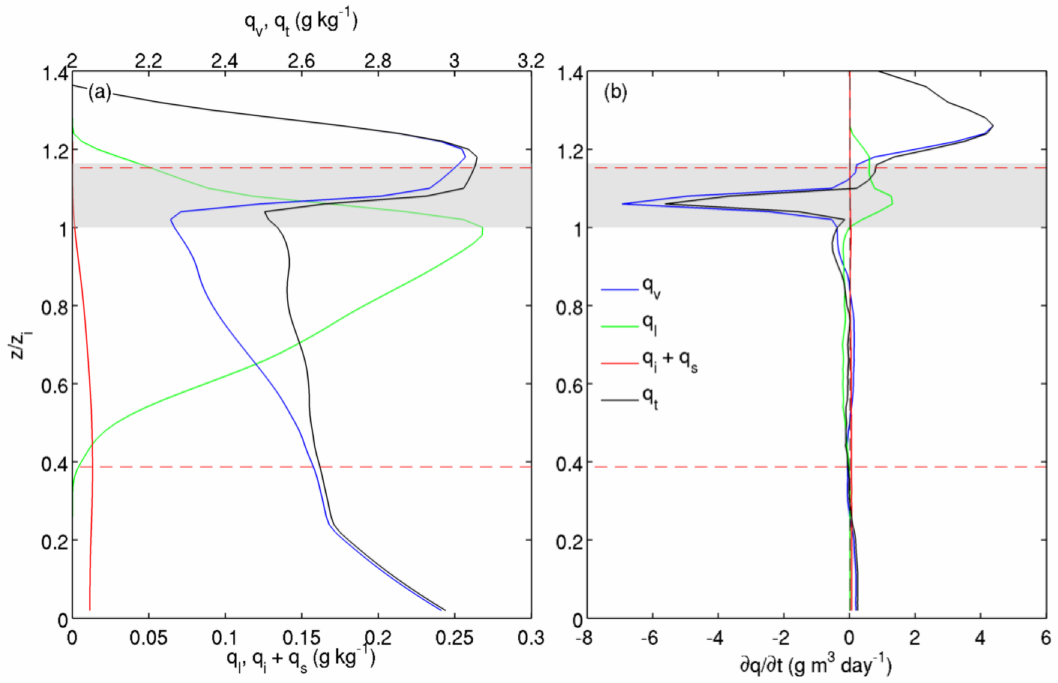

Figure 7.19: ls4g200m simulation. As for Figure 7.16 except for (a) the mean water species mixing ratios and (b) the mean water content tendencies. Note that in (a) the upper x-axis is for the water vapour and total water mixing ratios and the lower x-axis the liquid water and ice + snow water mixing ratios.

gradient in the water vapour inversion is less as the inversion EZ is deeper, and the top of the water vapour inversion is less well defined.

The water content tendencies also have essentially similar profiles to those simulated in the ls2g150m run. The greater water vapour forcing is evident in the water vapour and total water content tendencies above the EZ. The loss of water vapour and total water within the EZ is reduced to a peak of -7 g m^{-3} day^{-1} compared to more than -11 g m^{-3} day^{-1} in the ls2g150m simulation (Figure 6.29). Like the radiative cooling and condensational heating profiles the liquid water content tendency also has a vertical structure which influenced by the cloud-inversion adjustment - a peak tendency is found within the EZ, and a lesser peak is found at the height of the EZ top.

Normalised time-averaged water content budgets are shown in Figure 7.20. The liquid water budget shows that the unique structure of the liquid water tendency is caused by the condensation distribution near cloud top due to the cloud-inversion adjustment. The other liquid water content budget profiles are similar to that found in the ls2g150m simulation (Figure 6.30) except that sedimentation is spread higher in the EZ and the mass transport is reduced. In general the other water species budgets are consistent with those found in the ls2g150m simulation, though the eddy transport is weaker which is

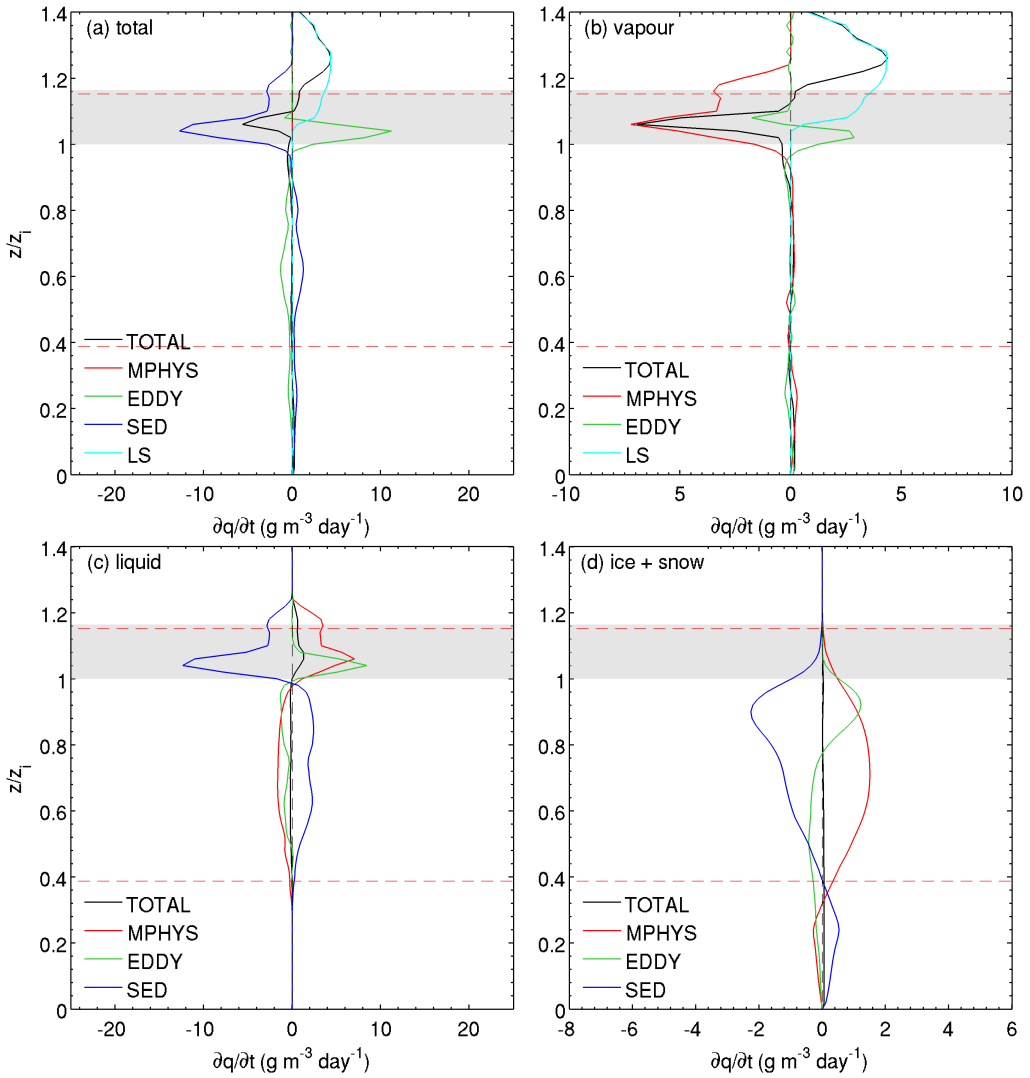

Figure 7.20: ls4g200m simulation. As for Figure 7.16 except for the (a) q_t budget, (b) q_v budget, (c) q_l budget and (d) $q_i + q_s$ budget. Terms described in Section 6.2.3.4 except LS, which is the source of water from large scale forcing, $(\partial q/\partial t)_{LS}$.

consistent with the reduction in TKE and $\overline{w'\theta'_v}$. In the water vapour and total water budgets the down gradient transport from the top of the water vapour inversion to its base is the main source term directly above z_{ib}, therefore its reduction leads to a greater drying in this region. Higher in the inversion the water vapour forcing dominates, as in the ls2g150m simulation the water vapour tendency at the height of the mean z_{ct} is equal to zero.

The mechanism which sustains the water vapour inversion is similar in the ls4g200m simulation to the ls2g150m run, with the loss of water from condensation, continuously replenished by the water vapour from the large scale advection which is transported downwards by eddies. Differential drying/moistening maintains the gradient across the water vapour inversion and keeps the region moist enough for liquid cloud to form there. In the ls4g200m simulation the eddy transport is weaker than in the ls2g150m run, however the forcing is stronger and so the reduction has little effect on the inversions maintenance.

7.2.4.5 Cloud-inversion development

The most significant difference in the time development of the cloud-inversion encroachment between the ls4g200m and ls2g150m runs, is that the encroachment is quasi-stable in the ls2g150m simulation while in the ls4g200m simulation the encroachment evolves with time. For the ls4g200m run the evolution of z_{i+}, the mass of inversion layer liquid water and the fraction of liquid water inside the inversion was discussed in Section 7.2.1, and the development of the cloud and temperature structure was shown in Figure 7.15. Generally the time development is a growth of cloud above z_{ib}, followed by a cooling and adjustment in the inversion boundaries. Over the duration of the simulation z_{i+} peaks at 219 m, however after the inversion base has adjusted to the clouds presence, z_{i+} is stable at 100 $\pm$ 20 m for the next 4 hours.

To help understand what causes the sudden inversion adjustment, Figure 7.21 shows the normalised profiles of θ_e, the heat budget terms and the stability numbers at different times between 5 and 15 simulation hours. At around five hours of simulation time the cloud is extended around 70 m into the inversion. The heat budget is similar to the mean of the control_N$_{in}$x2 simulation and the combined stability number shows that instabilities are generated throughout the cloud. Over the next two hours the cloud encroaches an extra 30 m into the inversion. As was demonstrated to occur in the mean heat budget of the ls2g150m simulation, the extra liquid mass above z_{ib} causes the peak in the radiative cooling to rise relative to the inversion and contribute a greater weight to the peak net cooling. As was discussed in Section 6.3.2.4, the movement of the radiative cooling further into the stable layer reduces the instability generation from radiative

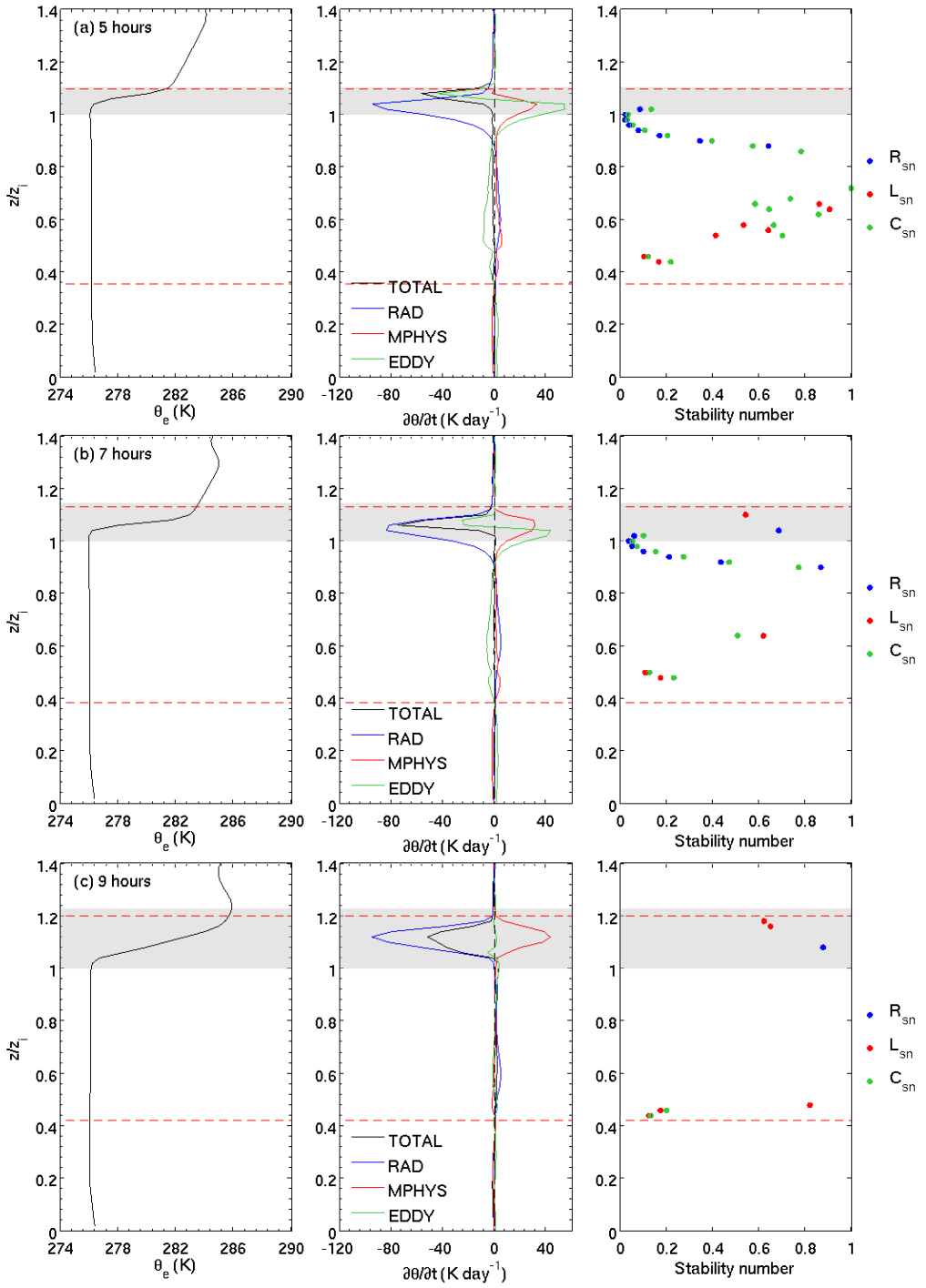

Figure 7.21: ls4g200m simulation. (a) - (c). Half hourly averaged profiles of θ_e, the heat budget terms and the stability numbers, normalised in height so the inversion base is equal to one and surface equal to zero. Averages centred on (a) 5 hours, (b) 7 hours, and (c) 9 hours.

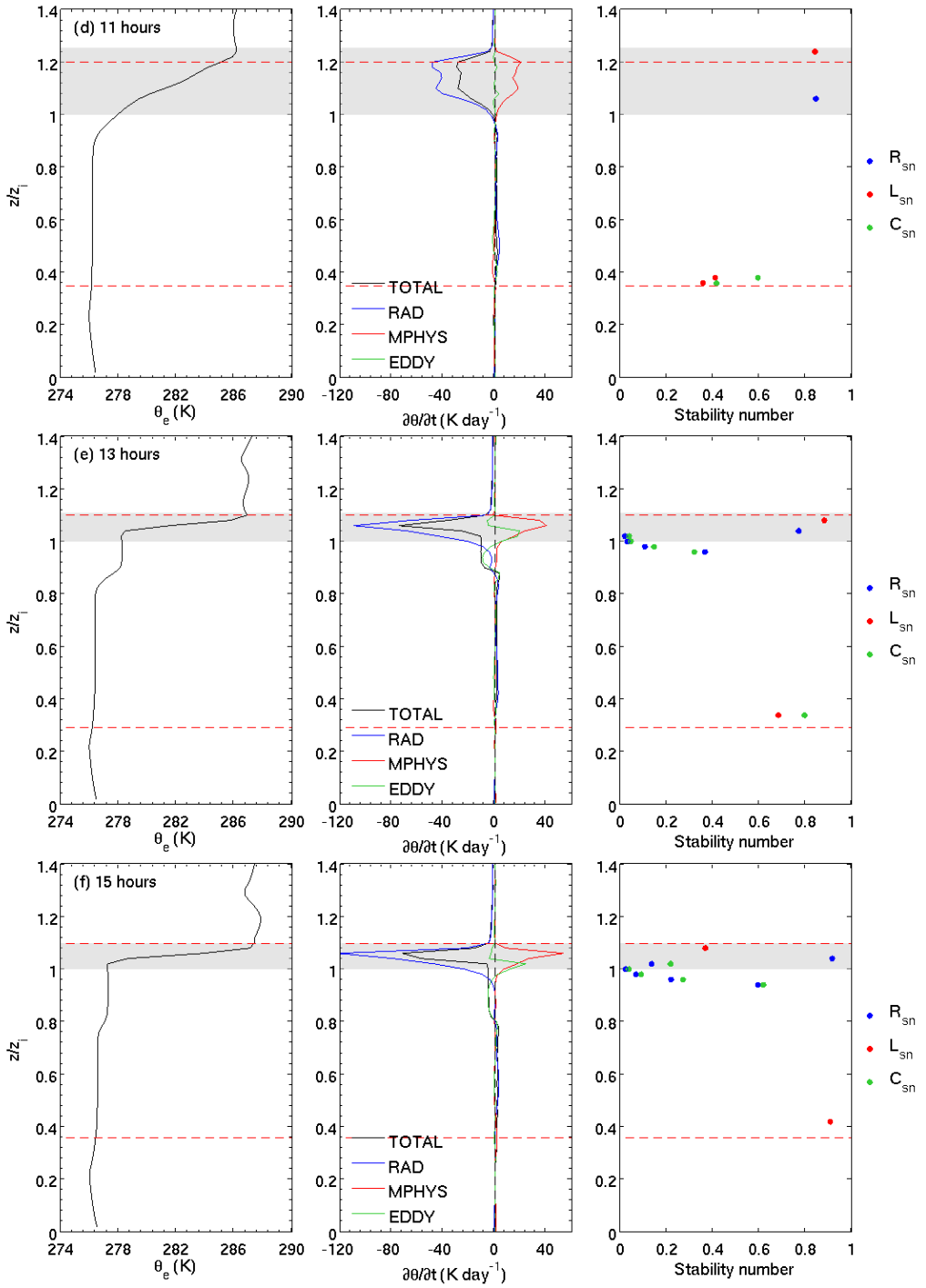

Figure 7.21: ls4g200m simulation. (d) - (f). Normalised profiles with averages centred on (d) 11 hours, (e) 13 hours, (f) 15 hours.

cooling and the eddy transport is reduced. Overall the integrated cooling of the cloudy part of the EZ at seven hours is 50 % greater than at five hours. Comparison with the budgets analysed in Chapter 6 suggests that the extension of cloud into the inversion is stable at this time, and the heat loss through the EZ doesn't lead to the rapid adjustment of the inversion boundaries.

Over the next few simulation hours, rapid condensation causes the cloud top to extend further into the inversion, with z_{i+} equal to a value of around 140 m at 9 hours and 200 m at 11 hours. The entire region of significant radiative cooling is confined to the stable inversion layer in these profiles, thereby suppressing the generation of instability and leading to an order of magnitude reduction in the eddy heat transport. In the absence of turbulence to redistribute heat down gradient through the inversion layer, the peak of the net cooling aligns with the peak radiative cooling and this causes the magnitude of the integrated cooling of the cloudy part of the EZ at 9 and 11 hours to be double that found at five hours. Cooling is now strong enough to cause the rapid redistribution of the temperature profile and by 15 hours the cloud extends a quasi-stable depth of around 100 m into the inversion.

Thus the mechanism for cloud encroachment under strong water vapour forcing is a quasi-stable cloud encroachment followed by rapid condensation in the inversion layer, an upwards shift in the longwave radiative cooling relative to the inversion, a shut off of turbulence as instability generation from radiative cooling is reduced and an increased cooling rate which causes the temperature profile to redistribute. The encroachment depth at which the adjustment mechanism is activated in the ls4g200m simulation around 100 m, though it is probable that altering microphysical parameters: droplet number, effective radius; or the inversion structure would impact on the depth.

7.3 Summary and conclusions

In this chapter the model configuration developed to simulate mixed-phase Arctic stratocumulus in Chapter 6 was expanded so as to test the sensitivity of the cloud-inversion encroachment to different water vapour forcings. As in the previous chapter the forcing was applied above the base of the inversion using the algorithm developed by Brooks (2003), however in this chapter a range of forcings were applied to the model; with the setup differing both the forcing rate and depth over which the forcing was applied.

Generally two types of cloud top encroachment were modelled. The first, of which the encroachment modelled in the ls2g150m simulation is an example, was a quasi-stable encroachment of cloud into the inversion. Generally this was found for clouds where the mean cloud top extended less than 100 m above z_{ib}. The mechanisms which con-

trolled the encroachment of this type are as found for the ls2g150m simulation, therefore because these processes were explained in detail in the previous chapter, quasi-stable encroachment will not be discussed here any further.

The second type of encroachment was characterised by more significant extension of cloud into the inversion and a temporal development of the cloud extension depth. Three simulations had encroachment which developed in this way: the ls3g200m simulation, the ls4g150m simulation and the ls4g200m simulation. These three simulations had the largest mean and maximum encroachment depths out of all the runs and the greatest magnitude of mass inside the inversion. In the ls4g300m simulation cloud top extended up to a maximum of 219 m into the inversion which is equal to around half of the cloud's total liquid water mass. However the extension of cloud into the inversion was variable.

In the ls4g300m simulation the evolution of z_{i+} through the simulation had a distinct cycle. Initially z_{i+} was quasi-static, then as the water vapour forcing increased the strength of the specific humidity inversion the cloud top rose further above z_{ib}, this was followed by a cooling of the cloud-inversion layer and readjustment of the inversion. The next few hours were then marked by a quasi-stable z_{i+}, before the cycle repeated.

Due to the growth of cloud top relative to the inversion base, time-averaged budget profiles which were normalised in height by z_{ib} had distinctive shapes with the budgets of the periods where cloud extended high into the inversion superimposed on budgets from the periods when the cloud was at quasi-stable depth inside the inversion. The most significant difference between the budgets of the ls4g300m simulation and those presented in Chapter 6 for the ls2g150m simulation was the reduction in the turbulent fluxes of buoyancy, heat and the water constituents. As buoyancy was the largest producer of turbulence within the cloud, the mean TKE profile and integrated TKE amount were also reduced significantly.

The reduction in the eddy transport was found to be integral to the encroachment-inversion adjustment mechanism. As described in Chapter 6, the generation of instability can be explained through a radiative, latent and combined stability number. These variables describe whether the cooling/heating from a diabatic process at a point in the atmosphere is strong enough to overcome the stability of the layer and generate instability.

In stratocumulus, cloud top radiative cooling is most important mechanism to generate instability, and during the quasi-stable period of the ls4g200m simulation the peak in the longwave radiative cooling was directly above z_{ib}, therefore instability from radiative cooling was able to be generated through a large portion of the cloud; either below z_{ib} or directly above where $\partial\theta_v/\partial z$ is only slightly positive. However as the cloud-inversion extension increased the peak radiative cooling was forced higher into the inversion layer

until it eventually reached a depth, were no instability could be generated by radiative cooling. Because there was little shear through the cloud, this lead to turbulence essentially switching off.

With regards to the inversion adjustment, the rapid reduction in turbulence meant that there was no eddy transport through the cloud to redistribute heat, and reduce the overall cooling rate within the cloudy part of the entrainment zone. Thus cooling was increased in the EZ and an adjustment of the inversion occurred. Overall this mechanism represents a local radiative-dynamical feedback within the cloud layer. However, while the thermal-adjustment mechanism acted as a strong limit to z_{i+} in the simulations, it was not apparent in ASCOS observations where despite the rising and falling cycle of z_{i+} over time suggesting the possibility of an encroachment-adjustment mechanism, analysis of the change to z_{i+} at periods of high longwave opacity in Section 5.1.3.3 suggested the thermal-adjustment mechanism didn't occur.

The lack of evidence for a thermal-adjustment mechanism in the observations is not conclusive and can't be determined from the ASCOS dataset with any certainty. However even if the mechanism was not active during ASCOS, its simulation by the LEM may not be artificial. Though this would suggest that thermal-adjustment is either prevented by aspects of atmospheric development not simulated by the LEM such as large-scale heat transport balancing the radiative cooling. Or may suggest that the LEM is particularly sensitive to encroachment and in reality thermal-adjustment might only occur when much greater masses of liquid water are found inside the inversion.

Thermal adjustment of the inversion was also absent from the simulations of Solomon *et al.* (2011). However the cloud modelled in Solomon *et al.* (2011) did not encroach as deeply into the inversion as those simulated in the ls3g200m, ls4g150m and ls4g200m runs, and in the LEM simulations where cloud encroached a similar depth above z_{ib} as found modelled in Solomon *et al.* (2011), the thermal-adjustment mechanism was also absent. It would also not be expected from the radiative transfer calculations made by (Sedlar *et al.*, 2012), however the modelling method in that study was not as detailed as that employed here, and their analysis appears to be too simplistic to capture the radiative-microphysical-dynamical interactions found to lead to thermal-adjustment in this study.

Analysis in this chapter also compared the relationships between z_{i+} and the mass of liquid water inside the inversion found using the ASCOS data, and from the range of simulations. Generally the scatter in the model runs was much smaller than in the observations, which is reasonable given the more restrictive conditions imposed on atmospheric development in the LEM. From the complete range of simulations, a number of strong relationships between the encroachment defining variables were identified. Both the fraction of total liquid mass inside the inversion and the absolute liquid cloud mass inside the

inversion were found to have a very strong correlation with the inversion encroachment depth. TKE was also found to have a high positive correlation with the encroachment, while the negative correlation with the encroachment rate suggests that the diagnostic of w_e from the change in BL depth is unsuitable for clouds which encroach into the inversion.

The primary aim of this research project was to determine the radiative-microphysical-dynamical mechanisms which control the encroachment of cloud into the temperature inversion. In this chapter, a range of simulations were made using varying large-scale water vapour forcing specifications to simulate different humidity inversion strengths, and a physically based mechanistic description of the encroachment was determined. Although the simulations made in this chapter only explored the sensitivity of encroachment to humidity inversion strength, the results found are a crucial step forward in understanding Arctic stratocumulus clouds and their influence on the Arctic boundary.

Another significant result of this chapter was the discovery that the thermal-adjustment of the inversion occurs when the buoyancy from cloud top radiative cooling is reduced by so much that vertical heat transport does not balance the longwave radiative cooling. This was only found when z_{i+} was high therefore some cloud-inversion collocations lead to a thermal-adjustment while others don't. Furthermore the reduction in the buoyancy flux was found to lead to a significant drop in the magnitude of BL turbulence and this was discovered to be proportional to z_i, thus a major effect of the encroachment on BL development was quantified.

Chapter 8

Conclusions and recommendations

8.1 Conclusions

This thesis presented a study of Arctic mixed-phase stratocumulus clouds and their encroachment into the temperature inversion which caps the central Arctic boundary layer. The primary aim of the study was to gain an insight into the physical mechanisms which support the extension of cloud into the inversion layer and understand the effect that cloud-inversion encroachment has on the development of the lower Arctic atmosphere. It is also hoped that the increased understanding provided by this study should act to support the development of Arctic stratocumulus parametrizations which are to able to incorporate the encroachment mchanisms; or the influence of encroachment on the lower Arctic atmosphere, into climate models.

To achieve these aims, the methodology of the project first involved a direct analysis of the ASCOS dataset so that the prevalence of clouds which encroached into the inversion during the campaign could be determined and related to measurements at other Arctic locations. A semi-idealised mixed-phase Arctic stratocumulus case study was then designed and modelled using large eddy simulations. The purpose of the simulations was to determine the fundamental radiative-microphysical-dynamical mechanisms which support the encroachment, and to quantify the relationship between cloud encroachment and the presence of specific humidity inversions; which had been previously been observed coincident to the temperature inversion over the central Arctic. Simulations used large-scale forcing of water vapour into the temperature inversion to test the sensitivity of encroachment to the strength and depth of the humidity inversion, with a novel inversion-finding algorithm (Brooks, 2003), incorporated into the LEM to determine the boundaries of the inversion layer.

Direct analysis of the ASCOS dataset showed that despite the central Arctic experiencing

seasonally uncharacteristic large-scale meteorological conditions during the summer of 2008, during periods where the lower atmosphere was dominated by stratocumulus clouds the collocation of cloud inside the inversion was the most prevalent cloud-inversion regime. Generally the structure of the lower Arctic atmosphere observed during ASCOS was simliar to that found in previous summer campaigns; AOE-2001 and SHEBA (Dai *et al.*, 2011; Tjernstrom, 2005, 2007; Tjernstrom *et al.*, 2004). With a shallow near-neutral or slightly stable BL, and cloud residing well above the BL at a height most commonly found to be between 500 and 950 m. In common with that found at other locations during the summertime, clouds were most often characterized as mixed-phase with a shallow liquid layer precipitating ice down to the surface below (Shupe *et al.*, 2008). Elevated temperature inversions were identified in 90 % of the atmospheric temperature profiles during the stratocumulus period while in 86 % of the atmospheric profiles where cloud was observed, the cloud top was found to encroach into the inversion layer. Encroachment depths, z_{i+} were diagnosed using the (Brooks, 2003) algorithm to determine the inversion base, z_{ib}, and were shown to be as high as 500 m, however the largest frequency of occurance was found at depths below 150 m. The common occurance of cloud encroaching more than 100 m into the inversion was is consistent with measurements at other central Arctic locations (Sedlar *et al.*, 2012), indicating the high prevalance of this regime under a variety of large-scale atmospheric conditions.

Numerical simulations modelled a mixed-phase Arctic stratocumulus cloud and in all the simulations the cloud was found to persist throughout the simulation, with the production of ice crystals too slow (Morrison *et al.*, 2012), to cause the glaciation of the whole cloud as found in other studies (Harrington *et al.*, 1999; Jiang *et al.*, 2000; Pinto, 1998). Simulations explored the radiative-microphysical-dynamical interactions which support the encroachment and three cloud-inversion regimes were identified. The first regime was characterised by modest encroachment of the cloud into an inversion where the water vapour mixing ratio fell of rapidly through the inversion layer. Within this regime cloud tops were supported up to 40 m above z_{ib} by the high relative humidity of the inversion, which in turn was maintained from evaporation of overshooting thermals in the entrainment zone. The identification of clouds encroaching into a dry temperature inversion is unexpected and suggests that sub-tropical stratocumulus cloud may also extend a modest distance into the inversion if the drop off of the total water mixing ratio above z_{ib} is not sufficiently high and/or the temperature inversion is not sufficiently sharp.

The second regime was of a cloud whose top extended a quasi-stable depth of over 100 m inside coincident temperature and humidity inversions. The humidity inversion was found to support the extension of cloud into the inversion despite the continual loss of moisture from the atmosphere in the form of ice precipitation. This regime was determined to be similiar to the one modelled by Solomon *et al.* (2011). The depth of the encroachment was

found to be proportional to the strength and depth of the humidity inversion. Radiative-microphysical-dynamical feedbacks within the cloud supported its encroachment into the inversion, with longwave radiative cooling at the top of the mixed layer, driving strong turbulent motions in the BL, overshooting thermals and condensation above z_{ib}. The presence of cloud inside the inversion was shown to cause a significant reduction in the strength of buoyancy production of TKE due to the cloud top radiative cooling occuring round about the stably stratified temperature inversion. However under this regime, the reduction in eddy tranport of heat through the cloud-inversion prevented a thermal-adjustment of the inversion layer to the presence of the cloud.

The third regime was found to occur under the strongest humidity inversions where z_{i+} reached a depth high enough for the peak radiative cooling to occur inside the temperature inversion. Within this regime the production of buoyancy from radiative cooling was essentially shut-off causing an inbalance between radiative cooling, condensation and eddy heat transport which resulted in the rapid thermal-adjustment of the inversion layer. This mechanism demonstrates the importance of radiative-microphysical-dynamical feedbacks in sustaining the cloud (Morrison *et al.*, 2012). However cloud growth inside the inversion followed by the layers adjustment to the cloud was found to be cyclic, with large-scale water vapour forcing into the temperature inversion, strengthening the humidity inversion which inturn induced further encroachment. In this regime the maximum z_{i+} was found was found to be up 200 m with around 40 % of the clouds liquid water mass residing inside the inversion.

Regimes two and three were found from simulations in which the humidity inversion was maintained by a source of inversion layer moisture. However simulations also demonstrated that so long as the inversion was relatively moist, cloud could be maintained over 45 m into the temperature inversion even in the absence of a source of inversion layer moisture. Once a cloud encroached into the inversion layer, condensation near the base of the inversion and the subsequent sedimentation of water droplets into the mixed layer below was shown to create a humidity gradient across the temperature inversion. This in turn led to a down-gradient tranport of water vapour from the top of the inversion towards its base, replenishing the water lost from condensation-sedimentation. So long as the humidity of the inversion remained strong enough for overshooting thermal to condense in the layer, this mechanism was shown to be self sustaining as the vertical distribution of condensation supported the humidity inversion structure. In this regime the cloud was continuously losing water from ice precipitating to the surface and so it would be expected that the cloud would dissipate eventually.

This mechanistic description of encroachment of cloud into the inversion demonstrates that rather than the two cloud-inversion collocations of either cloud capped by the inversion or cloud inside the inversion, a number of cloud-inversion regimes exist. Where

no specific humidity inversion exists the cloud can either be capped by the inversion or it can extend a modest height inside the inversion. This depends on the sharpness of the gradient in moisture and temperature profiles above cloud. Where a specific humidity is found coincident with the temperature inversion, the encroachment depth increases and cloud can either extend a quasi-stable depth into the cloud or at high encroachment depths follow a cycle of cloud growth into the inversion followed by a readjustment of the inversion boundaries.

The physics of these regimes was demonstrated to involve complex radiative-microphysical-dynamical feedbacks in the cloud, however across the range of regimes a simple relationship between the strength of the humidity inversion and the encroachment depth was determined within the model. Although direct analysis of ASCOS data showed that the modelled conditions are only a subset of those experienced in the real Arctic atmosphere, relationships determined in model suggest that parameterization of the encroachment mechanisms is possible. Therefore, there is a potential for cloud encroachment into the inversion to be respresented in GCMs and RCMs.

Development of the lower Arctic atmosphere was found to be affected by the encroachment throught the significant reduction in BL turbulence. The strength of the TKE reduction was found to be proportional to the encroachment depth, and in the simulations with the greatest encroachment, the vertically integrated TKE was reduced by up to 90 % compared to that simulated under the dry inversion regime. This reduction is likely to have important consequences on the amount of vertical mixing modelled by GCMs over the central Arctic and will have an effect on both the strength of surface fluxes and amount of cloud predicted by the model. Thus the absence of cloud top encroachment into the inversion in GCMs and RCMs may contribute their failure to properly predict cloud (Karlsson & Svensson, 2010; Tjernstrom *et al.*, 2008; Walsh *et al.*, 2002, 2009).

The influence of cloud encroachment into the inversion on the magnitude of vertical mixing within the BL may also be important to understand whether the major source of Arctic aerosol is from a surface or from above the free troposphere (Bigg *et al.*, 2001; Leck *et al.*, 1996, 2002), with a reduction in vertical mixing where cloud is inside the inversion preventing the tranport of aerosol through the BL. This may explain why cloud and fog formation is frequently limited by CCN availability (Bigg *et al.*, 1996; Mauritsen *et al.*, 2011) and sometimes lead to the tenuous cloud regime observed near the surface of the central Arctic (Mauritsen *et al.*, 2011), whereby CCN concentrations are too low for condensation to occur at typical relative humidities.

Although this study gives no indication of how the relative frequency of the cloud-inversion regimes would change as the Arctic warms as a consequence of anthropogenic climate change. A reduction in the prevalence of inversion encroaching clouds would suggest greater vertical mixing of the BL which could possibly lead to increased CCN

concentrations. As low-level clouds are the most significant factor controlling the Arctic surface radiation budget Intrieri *et al.* (2002b) and changes to cloud coverage and albedo can alter the equillibrium depth of sea-ice Curry *et al.* (1993), this could have feedbacks on the Arctic climate system. These consequences warrent further investigation.

8.2 Suggestions for future research

The results presented in this study are based on the analysis of ASCOS observations and a series of numerical simulations made using a single mixed-phase Arctic stratocumulus case study in which a large-scale water vapour forcing into the temperature inversion was varied to induce different levels of cloud encroachment into the inversion layer. Although this thesis has highlighted a number of interesting mechanisms which control the encroachment, these mechanisms were found under a limited parameter space and further research is required to provide a complete physical characterization of cloud top encroachment in a wider variety of conditions. To achieve this aim a number of suggestions for future research are provided:

- This study show a modest encroachment of Arctic stratocumulus cloud top into temperature inversion when the specific humidity falls of rapidly with height above the inversion base. Simulations should be made to understand whether modest cloud-inversion encroachment is found in sub-tropical stratocumulus clouds or whether the commonly held assumption that cloud top and inversion base are always coincident is true under all circumstances.

- Thermal-adjustment of the inversion to the cloud layer was found in simulations where the water vapour forcing was large, however this was only modelled in two-dimensions. Equivalent simulations should be carried to evaluate whether the effect is also apparent in three-dimensional simulations.

- The reduction in TKE as cloud encroaches into the inversion has implications on the transport of aerosol particles through the Arctic BL. A range of simulations which include some representation of aerosol transport; possibly through the introduction of tracers in the LEM, should be used to determine how cloud top encroachment influences their mixing through the atmosphere so as to help understand whether the as yet undefined source of central Arctic aerosol is from the free troposphere or the surface.

- Further Arctic stratocumulus case studies should be designed and simulated so that a characterization of the encroachment under a wider variety of Arctic atmospheric conditions can be understood.

- Parameterizations of the cloud top encroachment or its affect on the lower atmosphere should be developed and experiments should be carried out using the UM single column model or a comparable method to test their implementation in GCMs.
- Version 3.0 of the LEM is currently under development and the model incorporates a much more sophisticated explicit cloud microphysics scheme amongst other changes. Explicit microphysics models prognose both mass of cloud droplets/ice crystals of many different sizes allowing the droplet/crystal distribution to change as the simulation is integrated in time. Simulations of the cloud encroachment using the Version 3.0 of the LEM with explicit microphysics should be carried out to determine how the distribution of water droplets at the cloud top is affected by encroachment into the inversion, and results should be used to inform the specification of cloud microphysical parameters in LEM's bulk cloud microphysics model.
- It is suggested that a further summertime expedition to the central Arctic is carried out in the near future. A particular effort should be made to collect a more extensive set of measurements of cloud microphysical and thermodynamic properties either directly by way of dedicated aircraft flghts and/or remotely using a wider range of remote sensing instruments.

References

Abdul-Razzak, H. & Ghan, S.J. (2000). A parameterization of aerosol activation - 2. Multiple aerosol types. *Journal of Geophysical Research-Atmospheres*, **105**, 6837–6844. 40

Abdul-Razzak, H., Ghan, S.J. & Rivera-Carpio, C. (1998). A parameterization of aerosol activation - 1. Single aerosol type. *Journal of Geophysical Research-Atmospheres*, **103**, 6123–6131. 40

Ackerman, A.S., Kirkpatrick, M.P., Stevens, D.E. & Toon, O.B. (2004). The impact of humidity above stratiform clouds on indirect aerosol climate forcing. *Nature*, **432**, 1014–1017. 9

Ackerman, A.S., vanZanten, M.C., Stevens, B., Savic-Jovcic, V., Bretherton, C.S., Chlond, A., Golaz, J.C., Jiang, H., Khairoutdinov, M., Krueger, S.K., Lewellen, D.C., Lock, A., Moeng, C.H., Nakamura, K., Petters, M.D., Snider, J.R., Weinbrecht, S. & Zulauf, M. (2009). Large-eddy simulations of a drizzling, stratocumulus-topped marine boundary layer. *Monthly Weather Review*, **137**, 1083–1110. 36

Andreas, E.L., Guest, P.S., Persson, P.O.G., Fairall, C.W., Horst, T.W., Moritz, R.E. & Semmer, S.R. (2002). Near-surface water vapor over polar sea ice is always near ice saturation. *Journal of Geophysical Research*, **107**. 20

Beesley, J.A. & Moritz, R.E. (1999). Toward an explanation of the annual cycle of cloudiness over the Arctic ocean. *Journal of Climate*, **12**, 395–415. 14

Belchansky, G., Douglas, D. & Platonov, N. (2004). Duration of the Arctic sea ice melt season: regional and interannual variability. *Journal of Climate*, **17**, 67–80. 63

Bengtsson, L., Semenov, V. & Johannessen, O. (2004). The early twentieth-century warming in the Arctic - a possible mechanism. *Journal of Climate*, **17**, 4045–4057. 12

Bergeron, T. (1935). *Proces Verbaux de l'Association de Meteorologie*. International Union of Geodesy and Geophysics. 23

Bigg, E., Leck, C. & Nilsson, E. (1996). Sudden changes in Arctic atmospheric aerosol concentrations during summer and autumn. *Tellus Series B-Chemical and Physical Meteorology*, **48**, 254–271. 21, 22, 81, 172

Bigg, E., C. Leck, C. & Nilsson, E. (2001). Sudden changes in aerosol and gas concentrations in the central Arctic marine boundary layer - causes and consequences. *Journal of Geophysical Reasearch*, **106**, 32167–32185. 21, 81, 172

Bigg, E.K. & Leck, C. (2001). Cloud-active particles over the central Arctic ocean. *Journal of Geophysical Research-Atmospheres*, **106**, 32155–32166. 21

Birch, C., Brooks, I., Tjernstrom, M., Shupe, M., Mauritsen, T., Sedlar, J., Lock, A., Earnshaw, P., Persson, P., Milton, S. & Leck, C. (2012). Modelling atmospheric structure, cloud and their response to CCN in the central Arctic: ASCOS case studies. *Atmospheric Chemistry and Physics*, **12**, 3419–3435. 63

Birch, C.E. (2009). *Surface-Atmosphere coupling over the central Arctic Ocean.*. Ph.D. thesis, School of Earth and Environment, University of Leeds. 91

Boers, R., Eloranta, E.W. & Coulter, R.L. (1984). Lidar observations of mixed layer dynamics: tests of parameterized entrainment models of mixed layer growth rate. *Journal of Climate and Applied Meteorology*, **23**, 247–266. 9

Bretherton, C. & Wyant, M. (1997). Moisture transport, lower-tropospheric stability, and decoupling of cloud-topped boundary layers. *Journal of the Atmospheric Sciences*, **54**, 148–167. 102

Bretherton, C., Uchida, J. & Blossey, P. (2010). Slow manifolds and multiple equilibria in stratocumulus-capped boundary layers. *Journal of Advances in Modeling Earth Systems*, **2**, Art. 14. 28

Bretherton, C.S., Uttal, T., Fairall, C.W., Yuter, S.E., Weller, R.A., Baumgardner, D., Comstock, K., Wood, R. & Raga, G.B. (2004). The EPIC 2001 stratocumulus study. *Bulletin of the American Meteorological Society*, **85**, 967–977. 9

Bretherton, C.S., Blossey, P.N. & Uchida, J. (2007). Cloud droplet sedimentation, entrainment efficiency, and subtropical stratocumulus albedo. *Geophysical Research Letters*, **34**, 5. 9

Brooks, I. (2003). Finding boundary layer top: Application of a wavelet covariance transform to lidar backscatter profiles. *Journal of Atmospheric and Oceanic Technology*, **20**, 1092–1105. 10, 11, 42, 44, 64, 70, 72, 84, 92, 102, 111, 139, 165, 169, 170

Brooks, I. & Fowler, A. (2012). An evaluation of boundary-layer depth, inversion and entrainment parameters by large-eddy simulation. *Boundary-Layer Meteorology*, **142**, 245–263. 11

Businger, J.A., Wyngaard, J.C., Izumi, Y. & Bradley, E.F. (1971). Flux-profile relationships in atmospheric surface layer. *Journal of the Atmospheric Sciences*, **28**, 181–&. 41

Chapman, W.L. & Walsh, J.E. (2007). Simulations of Arctic temperature and pressure by global coupled models. *Journal of Climate*, **20**, 609–632. 13

Chlond, A., Mller, F. & Sednev, I. (2004). Numerical simulation of the diurnal cycle of marine stratocumulus during FIRE - an LES and SCM modelling study. *Quarterly Journal of the Royal Meteorological Society*, **130**, 3297–3321. 92

Chylek, P., Folland, C., Lesins, G., Dubey, M. & Wang, M. (2009). Arctic air temperature change amplification and the atlantic multidecadal oscillation. *Geophysical Research Letters*, **36**, L14801. 12

Cohn, S.A. & Angevine, W.M. (2000). Boundary layer height and entrainment zone thickness measured by lidars and wind-profiling radars. *Journal of Applied Meteorology*, **39**, 1233–1247. 10

Covert, D., Widensohler, A., Alto, P., Heintzenberg, J., P.H., M. & Leck, C. (1996). Aerosol number size distributions from 3 to 500 nm diameter in the Arctic marine boundary layer during summer and autumn. *Tellus Series B-Chemical and Physical Meteorology*, **48**, 197–212. 21

Curry, J. (1983). On the formation of continental polar air. *Journal of the Atmospheric Sciences*, **40**, 2278–2292. 28

Curry, J.A. (1986). Interactions among turbulence, radiation and microphysics in Arctic stratus clouds. *Journal of the Atmospheric Sciences*, **43**, 90–106. 25, 26

Curry, J.A. & Ebert, E.E. (1992). Annual cycle of radiation fluxes over the Arctic-ocean - sensitivity to cloud optical-properties. *Journal of Climate*, **5**, 1267–1280. 13, 25, 27

Curry, J.A. & Herman, G.F. (1985a). Infrared radiative properties of summertime Arctic stratus clouds. *Journal of Climate and Applied Meteorology*, **24**, 525–538. 26

Curry, J.A. & Herman, G.F. (1985b). Relationship between large-scale heat and moisture budgets and the occurance of Arctic stratus clouds. *Monthly Weather Review*, **113**, 1441–1457. 21

Curry, J.A., Schramm, J.L. & Ebert, E.E. (1993). Impact of clouds on the surface radiation balance of the arctic-ocean. *Meteorology and Atmospheric Physics*, **51**, 197–217. 14, 17, 173

Curry, J.A., Rossow, W.B., Randall, D. & Schramm, J.L. (1996). Overview of Arctic cloud and radiation characteristics. *Journal of Climate*, **9**, 1731–1764. 12, 14, 17, 18, 21

Curry, J.A., Pinto, J.O., Benner, T. & Tschudi, M. (1997). Evolution of the cloudy boundary layer during the autumnal freezing of the Beaufort sea. *Journal of Geophysical Research-Atmospheres*, **102**, 13851–13860. 16, 28, 133

Curry, J.A., Hobbs, P.V., King, M.D., Randall, D.A. & Minnis, P. (2000). FIRE Arctic clouds experiment. *Bulletin of the American Meteorological Society*, **81**, 5–29. 16, 18, 21

Dai, C., Gao, Z., Wang, Q. & Cheng, G. (2011). Analysis of atmospheric boundary layer height characteristics over the Arctic ocean using the aircraft and GPS soundings. *Atmospheric and Oceanic Science Letters*, **4**, 124–130. 18, 170

Davis, K.J., Lenschow, D.H., Oncley, S.P., Kiemle, C., Ehret, G., Giez, A. & Mann, J. (1997). Role of entrainment in surface-atmosphere interactions over the boreal forest. *Journal of Geophysical Reasearch*, **120**, 29219–29230. 10

de Boer, G., Morrison, H., Shupe, M. & Hildner, R. (2011). Evidence of liquid dependent ice nucleation in high-latitude stratiform clouds from surface remote sensors. *Geophysical Research Letters*, **38**, L01803. 25

Deardorff, J.W. (1976). Usefullness of liquid-water potential temperature in a shallow-cloud model. *Journal of Applied Meteorology*, **15**, 98–102. 89

Deardorff, J.W. (1980). Cloud top entrainment instability. *Journal of the Atmospheric Sciences*, **37**, 131–147. 9, 10, 33

DeMott, P., Prenni, A., Liu, X., Kreidenweis, S., Petters, M., Twohy, C., Richardson, M., Eidhammer, T. & Rogers, D. (2010). Predicting global atmospheric ice nuclei distributions and their impacts on climate. *Proceedings of the National Academy of Sciences of the United States of America*, **107**, 11217–11222. 23

Derbyshire, S.H., Brown, A.R. & Lock, A.P. (1999). The Meteorological Office large-eddy simulation model. Tech. rep., Met Office, Exeter, UK. 36

Devasthale, A., Sedlar, J. & Tjernström, M. (2011). Characteristics of water-vapour inversions observed over the Arctic by Atmospheric Infrared Sounder (AIRS) and radiosondes. *Atmospheric Chemistry and Physics*, **11**, 9813–9823. 18

Dobbie, S. & Jonas, P. (2001). Radiative influences on the structure and lifetime of cirrus clouds. *Quarterly Journal of the Royal Meteorological Society*, **127**, 2663–2682. 121

Driedonks, A.G.M. & Tennekes, H. (1984). Entrainment effects in the well-mixed atmospheric boundary-layer. *Boundary-Layer Meteorology*, **30**, 75–105. 10, 11, 102, 111

Ebert, E.E. & Curry, J.A. (1992). A parameterization of ice cloud optical properties for climate models. *Journal of Geophysical Research*, **97**, 3831–3836. 27

Edwards, J.M. & Slingo, A. (1996). Studies with a flexible new radiation code .1. Choosing a configuration for a large-scale model. *Quarterly Journal of the Royal Meteorological Society*, **122**, 689–719. 41

Ferrier, B. (1994). A double-moment multiple-phase 4-class bulk ice scheme. 1. Description. *Journal of the Atmospheric Sciences*, **51**, 249–280. 46, 48, 54

Findeisen, W. (1938). *Kolloid-Meteorologische 2nd edition*. American Meteorological Society. 23

Flamant, C., Pelon, J., Flamant, P.H. & Durand, P. (1997). Lidar determination of the entrainment zone thickness at the top of the unstable marine atmospheric boundary layer. *Boundary-Layer Meteorology*, **83**, 247–284. 10

Francis, J.A. & Hunter, E. (2007). Changes in the fabric of the Arctic's greenhouse blanket. *Environmental Research Letters*, **2**. 12

Fridlind, A., van Diedenhoven, B., Ackerman, A., Avramov, A., Mrowiec, A., Morrison, H., Zuidema, P. & Shupe, M. (2012). A FIRE-ACE/SHEBA case study of mixed-phase Arctic boundary layer clouds: Entrainment rate limitations on rapid primary ice nucleation processes. *Journal of the Atmospheric Sciences*, **69**, 365389. 97

Frisch, S., Shupe, M., Djalalova, I., Feingold, G. & Poellot, M. (2002). The retrieval of stratus cloud droplet effective radius with cloud radars. *Journal of Atmospheric and Oceanic Technology*, **19**, 835–842. 58

Gamage, N. & Hagelberg, C. (1993). Detection and analysis of microfronts and associated coherent events using localized transforms. *Journal of the Atmospheric Sciences*, **50**, 750–756. 42

Garratt, J. (1992). *The Atmospheric Boundary Layer*. Cambridge University Press, UK. 34

Garrett, T.J. & Zhao, C.F. (2006). Increased Arctic cloud longwave emissivity associated with pollution from mid-latitudes. *Nature*, **440**, 787–789. 26

Grabon, J.S., Davis, K.J., Kiemle, C. & Ehret, G. (2010). Airborne lidar observations of the transition zone between the convective boundary layer and free atmosphere during the International H2O Project (IHOP) in 2002. *Boundary-Layer Meteorology*, **134**, 61–83. 10

Grabowski, W.W., Xiaoqing, W., Mitchell, W. & Moncrieff, W.D., Hall (1998). Cloud-resolving modeling of cloud systems during phase iii of GATE. Part ii: Effects of resolution and the third spatial dimension. *Journal of the Atmospheric Sciences*, **55**, 3264–3282. 130

Graversen, R.G. & Wang, M.H. (2009). Polar amplification in a coupled climate model with locked albedo. *Climate Dynamics*, **33**, 629–643. 12

Graversen, R.G., Mauritsen, T., Tjernstrom, M., Kallen, E. & Svensson, G. (2008). Vertical structure of recent Arctic warming. *Nature*, **451**, 53–U4. 12

Gray, M.E.B., Petch, J., Derbyshire, S.H., Brown, A.R., Lock, A.P. & Swann, H.A. (2001). Version 2.3 of the Met. Office large eddy model. Tech. rep., Met Office, Exeter, UK. 36, 39

Gultepe, I., Isaac, G.A., Key, J., Intrieri, J., Starr, D.O. & Strawbridge, K.B. (2004). Dynamical and microphysical characteristics of Arctic clouds using integrated observations collected over SHEBA during the April 1998 FIRE-ACE flights of the Canadian Convair. *Meteorology and Atmospheric Physics*, **85**, 235–263. 100

Hallett, J. & Mossop, S. (1974). Production of secondary ice particles during the riming process. *Nature*, **240**, 26–28. 23

Hansen, J. & Travis, L. (1974). Light scattering in planetary atmospheres. *Space Science Reviews*, **16**, 527–610. 27

Harrington, J.Y., Reisin, T., Cotton, W.R. & Kreidenweis, S.M. (1999). Cloud resolving simulations of Arctic stratus - Part ii: Transition-season clouds. *Atmospheric Research*, **51**, 45–75. 23, 25, 28, 64, 97, 133, 170

Harrison, E., Minnis, P., Barkstrom, B., Ramanathan, V., Cess, R. & Gibson, G. (1990). Seasonal variations of cloud radiative forcing derived from the Earth Radiation Budget Experiment. *Journal of Geophysical Research*, **95**, 18,687–18,703. 14

Heintzenberg, J. & Leck, C. (2012). The summer aerosol in the central Arctic 1991 - 2008: Did it change or not? *Atmospheric Chemistry and Physics*, **12**, 3969–3983. 21

Herman, G. & Goody, R. (1976). Formation and persistence of summertime Arctic stratus clouds. *Journal of the Atmospheric Sciences*, **33**, 1537–1553. 21

Herman, G.F. & Curry, J.A. (1984). Observational and theoretical-studies of solar-radiation in Arctic stratus clouds. *Journal of Climate and Applied Meteorology*, **23**, 5–24. 16, 21, 25, 26

Hill, A.A. & Dobbie, S. (2008). The impact of aerosols on non-precipitating marine stratocumulus. ii: The semi-direct effect. *Quarterly Journal of the Royal Meteorological Society*, **134**, 1155–1165. 36

Hill, A.A., Dobbie, S. & Yin, Y. (2008). The impact of aerosols on non-precipitating marine stratocumulus. i: Model description and prediction of the indirect effect. *Quarterly Journal of the Royal Meteorological Society*, **134**, 1143–1154. 36

Hobbs, P. & Rangno, A. (1990). Rapid development of high ice particle concentrations in small polar maritime cumuliform clouds. *Journal of the Atmospheric Sciences*, **47**, 2710–2722. 23

Hobbs, P. & Rangno, A.J. (1985). Ice particle concentrations in clouds. *Journal of the Atmospheric Sciences*, **42**, 2523–2549. 25

Holland, M. & Bitz, C. (2003). Polar amplification of climate change in coupled models. *Climate Dynamics*, **21**, 221–232. 12

Holtslag, P., A.A.M. & Duynkerke, ed. (1998). *Clear and Cloudy Boundary Layers. Proceedings of the colloquium 'Clear and Cloudy Boundary Layers', 26-29 August 1998, Amsterdam, The Netherlands.*. Royal Netherlands Academy of Arts and Sciences. 7

Intrieri, J.M., Fairall, C.W., Shupe, M.D., Persson, P.O.G., Andreas, E.L., Guest, P.S. & Moritz, R.E. (2002a). An annual cycle of Arctic surface cloud forcing at SHEBA. *Journal of Geophysical Research-Oceans*, **107**. 14

Intrieri, J.M., Shupe, M.D., Uttal, T. & McCarty, B.J. (2002b). An annual cycle of Arctic cloud characteristics observed by radar and lidar at SHEBA. *Journal of Geophysical Research-Oceans*, **107**. 14, 173

Jiang, H.L., Cotton, W.R., Pinto, J.O., Curry, J.A. & Weissbluth, M.J. (2000). Cloud resolving simulations of mixed-phase Arctic stratus observed during BASE: Sensitivity to concentration of ice crystals and large-scale heat and moisture advection. *Journal of the Atmospheric Sciences*, **57**, 2105–2117. 23, 28, 64, 134, 170

Johannessen, O., Bengtsson, L., Miles, M., Kuzmina, S., Semenov, V., Alekseev, G., Nagurnyi, A., Zakharov, V., Bobylev, L., Pettersson, L., Hasselmann, K. & Cattle, A. (2004). Arctic climate change: observed and modelled temperature and sea-ice variability. *Tellus Series A-Dynamic Meteorology and Oceanography*, **56**, 328–341. 12

Kahl, J. (1990). Characteristics of the low-level temperature inversion along the Alaskan Arctic coast. *International Journal of Climatology*, **10**, 537548. 17

Kahl, J., Serreze, M. & Schnell, R. (1992). Tropospheric low-level temperature inversions in the Canadian Arctic. *Atmosphere-Ocean*, **30**, 511529. 17

Kahl, J.D. & Martinez, D.A. (1996). Long-term variability in the low-level inversion layer over the Arctic ocean. *International Journal of Climatology*, **16**, 12971313. 17

Karlsson, J. & Svensson, G. (2010). The simulation of Arctic clouds and their influence on the winter surface temperature in present day climate in the CMIP3 multi model dataset. *Climate Dynamics*, **36**, 623–625. 13, 172

Kay, J.E. & Gettelman, A. (2009). Cloud influence on and response to seasonal Arctic sea ice loss. *Journal of Geophysical Research-Atmospheres*, **114**, 18. 14, 63

Klein, S.A. & Hartmann, D.L. (1993). The seasonal cycle of low stratiform clouds. *Journal of Climate*, **6**, 1587–1606. 7

Klein, S.A., McCoy, R.B., Morrison, H., Ackerman, A.S., Avramov, A., de Boer, G., Chen, M.X., Cole, J.N.S., Del Genio, A.D., Falk, M., Foster, M.J., Fridlind, A., Golaz, J.C., Hashino, T., Harrington, J.Y., Hoose, C., Khairoutdinov, M.F., Larson, V.E., Liu, X.H., Luo, Y.L., McFarquhar, G.M., Menon, S., Neggers, R.A.J., Park, S., Poellot, M.R., Schmidt, J.M., Sednev, I., Shipway, B.J., Shupe, M.D., Spangenbery, D.A., Sud, Y.C., Turner, D.D., Veron, D.E., von Salzen, K., Walker, G.K., Wang, Z.E., Wolf, A.B., Xie, S.C., Xu, K.M., Yang, F.L. & Zhang, G. (2009). Intercomparison of model simulations of mixed-phase clouds observed during the ARM Mixed-Phase Arctic Cloud Experiment. i: Single-layer cloud. *Quarterly Journal of the Royal Meteorological Society*, **135**, 979–1002. 45, 46, 47, 48, 49, 50, 51, 52, 53, 91

Leck, C., Bigg, E.K., Covert, D.S., Heintzenberg, J., Maenhaut, W., Nilsson, E.D. & Wiedensohler, A. (1996). Overview of the atmospheric research program during the International Arctic Ocean Expedition of 1991 (IAOE-91) and its scientific results. *Tellus Series B-Chemical and Physical Meteorology*, **48**, 136–155. 17, 21, 55, 172

Leck, C., Nilsson, E.D., Bigg, E.K. & Backlin, L. (2001). Atmospheric program on the arctic ocean expedition 1996 (aoe-96): An overview of scientific goals, experimental approach, and instruments. *Journal of Geophysical Research-Atmospheres*, **106**, 32051–32067. 17, 55

Leck, C., Norman, M., Bigg, E.K. & Hillamo, R. (2002). Chemical composition and sources of the high Arctic aerosol relevant for cloud formation. *Journal of Geophysical Research-Atmospheres*, **107**. 21, 172

Lilly, D.K. (1968). Models of cloud-topped mixed layers under a strong inversion. *Quarterly Journal of the Royal Meteorological Society*, **94**, 292–309. 9, 134

Lindsay, R.W. & Zhang, J. (2005). The thinning of Arctic sea ice, 1988-2003: Have we passed a tipping point? *Journal of Climate*, **18**, 4879–4894. 12

Liu, Y., Key, J., Ackerman, G., S.A. andMace & Zhang, Q. (2012). Arctic cloud macrophysical characteristics from Cloudsat and CALIPSO. *Remote Sensing of Environment*, **124**, 159–173. 13

Luo, Y.L., Xu, K.M., Morrison, H. & McFarquhar, G. (2008a). Arctic mixed-phase clouds simulated by a cloud-resolving model: Comparison with ARM observations and sensitivity to microphysics parameterizations. *Journal of the Atmospheric Sciences*, **65**, 1285–1303. 97, 133

Luo, Y.L., Xu, K.M., Morrison, H., McFarquhar, G.M., Wang, Z. & Zhang, G. (2008b). Multi-layer Arctic mixed-phase clouds simulated by a cloud-resolving model: Comparison with ARM observations and sensitivity experiments. *Journal of Geophysical Research-Atmospheres*, **113**, 21. 134

Marshak, A. & Davis, A., eds. (2005). *3D Radiative Transfer in Cloudy Atmosphere*. Springer, Heidelberg, Germany. 27

Marsham, J.H., Blyth, A.M., Parker, D.J., Beswick, K., Browning, K.A., Corsmeier, U., Kalthoff, N., Khodayar, S., Morcrette, C.J. & Norton, E.G. (2007a). Variable cirrus shading during CSIP IOP 5. ii: Effects on the convective boundary layer. *Quarterly Journal of the Royal Meteorological Society*, **133**, 1661–1675. 36

Marsham, J.H., Morcrette, C.J., Browning, K.A., Blyth, A.M., Parker, D.J., Corsmeier, U., Kalthoff, N. & Kohler, M. (2007b). Variable cirrus shading during initiation of CSIP IOP 5. i: Effects on the convection. *Quarterly Journal of the Royal Meteorological Society*, **133**, 1643–1660. 36

Mauritsen, T., Sedlar, J., Tjernstrom, M., Leck, C., Martin, M., Shupe, M., Sjogren, S., Sierau, B., Persson, P.O.G., Brooks, I.M. & Swietlicki, E. (2011). An Arctic CCN-limited cloud-aerosol regime. *Atmospheric Chemistry and Physics*, **11**, 165–173. 22, 81, 172

McFarquhar, G.M., Ghan, S., Verlinde, J., Korolev, A., Strapp, J.W., Schmid, B., Tomlinson, J.M., Wolde, M., Brooks, S.D., Cziczo, D., Dubey, M.K., Fan, J., Flynn, C., Gultepe, I., Hubbe, J., Gilles, M.K., Laskin, A., Lawson, P., Leaitch, W.R., Liu, P., Liu, X., Lubin, D., Mazzoleni, C., Macdonald, A.M., Moffet, R.C., Morrison, H., Ovchinnikov, M., Shupe, M.D.,

Turner, D.D., Xie, S., Zelenyuk, A., Bae, K., Freer, M. & Glen, A. (2011). Indirect and Semi Direct Aerosol Campaign: The impact of Arctic aerosols on clouds. *Bulletin of the American Meteorological Society*, **92**, 183+. 16

Moeng, C.H., Cotton, W.R., Bretherton, C., Chlond, A., Khairoutdinov, M., Krueger, S., Lewellen, W.S., MacVean, M.K., Pasquier, J.R.M., Rand, H.A., Siebesma, A.P., Stevens, B. & Sykes, R.I. (1996). Simulation of a stratocumulus-topped planetary boundary layer: Intercomparison among different numerical codes. *Bulletin of the American Meteorological Society*, **77**, 261–278. 130, 134

Monin, A. & Obukhov, A. (1954). Basic laws of turbulent mixing in the surface layer of the atmosphere. *Tr. Akad. Nauk SSSR Geofiz. Inst*, **24**, 163–187. 41

Moran, K., Martner, B., Post, M., Kropfli, R., Welsh, D. & Widener, K. (1998). An unattended cloud-profiling radar for use in climate research. *Bulletin of the American Meteorological Society*, **79**, 443–455. 58

Morrison, H., Shupe, M.D. & Curry, J.A. (2003). Modeling clouds observed at sheba using a bulk microphysics parameterization implemented into a single-column model. *Journal of Geophysical Research-Atmospheres*, **108**, 17. 97, 133

Morrison, H., Curry, J.A. & Khvorostyanov, V.I. (2005). A new double-moment microphysics parameterization for application in cloud and climate models. Part i: Description. *Journal of the Atmospheric Sciences*, **62**, 1665–1677. 39, 40, 45, 47, 48, 54, 80, 91

Morrison, H., Pinto, J.O., Curry, J.A. & McFarquhar, G.M. (2008). Sensitivity of modeled Arctic mixed-phase stratocumulus to cloud condensation and ice nuclei over regionally varying surface conditions. *Journal of Geophysical Research-Atmospheres*, **113**, 16. 97, 100

Morrison, H., McCoy, R.B., Klein, S.A., Xie, S.C., Luo, Y.L., Avramov, A., Chen, M.X., Cole, J.N.S., Falk, M., Foster, M.J., Del Genio, A.D., Harrington, J.Y., Hoose, C., Khairoutdinov, M.F., Larson, V.E., Liu, X.H., McFarquhar, G.M., Poellot, M.R., von Salzen, K., Shipway, B.J., Shupe, M.D., Sud, Y.C., Turner, D.D., Veron, D.E., Walker, G.K., Wang, Z.E., Wolf, A.B., Xu, K.M., Yang, F.L. & Zhang, G. (2009a). Intercomparison of model simulations of mixed-phase clouds observed during the ARM Mixed-Phase Arctic Cloud Experiment. ii: Multilayer cloud. *Quarterly Journal of the Royal Meteorological Society*, **135**, 1003–1019. 36

Morrison, H., Thompson, G. & Tatarskii, V. (2009b). Impact of cloud microphysics on the development of trailing stratiform precipitation in a simulated squall

line: Comparison of one- and two-moment schemes. *Monthly Weather Review*, **137**, 991–1007. 39, 40, 45, 47, 48, 54, 80, 91

Morrison, H., Zuidema, P., Ackerman, A., Avramov, A., de Boer, G., Fan, J., Fridlind, A., Hashino, T., Harrington, J., Luo, Y., Ovchinnikov, M. & Shipway, B. (2011). Intercomparison of cloud model simulations of Arctic mixed-phase boundary layer clouds observed during SHEBA/FIRE-ACE. *Journal of Advances in Modeling Earth Systems*, **3**, M06003. 28, 91

Morrison, H., de Boer, G., Feingold, G., Harrington, J., Shupe, M.D. & Sulia, K. (2012). Resilience of persistent Arctic mixed-phase clouds. *Nature Geoscience*, **5**, 11–17. 21, 22, 23, 25, 27, 28, 65, 134, 170, 171

Mossop, S. (1985). Microphysical properties of supercooled cumulus clouds in which an ice particle multiplication process operated. *Quarterly Journal of the Royal Meteorological Society*, **111**, 183–198. 23

Nicholls, S. (1984). The dynamics of stratocumulus - aircraft observations and comparisons with a mixed layer model. *Quarterly Journal of the Royal Meteorological Society*, **110**, 783–820. 6, 8

Nicholls, S. & Leighton, J. (1986). An observational study of the structure of stratiform cloud sheets: Part i. structure. *Quarterly Journal of the Royal Meteorological Society*, **112**, 431–460. 102

Noonkester, R. (1984). Droplet spectra observed in marine stratus cloud layers. *Journal of the Atmospheric Sciences*, **41**, 829–845. 26

NSIDC (2012). Arctic sea ice extent settles at record seasonal minimum. [Online], Available: `http://nsidc.org/arcticseaicenews/2012/09/arctic-sea-ice-extent-settles-at-record-seasonal-minimum/`. 12

ODell, C., Wentz, F. & Bennartz, r. (2008). Cloud liquid water path from satellite-based passive microwave observations: A new climatology over the global oceans. *Journal of Climate*, **21**, 1721–1738. 26

Paluch, I.R. & Lenschow, D.H. (1991). Stratiform cloud formation in the marine boundary-layer. *Journal of the Atmospheric Sciences*, **48**, 2141–2158. 8, 108, 135

Perovich, D., Light, B., Eicken, H., Jones, K., Runciman, K. & Nghiem, S. (2007). Increasing solar heating of the Arctic ocean and adjacent seas, 1979-2005. Attribution and role in the ice-albedo feedback. *Geophysical Research Letters*, **34**, L19505. 12

Perovich, D.K., Grenfell, T.C., Light, B. & Hobbs, P.V. (2002). Seasonal evolution of the albedo of multiyear Arctic sea ice. *Journal of Geophysical Research: Oceans*, **107**. 20

Persson, P., Fairall, C., Andreas, E., Guest, P. & Perovich, D. (2002). Measurements near the atmospheric surface flux group tower at SHEBA: Near-surface conditions and surface energy budget. *Journal of Geophysical Research-Oceans*, **107**. 18, 28

Petch, J.C. (2006). Sensitivity studies of developing convection in a cloud-resolving model. *Quarterly Journal of the Royal Meteorological Society*, **132**, 345–358. 36

Pinto, J.O. (1998). Autumnal mixed-phase cloudy boundary layers in the Arctic. *Journal of the Atmospheric Sciences*, **55**, 2016–2038. 18, 21, 23, 27, 28, 64, 104, 133, 138, 170

Pinto, J.O., Alam, A., Maslanik, J.A., Curry, J.A. & Stone, R.S. (2003). Surface characteristics and atmospheric footprint of springtime Arctic leads at SHEBA. *Journal of Geophysical Research*, **108**. 20

Prenni, A.J., Harrington, J.Y., Tjernstrom, M., DeMott, P.J., Avramov, A., Long, C.N., Kreidenweis, S.M., Olsson, P.Q. & Verlinde, J. (2007). Can ice-nucleating aerosols affect Arctic seasonal climate? *Bulletin of the American Meteorological Society*, **88**, 541–550. 97

Pruppacher, H.R. & Klett, J.D. (1997). *Microphysics of Clouds and Precipitation.*. Kluwer Academic. 8, 23

Raes, F., Van Dingenen, R., Vignati, E., Wilson, J., Putaud, J.P., Seinfeld, J.H. & Adams, P. (2000). Formation and cycling of aerosols in the global troposphere. *Atmospheric Environment*, **34**, 4215–4240. 9, 80

Randall, D., Curry, J., Battisti, D., Flato, G., Grumbine, R., Hakkinen, S., Martinson, D., Preller, R., Walsh, J. & Weatherly, J. (1998). Status of and outlook for large-scale modeling of atmosphere-ice-ocean interactions in the Arctic. *Bulletin of the American Meteorological Society*, **79**, 197–219. 13

Rangno, A.L. & Hobbs, P.V. (2001). Ice particles in stratiform clouds in the Arctic and possible mechanisms for the production of high ice concentrations. *Journal of Geophysical Research-Atmospheres*, **106**, 15065–15075. 25

Rogers, D.C., DeMott, P.J. & Kreidenweis, S.M. (2001). Airborne measurements of tropospheric ice-nucleating aerosol particles in the Arctic spring. *Journal of Geophysical Research-Atmospheres*, **106**, 15053–15063. 23

Rothrock, D., Yu, Y. & Maykut, G. (1999). Thinning of the Arctic sea-ice cover. *Geophysical Research Letters*, **26**, 3469–3472. 12

Schweiger, A.J. (2004). Changes in seasonal cloud cover over the Arctic seas from satellite and surface observations. *Geophysical Research Letters*, **31**. 14, 15

Schweiger, A.J., Lindsay, R.W., Vavrus, S. & Francis, J.A. (2008). Relationships between Arctic sea ice and clouds during autumn. *Journal of Climate*, **21**, 4799–4810. 20

Screen, J.A. & Simmonds, I. (2010). The central role of diminishing sea ice in recent Arctic temperature amplification. *Nature*, **464**, 1334 – 1337. 12

Sedlar, J. & Tjernstrom, M. (2009). Stratiform cloud-inversion characterization during the Arctic melt season. *Boundary-Layer Meteorology*, **132**, 455–474. 18, 28, 109

Sedlar, J., Tjernstrom, M., Mauritsen, T., Shupe, M.D., Brooks, I.M., Persson, O.G., Birch, C.E., Leck, C., Sirevaag, A. & Nicolaus, M. (2011). A transitioning Arctic surface energy budget: the impacts of solar zenith angle, surface albedo and cloud radiative forcing. *Climate Dynamics*, **37**, 1643–1660. 14, 58, 62, 63

Sedlar, J., Shupe, M. & Tjernstrm, M. (2012). On the relationship between thermodynamic structure and cloud top, and its climate significance in the Arctic. *Journal of Climate*, **25**, 23742393. 28, 29, 30, 64, 71, 72, 76, 86, 88, 94, 99, 109, 119, 133, 134, 135, 153, 167, 170

Serreze, M. & Barry, R. (2011). Processes and impacts of Arctic amplification: A research synthesis. *Global and Planetary Change*, **77**, 85 – 96. 12

Serreze, M. & Francis, J. (2006). The Arctic amplification debate. *Climatic Change*, 241–264. 12

Serreze, M., Kahl, J. & Schnell, R. (1992). Low-level temperature inversions of the Eurasian Arctic and comparisons with Soviet drifting station data. *Journal of Climate*, **5**, 615629. 17

Serreze, M., Barrett, A., Stroeve, J., Kindig, D. & Holland, M. (2009). The emergence of surface-based Arctic amplification. *Cryosphere*, **3**, 11–19. 12

Shindell, D. & Faluvegi, G. (2009). Climate response to regional radiative forcing during the twentieth century. *Nature Geoscience*, **2**, 294–300. 12

Shupe, M. (2007). A ground-based multisensor cloud phase classifier. *Geophysical Research Letters*, **34**. 58

Shupe, M.D. (2011). Clouds at Arctic atmospheric observatories. Part ii: Thermodynamic phase characteristics. *Journal of Applied Meteorology and Climatology*, **50**, 645–661. 21, 22, 25, 64

Shupe, M.D. & Intrieri, J.M. (2004). Cloud radiative forcing of the Arctic surface: The influence of cloud properties, surface albedo, and solar zenith angle. *Journal of Climate*, **17**, 616–628. 26

Shupe, M.D., Uttal, T. & Matrosov, S.Y. (2005). Arctic cloud microphysics retrievals from surface-based remote sensors at SHEBA. *Journal of Applied Meteorology*, **44**, 1544–1562. 58

Shupe, M.D., Matrosov, S.Y. & Uttal, T. (2006). Arctic mixed-phase cloud properties derived from surface-based sensors at SHEBA. *Journal of the Atmospheric Sciences*, **63**, 697–711. 23, 24, 25, 26, 27, 59, 99, 100

Shupe, M.D., Kollias, P., Persson, P.O.G. & McFarquhar, G.M. (2008). Vertical motions in Arctic mixed-phase stratiform clouds. *Journal of the Atmospheric Sciences*, **65**, 1304–1322. 25, 64, 65, 100, 134, 170

Shupe, M.D., Walden, V.P., Eloranta, E., Uttal, T., Campbell, J.R., Starkweather, S.M. & Shiobara, M. (2011). Clouds at Arctic atmospheric observatories. Part i: Occurrence and macrophysical properties. *Journal of Applied Meteorology and Climatology*, **50**, 626–644. 13

Siebesma, A.P., Bretherton, C.S., Brown, A., Chlond, A., Cuxart, J., Duynkerke, P.G., Jiang, H.L., Khairoutdinov, M., Lewellen, D., Moeng, C.H., Sanchez, E., Stevens, B. & Stevens, D.E. (2003). A large eddy simulation intercomparison study of shallow cumulus convection. *Journal of the Atmospheric Sciences*, **60**, 1201–1219. 36

Sirois, A. & Barrie, L. (1999). Arctic lower tropospheric aerosol trends and composition at Alert, Canada: 19801995. *Journal of Geophysical Reasearch*, **104**, 11599–11618. 21, 81

Skamarock, W.C., Klemp, J.B., Dudhia, J., Gill, D.O., Barker, D.M., Duda, M.G., Huang, X., Wang, W. & Powers, J.G. (2008). A description of the advanced research WRF version 3. *NCAR Tech. Note, NCAR/TN-475+STR*, 113. 30

Slingo, A. (1989). A GCM parameterization for the shortwave radiative properties of water clouds. *Journal of the Atmospheric Sciences*, **46**, 1419–1427. 41

Smagorinsky, J. (1963). General circulation experiments with the primitive equations. *Monthly Weather Review*, **91**, 99–164. 38

Solomon, A., Shupe, M.D., Persson, P.O.G. & Morrison, H. (2011). Moisture and dynamical interactions maintaining decoupled Arctic mixed-phase stratocumulus in the presence of a humidity inversion. *Atmospheric Chemistry and Physics*, **11**, 10127–10148. viii, 28, 30, 31, 32, 33, 35, 76, 79, 86, 88, 89, 92, 128, 129, 133, 136, 137, 138, 167, 170

Solomon, S., Qin, D., Manning, M., Chen, Z., Marquis, M., Averyt, K.B., Tignor, M. & Miller, H.L. (2007). *Climate Change 2007 - The Physical Science Basis: Working Group I Contribution to the Fourth Assessment Report of the IPCC*. Cambridge University Press. 12, 13

Stephens, G.L. (1978). Radiation profiles in extended water clouds. 2. Parametization schemes. *Journal of the Atmospheric Sciences*, **35**, 2123–2132. 26, 74

Stephens, G.L., Paltridge, G.W. & Platt, C.M.R. (1978). Radiation profiles in extended water clouds. 3. Observations. *Journal of the Atmospheric Sciences*, **35**, 2133–2141. 26

Sterk, H.A.M., Steeneveld, G.J. & Holtslag, A.A.M. (2013). The role of snow-surface coupling, radiation, and turbulent mixing in modeling a stable boundary layer over Arctic sea ice. *Journal of Geophysical Research: Atmospheres*, n/a–n/a. 20

Stevens, B. (2002). Entrainment in stratocumulus-topped mixed layers. *Quarterly Journal of the Royal Meteorological Society*, **128**, 2663–2690. 10

Stevens, B., Cotton, W.R., Feingold, G. & Moeng, C.H. (1998). Large-eddy simulations of strongly precipitating, shallow, stratocumulus-topped boundary layers. *Journal of the Atmospheric Sciences*, **55**, 3616–3638. 8

Stevens, B., Lenschow, D.H., Faloona, I., Moeng, C.H., Lilly, D.K., Blomquist, B., Vali, G., Bandy, A., Campos, T., Gerber, H., Haimov, S., Morley, B. & Thornton, D. (2003). On entrainment rates in nocturnal marine stratocumulus. *Quarterly Journal of the Royal Meteorological Society*, **129**, 3469–3493. 91, 97

Stevens, B., Moeng, C.H., Ackerman, A.S., Bretherton, C.S., Chlond, A., De Roode, S., Edwards, J., Golaz, J.C., Jiang, H.L., Khairoutdinov, M., Kirkpatrick, M.P., Lewellen, D.C., Lock, A., Muller, F., Stevens, D.E., Whelan, E. & Zhu, P. (2005). Evaluation of large-eddy simulations via observations of nocturnal marine stratocumulus. *Monthly Weather Review*, **133**, 1443–1462. 36, 109

Stevens, B., Beljaars, A., Bordoni, S., Halloway, C., Kohler, M., Krueger, S., Savic-Jovcic, V. & Zhang, Y. (2007). On the structure of the lower troposphere in the summertime stratocumulus regime of the Northeast Pacific. *Monthly Weather Review*, **135**, 985–1005. 8, 108, 135

Stull, R.B. (1988). *An Introduction to Boundary Layer Meteorology*. Kluwer. 6, 9, 11, 34, 101

Sullivan, P.P., Moeng, C.H., Stevens, B., Lenschow, D.H. & Mayor, S.D. (1998). Structure of the entrainment zone capping the convective atmospheric boundary layer. *Journal of the Atmospheric Sciences*, **55**, 3042–3064. 11

Tjernstrom, M. (2005). The summer Arctic boundary layer during the Arctic Ocean Experiment 2001 (AOE-2001). *Boundary-Layer Meteorology*, **117**, 5–36. 18, 19, 28, 69, 70, 170

Tjernstrom, M. (2007). Is there a diurnal cycle in the summer cloud-capped Arctic boundary layer? *Journal of the Atmospheric Sciences*, **64**, 3970–3986. 18, 20, 28, 170

Tjernstrom, M. & Graversen, R.G. (2009). The vertical structure of the lower Arctic troposphere analysed from observations and the ERA-40 reanalysis. *Quarterly Journal of the Royal Meteorological Society*, **135**, 431–443. 17, 18, 19, 20, 70

Tjernstrom, M. & Rune, A. (2003). The structure of gradually transforming marine stratocumulus during the ASTEX first lagrangian experiment. *Quarterly Journal of the Royal Meteorological Society*, **129**, 1071–1100. 8, 108, 135

Tjernstrom, M., Leck, C., Persson, P.O.G., Jensen, M.L., Oncley, S.P. & Targino, A. (2004). The summertime Arctic atmosphere - Meteorological measurements during the Arctic Ocean Experiment 2001. *Bulletin of the American Meteorological Society*, **85**, 1305–1321. 17, 18, 20, 56, 170

Tjernstrom, M., Zagar, M., Svensson, G., Cassano, J.J., Pfeifer, S., Rinke, A., Wyser, K., Dethloff, K., Jones, C., Semmler, T. & Shaw, M. (2005). Modelling the Arctic boundary layer: An evaluation of six arcmip regional-scale models using data from the SHEBA project. *Boundary-Layer Meteorology*, **117**, 337–381. 13

Tjernstrom, M., Sedlar, J. & Shupe, M.D. (2008). How well do regional climate models reproduce radiation and clouds in the Arctic? An evaluation of ARCMIP simulations. *Journal of Applied Meteorology and Climatology*, **47**, 2405–2422. 13, 172

Tjernstrom, M., Birch, C.E., Brooks, I.M., Shupe, M.D., Persson, P.O.G., Sedlar, J., Mauritsen, T., Leck, C., Paatero, J., Szczodrak, M. & Wheeler, C.R. (2012). Meteorological conditions in the central Arctic summer during the Arctic Summer Cloud Ocean Study (ASCOS). *Atmospheric Chemistry and Physics*, **12**, 6863–6889. 59, 60, 61, 62, 88

Trokhimovski, Y.G., Westwater, E.R., Han, Y. & Leuski, V.Y. (1998). Air and sea surface temperature measurements using a 60-GHz microwave rotating radiometer. *IEEE Transactions on Geoscience and Remote Sensing*, **36**, 3–15. 58

Tsay, S.C. & Jayaweera, K. (1984). Physical characteristics of Arctic stratus clouds. *Journal of Climate and Applied Meteorology*, **23**, 584–596. 21, 25, 26, 100

Turton, J.D. & Nicholls, S. (1987). A study of the diurnal-variation of stratocumulus using a multiple mixed layer model. *Quarterly Journal of the Royal Meteorological Society*, **113**, 969–1009. 102

Twomey, S. (1959). The nuclei of natural cloud formation. Part ii: The supersaturation in natural clouds and the variation of cloud droplet concentration. *Pure Applied Geophysics*, **43**, 243–249. 8

Twomey, S. (1977). The influence of pollution on the shortwave albedo of clouds. *Journal of the Atmospheric Sciences*, **34**, 1149–1152. 9, 26

Uttal, T., Curry, J.A., McPhee, M.G., Perovich, D.K., Moritz, R.E., Maslanik, J.A., Guest, P.S., Stern, H.L., Moore, J.A., Turenne, R., Heiberg, A., Serreze, M.C., Wylie, D.P., Persson, O.G., Paulson, C.A., Halle, C., Morison, J.H., Wheeler, P.A., Makshtas, A., Welch, H., Shupe, M.D., Intrieri, J.M., Stamnes, K., Lindsey, R.W., Pinkel, R., Pegau, W.S., Stanton, T.P. & Grenfeld, T.C. (2002). Surface HEat Budget of the Arctic ocean. *Bulletin of the American Meteorological Society*, **83**, 255+. 16

vanZanten, M., Stevens, B., Vali, G. & Lenschow, D. (2005). Observations of drizzle in nocturnal marine stratocumulus. *Journal of the Atmospheric Sciences*, **62**, 88–106. 9

Vardiman, L. (1978). The generation of secondary ice particles in cloud-crystal collisions. *Journal of the Atmospheric Sciences*, **35**, 2168–2180. 23

Verlinde, J., Harrington, J.Y., McFarquhar, G.M., Yannuzzi, V.T., Avramov, A., Greenberg, S., Johnson, N., Zhang, G., Poellot, M.R., Mather, J.H., Turner, D.D., Eloranta, E.W., Zak, B.D., Prenni, A.J., Daniel, J.S., Kok, G.L., Tobin, D.C., Holz, R., Sassen, K., Spangenberg, D., Minnis, P., Tooman, T.P., Ivey, M.D., Richardson, S.J., Bahrmann, C.P., Shupe, M., DeMott, P.J., Heymsfield, A.J. & Schofield, R. (2007). The Mixed-Phase Arctic Cloud Experiment. *Bulletin of the American Meteorological Society*, **88**, 205+. 16, 25

Wallace, J. & Hobbs, P. (2006). *Atmospheric science: an introductory survey (2nd edition). International Geophysics Series 92*. Associated press. 27

Walsh, J. & Chapman, W. (1998). Arctic cloud-radiation-temperature associations in observational data and atmospheric reanalyses. *Journal of Climate*, **11**, 3030–3045. 26

Walsh, J.E., Kattsov, V.M., Chapman, W.L., Govorkova, V. & Pavlova, T. (2002). Comparison of Arctic climate simulations by uncoupled and coupled global models. *Journal of Climate*, **15**, 1429–1446. 13, 172

Walsh, J.E., Chapman, W.L. & Portis, D.H. (2009). Arctic cloud fraction and radiative fluxes in atmospheric reanalyses. *Journal of Climate*, **22**, 2316–2334. 13, 172

Wang, Q. & Wang, S.P. (2004). Turbulent and thermodynamic structure of the autumnal Arctic boundary layer due to embedded clouds. *Boundary-Layer Meteorology*, **113**, 225–247. 21

Wang, X. & Key, J.R. (2005). Arctic surface, cloud, and radiation properties based on the AVHRR polar pathfinder dataset. Part i: Spatial and temporal characteristics. *Journal of Climate*, **18**, 2558–2574. 13

Wegener, A. (1911). *Thermodynamik der Atmosphare*. Leipzig. 23

Weng, F. & Grody, N. (1994). Retrieval of cloud liquid water using the Special Sensor Microwave Imager (SSM/I). *Journal of Geophysical Reasearch*, **99(D12)**, 25535–25551. 26

Westwater, E.R., Han, Y., Irisov, V.G., Leuskiy, E.N., V .and Kadygrov & Viazankin, S.A. (1999). Remote sensing of boundary layer temperature profiles by a scanning 5-mm microwave radiometer and RASS: Comparison experiments. *Journal of Atmospheric and Oceanic Technology*, **16**, 805–818. 58

Westwater, E.R., Han, Y., Shupe, M.D. & Matrosov, S.Y. (2001). Analysis of integrated cloud liquid and precipitable water vapor retrievals from microwave radiometers during the Surface HEat Budget of the Arctic ocean project. *Journal of Geophysical Research-Atmospheres*, **106**, 32019–32030. 58

Wilde, N.P., Stull, R.B. & Eloranta, E.W. (1985). The LCL zone and cumulus onset. *Journal of Climate and Applied Meteorology*, **24**, 640–657. 10

Winton, M. (2006). Amplified Arctic climate change: What does surface albedo feedback have to do with it? *Geophysical Research Letters*, **33**, L03701. 12, 13

Wood, K. & Overland, J. (2010). Early 20th century Arctic warming in retrospect. *International Journal of Climatology*, **30**, 1269–1279. 12

Wood, R. (2006). Relationships between optical depth, liquid water path, droplet concentration, and effective radius in adiabatic layer cloud. [Online], Available: `http://www.atmos.washington.edu/robwood/papers/chilean_plume/optical_depth_relations.pdf`. 27

Wood, R. (2012). Stratocumulus clouds. *Monthly Weather Review*, **140**, 2373–2423. 6, 7, 94

Wood, R. & Bretherton, C.S. (2004). Boundary layer depth, entrainment, and decoupling in the cloud-capped subtropical and tropical marine boundary layer. *Journal of Climate*, **17**, 3576–358. 9

Yamaguchi, T. & Randall, D.A. (2008). Large-eddy simulation of evaporatively driven entrainment in cloud-topped mixed layers. *Journal of the Atmospheric Sciences*, **65**, 1481–1504. 9

Yang, X., Fyfe, J. & Flato, G. (2010). The role of poleward energy transport in Arctic temperature evolution. *Geophysical Research Letters*, **37**, L14803. 12

Zuidema, P., Baker, B., Han, Y., Intrieri, J., Key, J., Lawson, P., Matrosov, S., Shupe, M., Stone, R. & Uttal, T. (2005). An Arctic springtime mixed-phase cloudy boundary layer observed during SHEBA. *Journal of the Atmospheric Sciences*, **62**, 160–176. 21, 28